THE STUDY OF ULTRA-LOW ENERGY DEPOSITION OF HYDROGENATED AMORPHOUS CARBON THIN FILMS

Teodor Zaharia

Doctor of Philosophy

THE UNIVERSITY OF ASTON IN BIRMINGHAM

March 2007

Summary

This thesis is dedicated to the production and analysis of thin hydrogenated amorphous carbon films. A cascaded arc plasma source was used to produce a high density plasma of hydrocarbon radicals that deposited on a substrate at ultra low energies. The work was intended to create a better understanding of the mechanisms responsible for the film formation, by an extensive analysis on the properties of the films in correlation with the conditions used in the plasma cell.

Two different precursors were used: methane and acetylene. They revealed a very different picture for the mechanism of film formation and properties. Methane was less successful, and the films formed were soft, with poor adhesion to the substrate and decomposing with time. Acetylene was the better option, and the films formed in this case were harder, with better adhesion to the substrate and stable over time. The plasma parameters could be varied to change the character of films, from polymer-like to diamond-like carbon.

Films deposited from methane were grown at low deposition rates, which increased with the increase in process pressure and source power and decreased with the increase in substrate temperature and in hydrogen fraction in the carrier gas. The films had similar hydrogen content, sp^3 fractions, average roughness (R_a) and low hardness. Above a deposition temperature of 350°C graphitization occurred – an increase in the sp^2 fraction.

A deposition mechanism was proposed, based upon the reaction product of the dissociative recombination of CH_4^+. There were small differences between the chemistries in the plasma at low and high precursor flow rates and low and high substrate temperatures; all experimental conditions led to formation of films that were either polymer-like, soft amorphous hydrogenated carbon or graphitic-like in structure.

Films deposited from acetylene were grown at much higher deposition rates on different substrates (silicon, glass and plastics). The film quality increased noticeably with the increase of relative acetylene to argon flow rate, up to a certain value, where saturation occurred. With the increase in substrate temperature and the lowering of the acetylene injection ring position further improvements in film quality were achieved. The deposition process was scaled up to large area (5 × 5 cm) substrates in the later stages of the project.

A deposition mechanism was proposed, based upon the reaction products of the dissociative recombination of $C_2H_2^+$. There were large differences between the chemistry in the plasma at low and medium/high precursor flow rates. This corresponded to large differences in film properties from low to medium flow rates, when films changed their character from polymer-like to diamond-like, whereas the differences between films deposited at medium and high precursor flow rates were small.

Modelling of the film growth on silicon substrates was initiated and it explained the formation of sp^2 and sp^3 bonds at these very low energies. However, further improvements to the model are needed.

Keywords: cascaded arc plasma source, DLC films, sp^3 fraction, nanohardness, hydrogen content.

Acknowledgements

I would like to thank Professor John Sullivan, my supervisor, for the constant help, guidance, availability, patience and friendship he showed me throughout the duration of the project.

I would also like to express my gratitude to Dr. Sayah Saied, for her help and guidance during all those long hours of XPS analysis, peak fitting and spectra interpretation, but most of all for creating a family atmosphere within the group, which made me feel like I was at home.

Thanks are also due to Mr. Andrew Abbot, for all the interesting discussions we had, his help and patience in technical matters and his friendship. I am grateful that he managed to turn me into a proper vacuum engineer and taught me all those technical words and a lot of common British expressions too.

Special thanks go to Dr. Roel Bosch, Dr. Martin Bijker, Mr. Remco Pennings and Mr. Walter Staals, for making me feel welcome at OTB Engineering and creating a friendly atmosphere during the three months I spent in Eindhoven, as well as for their constant guidance and help during the project.

I would also like to thank my family (mum, dad and sister) for lifting my spirits in those difficult times when you feel like giving up and my group of good friends Stefan, George & Simona, Razvan & Ioana, Diana, Livia and Anca. They made me forget about the thousands of miles separating us and still feel like I was part of our group.

I am also grateful to Dr. Baogui Shi, Mr. Gavin Wilson, Dr. Mark Wild, Mr. Marek Havlicek, Mr. Michal Zlapetal, Mr. Bronislav Zlamal, Mr. David Hajny, Miss Simona Pospisilova and Mr. Petr Herzig for helping me with the film analysis and modelling, for the useful discussions we had and for creating a friendly atmosphere within the research group for all these four years.

Last, but not least, I would like to express my gratitude to Monica, whom I met a year ago and felt in love with. I cannot put into words what your love and friendship mean to me.

Table of contents

List of figure captions

List of table captions

1 Introduction

The project presented in this thesis is about the deposition of amorphous hydrogenated carbon thin films with a type of plasma ion beam source with low levels of the degree of ionisation, the cascaded arc plasma source. The aim of the project was to produce good quality amorphous hard hydrogenated carbon films, with submicron thickness (range 100–500 nm), with good mechanical and tribological properties, which could be later reproduced in an in-line industrial process.

The cascaded arc source produces an expanded thermal argon plasma in a vacuum chamber which, after interacting with a hydrocarbon precursor gas, gives rise to a flux of particles (radicals, ions, molecules) with energies of less than 0.5 eV per particle. The vast majority of deposition methods used for formation of good quality (hard) amorphous carbon and amorphous hydrogenated carbon films require energies of grater than 10 eV per carbon particle. A model to explain the formation of relatively hard amorphous hydrogenated carbon films with the cascaded plasma source was adopted.

In the early stages of the project methane was used as precursor gas and an argon-3% hydrogen mixture as carrier gas. Later on, the carrier gas was changed to pure argon. Due to unsatisfactory results the precursor gas was changed to acetylene and most of the experiments were performed with pure argon as carrier gas. The experimental set-up was modified several times during the length of the project, the most important modification being the extension of the deposition chamber and the use of a new design molybdenum cascaded arc plasma source - an upgraded version of an initial copper one.

The thesis first introduces a literature survey (Chapter 2) on DLC films, their methods of deposition, including the expanding thermal plasma technique, their growth mechanisms and applications. This is followed by the experimental methods and analytical tools (Chapter 3) used throughout the project. The results are presented in Chapter 4, followed by an attempt to model the film formation (Chapter 5). The overall discussions are presented in Chapter 6 and general conclusions of the work are drawn in Chapter 7.

2 Literature survey

2.1 Amorphous carbon

The interest in diamond thin films has increased exponentially in the last two decades due to the exceptional properties of this material that makes it suitable for various applications. In the quest for producing diamond films in a laboratory environment, another form of carbon has been discovered: the amorphous deposited carbon [1, 2 (p. 131), 3 (p. 2)]. This type of carbon film is characterised by the loss of crystalline structure and the wide range of properties it posses. The properties depend on the deposition conditions and films formed can vary from soft polymer-like to hard diamond-like. Most of the deposition techniques involve a plasma state, which is used to create an environment with active particles, from which carbonaceous material can be grown on a substrate. Commonly, hydrocarbon precursors are used in the deposition process, so not only carbon is incorporated in the film, but hydrogen also. The material thus obtained was denoted as amorphous hydrogenated carbon.

2.1.1 Bonding types in carbon and amorphous carbon

Carbon forms a great variety of crystalline and disordered structures because it exists in three hybridisations, sp^3, sp^2 and sp^1 (see Figure 2.1) [2 (p. 129)].

In the sp^3 hybridisation each of the four valance electrons of carbon enters a tetrahedrally oriented orbital, which makes a strong σ bond with an orbital of a neighbouring atom. For this reason these orbitals are called σ orbitals.

In the sp^2 hybridisation three of the four valance electrons belong to trigonally directed σ orbitals, which form strong σ bonds in a plane. The fourth electron of the sp^2 atom enters a $p\pi$ orbital, which is perpendicular to the other three. This π orbital forms a weaker π bond with another π orbital of one of the neighbouring atoms.

In the sp^1 hybridisation, two of the four valance electrons belong to σ orbitals, each oriented along the x axis, in opposite directions, to form σ bonds with adjacent atoms. The other two electrons belong to $p\pi$ orbitals oriented in the y and z directions.

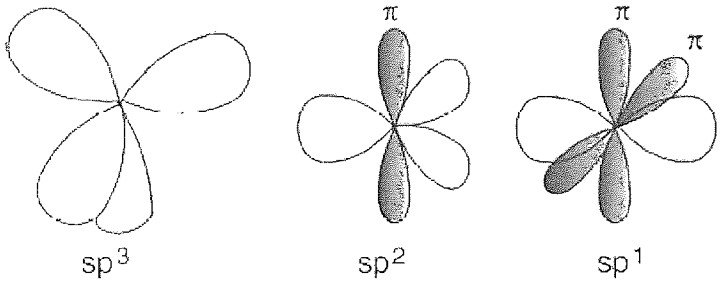

Figure 2.1 The sp^3, sp^2 and sp^1 hybridised bonding (from [2 (p. 130)])

The sp^1 bonding type can be found mostly in polymers and is of limited importance to the present work.

An example of sp^2 hybridization is graphite. The three strong σ bonds (energy 7.43 eV) form planes with two dimensional hexagonal configurations. Bulk graphite consists of a stacking of planes, with a weak interplanar bonding (energy 0.86 eV). This structure explains the anisotropic structure of graphite (Figure 2.2a). Within the plane the electron of the π bonding types are free, and lead to the high electrical and thermal conduction in the planes. Between the planes the conductive properties are poor and the bonding is weak, leading to practical applications such as: batteries, carbon brushes, electrodes for electrical arc furnaces, rods in the nuclear power plants, aerospace industry applications (composites of graphite) and as a lubricant [4 (p. 43), 5].

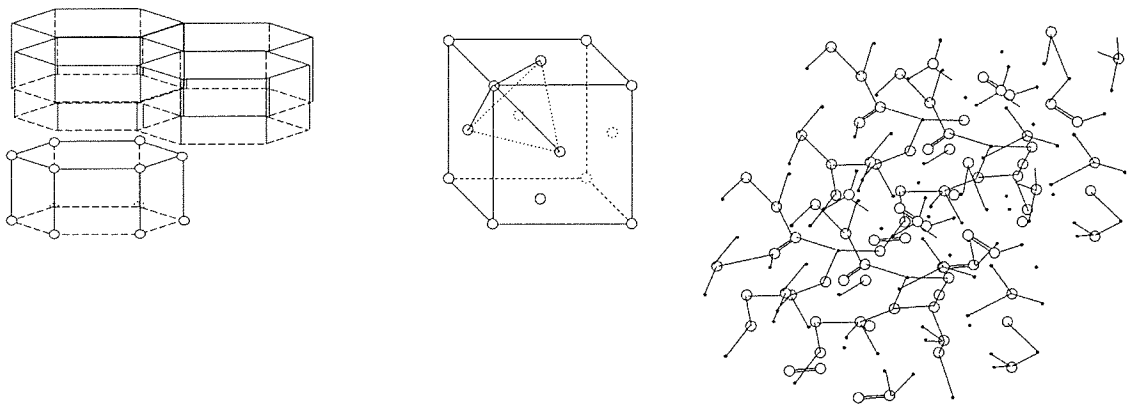

a) b) c)

Figure 2.2 Schematic representation of the structure of (a) graphite, (b) diamond and (c) amorphous hydrogenated carbon, with hydrogen depicted as the solid circles (after [6])

Diamond is an example of sp^3 hybridization, with four equivalent strong σ bonds in a tetrahedral configuration, with a C-C bond energy of 7.41 eV. Its structure is Face Centred Cubic (FCC), with a cubic unit cell (Figure 2.2b). Diamond has a high optical band gap, is chemically inert and extremely hard. Common applications of diamond films include: protective coatings on cutting tools, thermal devices (heat sink), optical devices, protective optical coatings and electronic devices (FET, field emission, UV photodetectors) [4 (p. 302), 7].

In amorphous carbon and amorphous hydrogenated carbon (a-C and a-C:H) all three bonding types are present (see Figure 2.2c). The structure can be considered as a random network of C atoms in the sp^2 and sp^3 hybridization state, with hydrogen saturating the dangling bonds. The amount of sp^1 bonds present in almost negligible. The properties of these films are influenced by two main factors: the ratio of sp^3 to sp^2 C–C bonds and the amount of hydrogen present in the films. With increasing sp^3/sp^2 ratio and decreasing hydrogen content the film changes from soft, polymer-like to hard, diamond-like.

2.1.2 Diamond like carbon

Diamond-like carbon (DLC) is a metastable form of amorphous carbon containing a significant fraction of sp^3 bonds. DLC has some properties similar to diamond, such as high mechanical hardness, chemical inertness, optical transparency and a wide band gap [2 (p. 129)]. These properties are achieved in an isotropic disordered thin film, which is much cheaper and easier to produce than diamond itself. DLC can consist of amorphous carbon (a-C), but also of its hydrogenated alloy, amorphous hydrogenated carbon (a-C:H). The presence of hydrogen confers to DLC other important properties, such as low friction and low wear coefficient [8]; these open up the possibility for new applications.

The most important applications where DLC films have been investigated can be categorised in: electronic applications; mechanical applications, as protective coatings; optical coatings and biomedical applications. These will be discussed later, in a separate section.

It is useful to present the different forms of amorphous C–H alloys on a ternary phase diagram, as depicted in Figure 2.3. There are many forms of a-Cs with disordered

graphitic ordering, such a soot, chars, glassy carbon, and evaporated a-C. These are situated in the lower left corner of the triangle. The shaded area in the right corner defines the area where no stable films can be formed. The region is limited by the two hydrocarbon polymers polyethylene $(-CH_2-CH_2)_n$ and polyacetylene $(-CH-CH)_n$. Any further incorporation of hydrogen into these polymers would determine the break-up of C–C bonds, which would lead to shorter and shorter chains and then to the production of volatile products. [9].

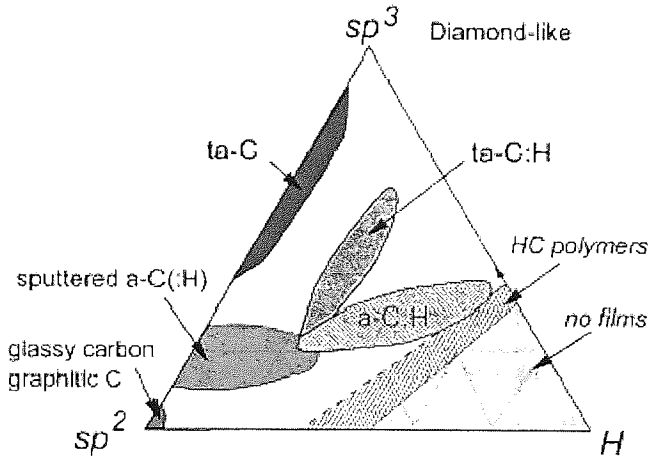

Figure 2.3 Ternary phase diagram of bonding in amorphous carbon – hydrogen alloys (from [2 (p. 131)])

Towards the upper corner of the triangle the fraction of sp^3 bonding reaches a high degree and the a-C formed is denoted as tetrahedral amorphous carbon (ta-C). A range of depositions methods, of which the most common is plasma enhanced chemical vapour deposition (PECVD), are able to produce a-C:H, depicted into the interior of the triangle. Although this is diamond-like, it is seen from Figure 2.3 that the content of sp^3 bonds is not so large, and its hydrogen content is rather large. High plasma density reactors can produce a material with more sp^3 bonds and less hydrogen, which has been called hydrogenated tetrahedral amorphous carbon (ta-C:H) [2 (p. 131)].

2.1.3 Properties of amorphous hydrogenated carbon films

The properties of a-C:H have conventionally been categorised into three different regimes, according to the ion energy per atom or the bias voltage used in the deposition process [2 (p. 211)].

At low ion energies (0-10 eV), the films should have high hydrogen content, high sp^3 fraction, low density and a large band gap, in the range 1.8–4 eV. They are called polymer-like a-C:H or soft a-C:H films. This is in contradiction with our findings, which show that film properties can vary from polymer-like to diamond-like even at very low energies below 1eV.

At intermediate ion energies (10-200eV) the hydrogen content and the sp^3 fraction decrease, the density is maximised and the band gap lies in the range 1.2–1.7 eV. The number of C–C sp^3 bonds reaches its maximum and the films have diamond-like character.

At higher ion energies (more than 200 eV) the hydrogen content decreases even further and the bonding becomes predominantly sp^2-like. These films are graphitic.

Besides the ion energy, another factor that influences the properties of a-C:H films is the precursor molecule; important are the number of C atoms present in the molecule and the number of H atoms corresponding to a C atom (H/C ratio). When scaled to the reduced energy per carbon atom, the maximum density for acetylene, for example, will occur at twice the bias voltage used for methane, in the same experimental system. The hydrogen content in the film will always be lower than the H/C ratio in the precursor gas molecule, due to chemical sputtering – the removal of H from a C–H bond by the incoming ions.

A comparison between the properties of amorphous hydrogenated carbons with those of some reference materials, such as diamond, graphite and polyethylene is given in Table 2.1.

Table 2.1 Properties of a-C:H (from [2 (p. 130)] with the value for gap energy of diamond corrected from 55 to 5.5eV)

	Sp^3 [%]	H [%]	Density [g/cm^3]	Gap [eV]	Hardness [GPa]
Diamond	100	0	3.515	5.5	100
Graphite	0	0	2.267	0	
C_{60}	0	0		1.6	
Glassy C	0	0	1.3-1.55	0.01	3
Evaporated C	0	0	1.9	0.4-0.7	3
Sputtered C	5	0	2.2	0.5	
ta-C	80-88	0	3.1	2.5	80
a-C:H hard	40	30-40	1.6-2.2	1.1-1.7	10-20
a-C:H soft	60	40-50	1.2-1.6	1.7-4	<10
ta-C:H	70	30	2.4	2.0-2.5	50
Polyethylene	100	67	0.92	6	0.01

2.2 Deposition techniques used in the production of hydrogenated amorphous carbon

Typical deposition systems for the production of amorphous hydrogenated carbon usually involve a plasma state. Plasma is a gas that is composed of free radicals, ions, molecules and electrons [10]. It behaves differently to a neutral gas, and is considered the fourth state of matter [11]. During the last decades, many different types of discharges have been used in the field of plasma surface modifications, etching and deposition. The most common methods are Direct Current (DC) glow discharges and Radio Frequency (RF) plasmas. Also widely used in the last decades are microwaves and pulsed plasma techniques.

The simplest DC plasma consists of a gas at reduced pressure introduced in a tube that has at its ends two electrodes, between which a uniform and constant electric field exists. A charge between these electrodes will be accelerated by the electrical field and will produce secondary ionizations. In time, ionization cascade takes place and, at low pressures, this leads to a glow discharge [10]. The ionisation in the gas, which is said to be in the plasma state, is determined by the parameters of the outer circuit. The potential drop between the anode and cathode is not linear, most of the potential being dropped over the small sheath that forms in front of the cathode. The typical regions present in a DC plasma are presented in Figure 2.4

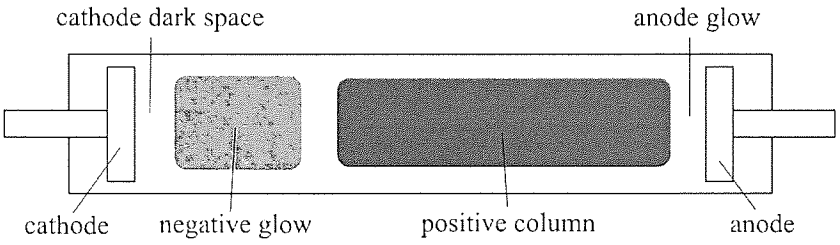

Figure 2.4 Regions in a DC plasma

The substrate is usually mounted at the cathode area where the high energy ions arrive and the deposition takes place.

A typical RF plasma system consists of a gas introduced in a reactor with two electrodes of different areas. The smaller electrode is usually capacitively coupled to an RF power supply. The larger electrode, which consists commonly of the chamber walls, is earthed (see Figure 2.5).

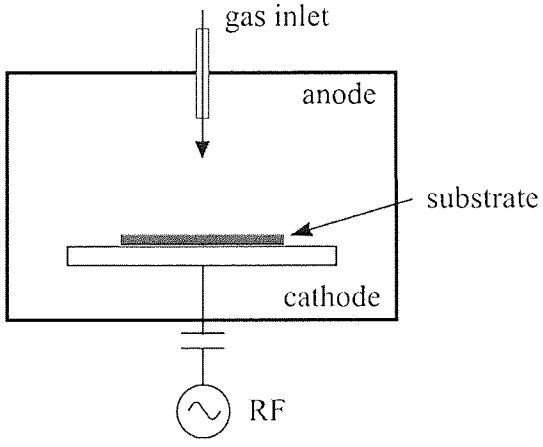

Figure 2.5 PECVD system (after [2 (p. 132)])

The RF power produces a plasma between the two electrodes. Because the electrons have higher mobility than the ions a sheath of spatial positive charges is formed next to each electrode. The plasma bulk acquires a positive potential in respect to the electrodes and the electrodes acquire DC self-bias voltages equal to the peak RF voltage. The RF voltage is divided between the two sheaths according to their inverse capacitance. Thus, the DC self bias voltage varies inversely with the square of the electrodes area [12], if equal ion currents flow to both electrodes:

$$\frac{V_1}{V_2} = \left(\frac{A_2}{A_1}\right)^2 \qquad \textbf{Eqn 2.1}$$

The smaller electrode (area A_1) with the smaller capacitance acquires the larger bias voltage and becomes negative with respect to the larger electrode (area A_2). For this reason the smaller electrode is sometimes denoted as cathode, whereas the larger electrode is denoted as anode. The substrate is mounted on the cathode, towards which the positive ions are accelerated by the negative voltage through the cathode sheath.

If an electrically floating surface is placed in contact with the plasma, it will rapidly charge negatively because of greater flux of electrons compared to ions. At some point, the surface will be sufficiently negative that enough electrons will be repelled to cause an equal flux of ions and electrons. The potential on this surface is known as the floating potential and it is typically negative with respect to the plasma potential. it is given by [12]

$$V_f = -\frac{k_B T_e}{2e}\left(\frac{m_i}{2\pi m_e}\right) \qquad \textbf{Eqn 2.2}$$

where m_e and m_i are the electron and ion masses and T_e the electron temperature.

2.2.1 Sputtering

2.2.1.1 Magnetron sputtering

Sputtering is a common deposition technique of DLC in industrial processes [13 ,14]. A graphite electrode is sputtered by an argon DC or RF plasma. Because of the low production rate of sputtered graphite, magnets are often used to increase the deposition rate in a technique known as magnetron sputtering (Figure 2.6). The magnets are placed behind the target to cause the electrons to spiral and increase their path length, in this way increasing the degree of ionisation in the plasma [2 (p. 133)]. If the magnetic field is configured in such a way that it forces the Ar ions to bombard the substrate, this gives rise to a so called "unbalanced magnetron" [15]. The energy of the particles bombarding the substrate can be varied by applying an additional DC bias or pulsed DC bias [16] on the substrate.

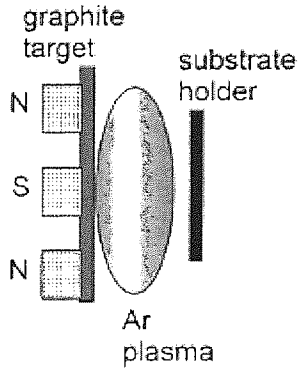

Figure 2.6 Schematic of a magnetron sputtering deposition (from [2 (p. 132)])

The ratio of ions/atoms arriving at the substrate dictates the growth rate and quality of the films formed. The deposition conditions can also be optimised to enhance the quality of the deposited films.

Different types of amorphous carbonaceous films can be produced with this technique, depending on the gases used in the sputtering reactor. For example, the films formed can be hydrogenated, if methane or hydrogen is used as precursor gas or nitrogenated, if nitrogen is used as a growth precursor. If the precursor gas is a carbon gas that is decomposed on a metallic sputtering target and then sputtered on to the substrate, the films formed are Me:CH.

2.2.1.2 Ion beam sputtering

If, instead of the argon plasma, an argon ion beam is used to sputter from the graphite target and create the carbon flux the technique is called ion beam sputtering (Figure 2.7). A second beam of argon ions can be used to bombard the growing film, with the purpose of increasing the density and the number of sp^3 bonds. This technique is called ion beam assisted deposition (IBAD) [2 (p. 133), 17].

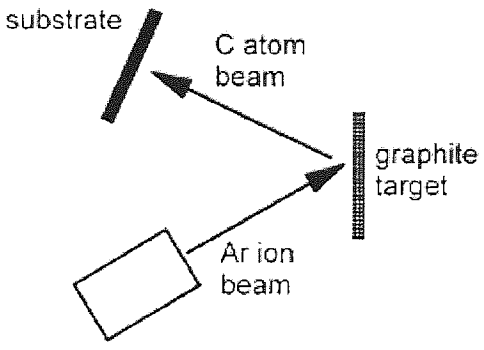

Figure 2.7 Schematic of ion beam sputtering deposition (from [2 (p. 132)])

The advantage of sputtering is that it makes it possible to deposit many different materials with a similar arrangement in a reactor with easily controllable deposition conditions. In the case of carbon sputtering, the formed DLC film properties can be adjusted by the plasma power and pressure and do not depend on the reactor geometry. Because of the low density plasma used, the ratio of ions to neutrals is relatively low, so it will produce softer DLC films. Methods to enhance the degree of ionisation in the plasma were developed [18], in order to produce sputtered DLC films with higher sp^3 fractions.

2.2.2 Plasma enhanced chemical vapour deposition (PECVD)

The most common laboratory deposition method of DLC is RF PECVD. The reactor consists of a smaller electrode (cathode), capacitively coupled to an RF power supply, inserted in a vacuum chamber. The larger electrode is made by the chamber walls, as shown in Figure 2.5. The substrate in mounted on the cathode, which acquires enough negative DC bias to accelerate the positive ions through the cathodic sheath. For DLC growth, a low pressure is desired during deposition, to maximise the fraction of ions to radicals in the plasma. The ions can loose energy by collisions in the cathode sheath; the low pressure would minimise these collisions and maintain a narrow ion energy distribution [19]. The low pressure could also lead to high bombardment energies that could cause "damage" to the substrate and the films. However, at 50 mTorr, the ions are only about 10% of the film-forming flux and the mean ion energy is only 0.4 of the sheath voltage [2 (p. 137)].

If a too low pressure is used, the plasma would no longer strike. With the help of a magnetic field the plasma can be confined to increase the electron path length and the ionisation efficiency. This would allow the plasma to operate at lower pressures and was later developed in a new deposition technique called plasma beam source (PBS) [20]. The confined plasma then exits through a grid at ground potential and arrives at the substrate to form high quality a-C:H.

If an additional RF signal is inductively coupled to the plasma through a single coil, a resonant transfer of power can be achieved into the plasma bulk. The resulting deposition technique was called the electron cyclotron wave resonance (ECWR). The plasma can exit the chamber as a neutral beam through a grounded grid electrode. The ECWR source produces an extremely high density plasma of 10^{12} cm^{-3}, with an independent control of the ion energy and ion current density [21]. It gives a narrow ion energy distribution. The ECWR produces ta-C:H at a much higher growth rate (1.5 nm/s) than PBS and gives uniform deposition over a diameter of 10 cm, which is scalable to larger values. It is the first industrialised, high density PECVD source for DLC [2 (p. 140)].

The properties of the deposited a-C:H film depend on the precursor gas used in the PECVD reactor. In the beginning gases with low ionisation potential, such as benzene, were used to achieve the maximum growth rates. Later on it was clear that to produce harder films required for mechanical applications the hydrogen content had to be reduced. That meant choosing a precursor with low H/C ratio (i.e. acetylene), as it was observed that the final H incorporation in the film is strongly dependent on the initial H/C ratio in the precursor gas [2 (p. 140)]. This is why acetylene is the preferred source gas for mechanical applications. The disadvantage of using acetylene is that it commonly has a high nitrogen impurity and it is very expensive in high purity form. The nitrogen impurity causes a problem for electronic applications, because nitrogen can cause a doping effect, which is not desired. Methane is the better option, because it is relatively cheap in high purity form. The disadvantages are that growth rate is lower and the amount of hydrogen incorporated into the film is high [2 (p. 141)].

2.2.3 Pulsed Laser Deposition

In the pulsed laser deposition (PLD), a pulsed excimer laser gives very short, intense energy pulses which are used as an intense plasma to vaporise different materials. The plasma then expands towards the substrate. The mean energy of the ions created by the plasma is proportional to the laser fluence concentrated at the target spot.

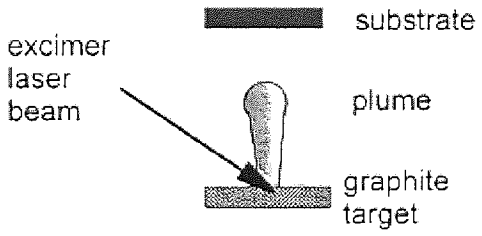

Figure 2.8 Schematics of the PLD principle (from [2 (p. 132)])

In this way pulsed laser deposition (PLD) produces high density ta-C films. The advantage of PLD is that it is versatile laboratory scale method, which can be used to deposit many different materials, from high temperature superconductors to hard coatings [2 (p. 135), 22].

2.2.4 Ion beam deposition

In an ion beam system carbon ions are produced by the plasma sputtering of a graphite cathode in an ion source. Alternatively a hydrocarbon gas (such as methane or acetylene) is ionised in a plasma [23]. An ion beam is extracted through a grid from the plasma source using a bias voltage.

The carbon or hydrocarbon ions are then accelerated to form the ion beam in the high vacuum deposition chamber. In both cases the beam also contains a large flux of unionised neutral species. Ion beam sources run best at higher ion energies of 100-1000 eV [2 (p. 132)].

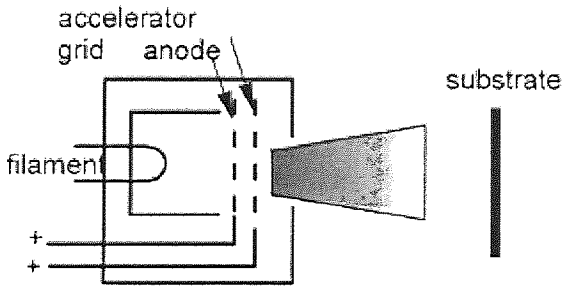

Figure 2.9 Schematics of an ion beam deposition system (from [2 (p. 132)])

A variant of the ion beam technique are the "saddle field" ion sources. The operation of these dc-energized cold cathode sources is based on the effect that electrons describe long oscillatory paths in the presence of an electrostatic saddle potential field. The gas present in the source is thus ionised and the discharge maintained at considerably lower pressures than in conventional cold cathode tubes without a magnetic field. Depending on the symmetry of the saddle-field, beams of various cross-sections are obtained: an axial field produces a high-intensity pencil beam, planar fields give rise to divergent beams. The beam contains a high proportion of energetic neutrals, or may be fully neutralized on emerging from the cathode aperture, depending on source geometry and applied field. Evaporation on a surface exposed to a saddle-field beam combines rapid deposition with strong adhesion characteristic of sputtered films. Applications include preparation of specimens for TEM and SEM, cleaning and profiling for surface analysis, ion beam machining and sputtering [24].

Another variant of the ion beam technique are the cascaded arc plasma sources. These are presented in more details in the following sections.

2.2.4.1 DC arc plasma

A variant of the DC plasma is the DC arc. This type of discharge has a few distinctive characteristics: the current density is very high and can reach up to 100 A/cm^2, much higher than in the case of glow discharges; the cathodic potential drop (~10V) is much smaller than for glow discharges [25]. In typical conditions, such as high pressures, forced cooling of the electrodes and the use of gas jets, the potential drop can be very

high, with values in the order of few tens of kV; the glow of the plasma in the arc is much brighter than for other types of plasma, especially in high pressure operating conditions.

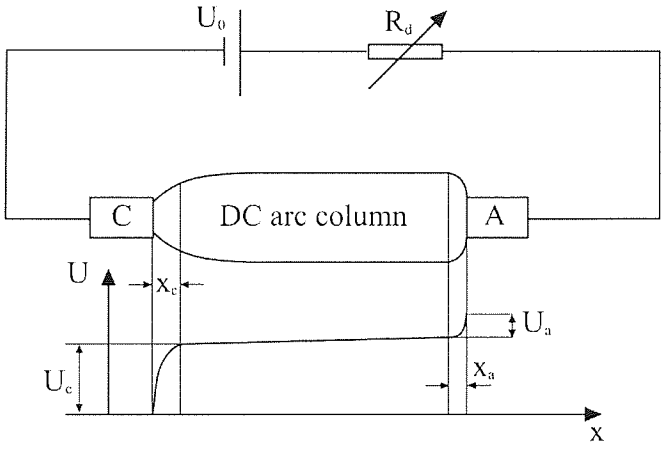

Figure 2.10 Potential distribution in the DC arc plasma. For clarity the cathodic and anodic area of the discharge are drawn longer than in reality, where x_a, x_c << the length of the arc column (from [25]).

In the space between the electrodes of the arc column, three different regions can be differentiated: the cathodic drop, the DC arc column and the anodic drop (Figure 2.10). The arc column is much longer than the anodic and cathodic regions, which are thin sheaths (tens of mm) of spatial charges. They have the role of maintaining the continuity of the electric current at the plasma-electrode interfaces.

In the arc column there is a gradient of potential of the electric field (Figure 2.10). This gradient is created by the equilibrium between the energy given by the electric field to the electrons, which form the active component of the plasma, due to their increased mobility, and the energy given by the electrons in the inelastic collisions with the atoms of the gas. Due to the high current densities and to the high operating pressures the plasma in the arc column can be considered in local thermal equilibrium. Consequently the electrons, positive ions and atoms have Maxwell distribution functions. At low pressures the temperature of electrons is higher than of ions and atoms. The temperatures become equal at high pressures (higher than 100 Torr).

The ionisation and excitation processes in the plasma are determined by the energetic electrons, towards the end of the distribution function and the probability of these processes is significantly dependent on the temperature of electrons. Local thermal

equilibrium is determined by the numerous collisions between the electrons and the heavy particles. The difference between the temperature of electrons and that of gas heavy particles is determined by the energy gain by the electrons during a mean free path (i.e. between consecutive collisions) $eE\lambda_e$ and the average kinetic energy of electrons $k_B T_e$. From the energy conservation equation, one can get the following relation for the temperature difference between the electrons and the heavy particles in the gas [25] (atoms and corresponding ions):

$$\frac{T_e - T_g}{T_e} = 0.13 \frac{m_g}{m_e} \left(\frac{eE\lambda_e}{k_B T_e} \right)^2 \qquad \text{Eqn 2.3}$$

where λ_e is the mean free path of electrons, $\frac{m_g}{m_e}$ is the ratio between the mass of the heavy particles in the gas and the mass of electron, T_e and T_g are the temperatures of electrons and of the heavy particles in the gas, respectively.

The DC arc can be used as a light source, when it is burning in an enclosed space, the arc column being delimitated by the walls of a quartz tube; in welding installations for metals and as a system of producing hot plasma jets in plasmotron devices [25]. The plasmotrons use the plasma from the electric arc, formed in a gas jet, for different applications: surface treatments, metals welding, etc.

2.2.4.2 The cascaded arc plasma source

In 1981 the flowing cascaded arc was introduced as a powerful particle source. A high-pressure source produces an intense DC arc plasma, which than expands supersonically into a high vacuum, giving rise to large fluxes of ions and radicals [6, 26, 27]. The main advantages of this method over the common deposition methods are the high deposition rates and the possibility to separate the three functions of production, transport and deposition [6, 28].

While the carrier gas (usually argon) is flowing through the plasma channel, a voltage is applied on the electrode and this gives rise to a DC discharge (see Figure 2.11). The potential drop between the electrode and the grounded anode sustain this glow discharge

(flowing DC arc plasma). The electrically insulated cascade plates between the anode and electrode (cathode) have the role to make the potential drop gradual, in order to prevent the formation of high electric fields which could break through the insulating material between the plates.

Typically, the carrier gas is injected at a pressure of 100 to 500 mbar (75 to 375 Torr) at the beginning of the arc channel. The flow rate is typically 2.5 standard litres per minute (slm). The electron temperature is approximately constant in the axial direction in the arc channel and is around 15000 K for standard operating conditions. The heavy particles temperature reaches a value of 12000 K in the middle of the arc. The ionisation degree of the plasma in the arc channel is typically 2 - 10%, depending on the composition of carrier gas, the flow rates used and the pressure in the channel and vessel. Hydrogen can be injected through the cathode space or in the nozzle. To prevent obstruction of the channel by formation of graphite, the precursor gas is injected through the nozzle at the end of the anode or via an injection ring [6]

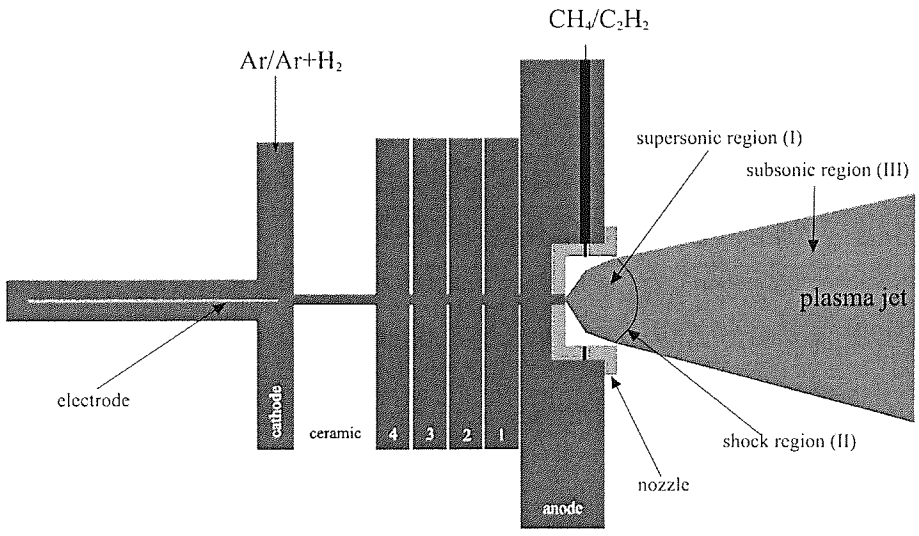

Figure 2.11 Cascaded arc plasma source

The plasma expands supersonically through the nozzle into a low-pressure vacuum chamber, usually pumped down by a Roots blower backed up by a rotary pump. This selection of pumps is used because it is able to pump out large quantities of gas in a short period of time. This gives the desired pressure in the arc channel and in the vacuum chamber for the source to operate at optimum conditions. A beam of ions, electrons (up to 10%) and atoms emerges from the source. Three regions can be distinguished in this

expanding plasma beam: a region of supersonic expansion, a shock region and a subsonic expansion region (see Figure 2.11). Model calculations and measurements have been carried out on the plasma parameters in these three regions, as well as in the arc channel [29–34].

In region I the particles are accelerated to supersonic velocities (~4000 m/s). During this expansion the electron and heavy particles temperature decreases to ~2500 K., and the electron density decreases strongly to the order of 10^{13} cm^{-3}. At a distance of about 5 – 10 cm from the nozzle (depending on the chamber pressure) a shock region exists (region II). The temperatures and the electron density rise again to 4000 K and 10^{14} cm^{-3} respectively. Beyond the shock the plasma expands subsonically and the plasma composition remains constant (region III). The temperatures drop to values in the range 1500-2000 K [6, 30].

The cascaded arc plasma source developed by OTB Engineering consists of a cathode fixed in a torch holder by a shaft clamp, a ceramic top, a stack of 4 insulated cascaded plates and an anode. The 4 cascaded plates have a 4-mm inner bore and are insulated with 1-mm thick boron nitride discs. The anode plate incorporates a conical shaped ring – the nozzle. All these together form the plasma channel. The cathode is a 2.4-mm tungsten electrode tip situated at the far end of the plasma channel (see pictures in Figure 2.12a and b). The arc is vacuum-sealed with O-rings and the cathode, anode and cascade plates are all water-cooled (Figure 2.12e).

When the hydrocarbon gas is introduced in the reactor, it is effectively dissociated in to carbon-containing radicals and in excited and ionised carbon particles by the argon thermal plasma jet. A high density flux of radicals (CH, CH_2, C_2H), ions and atoms (carbon, hydrogen) is obtained through charge exchange reactions with the argon ions, and the plasma cools down. This flux of radicals is directed toward the substrate situated on the sample support. Deposition rates of tens of nanometres per second have been achieved for amorphous hydrogenated carbon films [6]. The main feature of the method is the separation of the three functions of production, transport and deposition. Varying the reactor parameters can control the type, quality and growth rates of the films. For higher substrate temperatures and with addition of H_2 to the gas flow, the growth rate is strongly reduced.

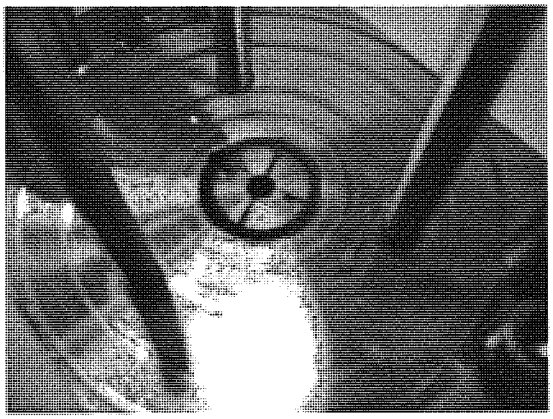

a

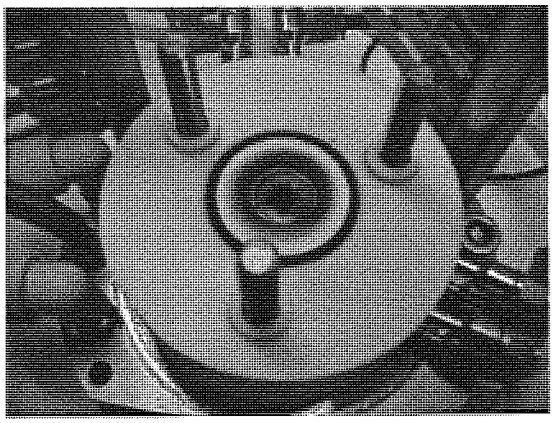

b

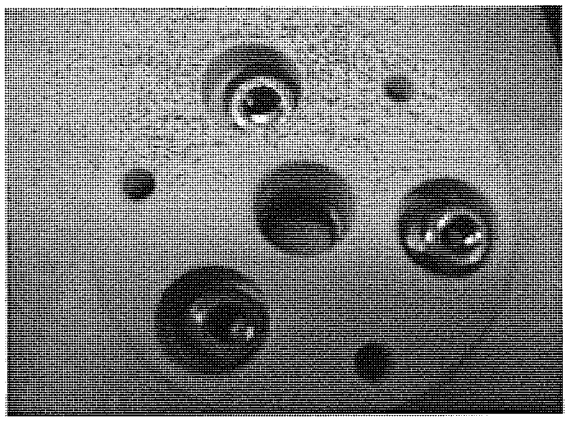

c

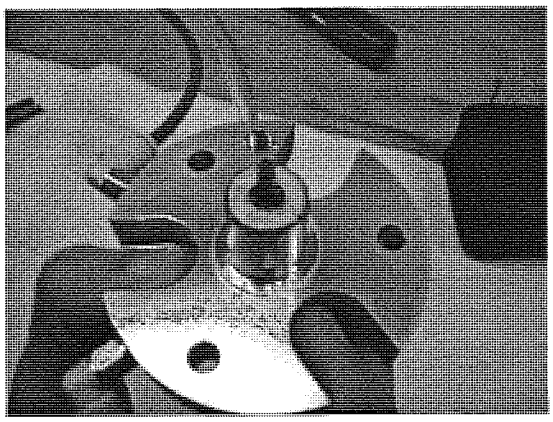

d

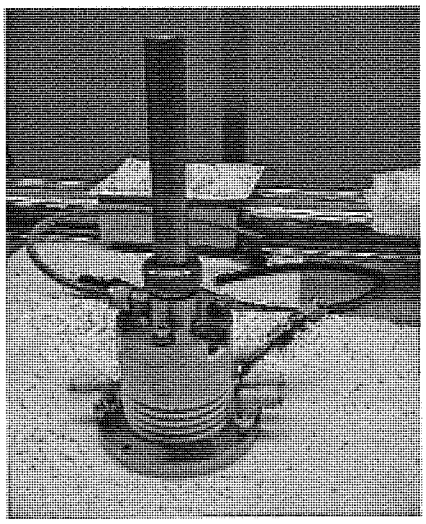

e

Figure 2.12: a) anode; b) cascade plates; c) ceramic; d) torch holder with electrode; e) cascaded arc plasma source

2.2.5 Mass selected ion beam

It is often desirable to have a controlled deposition from a single ion species at defined ion energy. This is achieved by mass selected ion beam deposition (MSIB). Carbon ions are produced in an ion source from a graphite target with a low spread of energy (1 – 10eV), then accelerated to 5-40 keV and passed through a magnetic filter. This filters out any neutrals and selects ions with a $\frac{e}{m}$ ratio corresponding to the C^+ ion. The ions are then decelerated to the desired ion energy by an electrostatic lens and the beam is focused on the substrate, situated in high vacuum (10^{-8} Torr), to produce a ta-C film. The advantages of MSIB are: controllable deposition species and energy; filtering out the non energetic species and the ability to dope by switching the ion species. The disadvantages are the very low deposition rates (0.0001 nm/sec) and the high cost and size of the apparatus [2 (p. 133), 35].

2.2.6 Filtered cathodic vacuum arc

A method for producing very hard DLC films is the filtered cathodic vacuum arc method. An arc is initiated in a high vacuum by touching the graphite cathode with a small carbon striker electrode and withdrawing the striker. This produces an energetic plasma with a high ion density of up to 10^{13} cm^{-3} (see Figure 2.13) [2 (p. 133)].

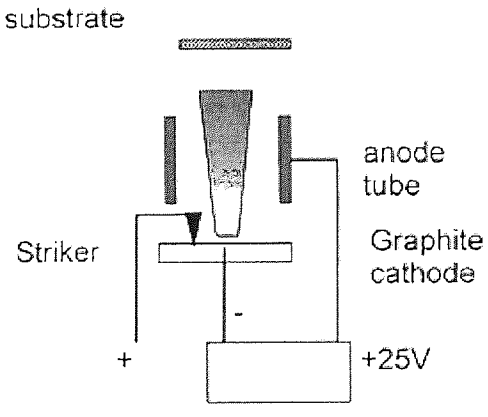

Figure 2.13 Schematic of the FCVA system (from [2 (p. 132)])

The plasma is passed through a toroidal magnetic filter duct to mass select and filter out the undesired particles. This is known as filtered cathodic vacuum arc (FCVA). This filter

raises the ionisation degree in the plasma to nearly 100% towards the end of the filter. The highly ionised dense plasma is then extracted towards the substrate where it deposits the ta-C film.

The plasma has a mean ion energy of 10–30 eV, depending on the arc parameters, when it reaches the cathode. A DC or RF self bias voltage can be used to increase the incident ion energy.

The advantages of the FCVA are that it produces a highly ionised plasma with an energetic species, a narrow ion energy distribution, but the growth rates are low (~1nm/s) and the overall cost of the system is high. The depositing beam in FCVA is a neutral plasma beam so that it can deposit onto insulating substrates.

2.3 Deposition mechanism of amorphous hydrogenated carbon films

2.3.1 Deposition when ion energy is above the penetration limit

The existing deposition models state that high sp^3 content material should not be formed at low energies (less than 6 eV).

Sub-plantation models, proposed by Robertson [2 (p. 143)] and Lifshitz [36], assumes subsurface implantation of energetic species generates an increase in density, which leads to an increase in sp^3 bonding. In his review of the subject, Roberson [2 (p. 144)] suggests that the process responsible for deposition of DLC films with high sp^3 bonding is a physical process, ion bombardment. With the conventional deposition methods, the highest sp^3 ratios, and thus the best quality unhydrogenated material, are formed by C+ ions with an optimum energy of around 100 eV per incident carbon atom. The model calculates a penetration threshold energy equal to the sum of the surface binding energy (7.4 eV) and the displacement energy; below the threshold limit penetration of the surface does not occur and therefore diamond like carbon material (high sp^3 content) should not be formed.

An alternative thermal spike model, proposed by Hofsass [37] assumes that all excess energy generated by ion impact is converted to thermal energy which then diffuses

outwards, favouring sp^3 bonding during atomic rearrangements. According to this model, the required energy for sp^3 bond formation falls in the range 50 to 2000 eV.

McKenzie et al [38] suggested that the compressive stress generated during film growth is the cause of the high sp^3 bond content in the films, where the optimum energy for formation lies in the interval 15 to 70 eV.

In the model proposed by Koponen et al [39] the formation of diamond like bonding is attributed to transient high pressure created by the energetic ion impact. The relaxation to energetically favoured graphitic state is assumed to proceed through a succession of metastable states.

Even the more recent molecular simulations by Marks [40] show that a threshold energy of around 6 eV is required for the formation of sp^3 σ bonding in these films. These simulations are based on a model of surface insertion in which energetic burial leads to the simultaneous processes of sp^3 promotion, densification, stress generation and surface growth.

All the above models apply to the formation of unhydrogenated amorphous carbon material, but the energies per carbon atom are expected to be similar in the case of hydroganated material. The presence of hydrogen in the precursor gas is known to favour the formation of sp^3 rich carbon systems and to enhance the degree of disorder in amorphous carbon [41]. Robertson [2 (p. 150)] identifies many processes occurring in the depositon of a-C:H, as shown in Figure 2.14. The fact that the ions still play a critical role in the deposition process [2 (p. 150), 42, 43] is confirmed by the strong dependence of the film properties on the ion energies. A typical PECVD system used for the deposition of amorphous hydrogenated carbon has an ion flux fraction of about 10% and can use different source gases such as methane, acetylene or benzene.

The action of ions is still by subplantation [2 (p. 150), 42]. A molecular ion that arrives at the surface of the film will break and transfer its energy evenly to the atomic ions formed. Then, each atomic ion will use this energy to subplant separately into the film surface.

For an overall "picture" of the growth mechanism it should be taken into account that there are chemical processes involving the neutrals, besides the physical processes of dehydrogenation, in which hydrogen is removed from C–H bonds at the film surface, and subplantation.

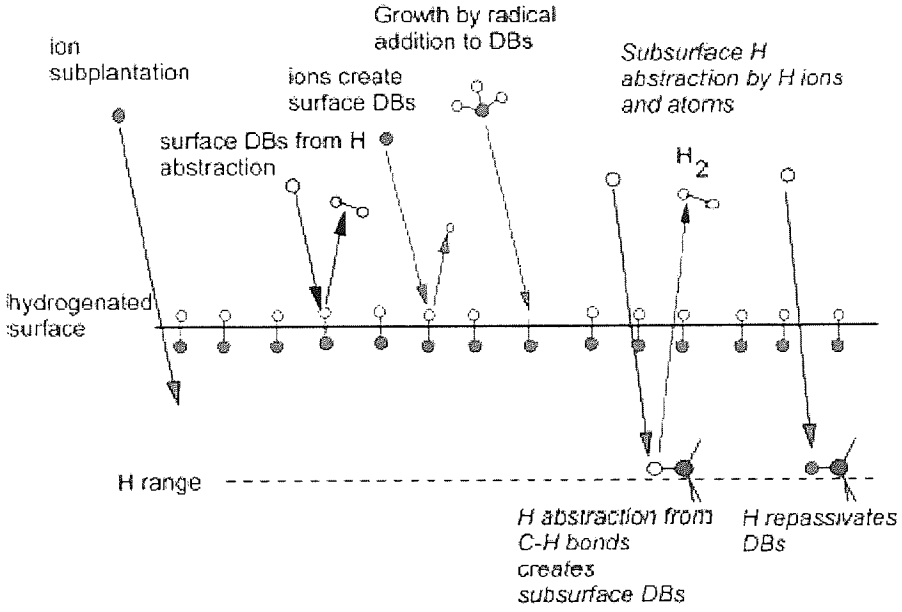

Figure 2.14 - Processes in the growth mechanism of a-C:H (from [2 (p. 150)])

In general, three stages can be distinguished in a plasma deposition system: the reactions that take place in the plasma (dissociation, ionisation etc.), the plasma–surface interaction and the subsurface reactions that happen in the film.

The plasma reactions between the neutrals are driven by the energetic electrons, as defined by the electron energy distribution (EED). Secondary reaction, such as polymerisation, also take place producing other neutral species, even though the undissociated source gas molecules are still the dominant species in the plasma [2 (p. 151)].

At the surface of the growing film a small fraction of ions and a large fraction of neutrals arrive. The ions will be mainly ionised source gas molecules whereas the neutrals will be undissociated gas molecules, mono radicals, di-radicals and other unsaturated species. Also, a large amount of atomic hydrogen H will be present in the plasma. The neutral

species contribute also to growth because the mass deposition rate of the films formed exceeds the rate due only to ions [2 (p. 151)].

It was observed that the growth rate decreases with temperature. This was first attributed to low absorption of the neutrals into the surface, which, as the temperature increased, would be released from the film. Later it was proven that the temperature dependence is due to etching of the film by atomic hydrogen [2 (p. 151)]. The growth of the film is independent of temperature, but the etching rate increases with increasing temperatures, so that, overall, the total growth rate of the film decreases.

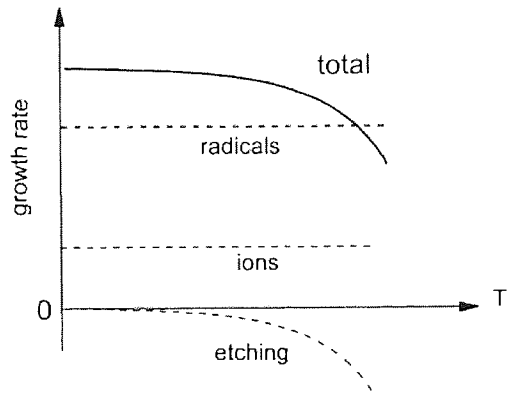

Figure 2.15 Temperature dependence of net growth rate, actual growth rate and etching rate (from [2 (p. 151)])

In the case of an amorphous hydrogenated carbon film grown from methane, for example, the main molecular ion would be CH_3^+ and the neutral species would be CH_3– radicals and unsaturated di-radicals like C_2H_4, and C_2H_2. Each of these neutral species has a different sticking coefficient to the surface of the a-C:H film, which is fully covered with C-H bonds, so it is chemically passive.

The di-radicals and other unsaturated species react strongly with the surface of the growing film. They insert directly into existing C–C or C–H bonds at the surface of the film. At the opposite pole are neutrals like CH_4 which have very little interaction with the film surface. Their effect is almost negligible. The monoradicals, like CH_3–, have a moderate effect. They cannot insert directly into the surface bonds. To react with the film they need the presence of a dangling bond on the surface. They will then add to this bond to form C–C bond. The dangling bond must be created by removing an H atom from a

surface C–H bond [2 (p. 151)]. This can occur by either an incident ion or hydrogen displacing an H from a surface C-H bond:

$$\equiv C - H + H' \rightarrow \equiv C - + H_2 \qquad \textbf{Eqn 2.4}$$

or by another radical, like $-CH_3$, abstracting H from the C–H bond. Atomic H is the most efficient species for abstraction and it was found that it extracts the hydrogen from the C–H bond 30 times faster than CH_3 [44]. The CH_3 radical attaches to this newly created dangling bond:

$$\equiv C - + - CH_3 \rightarrow \equiv C - CH_3 \qquad \textbf{Eqn 2.5}$$

Thus, the effective sticking coefficient of a standalone CH_3 radical is small, but it is increasing in the presence of atomic hydrogen. This leads to a synergistic effect of atomic H on the sticking probability of CH_3 [43, 44].

The neutral hydrocarbon species do not have enough energy to penetrate the film; they only interact with its surface. The H atoms, being so small, can penetrate about 2 nm into the film. They can remove H from C-H bonds up to this depth and create subsurface dangling bonds recombining to form H_2 molecules. Some of these dangling bonds will be again saturated by incoming atomic H [2 (p. 152)].

Carbon and hydrocarbon ions can break up and penetrate the film surface to cause subplantation. If that does not happen, the molecular ions can remove H from C–H bonds. This displaced H can then recombine with other H atoms to form H_2 molecules, and then desorb from the film. This is the main process which causes the H content of PECVD a-C:H to decrease with increasing ions energies [2 (p. 152)]. It is possible that some of the atomic H can not recombine. These H atoms will find other subsurface dangling bonds to re-saturate.

The H^+ ions, due to their energy and the weak interaction with the C atoms in the film, penetrate deepest under the surface. They take part in similar reactions to those undergone by H atoms, but to a larger depth.

The a-C:H films have three characteristic depths: the surface itself, where hydrocarbon and hydrogen species react with the growing film; the upper 2 nm in which reactions are controlled by atomic H; and a larger depth, depending on ion energy, in which reactions are controlled by H^+ ions [2 (p. 152)].

2.3.2 Deposition when ion energy is below penetration limit

The above deposition "picture" is only valid in the case of ions with high energy arriving at the surface, which leads to subplantation - a physical process. However, in the case of low energy species incident on the film's surface, which is the case for films deposited with the cascaded arc plasma source, chemical processes may be responsible for the growth of the films.

A. von Keudell et al. [45] proposed an absorbed layer model to explain the formation of dense hydrogenated amorphous carbon (~2 g/cm^3) at low energies. The deposition set up was an ECR plasma source and the precursor gas was methane. No additional bias was applied on the substrate and the ions energy was estimated of the order of 10 eV. The model proposed that the substrate was first covered with neutral species from the plasma. After a characteristic time, these species would chemisorb into the growing film using a part of the energy transferred from incident ions on the film surface. With the rest of the energy new chemical bonds could be formed between the adsorbate and the growing layer.

Also it was found that deposition rate decreased with temperature, because the residence time of the neutral species decreased exponentially with increasing temperature. A threshold temperature was found (~150°C), which separated the deposition into two regimes. Below the threshold temperature the deposition via the chemical adsorbtion under ion bombardment is the dominant mechanism. Above the threshold temperature the incorporation of ions directly into the growing film becomes the more important mechanism. In the latter case more energy is available and is used to break C–H bonds and release the H from the film.

Another interesting finding was that decreasing the absorbed energy in the plasma increased the density in the films at the same substrate temperature. Thus films with high

densities, in the same range as for film deposited under energetic ion bombardment, were obtained from ions with low energy. The explanation was attributed to the surface being covered with more C–H bonds under these conditions. These C–H bonds require less energy to break up than the C–C bonds, which ultimately leads to more C–C bonds per deposited carbon atom being formed, resulting in higher density. Thus the structure of the films changes from graphite-like to diamond-like with the decreasing flux of atomic hydrogen toward the substrate [45].

Another study conducted by Gielen [3 (p. 10)] concluded that the best a-C:H material (with highest hardness and density) that can be deposited with cascaded plasma source technique is obtained when the admixed acetylene flux is equal to the argon ion flux emerging from the source. In other words, for each acetylene molecule that is injected in the system there is an incoming argon ion and electron emerging from the source. A new parameter was introduced: the ratio between the injected acetylene flux and the emerging flux of ions and electrons from the plasma source $F = \frac{\Phi(C_2H_2)}{\Phi(Ar^+, e^-)}$. This resulted in the loading criterion [3 (p. 90)]: when the acetylene flux is less than the ion flux (F<1), the source is underloaded; when these fluxes are equal (F=1) the source is at optimum loading and when the acetylene flux exceeds the ions flux (F>1) the source is overloaded.

Because of the very low energy argon ions and electrons, conventional ion or electron impact dissociation can be excluded. The only possible reaction between the argon ions and the precursor molecules could be via a charge transfer reaction, followed immediately by a dissociative recombination [46]. In this case the plasma is said to have an ion induced chemistry, because the ions are controlling the processes in the plasma (in conventional deposition systems using plasma, the chemistry is usually electron induced). This leads to the following dissociation products and probabilities [47], in the case of acetylene:

$$Ar^+ + C_2H_2 \rightarrow Ar + C_2H_2^+ \qquad \textbf{Eqn 2.6}$$

$$C_2H_2^+ + e^- \rightarrow \begin{cases} C_2H + H & (50\%) \\ C_2 + H + H & (30\%) \\ C_2 + H_2 & (2\%) \\ CH + CH & (13\%) \\ CH_2 + C & (5\%) \end{cases} \qquad \textbf{Eqn 2.7}$$

The probabilities of the above reactions were calculated for electron induced plasma chemistry.

The changes in film quality were explained as follows: in under-loading conditions (F<1) the surplus of argon ions contributes to the further dissociation of the C_2H and C_2 radicals by secondary charge transfer and dissociative recombination reactions. This mechanism leads to poor cross-linking between the C atoms and consequently to poor quality a-C:H films being formed. At critical loading (F=1) the flux of C_2H radicals reaches its maximum compared to the under-loading and over-loading conditions; this radical is responsible for the growth of good quality amorphous hydrogenated carbon. At critical loading only primary acetylene dissociations take place which lead in the main to C_2H production. However, complete dissociation is not possible, due to the recirculation of H atoms that re-enter the plasma jet and partially consume a fraction of the Ar ions [3 (p. 90)]. In over-loading conditions even more C_2H_2 molecules remain undissociated in the plasma jet but the C_2H radical flux remains essentially the same. The quality of the films is the same or decreases slightly. This is because in some cases it is possible that the acetylene molecules would incorporate in the growing film, which would increase the H content in the film and the fraction of sp^1 bonds.

Regarding the deposition rate it was found that changing the plasma composition from under-loading to critical loading results in a large increase in deposition rates. Over-loading the source does not result in a further increase in deposition rate.

A more recent study conducted by Benedikt has shown that the plasma chemistry at the substrate level is much more complicated that is was initially believed [48]. The branching ratios in Eqn 2.7 should be corrected to the values 0.26, 0.41, 0.07, 0.26 and 0.00 for the ion induced plasma chemistry to have a reasonable agreement between the experimental measurements and simulation results. It was proposed that the C_2H radical is

not the radical responsible for the growth of good quality a-C:H material; it only reacts with the excess of undissociated C_2H_2 molecules present in the plasma jet in overloading conditions. These reactions lead to production of specific radicals, such as C_3, C_3H, C_3H_2, C_4, C_4H, C_4H_2 (see Figure 2.16), abundant at the substrate level. From these C_3 and C_3H were identified to be the radicals from which the growth of good quality hydrogenated amorphous carbon films takes place [48].

The C_3 and C_3H can exist either as a linear or cyclic isomer [49]. It is not yet clear how these radicals, after being incorporated into the growing film, produce the high cross-linked C–C sp^3 network necessary to form the diamond-like hydrogenated amorphous carbon film. The answer to this question could be solved by molecular dynamics modelling in the near future.

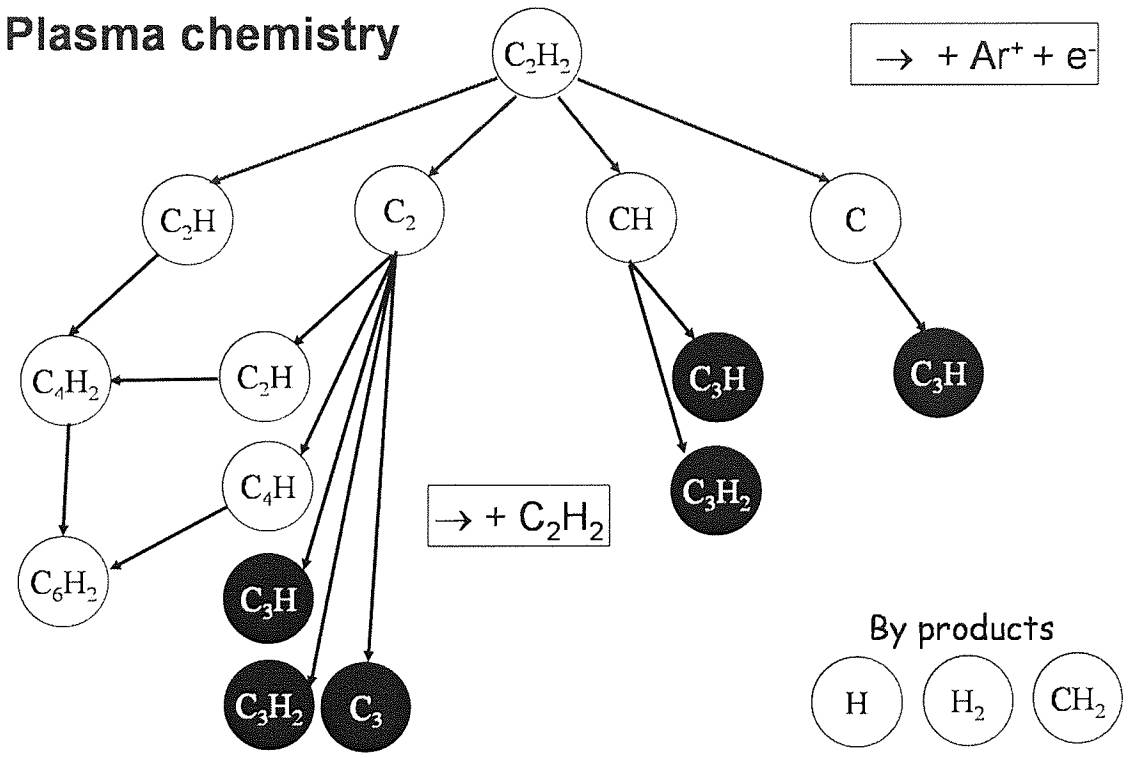

Figure 2.16 Plasma chemistry in an argon-acetylene expansion (from [48])

One of the important advantages of the low energy deposition is that no damage would be caused to sensitive substrates and that the unsaturated bonds of these radicals are preserved by the absence of high energy bombardment. Thus films are produced with low defect density and medium-high hardness.

If methane is used as a precursor gas with the cascaded arc plasma source the charge transfer and dissociative recombination reactions are assumed to be similar to the acetylene case, as suggested by [50]:

$$Ar^+ + CH_4 \rightarrow Ar + CH_4^+ \qquad \textbf{Eqn 2.8}$$

$$CH_4^+ + e^- \rightarrow \begin{matrix} CH_3 + H \\ CH_2 + H_2 \\ other\ products \end{matrix} \qquad \textbf{Eqn 2.9}$$

The branching ratios for the above reactions are not known at the moment, but it is likely that the first one has the highest probability. Also, methane is less likely to react further with the dissociation products from Eqn 2.9 [51]. However, if small fractions of the formed CH_3 radicals react with the excess of methane molecules, the most likely reaction products, after [52], would be:

$$CH_3 + CH_4 \rightarrow C_2H_6 + H \qquad \textbf{Eqn 2.10}$$

As seen from the acetylene study, the radicals with an even number of carbon atoms were not important for film growth [48]. It is likely that in this case the dominant species at the substrate level is still CH_3. A rigorous study of the reactions and radicals present in the plasma at these very low ion energies has not been yet conducted.

2.4 Applications of DLC layers

As mentioned in section 2.1.2., the major applications for which DLC films have been investigated can be categorised as follows:

Electronic applications (anti fuses, ultra large scale integrated circuits (ULSI), field emission etc.); for these applications films grown from methane are preferred, due to the fact that is available in high purity form. However, these films are softer and the hydrogen content is quite high.

Mechanical and optical applications, as protective coatings for optical windows, fibres, solar cells, magnetic storage disks, car parts, in micro and nano electromechanical devices (MEMs and NEMs). For a better mechanical protection thick films grown from acetylene

are preferred, which maximise the wear life of the coating. However, the compressive stress limits the maximum thickness of adhesive films [2 (p. 262)]. Some of the applications mentioned above (magnetic storage disks, MEMS, NEMS) require the presence of thin films only.

Biomedical applications, as coatings on replacement hip joints, heart valves and stents.

2.4.1 Electronic applications

2.4.1.1 Antifuses

Fuses are metallic links that go open circuit when large currents are passed through them. Antifuses are the opposite; they change from high to low resistance when a large current is passed through them. Antifuses act by a thermal runaway mechanism, as the conductivity of the semiconductor increases with the rising temperature. The current is concentrated through a narrow channel, to maximise the temperature increase. Amorphous carbon makes useful antifuses. The process is likely to involve a change towards more sp^2 bonding. It was found that doping with nitrogen makes this transition easier [2 (p. 244)].

2.4.1.2 Integrated circuits (IC)

2.4.1.2.1 Resist materials in lithography

The rapid advance in the packing density and complexity of ultra large scale integrated (ULSI) devices demands the use of high performance resist materials. Diamond-like carbon (DLC) films which have high mechanical integrity, thermal stability and chemical inertness are potential candidates as positive-acting resists for lithography. DLC films can be easily deposited on large area substrates with diameter of above 500 mm at room temperatures. In addition, the roughness of DLC films is comparable with that of the mirror surface of silicon (Si) wafer. Furthermore, both deposition and etching of DLC films are easily carried out using chemical vapour deposition (CVD) or plasma etching in dry atmosphere.

During a full dry process, DLC films were utilized for IC fabrication as a mask material. An excellent yield rate of pn junction, better than with polymer mask materials (solutions), was obtained with DLC films, because it reduces concentration and diffusion depth of the implanted dopants in the films. Excellent *V–I* characteristics were obtained and these were comparable with those of pn junctions made by normal wet processes [53].

For the IC fabrication process, it was found that the optimum condition of deposition and etching for the DLC film is at 400°C substrate temperature [53] and at low pressure [54], in a standard RF PECVD plasma cell. The use of DLC films is a useful alternative because it overcomes some of the problems that exist in the standard resist technology, such as: environmental damages and contamination, short comes of the wet process and cost performance. Several processes may be reduced by the use of DLC films, thus increasing the cost-effectiveness of the IC fabrication process.

Alternative processes exist for the etching of the resist materials, based on the enhancement of O_2 Reactive Ion Etching (RIE) rates of DLC by laser-induced graphitization [55]. Since the laser fluences required for graphitization of DLC resist are low, higher throughput may be achieved with no substrate damage.

The etch rates of DLC films in an O_2 plasma can be selectively enhanced by exposure to 248 nm laser pulses. When the fluence exceeds 100 mJ/cm^2, the exposed regions are graphitized. Using this property, graphitized patterns were delineated in DLC films and developed subsequently by etching in an O_2 plasma. The developed patterns were then transferred to the underlying silicon substrate by reactive ion etching in a CF_4 plasma; 5 pm features with rather vertical walls were obtained, indicating that this combined laser-RIE approach is feasible [55].

2.4.1.2.2 Low dielectic constant films for ultra large silicon integrated circuits

Due to the continuous reduction in size of ultra large silicon integrated circuits (ULSI) devices, low dielectric constant materials are required for the interconnect dielectric (ILD) to reduce propagation delays, cross-talk noise between metal wires and power dissipation from *RC* coupling (*R* is the resistance of the metal lines and *C* is the line

capacitance). It is, therefore, necessary to replace the SiO_2 dielectric, characterized by a dielectric constant (k) of up to 4.2, with materials having dielectric constants below 3.0 [56]. A variety of materials have low dielectric constant, which make them candidates for future ULSI chips; however, they have to overcome many obstacles in order to be incorporated in integrated circuits. The integration of a new, low-k dielectric material in a ULSI device imposes a significant number of requirements that such a material has to satisfy, among which are: electrical properties (low-k, low dissipation factor, low leakage current); thermal properties (stability at 400°C); mechanical properties (low stresses, minimal Young's modulus and hardness); adhesion and compatibility with other materials; patternability; and chemomechanical polishing (CMP) capability. In addition, the choice of which low-k dielectric to adopt is associated with a competition between spin-on polymeric materials and plasma-enhanced chemical vapour deposited (PECVD) materials and a debate over the advantages of each type. The advocates of the PECVD low-k materials claim that such films have better mechanical properties than the polymeric films and that their integration process is more evolutionary than for spin-on films, as it can be developed in the existing manufacturing tool sets [56].

Hydrogenated DLC with dielectric constant values of 2.7–3.0 has been demonstrated as a potential interconnect dielectric for Cu damascene metallization. In contrast, fluorinated DLC with dielectric constant values below 2.7 does not seem to be suitable as the back end of the line (BEOL) dielectric at the currently used processing temperatures of the BEOL. In order to improve the integration and reliability of the low-k materials, a hybrid composition of DLC and SiO_2 has been developed [56]. Carbon-doped oxides (CDO) or SiCOH films, comprising Si, C, O, and H and deposited by PECVD, have achieved dielectric constant values lower than 2.8. The dielectric constant of such materials can be further lowered by depositing multiphase films, containing at least one thermally unstable phase, and annealing the films to remove this unstable phase from the material. This process enhances the atomic level porosity in the films and further reduces the dielectric constant. Dual-phase materials have been prepared by PECVD from mixtures of SiCOH precursors with organic precursors. Proper choice of precursor and optimization of the deposition conditions can reduce the dielectric constant of the stabilized films to values below 2.2 [2 (p. 244), 56].

2.4.1.3 Field emission

Field emission is the emission of electrons from a solid under an intense electric field at ambient temperature. Emission occurs by tunnelling of the electrons through the surface potential barrier. The typical local field required for emission from solids is 1000 V/μm. The simplest way to achieve such fields is to use sharp shapes such as Spindt tips [57]. Various types of carbon, such as carbon nanotubes, diamond and DLC show field emission at much lower applied fields of order 10 V/μm (Figure 2.17). This could open up opportunities for electronic devices.

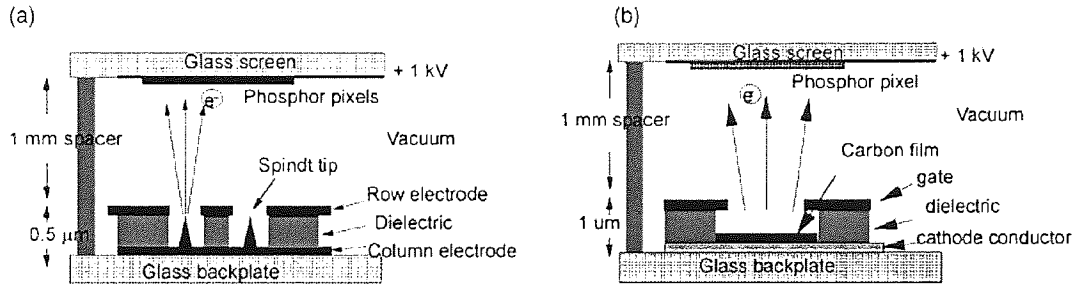

Figure 2.17 Field emission display, with (a) Spindt tips and (b) carbon film cathodes (from [2 (p. 245)])

Flat panel displays, field emission displays (FED), active matrix liquid crystal displays (AMLCD) and plasma display panels (PDP), with a very high picture quality are subjects of interest around the world. The FEDs of the various flat panel displays have great potential for cold cathode display applications. A flat panel display is a device in which the image is formed from a large array of pixels, each addressed by a controllable cathode. The use of thin films emitters rather than Spindt tips simplifies the manufacturing process.

Hydrogen terminated polycrystalline chemical vapour deposition (CVD) diamond films have an extensively known negative electron affinity (NEA), excellent electron field emission characteristics with high current density and low turn-on electric field. CVD diamond films usually require high growth temperatures, however, which leads to a dramatically high manufacturing cost and to limited large area coatings. On the other hand, DLC films deposited at relatively low temperature by PECVD have similar

characteristics to diamond. Accordingly, DLC is a more attractive candidate for the realization of large area FEDs. In particular, DLC films deposited by PECVD can be easily deposited on glass at a low substrate temperature over a large area by relatively low cost techniques. In recent years, good electron field emission characteristics of DLC films deposited by various deposition techniques were observed by many groups. Some researchers suggest that field emission is due to the low electron affinity of DLC, field enhancement due to film microstructures conductive paths caused by localized sp^2 sites or the presence of nanocrystalline diamond particles in the DLC films. Despite numerous studies of DLC field emission, the field emission mechanism of DLC film is not yet clearly understood [58].

The field emission properties of DLC films grown by PECVD change with the growth conditions. The surface morphology of DLC films is sensitive to the substrate temperature during growth. Although the turn on electric field F_T value is not significantly influenced by differences in the surface morphology, F_T *is* sensitive to the sp^2/sp^3 ratio and doping with nitrogen [2 (p. 248)]. An optimum sp^2/sp^3 bonding ratio provides a high emission current and a low F_T value [59]. By comparing the field emission properties of DLC, undoped diamond and B-doped diamond films, DLC films were found to be the most favorable for cold cathodes [58]. However, F_T values are still high and the emission is unstable. This problem needs to be solved before replacement of conventional Mo emitters can be achieved.

In designing flat cathodes based on amorphous carbon, it is important to firstly understand the material properties. It has been demonstrated that cathodes with suitable current densities and low enough threshold fields can be produced for the cathodes to be useful in a flat panel device structure. It is possible to compensate for problems associated with emission uniformity and site density by carefully designing the driver circuits used to integrate these flat cathodes into display like applications. It is also possible that a light emitting device, which uses carbon as its electron source and a polymer as its electroluminescent material will enter the market before these flat cathodes are used for flat panels [60].

In recent years, carbon nanotubes are the preferred form of carbon for field emission applications. They are conductive and can carry large quantities of current if needed [2 (p. 254)]. The disadvantage is that they require high temperatures for deposition.

2.4.2 Mechanical and optical applications

2.4.2.1 Coatings of magnetic hard disks

DLC films can be used as protective coatings on magnetic storage hard disks. Magnetic storage as in computer hard drives is presently the most economic form of mass storage. Its great advantage is that the storage density is increasing very fast (100% per year) since the introduction of giant magneto-resistive (GMR) heads [2 (p. 268), 61].

The disk consists of a magnetic layer of Co-Cr-Pt alloy thin film that stores the data. A protective layer of DLC coating is applied over the Co layer and one-two monolayers of a perfluoro-polyether (such as ZDOL or Fomblin) is used as a molecular lubricant. A read/write head flies above the rotating disk on an aerodynamic bearing. The read/write head consists of many layers of thin films and is also protected by a DLC film [2 (p. 268)].

The need for even higher storage densities means a smaller bit size; this requires a smaller magnetic spacing, which is the vertical distance between the read head and the Co storage layer. Reducing the fly height requires that the carbon layer must be further reduced from 4 nm to 2 nm, which is a thickness of about 12 atomic layers.

DLC is used because it makes extremely smooth, continuous and chemically inert films, with a surface roughness below 1 nm. Initially the role of the diamond-like carbon film was to provide protection against corrosion. Simple a-C was used, deposited by magnetron sputtering. Later this was replaced with a-C:H produced by reactive sputtering. This layer has the enhanced role of providing protection against mechanical wear and damage during head crashes. Most recently a-C:N is used, for better interaction with the lubricant layer. The primary role is now to form a continuous film, to give protection against corrosion and to separate the Co layer and read/write head from the ambient [61].

DLC has no competitors as a coating material for this application. The only deposition methods able to make continuous very thin films with the required specifications are cathodic arc or high-density PECVD.

2.4.2.2 Protective mechanical coatings (for cutting tools)

Modification of the surfaces of metal-cutting tools based on covering them with materials of increased resistance to abrasion improves their life. All attempts to employ anti-abrasive materials, which are applied with very good results in metal cutting, are facing difficulties in wood processing, caused by differences in wood's physical and chemical structures compared to metals. Wood material stands alone in many characteristics when compared with synthetic materials such as steel, plastics, concrete, etc. It is a multifunctional, multicomponent, hygroscopic, anisotropic, heterogeneous, fibrous, porous, biodegradable, renewable material [62]. These features give wood exceptional specific mechanical properties, especially in the longitudinal direction, and a great machinability level allowing high cutting and feed speeds. Taking most of the coatings' advantages, their hardness and resistance to corrosion, it is supposed that they could ameliorate the wood peeling process. In peeling, the wood being already wet and heat-treated might be a corrosive material.

Different antiabrasive coatings have been tried on the cutting tool surface to improve the wood peeling process: 60SMD8 Nitride, TiN, (Ti, Zr), CrN, Cr, W-C:H (DLC with WC precipitation) – the latter deposited by a reactive magnetron sputtering method. The material subjected to cutting was beech wood. The process was conducted with a laboratory micro-lathe test apparatus. The lowest reduction of the cutting edge has been observed in CrN and W-C:H coated knives. After 4000 m of the cutting path, the CrN coated knives retained the best adhesion to the steel substrate. Covering tools with W-C:H and CrN coatings decreases the reduction of the knives' edges wear, respectively, by 38 and 52% [62, 63].

DLC coatings were also applied to dry cutting tools made of cemented carbide material by using a vacuum arc discharge with a graphite cathode. The performance and tribological behavior of DLC coated tools against aluminum alloys were investigated.

Since DLC coated tools have a smooth surface, a low friction coefficient and an excellent adhesion, the formation of built up edge was prevented. The edge maintained sharp and the machinability was improved. Under dry conditions, the machined alloy surface roughness decreased to about half and was equal to that produced by the uncoated insert under wet conditions. DLC coatings improve the quality of the cutting tools even in dry machining, resulting in an important increase in the life-time of the tool [64].

In a similar application, a DLC over-layer was deposited on two types of diamond coated tools and the friction properties were examined by pin-on disk sliding test. Cutting performance of tools with these composite coatings was also examined in semi-dry cutting condition. Only the combination of DLC and fine crystal smooth surface diamond was able to achieve very low surface friction coefficient against aluminum alloys. In the case of drilling die casting aluminum alloy including 12% silicon (JIS ADC12), excellent anti-sticking property of DLC on fine crystal diamond coating lead to much longer durability of drills than other types of diamond coatings in semi-dry cutting conditions [65].

2.4.2.3 Solar cells based on DLC films

The optical refractive index and the good mechanical properties of DLC films suggests that DLC film may be used as hard antireflecting coating for solar cells made of semiconductor materials and/or as protecting coating in corrosive and abrasive environment.

Amorphous diamond-like carbon films were used as hard anti-reflecting coatings for Non Anti Reflective (NAR) solar cells and as a hard protective material for Anti Reflective (AR) solar cells. The short circuit current and the efficiency of the NAR solar cell were improved after coating the cells with a-C films. The dependence of the solar cell efficiency, η, with the a-C film thickness was examined and an optimum thickness of t = 55 nm was found, for which the efficiency improved by more than 30% relative to the uncoated NAR solar cell. It was also found that a-C films act as a protective film for AR solar cells under abrasive conditions. However the short circuit current and the efficiency

decreased after the a-C film deposition. For 40 nm, the efficiency decreased by about 2% [66]. Similar results were found for solar cells formed on GaAs substrates [67].

In a similar application thick (1.3 – 1.5 μm) DLC films were deposited on the working side of the solar cells and increased their stability relating to the effect of proton and ultraviolet (UV) irradiation. Moreover, solar cells covered by DLC film after UV irradiation shows improvement of efficiency both for proton-implanted and unimplanted samples. At the same time the unprotected SC deteriorated after those treatments. The effects observed are connected with the decrease in reflection losses due to the deposition of DLC films and self-annealing of radiation damages in implanted DLC films due to light-induced hydrogen bonding. Reemission by DLC film of the absorbed ultraviolet light in visible spectral range was observed. Application of nitrogen-doped DLC film as a fluorescent layer allows improving Si SC efficiency in UV spectral range. These findings have opened up a wide variety of potential applications of DLC films, especially for space solar cells [68].

2.4.2.4 Use of DLC films as protective optical coatings

One of the important applications of DLC films could be as a protective coating for large area glass substrates. Processes, materials and equipment were developed for this application [69]. Highly tetrahedral, hydrogenated amorphous carbon optical thin films were deposited, which demonstrate high scratch and abrasion resistance, optical transparency, low coefficient of friction, and high degrees of hardness. In addition to producing scratch and abrasion resistant glass, the DLC can be combined with other PVD techniques to produce low maintenance or easy clean glass products with superior hardness and scratch resistance.

The attractiveness of ta-C:H in the glass industry lies in the fact that atomically smooth films can be deposited at relatively low temperatures (<60°C) over large areas. Its combination of extreme hardness (up to 60 GPa), chemical inertness, low coefficient of friction and high wear resistance mean that when applied onto soda lime glass it greatly improves resistance to abrasion. Its high optical transparency coupled with its neutral color shift help maintain one of the most important attributes of glass: its transparency.

The high density of ta-C:H also provides a barrier to sodium ions diffusion and seals the soda glass surface from corrosive environments.

Infrared communication through the atmosphere or in space requires thin films with excellent mechanical, chemical and thermal properties to enhance signal transmission, in the 3–5 and 8–12 μm wavelength ranges. Infrared sensors or transducers for these windows use substrate materials such as Si and Ge. These materials have high refractive constants that make necessary the deposition of antireflection layers. Unfortunately, conventional infrared antireflection thin films have some drawbacks, namely poor mechanical properties, low density, and moisture sensitivity. New infrared antireflection thin film materials are required for this application.

Diamond-like carbon (DLC) thin film is unique in a number of properties for infrared transmission enhancement applications, including infrared transparency, high mechanical hardness, and chemical inertness. As the optical constant of DLC in the infrared range is about 2, substrates to match the antireflection coating of DLC should have optical indexes close to 4, such as silicon and germanium. In addition, silicon in the 3–5 μm infrared window and germanium in both 3–5 and 8–12 μm infrared windows have low absorption. It is widely recognised that DLC films are often produced with high mechanical stresses. Cathodic arc deposition produces DLC films with compressive stress in the range 4–14 GPa. PECVD DLC has relatively low stress, in the range 0.2–4.7 GPa. However, PECVD DLC often has low hardness and significant infrared absorption of hydrocarbon. Stress level in magnetron sputtering DLC films is usually between that of the cathodic arc and PECVD. In other applications, an adhesion layer between substrate and DLC films may be deposited or formed by means such as high-energy ion bombardment. Unfortunately, such methods are not applicable for infrared transmission enhancement applications because they introduce either significant absorption in the adhesion layer or complication in antireflection optimisation [70]. Diamond-like carbon (DLC) films were deposited using the unbalanced magnetron sputtering (UBMS) method and optimised for applications in infrared transmission enhancement. Thick DLC films were deposited which satisfied the requirements for the infrared windows at 3–5 and 8–10 μm. At the optimised conditions the stress in the DLC films decreased with increasing thickness, approaching 1 GPa. Low infrared absorption coefficient DLC films up to 2 μm thick were

deposited on silicon and germanium substrates without adhesion failure. For single side DLC coated silicon substrate, about 69% transmittance was achieved at wavelengths near 5 μm, close to the theoretical value for non-absorbing DLC material [70].

In another application, the possibility to use multilayer structures based entirely on diamond-like carbon films as reflecting coatings for X-ray optics elements was analysed. The structures grown by plasma deposition technique contained up to 100 superthin supersmooth layers. It was shown that X-ray interference can be observed in such structures.

Parameters of multilayer structures consisting of superthin carbon layers were calculated for various wavelengths in the soft X-ray range. It was shown that the reflection coefficient of such structures is comparable to that of traditional Me/Me, Me/Si and Me/C X-ray mirrors but the resolution is greater by a factor of 2 to 3. Samples of X-ray mirrors were made with satisfactory characteristics [71].

Another application of DLC films could be as hermetic coatings on optical fibres. Films with refractive indices in the range 1.7 – 2.0 (at λ = 675 nm) were deposited at pressures up to 5 Torr. The hermeticity of the coatings was determined using water penetration studies monitored using a combination of spectroscopic ellipsometry and atomic force microscopy. The resistance to moisture penetration was found to be better for higher refractive index films. The coatings were applied to optical fibres in a continuous in-line system as the fibre was drawn. Coatings of thicknesses in the range 10 – 30 nm were achieved on quartz fibres with outer diameters of 200-1000 μm at fibre drowning speeds of up to 3m/min [72]. In a similar application DLC coatings were applied with an RF PECVD system on silica optical fibres and tested for use as invasive medical probes [73].

2.4.3 Biomedical applications

There is considerable interest in using various forms of DLC as biocompatible coatings on parts such as replacement hip or knee joints, heart valves and stents, catheters, biosensors. This is due to the low friction coefficient of DLC and the fact that carbon material is biologically compatible. In many coatings, the main requirement is that the DLC has good adhesion to the underlying unit and does not produce metallic wear debris

[2 (p. 268)]. Hydrogenated films proved to be particularly useful for these applications, since they tend to be more mechanically compliant and less liable to delaminative failure and they have low friction and low wear coefficients. Thus hydrogenated amorphous carbon films (a-C:H) are an ideal candidate for the coating of medical devices [74-79]. The physical and chemical properties of a-C:H can be tailored to give optimum short term compatibility with a given bio-system by alteration of deposition conditions and doping.

In devices like artery stents, synthetic heart valves and artificial hearts the common current problems include thrombus formation, infection, wear and fracture. Diamond-like coatings demonstrate outstanding haemocompatibility, reducing the thrombus formation. They do not absorb fibrous proteins or cellular material, unlike many metal or polymer surfaces.

In another medical application, for hip or knee joint prostheses, the current problems include uneven stress, wear, corrosion and compatibility of the current implants with the human body. Diamond-like carbon is an ideal surface coating for prosthetic joints, because it is very smooth, low friction, wear resistant, inert and immune to scratching by third body wear particles. Furthermore, it prevents the release of metal ions from the prosthesis to the surrounding tissues. Hydrogen free DLC is preferred for this application, because of its increased hardness, that can sustain the high loads present in this case.

No histopathological changes have been seen so far during in vivo studies in which DLC-coated metals have been implanted in animals [78].

3 Experimental set-up and diagnostic tools

3.1 The Expanding Thermal Plasma source testing chamber

The initial tests on the Expanding Thermal Plasma (ETP) source were carried out at OTB Engineering (Eindhoven, The Netherlands) in the system outlined below. The cylindrical vacuum chamber had a height of ~70 cm and a diameter of 40 cm, with a central window for plasma observation and three flanges for the insertion of a double Langmuir probe. The chamber was pumped down by an Edwards 500 m^3/h Roots blower backed up by a Pfeiffer dry pump (Figure 3.1).

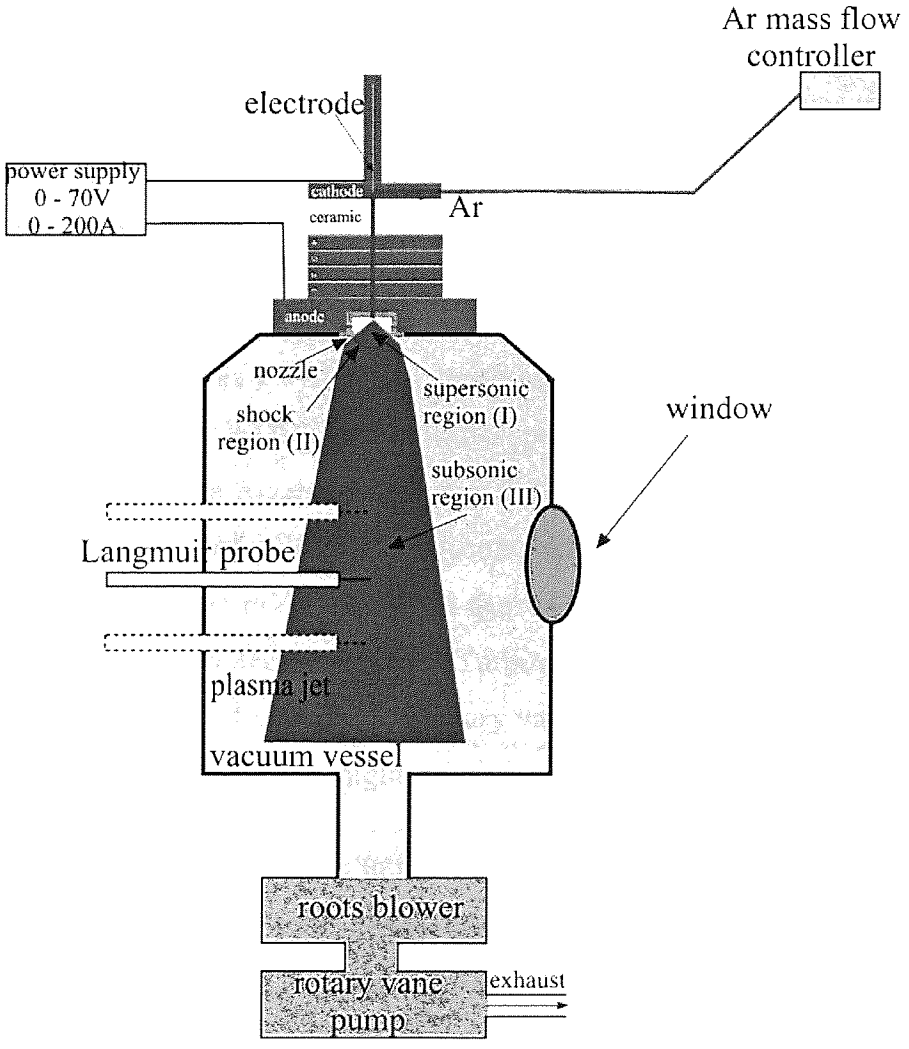

Figure 3.1 The ETP source testing chamber at OTB Engineering

The source mounted on top of the vessel was operated using pure argon as carrier gas. The flow of argon introduced into the chamber was controlled by a mass flow controller

and the flow rate was measured in litres per minute at standard temperature and pressure (slm). The pressure was monitored with a Pfeiffer Pirani gauge.

The power injected in the plasma was controlled by varying the current supplied to the ETP plasma source. The current could be varied from 0 to 200A, but problems with overheating of the cascaded plates and the discharge switching off reduced this range to practical limits of 30 to 70A. This corresponds to a power range of ~1 to 3 kW.

The Langmuir probe could be inserted into the chamber at three different heights and could be moved in the horizontal plane, allowing the measurement of the radial profile of the density of the ions in the plasma.

3.2 The deposition chamber

The deposition experiments were carried out at Aston University in a similar type of set-up, consisting of a vacuum vessel with additional diagnostic tools and features, as outlined in Figure 3.2.

The deposition chamber was a cylindrical stainless steel vessel (~100 cm height, 30 cm diameter) connected to a WOD 222B Pfeiffer pumping station through a Centerline butterfly valve that allow a rough control over the operating pressure in the vessel. The pumping station consisted of a WKP 250A Roots pump (250 m^3/h) backed up by a DUO 035 D rotary vane pump (35 m^3/h). The main deposition vessel was connected through an isolation valve to a turbo molecular Leybold Turbovac 151 Turbo pump (145 l/s), backed up by an Leybold Trivac B 4 D (4.8 m^3/h) rotary vane pump, to pump down the chamber in between experiments and for overnight use.

The ETP source was mounted on the top of the vessel. The power range was 1 to 3 kW, the source and power supply being very similar to the ones used on the ETP source testing chamber. The carrier gas could be selected from pure argon, 3% hydrogen to argon mixture and 12% hydrogen to argon mixture. The precursor gas was either acetylene or methane and the injection point was either the source nozzle or an injection ring. The injection ring could be fixed in two different positions: outside the argon stream, about 9 cm from the source nozzle (position UP) and in the argon jet, about 37 cm

from the nozzle (position DOWN). The flow of all the gases used was controlled by a system of mass flow controllers and all the flow rates were measured in standard litres per minute. The pressure in the chamber was monitored with a Pfeiffer full range gauge and a Baratron gauge, which is more accurate when a mixture of gases is used, but it can measure a narrower pressure range.

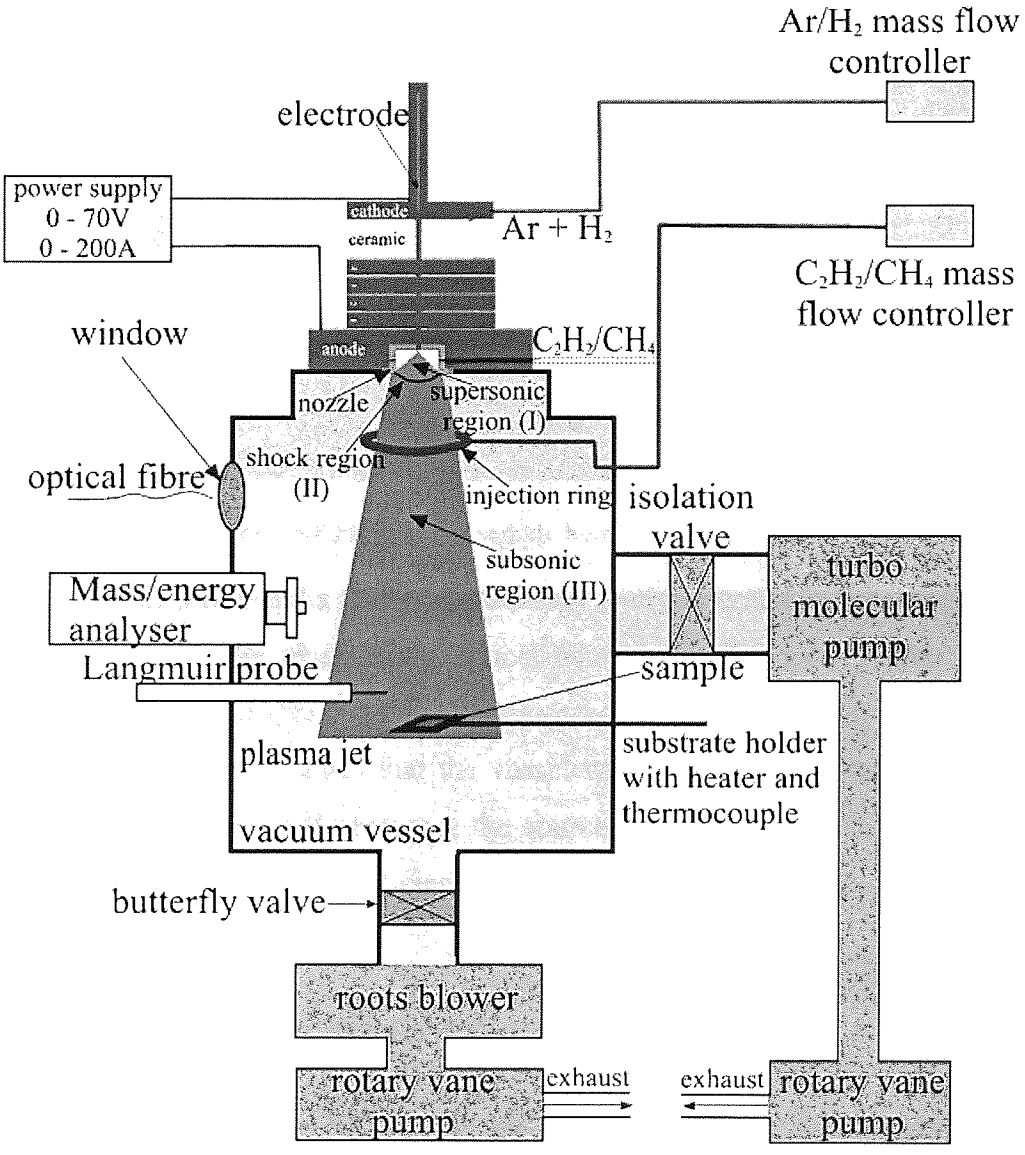

Figure 3.2 The deposition chamber at Aston University

The substrate holder, fitted with an electrical heater, a thermocouple and a shutter could be introduced through one of the side flanges, at different distances from the source nozzle. A special pocket (10×10×0.6mm) was made in the sample holder for fixing the samples. The dimensions of the samples were around 8×8 mm^2 and the substrate was

chosen to be pure silicon (99.999% purity), in orientation <100>, with 0.6 mm thickness, 2-4 Ω/cm resistance, N doped with phosphorous and mounted as shown in Figure 3.3. The wafers had two sides, one polished (mirror finish) and one etched; the films were deposited on the polished side.

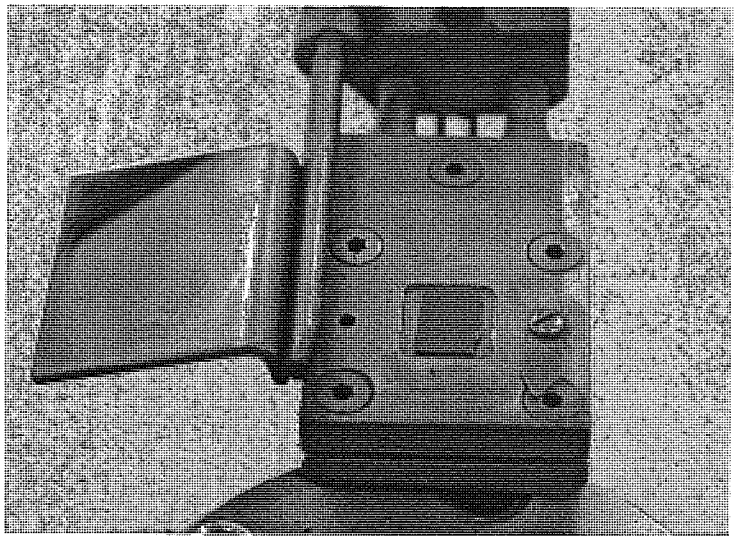

Figure 3.3 Picture of the sample holder – shutter system

A Hiden Langmuir probe and a Hiden mass/energy analyser could be mounted on the side flanges to investigate the plasma. An optical fibre connected to a 270M Spex Rapid Scanning Imaging Spectrograph/Monochromator could be placed in front of one of the side windows. The many flanges that the vessel was designed with gave the facility to vary the distance incrementally between the source and the substrate from 33 to 80 cm and to use the Langmuir probe and mass/energy analyser at different positions along the plasma stream.

3.2.1 Technical data on the ETP plasma source

Some technical data for the ETP plasma source is presented in the following table:

Table 3.1 Technical data for the cascaded arc source developed by OTB B.V. (from [80])

	Specifications
Vacuum	Source is considered leak tight if there are no leaks at He flows < 1×10^{-8} mbar l/s
Cooling water	There is no leak in cooling water (conductivity < 1500 mS/cm, water pressure 3-5 mbar, temperature range 17-100°C)
Electrical short circuit	There is no short circuit between: • The cascaded plates • The anode and cascaded plates • The cathode and cascaded plates
Maximum power	The source will resist high currents (powers) up to a maximum of 80A cathode current
Reliability	The source will resist repeated start-stop actions
Geometry	The cathode tip is situated exactly in the centre of the upper part of the plasma channel
Operation time	The source has an industrial design and resists to long processing times, up to 22 hours/day
Operating range	With Lincoln V200 – TIG power supply: • Cathode current: 20A – 80A • Voltage: 30V – 65V • Ar flow > 2 slm

3.2.2 Mounting a cascade arc plasma source

It is important that great care is taken when the cascade arc plasma source is assembled. The boron-nitride plates built in the source, to cover the cathode feed through, break easily. If the cascade plates are not fixed and centred well enough, then eventually parts of the cascade plates will be sputtered off and will be incorporated in the deposited film. It is also important that there is enough flow of cooling water in the individual plates and that the source is not leaking air (leak tight $<1\times10^{-8}$ mbar×l/s), because the presence of oxygen in the plasma channel would damage the source.

If the source is mounted following the flow diagram in Figure 3.4, then it can be used on the experimental set-up [80].

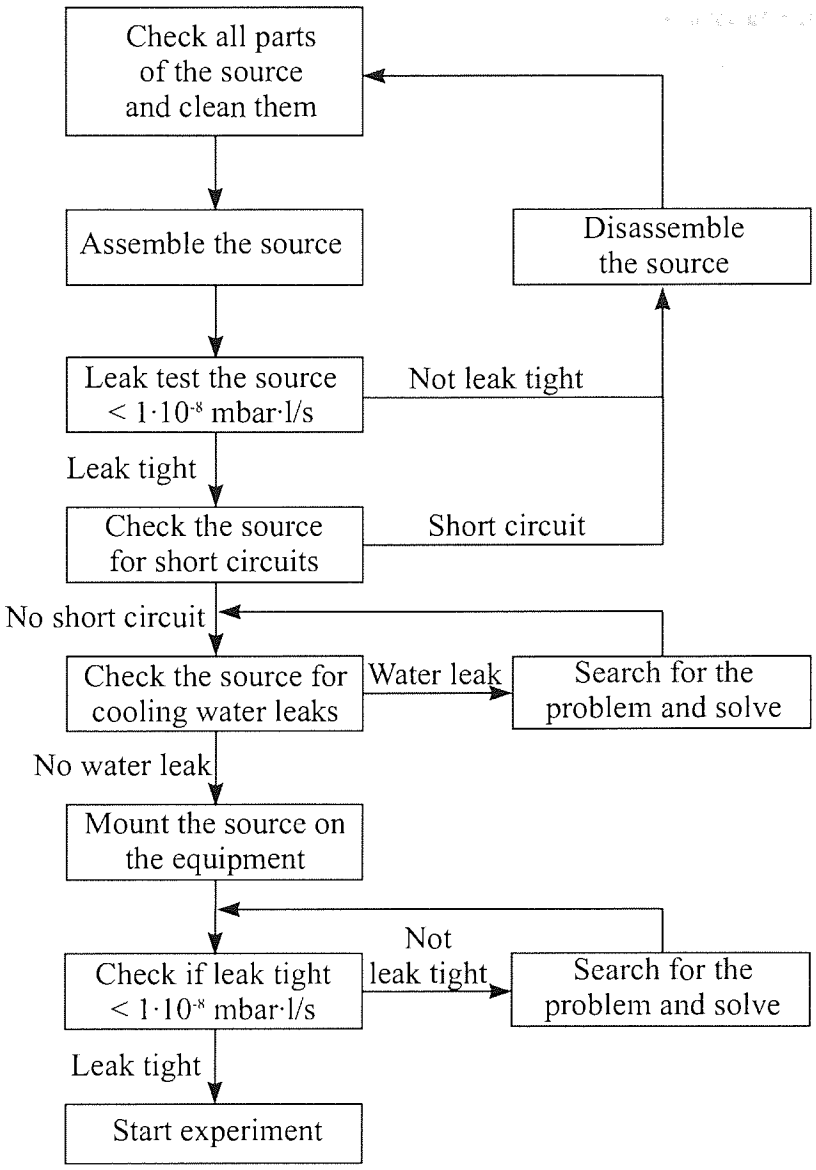

Figure 3.4 Steps in assembling the cascaded arc plasma source (from [80])

The technical specifications on the gases and equipment used during the experiments are presented in the following tables, for the experiments performed at OTB Engineering and at Aston University.

Table 3.2 Specifications on used materials and equipment with plasma source at OTB B.V. (from [80])

Gases	Argon (grade 5.0) and Helium (grade 4.5)
Cooling water	• Temperature cooling water in: 18-25°C • Water chiller: MTA-TAE 015 • Water pressure: 3-5 bar
Power supply	Lincoln V200-TIG

Table 3.3 Specification on used materials and equipment with plasma source at Aston University

Gases	• Argon (grade 4.8) • Argon/hydrogen 3% mixture (grade 4.8) • Helium (grade 4.5) • CH_4 (grade 4.5) • C_2H_2 (grade 1.85)
Cooling water	• Temperature cooling water in: 16-18°C • Water chiller: Cool Flow μ chiller • Water pressure: 4-5 bar
Power supply	Lincoln V200-TIG

3.2.3 Chamber and setup modifications

The deposition system was modified several times during the course of the programme. Initial experiments were carried out in a chamber half the height of the final one (about 40 cm height) with an older version of the ETP source. After eight months of experiments with methane the chamber was extended by introducing an adapter chamber in between the existing old chamber and the bottom flange. At the same time the precursor gas was changed from methane to acetylene and the substrate holder, which originally was made out of copper, was plated in zinc, due to an incompatibility between acetylene and copper.

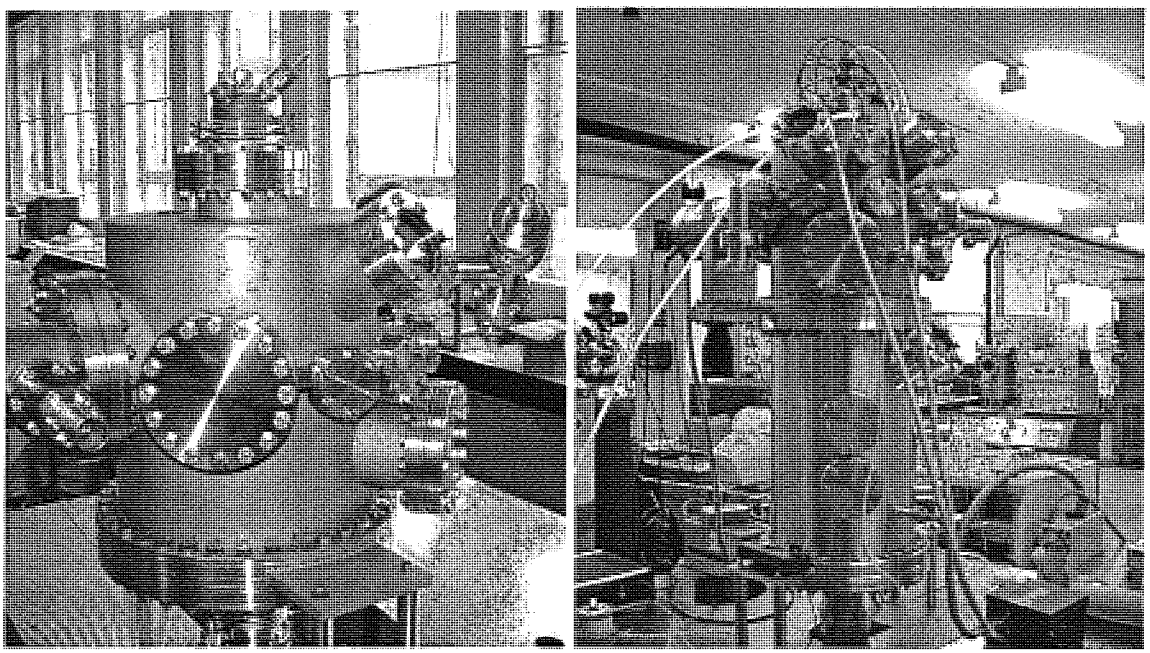

(a) (b)

Figure 3.5 (a) Initial and (b) final chamber configuration with ETP copper source

The additional turbo molecular pump was connected to the vessel using an isolating valve, whereas initially the turbo pump was fitted on the bottom of a cold trap, connected to the side of the deposition chamber. This simplified the operating procedures and allowed the achievement of a much better vacuum in between the experiments, improving the reproducibility of the films.

Films grown from acetylene showed a deposition rate seven times faster than the films grown from methane. However, their quality decreased and roughness of the surface increased significantly. This was due to the very fast deposition rates which resulted in the growth of a thick black sooty carbon layer on the chamber walls and even on the sides of the source nozzle. The second modification, therefore, was to introduce a special angled adapter in between the source and the deposition chamber, which allowed the plasma to self clean the nozzle area.

Still, particles from the thick sooty film that was deposited on the bottom part of the source were randomly incorporating in the films and the third modification was to introduce the acetylene through an isolated injection ring. At the same time a new, improved version of the ETP source was fitted on the chamber, which allowed films to be deposited at higher injected powers. The Roots pump was fitted with a frequency inverter, which allowed lower pressures to be obtained at the same flow rates, by increasing the frequency of the current supplied to the pump and thus the rotational speed.

The fourth modification was to apply a negative DC bias (up to –200V) on the substrate holder, which however did not improve the quality of the films, due to their insulating properties.

The fifth modification was to introduce two electrodes in the chamber and strike an air glow discharge between them and the grounded chamber walls to clean the substrates in situ [81, 82], due to low adhesion coefficients between the films and the substrate. In the later stages of the project different substrate materials were tried, such as silicon oxide, glass and several types of plastics (PET, PEEK). The power injected in the glow discharge was ~10W (1.1kV, 100mA); it removed surface contamination from the

substrates and improved the adhesion significantly in the case of films produced at low temperatures.

The sixth modification was to design and use a new substrate holder, to check the homogeneity of the films on larger samples (5×5 cm^2). The substrate holder was insulated thermally and electrically from the chamber walls. A thin steel sheet was fitted on top, insulated from the rest of the substrate, to be able to raise the temperatures to the desired values. There was no actual temperature control over this thin sheet and its heating was due solely to the plasma source.

3.2.4 Chamber cleaning

As mentioned before, the walls of the chamber had to be periodically cleaned due to the thick sooty film depositing on the chamber walls. Particles emerging from this film covering the walls were randomly incorporated in the amorphous carbon layers. In the case of methane, when deposition rates were very low for the lower pressures, this was not much of a problem. After switching to acetylene as precursor gas the chamber walls were periodically mechanically cleaned with paper, iso-propyl alcohol and acetone. This was not an easy task, mainly due to the height of the vessel and the limited number of flanges large enough to be used for the manual cleaning.

In the later stages of the project oxygen/argon plasma was used to etch away the films deposited on the substrate holder and on the chamber walls [83]. The oxygen was introduced via the injection ring and the plasma was run for 20-25 minutes, after each 3-4 experiments performed. The source current was kept to 50A and the oxygen relative flow was about 6-8% of the argon flow.

3.2.5 Sample preparation

Initially the samples were cleaned ultrasonically in iso-propyl alcohol (IPA) for 15 minutes, prior to insertion in the deposition chamber. Problems with low deposition rates and weak adhesion led to a refinement of this process detailed below:

- Ultrasonic cleaning for 6 minutes with distilled water, rinsing well with distilled water afterwards.

- Ultrasonic cleaning in hot Neutrocon decon industrial detergent (60°C) for 6 minutes, rinsing very well with distilled water afterwards (at least 10 times).
- Ultrasonic cleaning in IPA for 6 minutes, rinsing well with distilled water afterwards.
- Final rinsing with IPA and storing the samples sunk in IPA in a glass container.
- Submerging the samples in warm IPA (40°C), taking them out vertically and blow drying nitrogen or helium on them, just before inserting them into the deposition chamber.

3.2.6 Experimental procedure

The cleaned silicon samples were glued with Electrodag 1415M silver paste (silver in Methyl Isobutyl Ketone) onto the substrate holder, to provide a good thermal contact. The substrate holder was then introduced in the chamber through one of the side flanges, with the pocket holding the samples in the centre of the chamber. The Roots pumping line was then switched on and at the same time, with the isolating valve closed, the turbo molecular pumping line was turned on. When the base pressure in the chamber reached the value of 10^{-4} Torr (after 5-7 minutes), air was leaked into the chamber through a leak valve and a DC glow discharge cleaning plasma was started. The time used for the in situ substrate cleaning varied function of the substrate holder used (small or large), and the power supply used. The cleaning plasma was switched off when the substrate reached the maximum temperature desired for the deposition process (~100°C). The leak valve was then closed, the pressure dropping quickly to 10^{-4} Torr, and then the butterfly valve was closed, isolating the Roots pumping line from the chamber. Then the isolating valve was opened and the chamber pumped down with the turbo line, until a pressure of less than 7.5×10^{-6} Torr was reached. The time needed to reach this pressure depended on the time the vessel was previously exposed to atmospheric air and was generally a good indication if there were any leaks present in the vacuum system.

During the time the chamber was pumped down with the turbo line, the cooling water for the cascaded plates of the ETP source was switched on, allowing the temperature and flow rate to reach optimum values before the plasma was ignited.

After the base pressure was less then 7.5×10^{-6} Torr, the isolating valve was closed and the butterfly valve was opened, the chamber being now pumped with the Roots line again and the base pressure rising again to 2×10^{-4} Torr. Then a flow of 2.5 slm of argon or argon/hydrogen mixture was inserted into the chamber through the source channel, the power supply connected to the source switched on (at 40 A) and the ETP was ignited. Then the arc current was adjusted for deposition conditions and when the substrate holder's temperature was close to the desired value, the precursor gas (methane/acetylene) was injected, either in the nozzle or in the injection ring. After few seconds, needed for the pressure to stabilise, the shutter was opened and the deposition process began. This was typically between 30 to 60 seconds. After that the shutter was closed, the precursor gas flow was stopped, the argon plasma was run for another ten seconds, then the power for the plasma source was switched off. The argon flow was then cut, and the pressure dropped again to 2×10^{-4} Torr. The Roots pump was switched off, then the backing rotary vane pump was switched off and the chamber vented with filtered air.

The temperature was allowed to drop below 100°C before the sample was unloaded from the chamber and then the whole process repeated for the next sample.

After every major modification made to the vacuum system, the chamber was tested for leaks with a residual gas analyser (RGA). The RGA head was switched on after a pressure of less that 5×10^{-5} Torr was reached, the mass set to the atomic mass of helium (4 a.m.u.), and helium gas was sprayed onto the joints of the vacuum vessel.

3.2.7 Matrix of experiments

3.2.7.1 Conditions used with methane

All the possible combinations of parameters are presented in Table 3.4. The experiments performed were just a selection of the conditions presented and resulted in a total of about 150 experiments performed with methane.

Table 3.4 Matrix of experiments for conditions used with methane as precursor gas

Gas mixture	97% Argon – 3% Hydrogen mixture						Argon (pure)					
Dist. source-sample [cm]	33			60			33			60		
Pressure [Torr]	0.6		1		6		0.6			1.5		
Arc current [A]	30		40		50		22	30		40		50
Substrate temperature [°C]	100		250		400		100		250		400	
CH_4 relative flow	1%	2%	3%	4%	6%		1%	2%	3%	4%	6%	8%

3.2.7.2 Conditions used with acetylene

Table 3.5 Matrix of experiments for conditions used with acetylene as precursor gas

Gas mixture	Argon (pure)					97% Argon – 3% Hydrogen mixture				
Injection position	nozzle		injection ring up		injection ring down	nozzle				
Pressure [Torr]	0.5		0.6		0.75	0.6			0.75	
Arc current [A]	50			70		50				
Substrate temperature [°C]	100		200		300	100		200		300
Substrate material	Si		glass	PEEK	PET	Si				
C_2H_2 relative flow	2%	4%	6%	8%	10%	2%	4%	6%	8%	10%

Not all the possible combinations of parameters from Table 3.5 were performed during the experiments. The deposition conditions were selected from the conditions above to give the best quality amorphous hydrogenated carbon films. This resulted in about 200 experiments performed with acetylene.

3.3 Plasma diagnostic tools

3.3.1 Langmuir probe

A Langmuir probe is a metallic electrode with an active surface that comes in contact with the plasma. Measuring the probe current as a function of the applied probe voltage gives information about the electrons temperature and electrons and ions densities in the plasma [25].

A necessary condition is that the conditions in the plasma do not change during the measurement. In a deposition environment this condition cannot be fulfilled. When a highly conductive material is deposited on the probe the potential drop is small and the measurements will not be influenced. If the material is less conductive (the case of a-C:H films) the potential drop cannot be ignored.

At lower deposition rates (changes in successive current – voltage characteristics are small) the data can be analysed taking into account the growing film on the probe. It is even possible to determine the deposition rate on the film if the conductivity of the a-C:H is known.

At higher deposition rates (the case of hydrogenated amorphous carbon films grown from the ETP source) the tip of the probe is covered with an insulating layer in a matter of seconds. This causes the probe signal to drop quickly and makes the interpretation of the results difficult and ambiguous [3 (p. 32)]

Due to this reason, the use of the Langmuir probe was limited to investigating argon and argon/hydrogen plasma, in order to determine the electron temperature and densities in the flowing plasma jet.

Figure 3.6 shows a typical probe current-voltage characteristic for a cylindrical probe immersed in argon plasma.

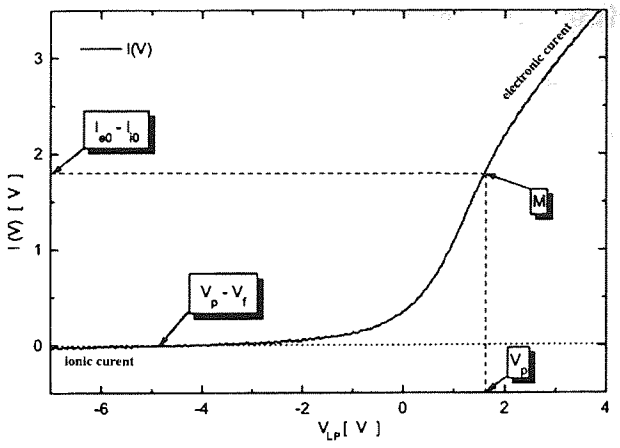

Figure 3.6 I-V characteristic taken with a cylindrical Langmuir probe (from [25])

If the potential of the Langmuir probe is equal to the surrounding potential of the plasma ($V_{LP} = V_P$), the probe will collect free moving particles (point M in Figure 3.6). Because the thermal density of the electronic current is greater than of the ionic one, the collected current will be predominant electronic: $I_M = I_{e0} - I_{i0}$, where I_{e0} and I_{i0} are the thermal currents of electrons and ions at the surface of the probe.

If the potential of the probe is positive compared to the potential of the plasma ($V_{LP} > V_P$) the probe will collect the electronic current, since the negative ions are repelled by the negative spatial charge sheath formed around the probe tip, while the electrons are accelerated by it.

If the probe potential is negative compared to the plasma potential ($V_{LP} < V_P$), the electrons are repelled by the probe and on the tip surface will arrive only the electrons with sufficient kinetic energy to overcome the work of the repulsive forces exerted by the electric field of the positive charge sheath formed around the probe. At even more negative potential of the probe fewer and fewer electrons arrive at the surface of the probe, and the intensity of the electronic current decreases. Eventually the current falls to zero as the ion and electron fluxes are equal. At this point the potential of the probe is at the floating potential (V_f), or the potential that would be assumed by an insulating object placed in the plasma. As the potential of the probe is made more negative still, even the energetic electrons are not able to reach the surface of the probe, and the collected current is purely ionic [12, 25].

The software supplied with the probe can either automatically analyse the data or allow manual analysis. The shape of the area of the graph between $V_{LP} = 0$ and point M gives the electron temperature and the magnitude of the electron saturation current gives the plasma density. The floating potential (V_f) is given by the point at which the probe current is zero. If the electron energy distribution function (EEDF) is Maxwellian, then a plot of the logarithm of the probe current versus the probe potential will yield a straight line for this part of the graph with the gradient being: $\frac{e}{KT_e}$, where e is the electron charge, K is Boltzman's constant and T_e is the electrons temperature [25, 84].

$$\ln\left(-I_{LP}(V_{LP})\right) = \frac{eV_{LP}}{KT_e} \qquad \textbf{Eqn 3.1}$$

Considering two different point on the straight line, one would obtain:

$$\tan(\alpha) = \frac{\ln(I_{LP2}) - \ln(I_{LP1})}{V_{LP2} - V_{LP1}} = \frac{e}{KT_e} \qquad \textbf{Eqn 3.2}$$

If the electrons temperature is expressed in electron volts (eV), the previous formula can be re-written as:

$$KT_e(eV) = \frac{V_{LP2} - V_{LP1}}{\ln(I_{LP2}) - \ln(I_{LP1})} \qquad \textbf{Eqn 3.3}$$

The ionic saturation current is equal to the product of the thermal ionic current density and the area collecting the ions from the plasma, which ideally can be considered to coincide with the probe surface:

$$I_{i0} = j_{i0}S = \frac{1}{4}en_i < \mathrm{v}_i > S = en_iS\sqrt{\frac{k_BT_i}{2\pi m_i}} \qquad \textbf{Eqn 3.4}$$

Thus, finding the ionic saturation current leads to the determination of the ions density in the plasma, if it is assumed that $T_i \approx T_e$.

3.3.2 Mass/energy analyser

A mass energy analyser is a probe inserted into the plasma to measure the energies of the ions/neutrals extracted from the bulk of the plasma. A layout of the probe which was bolted onto the side of the deposition chamber is shown in Figure 3.7:

The extractor behind the orifice can be set at a potential between –100V and +100V to extract either positive or negative ions from the plasma. From the orifice the ions travel to a transfer lens, which is used to refocus the ion beam onto the exit aperture of the electron impact ion source. A drift space and a lens are used to transfer the ions to the input of the Sector Energy Analyser. The ions are accelerated in this drift space and then refocused by the lens. The energy of the ions is selected on travelling through the energy filter, which is a 45° sector field energy analyser. A decelerating lens reduces the energy of the ions before injecting them into the quadrupole mass filter (QMF). The QMF is constructed in three sections: prefilter (RF only), main filter (RF and DC) and post filter. The ions finally reach the detector, which is an off axis mounted electron multiplier [85].

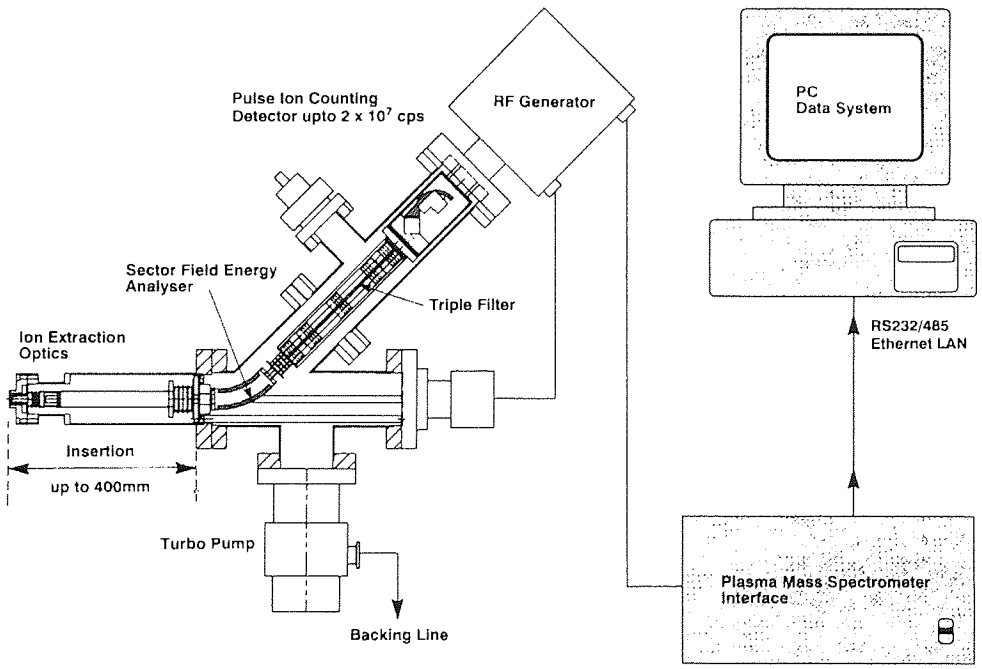

Figure 3.7 Schematic layout of the mass/energy analyser system (from [85])

The mass/energy analyser used was a Hal Hiden EQP plasma diagnostic system which was run from a PC using MASsoft software under Windows 3.1. The mass probe could be operated in two distinct modes: Residual Gas Analysis mode (RGA) to check for leaks and contaminants and also for the mass distribution of the particles in the buffer gas or in Secondary Ions Mass Spectroscopy mode (SIMS) to sample ions from the plasma and measure their energies.

Similar to the Langmuir probe case, during the deposition process, the 30 μm entrance aperture would be easily covered with an insulating film, which made the interpretation of the results difficult. Due to this reason and to the fact that the MAE could be only mounted sideways on the vessel, its use was limited to measuring the ions' energies in the argon jet, close to the substrate level.

3.3.3 Optical spectrograph

When atomic or molecular species are in an excited state, they may decay to a lower state by emitting electromagnetic radiation. For atoms this decay occurs between electronic states, while for molecules and radicals transitions between rotational and vibrational states are also possible. Many particles in the plasma will be excited. For certain species the electronic, rotational and vibrational transitions determinate the emission of visible light which can be detected via emission spectroscopy [3 (p. 34)].

The optical set-up consisted of an optical fibre, fixed in front of a window on the side of the vessel, connected to a 270M Rapid Scanning Imaging Spectrograph/Monochromator. The scanning range of the spectrograph was 0 – 1100 nm and the resolution was 0.1 nm [86].

The spectrograph was connected to a computer that has an interface card and dedicated software, which allows automatic control over the spectrograph and different types of analysis and processing procedures for the recorded spectrum, presented in Figure 3.8.

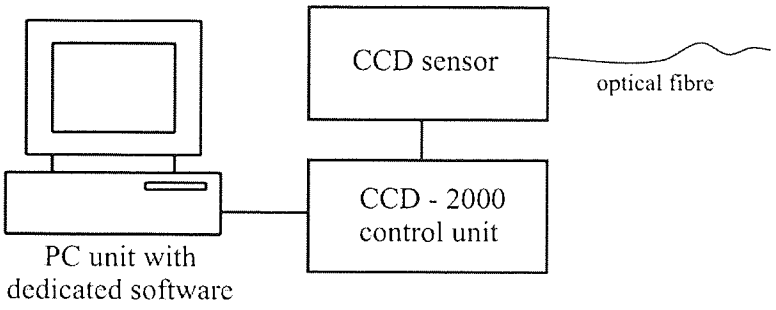

Figure 3.8 Block diagram of 270M SPEX optical spectrograph

The spectrum gives information about the neutral and ion species present in the plasma. The signal collected is an integral signal and cannot differentiate between different regions in the plasma (e.g. the plasma jet and the background region). For this reason the spectrograph was only used to check the changes in plasma chemistry when methane or acetylene was injected in the argon jet.

3.4 Thin film analysis techniques

The techniques described below were used in the analysis of some or all of the samples in order to gain as complete a characterisation as possible of the physical and mechanical properties of the films produced and hence correlate these with the deposition conditions.

3.4.1 Optical Microscopy

An Olympus optical microscope was used to investigate the surface of the films and of the virgin samples, to check for pinholes in the film and dirt particles. A Nikon Coolpix 4500 digital camera was attached, through a system of lenses, to the microscope and could transfer the images to a computer. The combined magnification of the lens system and the camera zoom gave a maximum magnification of 600 times, which was commonly used.

3.4.2 Ellipsometry

Ellipsometry is based on measuring the changes of the amplitude and phase of polarised light when reflected on a sample surface under defined angle. The principle is illustrated in Figure 3.9.

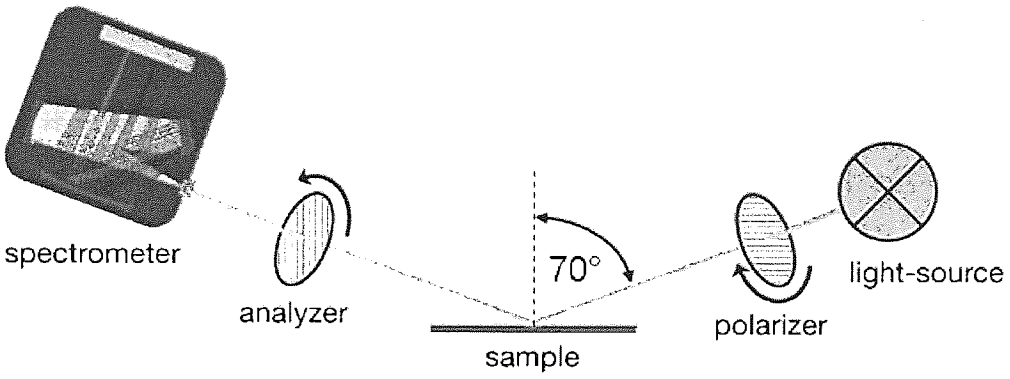

Figure 3.9 The ellipsometric principle (from [87])

Spectroscopic ellipsometry measures these parameters (Ψ and Δ) not only for one specific wavelength but for a complete spectral range. By fitting the simulated spectra of $\tan\Psi$ and $\cos\Delta$ it is possible to measure beside the layer thickness much more complex layer characteristics like refractive index, absorption, roughness, components ratio, depending on the physical model used in the fitting algorithm.

The interaction between the light and the sample surface changes the linear polarised light into elliptically polarised light. This change is analysed by the spectrometer after travelling through a defined analyser. The high sensitivity to phase changes during the reflection makes ellipsometry one of the most precise and accurate methods for thin film measurement and characterization [87]

The polarisation change is given by the complex ratio ρ by:

$$\rho = \frac{R_p}{R_s} \qquad \textbf{Eqn 3.5}$$

R_p and R_s are complex reflection coefficients for the light components polarised parallel and perpendicular to the plane of incidence. So ρ is a complex quantity and is generally expressed in the ellipsometric angles Ψ and Δ:

$$\rho = \tan\Psi \exp j\Delta \qquad \textbf{Eqn 3.6}$$

In measurement set-ups either a rotating analyser or a rotating polariser system is used. In both methods a periodic signal is sent to the detector. By Fourier analysis of this signal

the ellipsometric Fourier coefficients a and b are determined. When the polariser angle is chosen at 45°, these coefficients are related to the ellipsometric angles Ψ and Δ by the following relationships:

$$a = -\cos 2\Psi \qquad \textbf{Eqn 3.7}$$

$$b = \sin 2\Psi \cos \Delta \qquad \textbf{Eqn 3.8}$$

The refractive index n and the extinction coefficient k enter the formulas through the Fresnel reflection coefficients R_p and R_s. The band gap can be introduced in the formula using the Tauc relation [2 (p. 189)]:

$$\sqrt{\alpha E} = G\left(E - E_g\right) \qquad \textbf{Eqn 3.9}$$

where E is the photon energy (in eV), E_g is the band gap (in eV), G is a density of states coefficient (in $cm^{-1/2}eV^{-1/2}$) and $\alpha = 4\pi k/\lambda$, where λ is the wavelength [6].

The ellipsometer used in the current set-up was a Rudolph Research Auto EL® III automatic ellipsometer. The light source used was a low power helium-neon laser which emits only the 632.8nm red line.

A collimated beam of unpolarised monochromatic light is transmitted through a polariser and quarter wave compensator to the surface of the sample, which it strikes at an angle of incidence set by the operator. The beam is reflected by the sample through the analyser to a photomultiplier detector.

The polariser converts the collimated beam of unpolarised monochromatic light into a linear-polarized beam. The quarter-wave compensator converts the linearly polarised light into elliptically-polarised light, which strikes the sample. The compensator is orientated at an angle of 45° to the plane of incidence. The optical properties of the sample surface cause the polarisation form of the reflected beam to differ from that of the incident beam. The reflected beam passes through the analyser to the photomultiplier tube, the output of which is indicated by a meter on the electronics unit. An operator adjusts the orientations of the polariser and analyser to reduce the meter indication to a minimum (the condition of null or extinction point). As the analyser is rotated, the meter will indicate minimum

intensities at two different positions 180° apart. In general these minima will not correspond to true extinction, which can be achieved only if the reflected light is linearly polarised. For each sample there is some polariser orientation at which the reflected light is linearly polarised, so that true extinction may be obtained by means of the analyser. The operator finds these orientations by alternately adjusting the polariser and the analyser orientation to deepen the minimum of the meter, until a null corresponding to true extinction is obtained. From the polariser, analyser and compensator orientations at which the null is obtained, the optical properties of the sample may be calculated.

The AutoEL®-III is a microcomputer controlled automatic-nulling ellipsometer (i.e., an automated manual ellipsometer) in which the null seeking decisions are not made by the operator, but by an internal microcomputer. The iterative nulling adjustments are not performed manually but by stepper motors controlled by the microcomputer [88].

3.4.3 Atom force microscopy (AFM)

Throughout this project, atomic force microscopy (AFM) was used to map the topography of the virgin substrates and of the deposited amorphous carbon films. The surface roughness was calculated and compared for different types of films.

Atomic force microscopy in contact mode measures the repulsive forces between atoms in the probe tip and atoms in the sample surface. The tip is located at the end of a flexible cantilever. As the tip responds to the peaks and valleys of the sample surface, the cantilever bends. A laser beam reflected by the cantilever falls onto the face of a four-section photodetector. The force sensor (Figure 3.10) measures the deflection of the cantilever by measuring the difference in light intensity on the upper and lower halves.

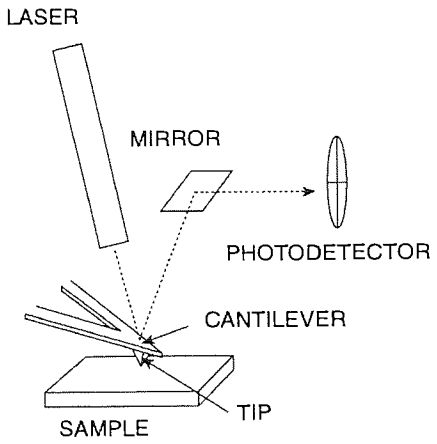

Figure 3.10 AFM force sensor

The deflection of the sensor is proportional to the force exerted by the surface according to Hook's law: $F = -kx$. A feedback electronic circuit is combined with the sensor and piezoelectric ceramics (Z PIEZO) to create the positioning mechanism (Figure 3.11), maintaining the sensor at a constant distance from the surface. These piezoelectric materials are constructed such that a change in their physical dimensions occurs when an electric field is applied.

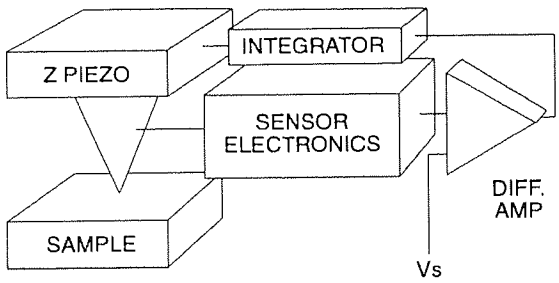

Figure 3.11 The feedback circuit (from [89])

When the sensor moves toward the surface, the output of the sensor electronics increases. The differential amplifier compares the increased value from the sensor electronics to the reference value and outputs a correction voltage. The correction voltage excites the piezoelectric ceramic such that the sensor is pulled away from the surface.

The microscope is created by adding two ceramics to scan the sensor in the X-Y plane and a computer to capture the error signal from the integrator to the positioning device (Figure 3.12).

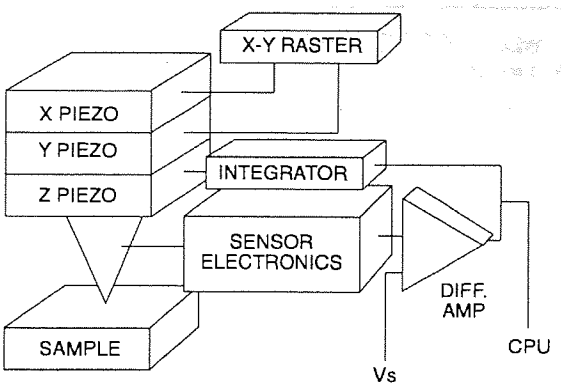

Figure 3.12 Scanning probe microscope system (from [89])

An image of the surface is generated by rastering the sensor over the surface and storing the piezo driver signal on the computer [89].

The films were mapped using a ThermoMicroscopes™ Autoprobe M5 fitted with ThermoMicroscopes™ ProScan Sotfware (Version 2.1). The instrument was used in contact mode and the scanned area was usually between 100 μm × 100 μm to 5 μm × 5 μm.

3.4.4 X-Ray Photoelectron Spectroscopy (XPS)

The principle of XPS technique is based on the photoelectric effect. A copper anode coated with aluminium (Al) or magnesium (Mg), with characteristic energies of 1253.6 eV and 1486.6 eV respectively, emits X-ray photons that ionise the target atoms. These atoms relax by emitting photoelectrons and the spectrum of these photoelectrons, directly related to the discrete binding energies of the electrons from the target atoms, gives the chemical 'fingerprint' of the surface [90].

The energy scale may refer to binding energy (BE) of the level of origin or to the kinetic energy (KE) of the photoelectrons collected by the analyser. Kinetic and binding energies are related as follows:

$$KE = h\nu - \Phi - BE \qquad \text{Eqn 3.10}$$

where $h\nu$ is the energy of the incident X-Ray photon and Φ is the work function of the apparatus.

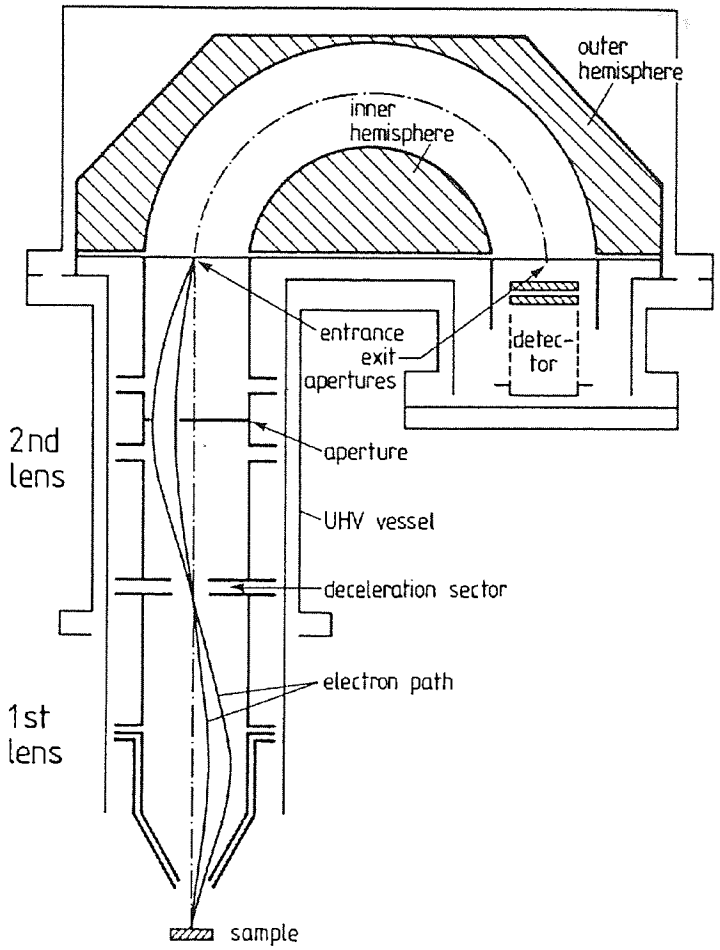

Figure 3.13 Cross-section of a concentric hemispherical analyser

The spectrum consists of a series of peaks observed on a background which generally increases to high binding energy (low kinetic energy) and which also shows step-like increases on the high binding energy side of each significant peak. Eqn 3.10 assumes that the photoemission process is elastic. Thus each characteristic X-ray will give rise to a series of photoelectron peaks which reflect the discrete binding energies of the electrons present in the solid. The peak intensity depends on the atomic photoemission cross-section, as well as on the transmission characteristics of the analyser, itself function of the electrons energy. The peak width, or full width at half maximum (FWHM) ΔE, is the convolution of several contributions:

$$\Delta E = \sqrt{\left(\Delta E_n^2 + \Delta E_p^2 + \Delta E_a^2\right)} \qquad \textbf{Eqn 3.11}$$

where $\Delta E_n, \Delta E_p$ and ΔE_a are the natural widths of the core level, the photon source (X-ray line) and of the analyser resolution, respectively.

The peaks are of three types: peaks due to photoemission from core levels (at high BEs) and valance levels (at low BEs) and peaks due to X-ray excited Auger photoemission. The photoemission cross section, and therefore the peak intensity, is much smaller for valance than for core levels.

Changing the X-Ray source from Mg K_α to Al K_α will increase the photoelectron kinetic energy by 233 eV, leaving the Auger peaks unchanged.

The step like background is raised by an inelastic photoemission process: a fraction of the photoelectrons contributing to significant peaks are scattered and loose energy before they eventually leave the surface and reach the analyser.

Throughout the project an XPS unmonochromated source from a VG Escalab 200D system was used for finding the chemical state of elements present in the film and for determining the ratio of the sp^3/sp^2 bonded carbon atoms.

Sp^3 fractions were determined by XAES technique [91-96]. The X ray source used was Al Kα (1486.6 eV). The C 1s and O 1s peaks were collected with a pass energy of 20 eV at steps of 0.1 eV/channel, the C KLL spectra was collected with a pass energy of 20 eV in steps of 0.2 eV/channel. The samples were stored in plastic boxes after deposition and then inserted in the XPS analysis chamber in batches of 6. The analysed area was 2×3 mm^2 for each sample and the base pressure during the analysis was less than 5×10^{-9} mbar.

The collected spectra were then analysed with Eclipse 5.1 software run under an OS2 operating system. The derivative of the XAES spectra was obtained by a Savinsky-Golay method, after a smoothing with 27 points, 2 passes was performed. The difference between the mean of the positive and negative peaks in the differentiated XAES spectra (D) was monitored for all films.

The C 1s and O 1s were smoothed with 9 points and 10 passes. A typical surface contamination of 7-10 % atomic concentration of oxygen was found for all the a-C:H films analysed. More details can be found in the next chapter, at the XAES results section.

3.4.5 Raman spectroscopy

Raman spectroscopy is a fast technique for the analysis of the deposited carbon materials. The technique is based on the principle that the frequency of light scattered by matter shifts by a small value depending on the vibrational properties of the matter. The specific advantage of the method is that is can distinguish clearly between the different allotropes of one element [97-101].

A practical guide to the technique can be found in [102]. In the classical approach the Raman effect can be regarded as the scattering of light by a collection of atoms undergoing simple harmonic vibrations. When a molecule is subjected to an electric field the atoms acquire an electric dipole moment. For small fields, the induced dipole moment μ_i is proportional to the field strength E.

$$\mu_i = \alpha \cdot E \qquad \textbf{Eqn 3.12}$$

The proportionality constant α is the polarisability of the molecule. Electromagnetic radiation generates an electric field that can be expressed as:

$$E = E^0 \cos(2\pi\nu_0 t) \qquad \textbf{Eqn 3.13}$$

E^0 is the equilibrium field strength and ν_0 is the angular frequency of the radiation. When a diatomic molecule vibrates harmonically at a frequency ν_v, its vibration as a function of time t can be expressed as:

$$q_v = q_0 \cos(2\pi\nu_v t) \qquad \textbf{Eqn 3.14}$$

with q_v the elongation of the molecule along the axis and q_0 the equilibrium elongation of the molecule.

A necessary condition for the occurrence of Raman scattering is that the polarisability α changes during the vibration. For small vibrational amplitudes its value will be:

$$\alpha = \alpha_0 + \left(\frac{\partial \alpha}{\partial q_v}\right)_0 q_v \qquad \textbf{Eqn 3.15}$$

Substituting Eqn 3.13 and Eqn 3.15 into Eqn 3.12 and using equation Eqn 3.14 the effect of the incident radiation of frequency ν_0 on the induced dipole moment μ_i can be written as:

$$\mu_i = \alpha^0 E^0 \cos(2\pi\nu_0 t) + \left(\frac{\partial \alpha}{\partial q_v}\right)_0 E^0 \frac{q_0}{2}\left[\cos(2\pi(\nu_0 + \nu_v)t) + \cos(2\pi(\nu_0 - \nu_v)t)\right] \qquad \textbf{Eqn 3.16}$$

The first term in Eqn 3.16 describes the Rayleigh scattering and the remaining term describes the Stokes and anti-Stokes Raman scattering. Eqn 3.16 shows that light will be scattered with frequencies: ν_0 = Rayleigh scattering and $\nu_0 \pm \nu_v$ = Raman scattering.

The Raman technique was used partially at Aston University and partially at Jobin Yvon UK Ltd. - Raman division, only in the initial stages of the project, to analyse and compare the results from some films deposited from methane with the results from XPS/XAES technique. A standard LabRAM 300 system was used, configured with a 532 nm visible laser excitation. The samples did not need any special preparation, the laser beam being sent onto the films' surface and the reflected signal recorded, analysed and interpreted.

3.4.6 Nano test module

The NanoTest module is a testing centre that analyses the nanomechanical properties of materials (films) [103]. The system has three different modules: indentation, scratch and impact. The indentation module was used for determining the hardness and elastic modulus of the deposited films, whereas the scratching module was mainly used to determine the adhesion of the films to substrates.

At the heart of the NanoTest system is a pendulum that can rotate on a frictionless pivot (see Figure 3.14). A coil is mounted at the top of the pendulum; with a coil current present, the coil is attracted towards a permanent magnet, producing motion of the

diamond towards the sample and into the sample surface. The displacement of the diamond is measured by means of a parallel plate capacitor, one plate of which is attached to the diamond holder. When the diamond moves, the capacitance changes, and this is measured using a capacitance bridge. The capacitance bridge unit is located close to the measuring capacitor, in order to minimise stray capacitor effects [103].

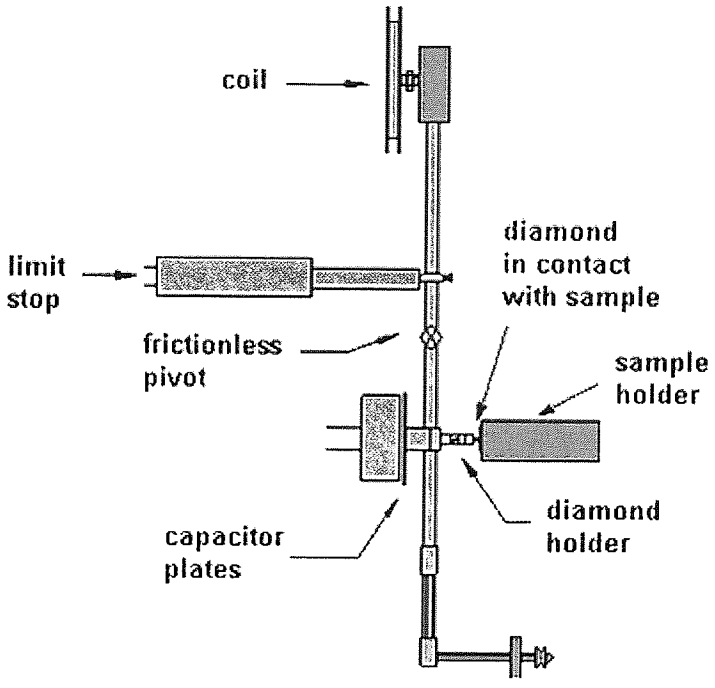

Figure 3.14 Schematics of the NanoTest module (from [103])

The sample manipulation is done by three DC motors driving micrometer stages in an XYZ configuration. The motor control electronics consists of a mother board containing three power modules, a networking interface module and a backlash control board. These plug into expansion slots in the computer.

The limit stop defines the maximum outward movement of the diamond, and also the operating orientation of the pendulum, when a load is applied. Its position is manually adjusted with a micrometer. The equilibrium position of the pendulum, with zero load current, is adjusted with balance weights which are movable along both the horizontal and vertical axes [103]

3.4.6.1 Nanoindentation

In the nanoindentation technique the NanoTest measures the movement of a diamond probe in contact with a surface. In order to make a measurement, an increasing load is applied and the probe indents the surface, as shown schematically below:

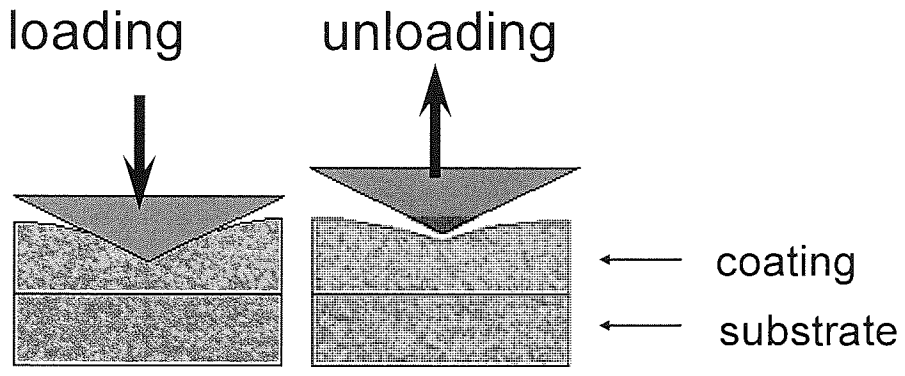

Figure 3.15 Schematic of the loading –unloading process used by the NanoTest during indentation (from [103])

In a pyramidal indentation, the NanoTest measures the penetration depth of the calibrated diamond Berkovich indenter as a function of the applied load during a load-unload cycle. On unloading the elastic component of the displacement starts to recover producing a sloped rather than horizontal unloading curve. It is from this slope that the elastic and plastic properties can be derived.

For statistical purposes, it is good practice to quote mean values of hardness and reduced modulus from 5-10 indentation curves acquired under the same parameters.

The NanoTest data analysis software produces values of h_{total} ($h_{\max}$) and $h_{plastic}$ (h_c, contact depth) together with the derived hardness and elastic modulus.

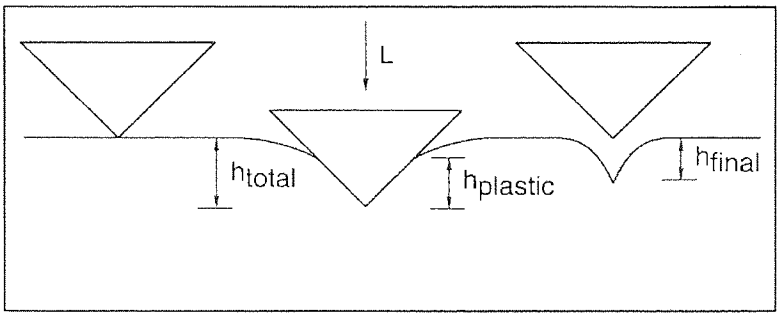

Figure 3.16 Plastic depth during an indentation

In Pyramidal analysis, the depth vs. load unloading data can be fitted to either: a) a linear fit – a tangent to the unloading curve at the maximum load or b) a power law fit (Oliver and Pharr fit) [104].

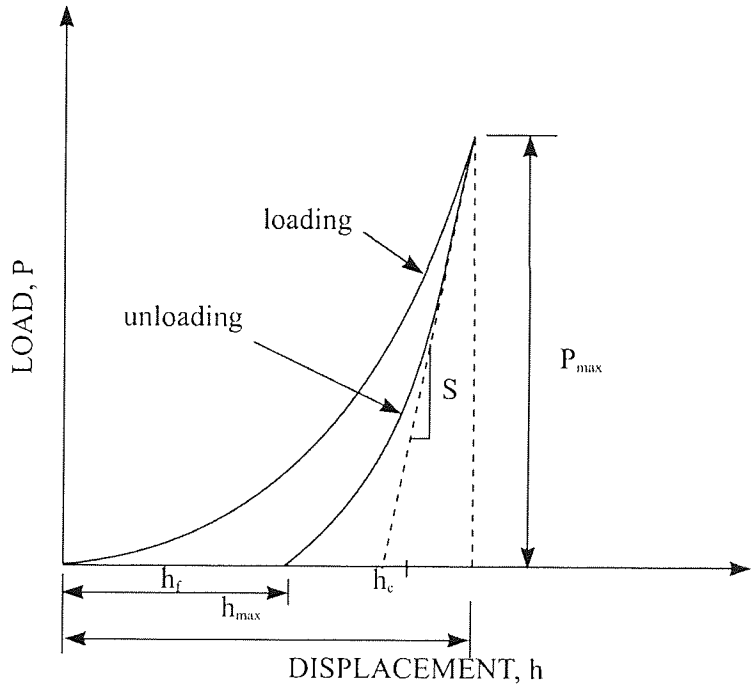

Figure 3.17 Plastic depth determination from loading-unloading curve

Both methods are described in more detail below.

Hardness and Modulus: Linear Fitting

The Meyer hardness is defined by $H = \frac{P_{max}}{A_{max}}$ where P_{max} is the maximum load and A_{max} is the projected contact area at maximum load calculated from the contact depth h_c. For a

material exhibiting elastic recovery, it is assumed that the contact area between the indenter and the material remains constant and moves elastically during unloading. A further assumption is that the plastic area is always equal to the contact area; in practice, the plastic area may be larger or smaller. For a constant cylindrical contact area, the elastic recovery in this case is described by the equation:

$$P = 2E_r a d_e \qquad \textbf{Eqn 3.17}$$

where: P = Maximum load, E_r = Reduced modulus, a = Radius of contact area, d_e = Elastic deformation [105].

$$\frac{1}{E_r} = \frac{1-n^2}{E} + \frac{1-n_0^{\,2}}{E_0} \qquad \textbf{Eqn 3.18}$$

where: n = Poisson's ratio for the sample, n_0 = Poisson's ratio for the indenter (0.07), E = Young's Modulus for the sample, E_0 = Young's modulus for the indenter (1141 GPa).

Linear unloading down to the contact depth h_c at zero load is predicted. This is never observed since the indent begins to "open", i.e., "a" changes, leading to a departure from linearity which is greater in materials with a higher $\frac{H}{E}$ ratio. However, the initial part of the curve is reasonably linear for most materials, and the plastic depth is therefore defined by fitting the first 20% of the data points to a straight line, extrapolating this to zero load, and taking the intercept on the depth axis as the final plastic depth.

For a homogeneous material and a perfect indenter geometry, an Elastic Recovery Parameter, R, is defined. This, which is indicative of the slope of the unloading curve, is related to the $\frac{H}{E}$ ratio as follows:

$$R = \frac{h_{\max} - h_c}{h_c} = \frac{H(1-n^2)(kp)^{0.5}}{2E} \qquad \textbf{Eqn 3.19}$$

where k is a diamond geometry factor [105].

From Eqn 3.17 the unloading slope is given by [104]:

$$C = \frac{\sqrt{\pi}}{2E_r\sqrt{A}} \qquad \textbf{Eqn 3.20}$$

where C is the frame compliance.

After correction of the data for frame compliance, this allows the modulus of the material to be determined.

Hardness and Modulus: Power Law Fitting

After frame compliance correction, the Depth vs. Load raw data is fitted to a power law expression of the form:

$$P = a(h - h_f)^m \qquad \textbf{Eqn 3.21}$$

where a, h_f and m are constants. This is justified on the basis of elasticity theory. The true contact depth is then determined from the expression:

$$h_c = h_{\max} - \varepsilon(C \cdot P_{\max}) \qquad \textbf{Eqn 3.22}$$

where C is the contact compliance equal to the tangent at maximum load. The value of ε depends on the indenter geometry, e.g., for a paraboloid of rotation it is 0.75. Experimentally, the Berkovich diamond produces the elastic recovery behaviour expected of a paraboloid of rotation.

Diamond Area and Frame Compliance Calibration

No diamond is perfectly sharp, so it is necessary to determine the real contact area as a function of contact depth. The NanoTest has an automatic procedure for this which utilises results from a series of indentations performed at different loads in fused silica. Using measured contact compliance values and literature values for the properties of fused silica (E = 72 GPa and n = 0.17), Eqn 3.20 allows a series of contact area values to be calculated. A least squares fitting procedure is then used to obtain a quadratic diamond area function given by $A = a \cdot h_c^2 + b \cdot h_c$, where a and b are constants and h_c

is the contact depth. An ideal Berkovitch indenter has a contact area given by $A = 24.5 \cdot h_c^2$

For the determination of material elastic properties, it is necessary to subtract any small elastic deformation of the instrument itself. In the NanoTest, automatic frame compliance determination is based on elastic recovery data obtained from well-documented reference materials. Again, fused silica is normally used.

Throughout the project, Hardness and Reduced Modulus were measured with a Micro Materials NanoTest 500 instrument using a NT Berkovich indenter (radius ~150 nm). The indentation depth was kept to 10-15% of the film thickness to minimise the influence from the Si substrate [106-110]. The temperature in the cabinet was kept constant at 2 degrees above the room temperature. The samples were glued with superglue to a stub and removed by heating afterwards. The indenter was periodically calibrated and standard tests were performed daily.

3.4.6.2 Scratch test

In the scratch tests the NanoTest keeps the indenter pendulum fixed, while moving the sample. An increasing force is applied to the indenter and the load, penetration depth and distanced travelled (from a point of reference) are recorded. The indenter used is of different geometry compared to the one used for nanoindentation. This is because the scratch technique would damage the very sharp intenter used in nanoindentation.

Multiple scratch tests were performed on each sample with a NT Rockwell indenter, with a radius of 25 μm. The scratch length was 500 – 600 μm and the maximum force applied during the tests was typically 70 or 200 mN. To quantify the adhesion of the film to the substrate for films with different thicknesses, a new parameter was introduced, $r = \frac{critical\ load}{thickness}$. This parameter was calculated and compared for each sample. The critical load from the above relation was defined as the load at which the indenter would penetrate through the coating onto the substrate. This was observed primarily by analysing the data collected with the software and also by observing the image collected via the optical microscope.

3.4.7 Fourier Transformed Infra Red Spectroscopy (FTIR)

In a molecule, the atoms are not held rigidly apart. Instead they can move, as if they are attached by a spring of equilibrium separation R_e. This bond can either bend or stretch. If the bond is subjected to infrared radiation of a specific frequency (between 300 – 4000 cm^{-1}), it will absorb the energy, and the bond will move from the lowest vibrational state, to the next highest. In a simple diatomic molecule, there is only one direction of vibrating, stretching. This means there is only one band of infra red absorption. Weaker bonds require less energy, as if the bonds are springs of different strengths. If there are more atoms, there will be more bonds, and therefore more modes of vibrations. This will produce a more complicated spectrum. For a linear molecule with n atoms, there are $3n-5$ vibrational modes; if it is nonlinear, it will have $3n-6$ modes. For example, water (H_2O), has 3 atoms, and is non-linear, therefore it has $(3\cdot 3)-6=3$ modes of vibration [111].

There is one important restriction: the molecule will only absorb radiation if the vibration is accompanied by a change in the dipole moment of the molecule. A dipole occurs when there is a difference of charge across a bond. If the two oppositely charged atoms get closer or further apart as the bond bends or stretches, the moment will change. The frequency of the light absorbed can be calculated from Hook's law:

$$\nu_{osc} = \frac{1}{2\pi}\sqrt{k\frac{m_1+m_2}{m_1 m_2}} \qquad \textbf{Eqn 3.23}$$

where: k is a force constant indicating the strength of the bond, m_1 and m_2 are the masses of the two atoms.

From the above equation, it can be seen that if there is a high value of k, i.e. the bond is strong, it absorbs a higher frequency of light. So, a C=C double bond would absorb a higher frequency of light than a C–C single bond. Also, the larger the two masses, the lower the frequency of light absorbed.

Because chemical bonds absorb infrared energy at specific frequencies (or wavelengths), the basic structure of compounds can be determined by the spectral locations of their IR

absorption peaks. The plot of a compound's IR transmission vs. frequency is its "fingerprint", which when compared to reference spectra identifies the material. FTIR spectrometers offer speed and sensitivity impossible to achieve with earlier wavelength-dispersive instruments.

The schematic principle of a FTIR spectrometer is shown in Figure 3.18:

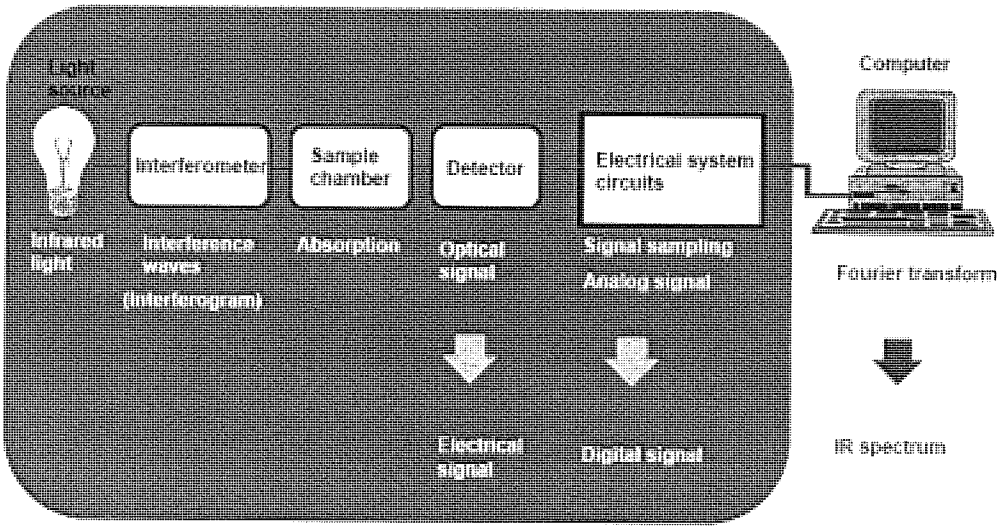

Figure 3.18 Schematic diagram of an IR spectrometer (from [111])

The incident beam is split into two beams, one of which is passed through a reference cell, and the other through the sample to be analysed. The detector then compares the two beams it receives and outputs a differentiated signal.

The graph produced shows percentage transmission against wave number. If no radiation is absorbed at a particular frequency, then the line on the graph will be be at 100% at the corresponding wave number. Different types of bonds have characteristic regions of the spectrum where they absorb:

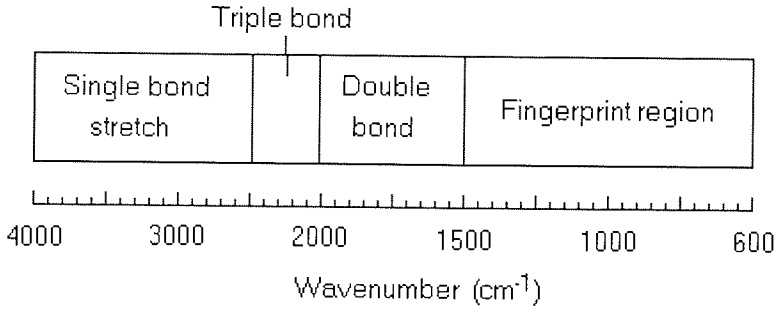

Figure 3.19 Diagram of specific FTIR absorption bands (from [112])

Most functional groups absorb above 1500 cm^{-1}. The region below 1500 cm^{-1} is known as the "fingerprint region", where every molecule produces a unique pattern [112].

The relative hydrogen content in some of the films was measured with a FTIR Bruker Vector 22 spectrometer at OTB Engineering by the author. The software used to collect and analyse the spectra was Opus 4.0. First a virgin silicon sample was measured, to find a background level, then the absorption spectra were collected for all samples and the silicon signal subtracted. Care was taken when preparing the samples for analysis, i.e. all traces of silver paste were carefully removed from the back side of the silicon sample, because silver peaks interfere with the a-C:H peaks. Because FTIR is based on the vibration modes of the C-H bonds, this technique is not able to detect the unbonded hydrogen present in the films; however this is a less critical issue in the case of amorphous carbon films, where the amount of unbonded hydrogen is small [2 (p. 180)].

4 Results

4.1 Results on testing the industrial plasma source at OTB Engineering

4.1.1 Measuring source parameters and the ionisation profile

A large part of the initial work done by the author (the training programme at OTB Engineering) involved testing different types of plasma cascaded arc sources, developed inside the company or produced by other external companies. The first part of the tests consisted of measuring the source parameters (flows, currents, voltages, and pressures) and the ionisation profile of the plasma jet, with the Langmuir probe. It was interesting to follow how the different improvements to the plasma source affected these parameters and how the final version of the source was built.

4.1.1.1 Source OTB - 3 mm plasma channel diameter (OTB 3mm source)

The tests started with a plasma source with a 3mm channel. Several parameters were recorded, such as the voltage across the source, the pressure in the chamber and in the source channel as a function of the admixed argon flow in the channel, for two (or three) different source currents (powers). The variations of these parameters are presented in the following graphs:

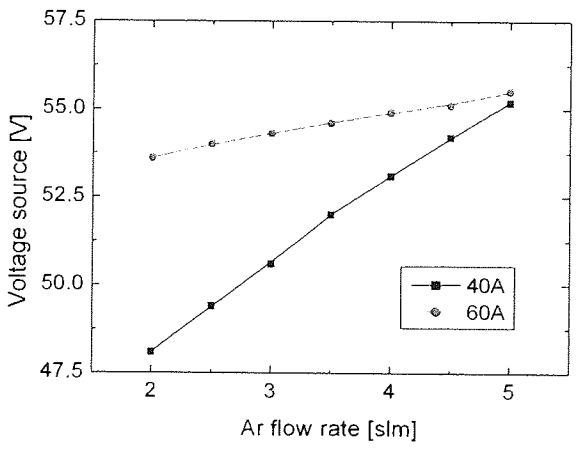

Figure 4.1 Voltage across the source function of Ar flow for a OTB 3mm source at two different current intensities

As can be seen from Figure 4.1, the voltage over the source increased with the increase in flow rate and source current, which was to be expected. The slope was different for 40A and 60A source current due to the different dissociation degrees in the plasma channel. At higher flows the voltage was almost the same for 40 and 60A source current.

The errors in measuring the flow rates throughout these tests are very small, always less than 1% relative error. This would correspond to an average absolute value of 0.035 slm. For convenience these errors are not presented in the graphs. Very small errors were also calculated for the voltages across the source, which were measured by a digital voltmeter. In this case the relative error was less than 0.5% and was plotted in all the graphs, but it is sometimes difficult to distinguish the error bars from the actual experimental points, like in Figure 4.1. For all other parameters an average relative error was calculated and plotted in all the following graphs.

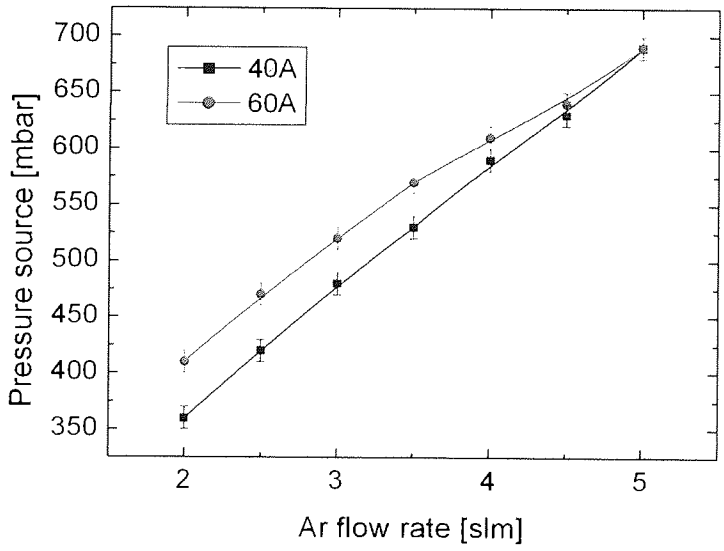

Figure 4.2 The pressure in the source as a function of the Ar flow for OTB 3mm source at two different current intensities

The pressure in the source channel increased with the increase in Ar flow and the increase in source current (power), more easily observed at lower Ar flows (Figure 4.2) Pressure in the chamber did not depend on the current intensity; it increased with the Ar flow and it was the same for a given Ar flow and different source currents (Figure 4.3).

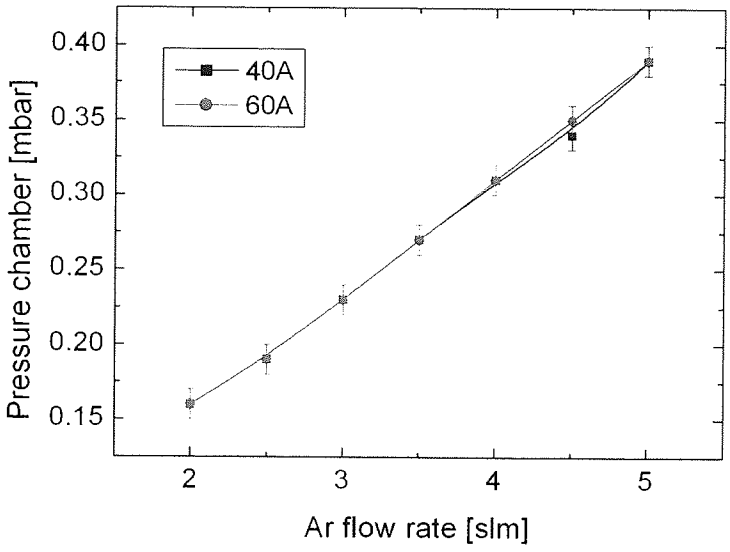

Figure 4.3 Pressure in the chamber (operating pressure) vs. Ar flow rate for 3mm OTB source at two different current intensities

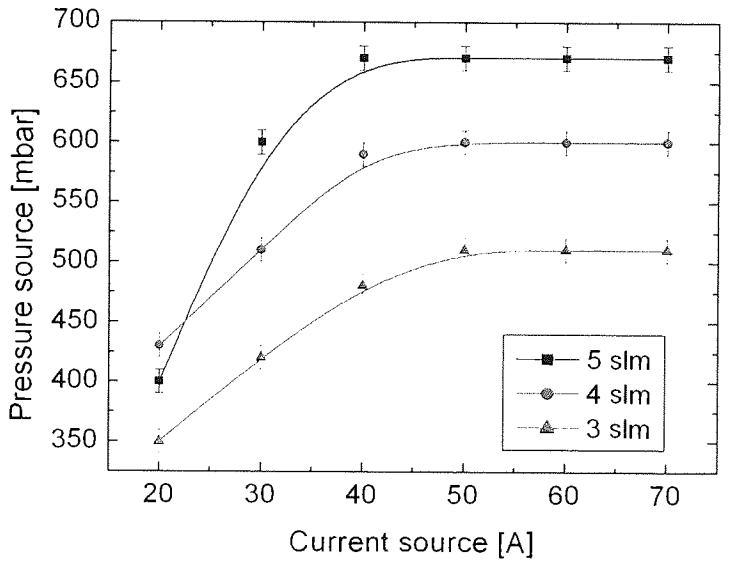

Figure 4.4 Pressure in the source channel as a function of source current for OTB 3 mm source at 3 different Ar flow rates

The increase in cathode current caused an increase in the degree of dissociation in the plasma in the source channel which, in turn, led to an increase in pressure in the source channel. After the source current exceeded a certain value (50A), the degree of ionisation and source pressure remained constant (Figure 4.4). This could be explained as follows:

because the volume of the plasma channel is small (3 mm diameter), the extra ions produced with the additional input energy recombine with electrons before reaching the exit of the plasma channel and thus the overall degree of ionisation remains constant.

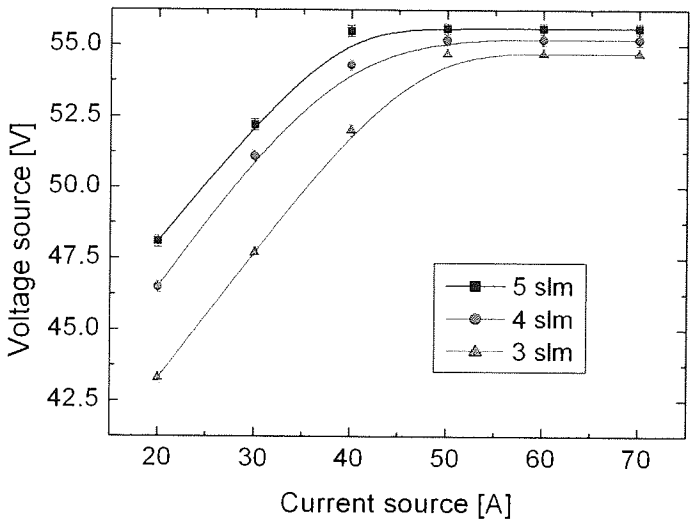

Figure 4.5 Voltage over the source as a function of source current for OTB 3 mm source at 3 different Ar flow rates

The voltage across the source for a given flow rate increased with the increase of current (the plasma has the same resistance) up to a point (~50A), and remained constant for higher currents, as explained above.

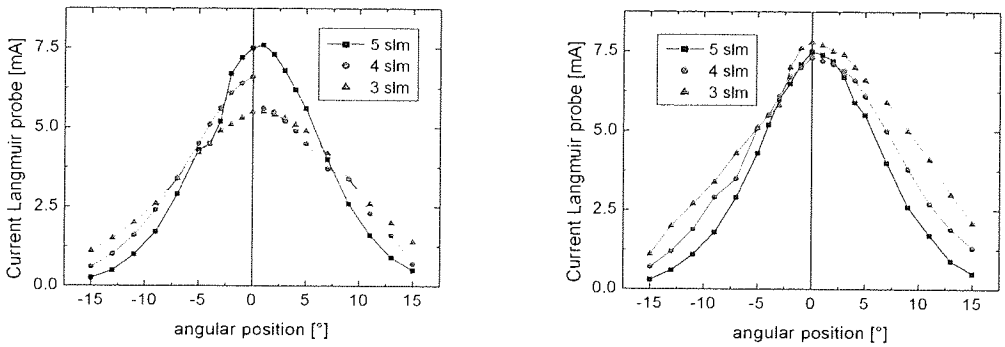

Figure 4.6 Argon ions density profiles for a distance of 18 cm from the source nozzle to the probe for a source current of 40 A (left image) and 60A (right image) for 3mm OTB source

The radial profiles of the argon ions were measured with a Langmuir double probe. The probe was inserted in the plasma jet at different distances from the source nozzle and then

radially swept from -15° to 15° angular position to determine the profile of the ions in a plane perpendicular to the central jet axis. Again, for convenience, the absolute errors are not presented, being very small. The results are presented in Figure 4.6 and Figure 4.7.

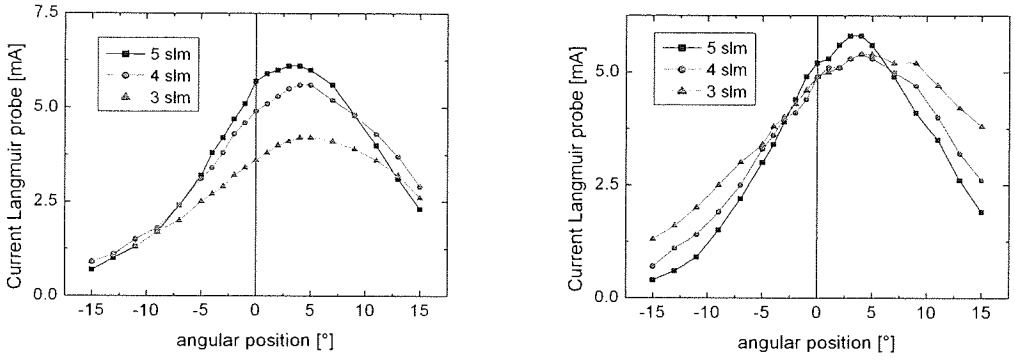

Figure 4.7 Argon ions density profiles for a distance of 30 cm from the source nozzle to the probe for a source current of 40 A (left image) and 60A (right image) for 3mm OTB source

At higher currents the ion density in the vicinity of the central axis was similar for different flows and the density profile suggests that with these settings small area substrates should be coated. At lower source currents (powers) and lower argon flows the profiles had a better distribution, which makes them suitable for larger area deposition. The distance from the nozzle to the probe did not affect the distribution of the profile, but only the absolute values.

As can be observed, sometimes the distribution of the ion density was not central (i.e. the maximum values are not at 0° angular position); this was due to the entire source (and the plasma channel) being unintentionally mounted off the central axis.

4.1.1.2 Source DSE - 4 mm plasma channel diameter

For a source with the 4 mm plasma channel the volume of plasma contained in the channel was almost double, which changed trends and absolute values. The voltage required to sustain the same current was much lower than in the case of the 3mm OTB source. The slopes were now identical for the different currents (see Figure 4.8).

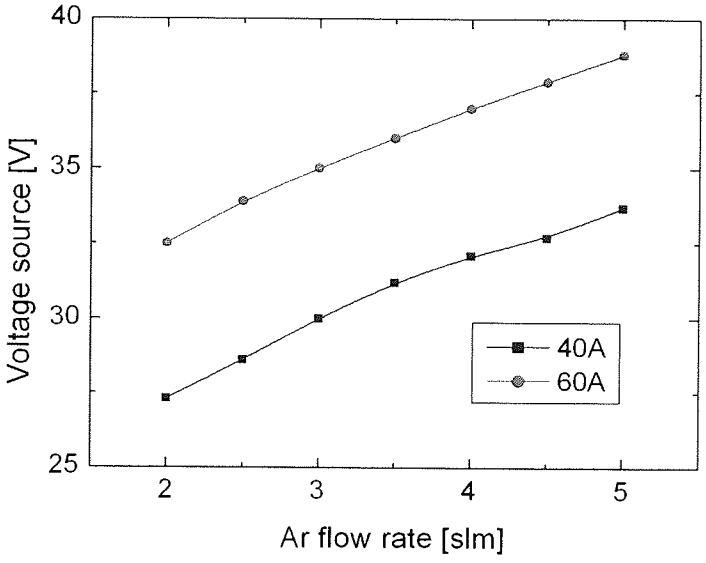

Figure 4.8 Voltage across the source function of Ar flow for a DSE 4mm source at two different current intensities

Pressure in the source was lower than in the 3 mm OTB case, which is to be expected, since the channel volume had increased (see Figure 4.9).

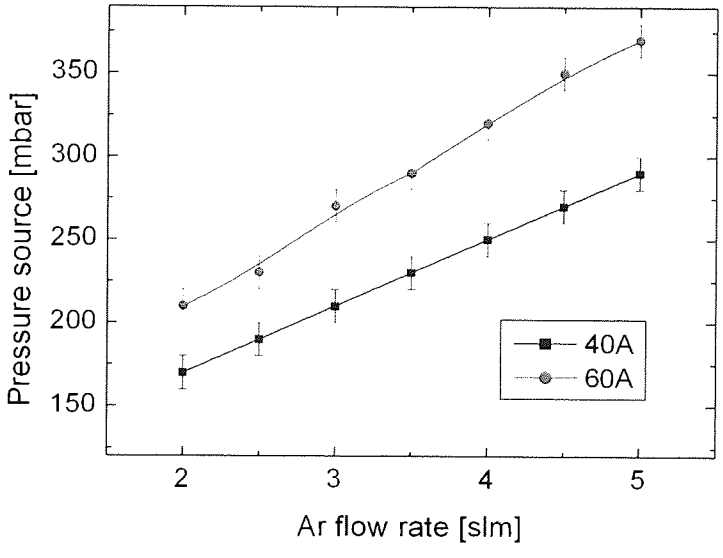

Figure 4.9 Pressure in the source function of Ar flow for a DSE 4mm source at two different current intensities

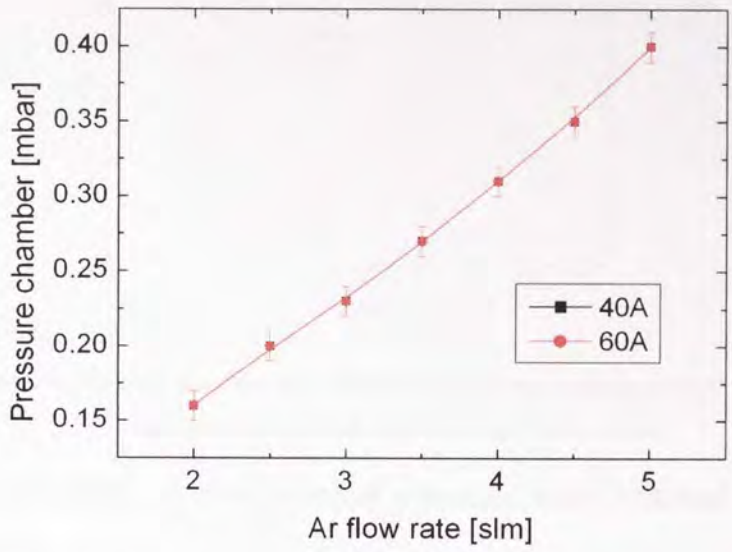

Figure 4.10 Pressure in the chamber function of Ar flow for a DSE 4mm source at two different current intensities

The pressure in the chamber was the same as in the 3mm OTB source case, which was to be expected, since the flow of argon and the volume of the chamber were the same.

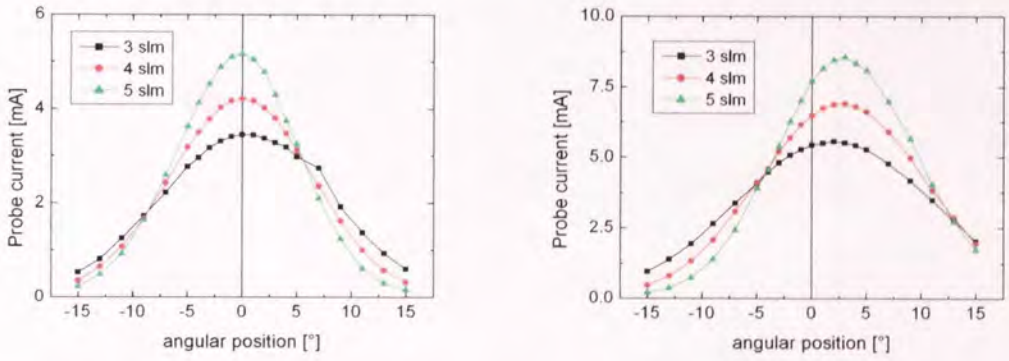

Figure 4.11 Argon ions density profiles for a distance of 18 cm from the source nozzle to the probe for a source current of 40 A (left image) and 60A (right image) for 4mm DSE source

Compared to the 3mm source case the density profiles were better separated from each other at the three different flows and the absolute values for the Langmuir Probe currents were lower. A clear difference in absolute current values was observed from the 40A to the 60A case (see Figure 4.11). The shape of the profiles had improved due to the change of the diameter of the plasma channel.

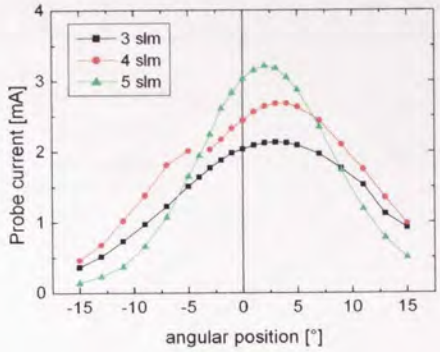

Figure 4.12 Argon ions density profiles for a distance of 30 cm from the source nozzle to the probe for a source current of 40A for 4mm DSE source

4.1.1.3 Source OTB - 4 mm plasma channel with internal cooling (OTB IC source)

This plasma source had the particularity that the cooling water for the cascaded plates was flowing from plate to plate (internal flow).The variations of the source parameters are presented in the following graphs:

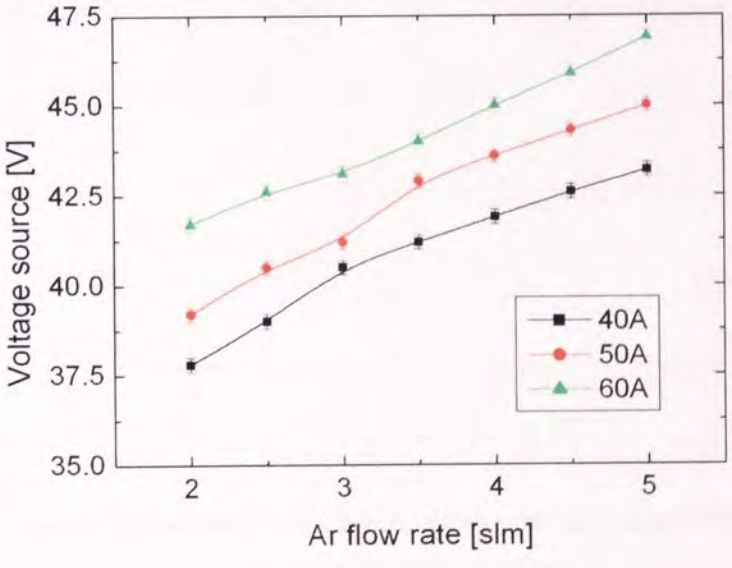

Figure 4.13 Voltage across the source function of Ar flow for 4 mm OTB IC source at three different current intensities

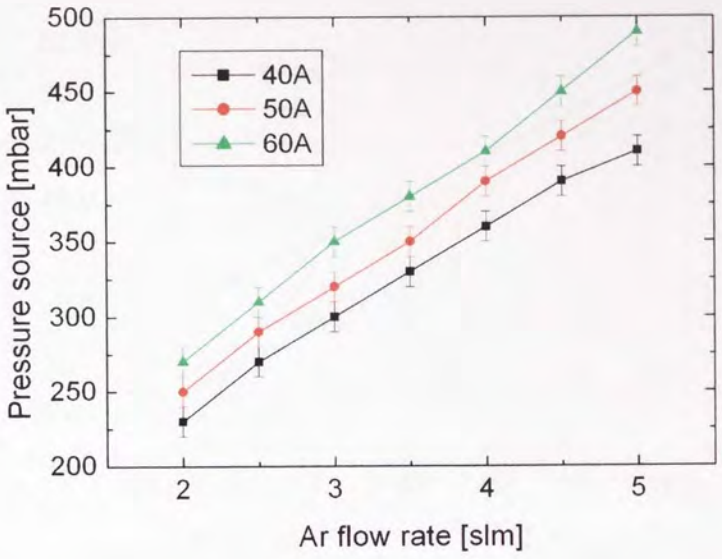

Figure 4.14 Pressure in the source as a function of Ar flow for 4mm OTB IC source at three different current intensities

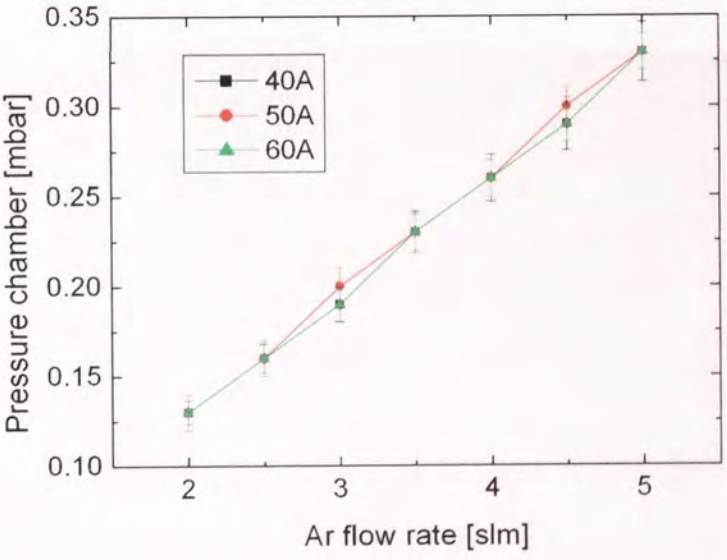

Figure 4.15 Pressure in the chamber as a function of Ar flow for 4mm OTB IC source at three different current intensities

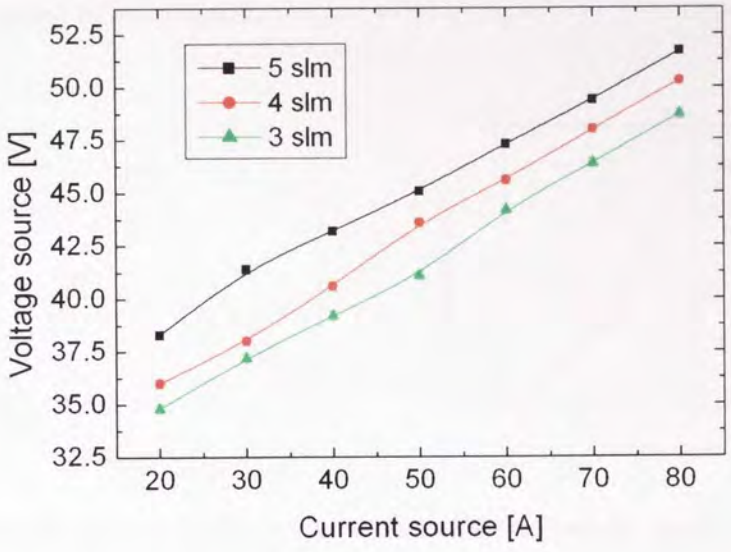

Figure 4.16 Voltage across the source as a function of source current for 4mm OTB IC source, for three different Ar flows

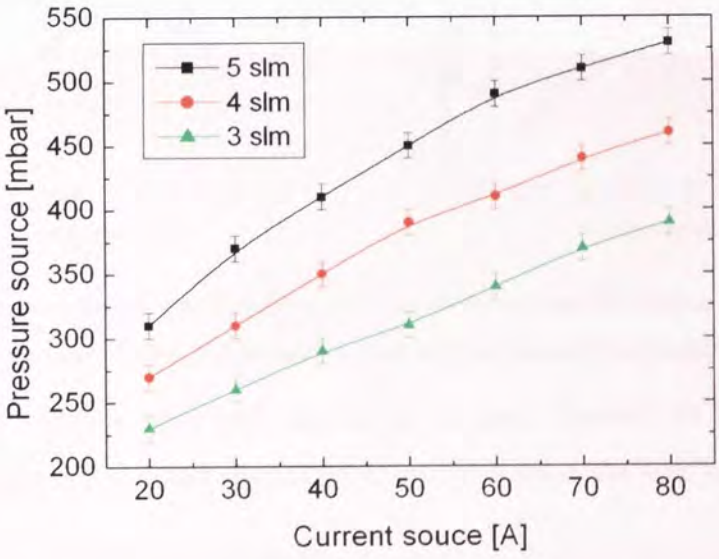

Figure 4.17 Pressure in the source as a function of source current for 4mm OTB IC source, for three different Ar flows

The plasma source parameters and trends were very similar to the 4mm DSE case. There were small shifts in absolute values, due to the different water cooling systems A major difference when comparing the 4mm plasma channel sources to the 3 mm one was that the voltage and the source pressure are not saturated any more, when the source current is

increased. This allowed more power to be injected in the plasma jet and thus a higher degree of ionisation to be attained.

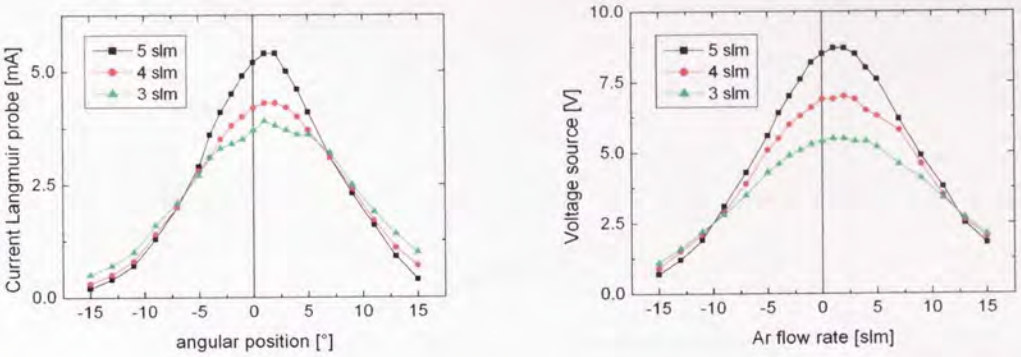

Figure 4.18 Argon ions density profiles for a distance of 18 cm from the source nozzle to the probe for a source current of 40 A (left image) and 60A (right image) for 4mm OTB IC source

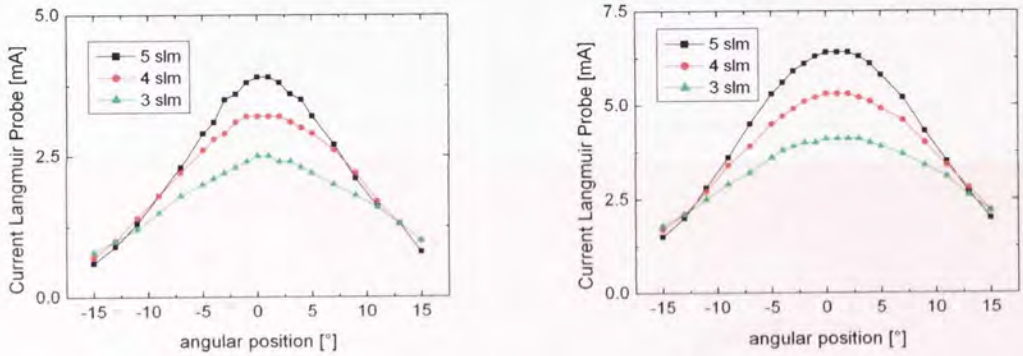

Figure 4.19 Argon ions density profiles for a distance of 30 cm from the source nozzle to the probe for a source current of 40 A (left image) and 60A (right image) for 4mm OTB IC source

The ion density profiles were very similar to the ones obtained in the 4mm DSE case, with better separated and better shaped profiles, but similar absolute values.

4.1.1.4 Source OTB 4 mm plasma channel no.1, new design (OTB No1)

The new design for the 4 mm source and the different choice of materials allowed the source to be operated at higher currents for longer times. The trends and absolute values were similar to the other two 4 mm channel sources.

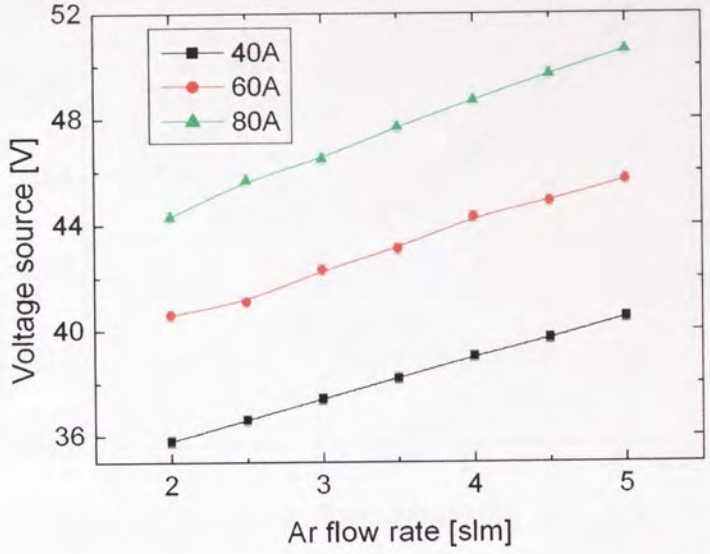

Figure 4.20 Voltage across the source as a function of Ar flow for 4mm OTB No1 source, for three different source currents

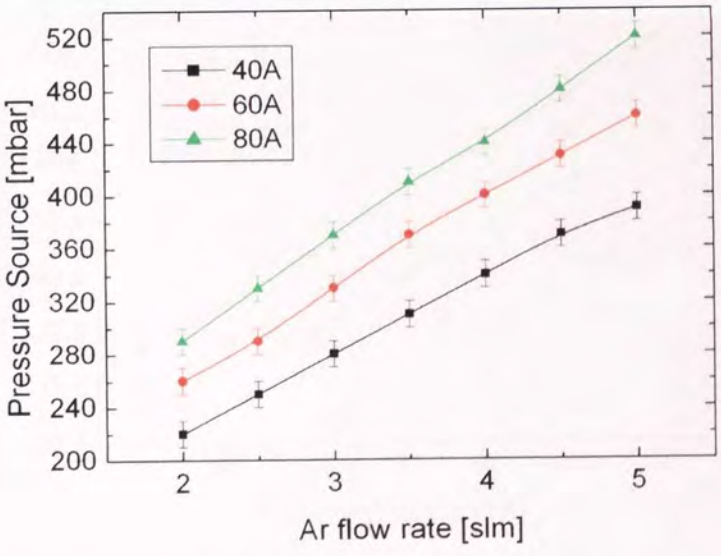

Figure 4.21 Pressure in the source as a function of Ar flow for 4mm OTB No1 source, for three different source currents

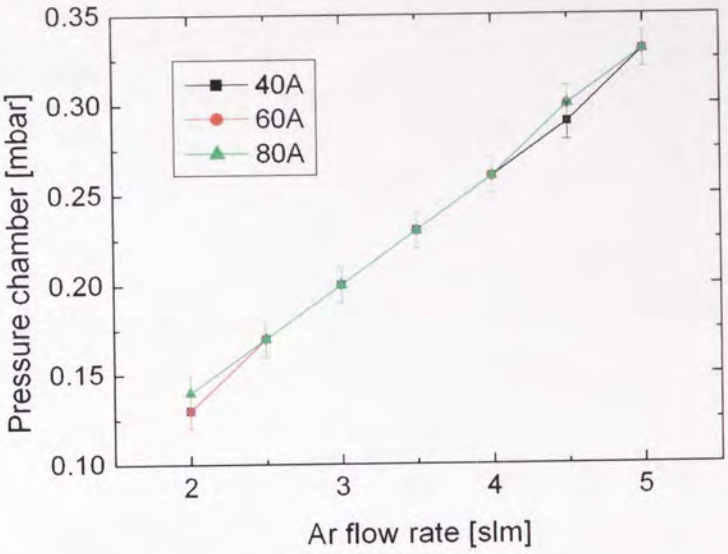

Figure 4.22 Pressure in the chamber as a function of Ar flow for 4mm OTB No1 source, for three different source currents

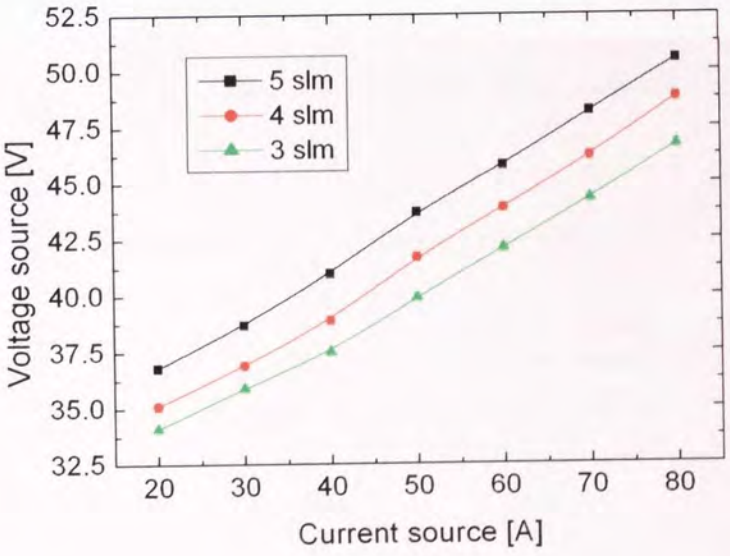

Figure 4.23 Voltage across the source as a function of source current for 4mm OTB No1 source, for three different Ar flows

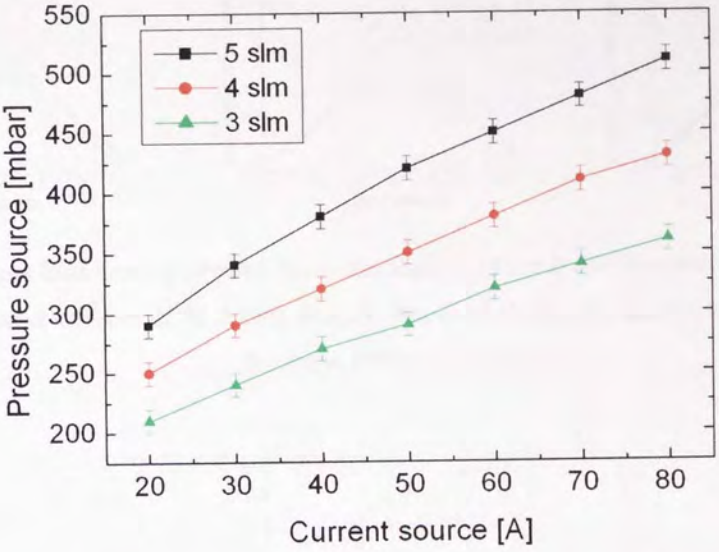

Figure 4.24 Pressure in the source as a function of source current for 4mm OTB No1 source, for three different Ar flows

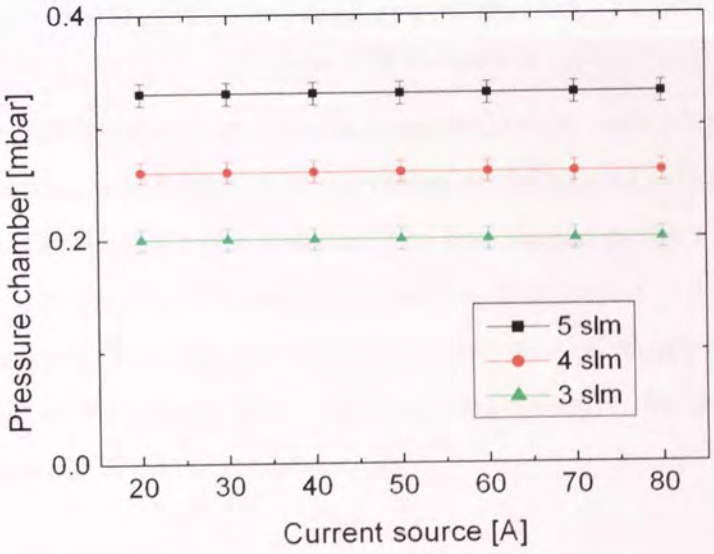

Figure 4.25 Pressure in the chamber as a function of source current for 4mm OTB No1 source, for three different Ar flows

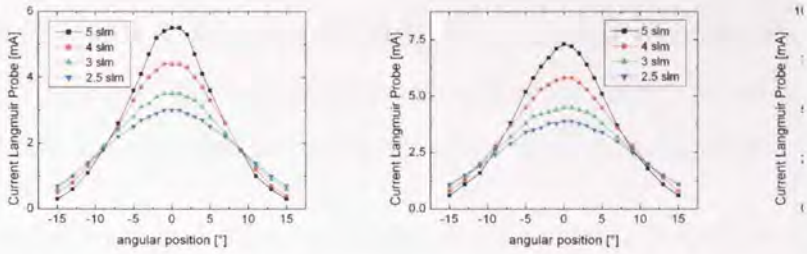

Figure 4.26 Argon ions density profiles for a distance of 18 cm from th for a source current of 40 A (left image), 50A (middle image) a for 4mm OTB No1 source

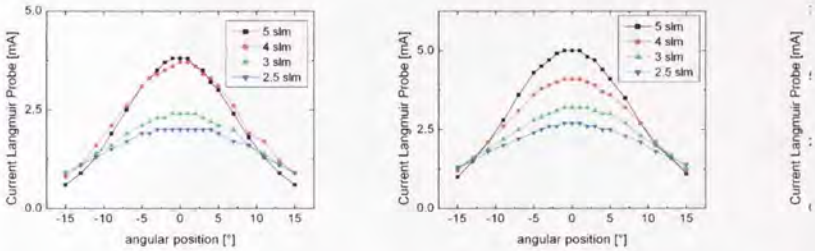

Figure 4.27 Argon ions density profiles for a distance of 30 cm from th for a source current of 40 A (left image), 50A (middle image) a for 4mm OTB No1 source

The ion density profiles were very similar compared to the on 4mm channel sources, with higher absolute values on the centra currents, and smaller nozzle-probe distance. The best shaped pr and 30 cm nozzle probe distance, in which case the distributio higher source currents. This was the reason why this type of sc were selected for coating large area substrates. Additionally, robust and reliable out of all the tested sources.

4.1.2 Start – stop tests

The second part of the tests on the sources consisted in trying the design of the top part of the source, which is responsible fo plasma. The sources chosen for these tests were all 4 mm c improved material and improved design, similar to the 4 mm O

If the plasma was flickering too much when starting the source and also there were too many sparks, then the shaft clamp, electrode and even the torch holder would eventually melt together. This raised the problem that the electrode could not be changed very easily, which was desirable for industrial usage of the plasma source.

Several tests had been performed to find the right solution to bring the sputtering to a minimum. Different shape types of tops for the torch holder and different protections with boron nitride (BN) discs were tried.

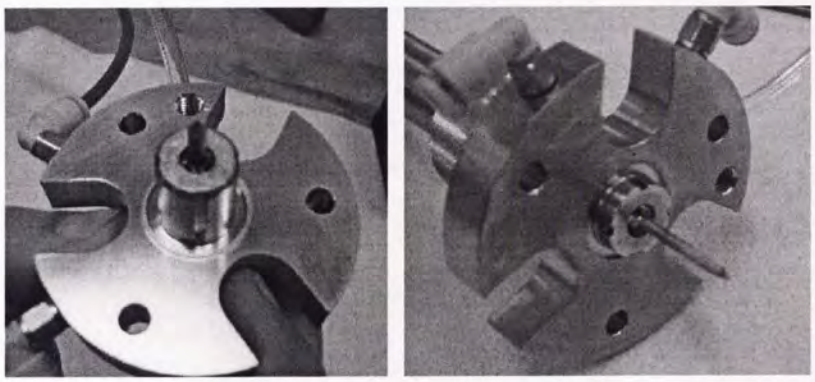

Figure 4.28 Different types of tops used for the torch holder

Because the top of the torch-holder melted together with the shaft clamp by starting and stopping the cascade arc plasma source some tests had been done to compare the long-shaped top of the torch holder and with a short-shape top (see Figure 4.28). In turn, these tops were protected with pieces of boron nitride (BN) that had different thicknesses and designs (Figure 4.29).

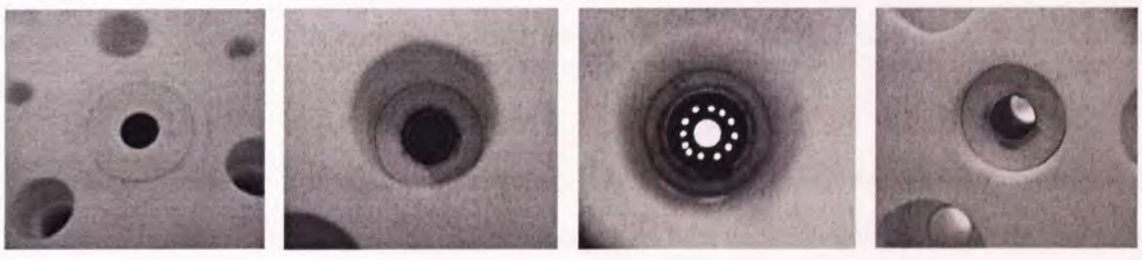

a b c d

Figure 4.29 Different types of BN protection for the top of the torch holder

4.1.2.1 Improvement of the cooling water system

Since the anode plate was cold (temperature below 20°C) during the tests and the two bottom cascaded plates had problems with cooling at higher currents, it has been decided that the anode should not be cooled separately. The holes for the last two bottom cascaded plates were enlarged and the cooling manifolds were connected to the anode plate. The hose that previously cooled the anode was blocked, and thus the flow was increased for the two bottom plates. These plates were connected to the first two outlets of the manifolds in and out (see Figure 4.30).

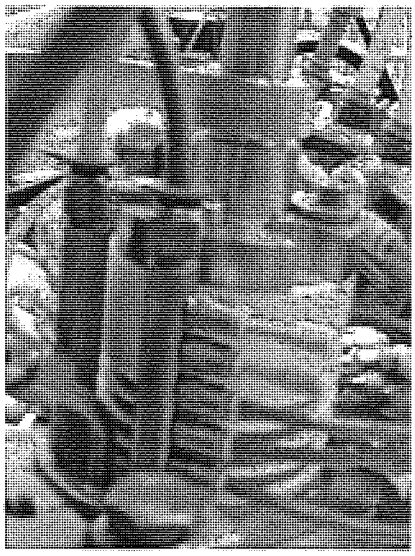

Figure 4.30 Manifolds connected to the anode plate directly while the two bottom plates are cooled separately

For even better cooling of the last two bottom plates, the hose that previously cooled the anode was split into two smaller hoses, each of them cooling one of the two bottom cascade plates with an increased flow.

Pictures of the source and its parts were taken before starting the tests and in between the experiments so that the source could be compared before, in between and after the tests. The ignition of the cascaded arc plasma source had always been visually inspected to see if the plasma was flickering, if there were sparks or blue edges to the plasma jet or other phenomena could be seen.

4.1.2.2 The tests performed

The tests performed on the sources had the aim to improve the starting capacity of the source, to reduce the sputtering to a minimum, to improve the reliability and performance over time of the source.

Test 1 (T1) consisted of 10 times start-stop actions, with 5 minutes plasma on and 1 minute plasma off, using a flow of 2.5 slm argon and a source current of 40 A. The source was investigated for sparks, flickering, failure of ignition of plasma and temperature of the cooling water in the bottom cascaded plates. After the test, the head of the source was disassembled and pictures of different parts were taken. When possible (the damage produced to the electrode was minor) the tests were continued on the same source arrangement.

Test 2 (T2) consisted of 10 times start-stop actions, with 30 seconds plasma on and 30 seconds plasma off, using a flow of 2.5 slm argon and a source current of 40 A. The source was investigated for sparks, flickering, failure of ignition of plasma and temperature of the cooling water in the bottom cascaded plates. After the start-stop action, the plasma was ignited for 5 minutes, then it was switched off; and the head of the source was disassembled and pictures of the various parts were taken.

Test 3 (T3) consisted of 20 times start-stop actions, with 5 seconds plasma on and 5 seconds plasma off, using a flow of 2.5 slm argon and a source current of 40 A. The source was investigated for sparks, flickering, failure of ignition of plasma and temperature of the cooling water in the bottom cascaded plates. After the start-stop action, the plasma was ignited for 5 minutes, then it was switched off; and the head of the source was disassembled and pictures of the various parts were taken.

4.1.2.3 Results for start-stop tests

After many configurations have been tried, with or without the boron nitride protection, with different shapes of the protection BN piece, with different diameter electrodes and different shapes and materials for the shaft clamp and with different shapes for the

electrode holder, a final configuration was reached, which is described in the following table and presented in Figure 4.31:

Source no:	OTB 4 mm no 4
Leak proof up to:	1×10^{-9} mbar l/s
Electrode:	2.4 mm red
Shaft clamp:	Steel 2
Boron nitride protection:	Yes, Φ = 3.5 mm.
Ar flow:	2.5 slm
Pressure source plasma on/off	280 / 150 mbar
Operating pressure	0.16 mbar
I cathode:	40A

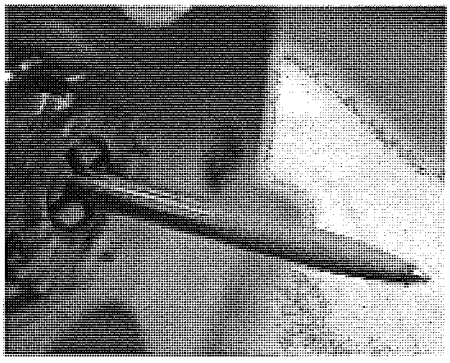

Figure 4.31 - Pictures taken after T1, T2 and T3 and plasma on for 40 min at 70A cathode current

4.2 Results at Aston University

The results present the measurements performed on the ETP plasma (density, energy of the argon ions, species present in the plasma), followed by the properties of the deposited films, separated in physical properties (deposition rates), chemical properties (sp^3 fraction, hydrogen content), mechanical properties (hardness, elastic modulus and adhesion) and optical properties (film density, refractive index and absorption).

4.2.1 Plasma characterisation

4.2.1.1 Mass energy analyser measurements

The mass energy analyser was inserted horizontally into the deposition chamber to measure the energy of the argon ions close to the substrate region. Because the jet is flowing vertically and the axis of the probe is horizontal, the probe will only collect those

ions with a horizontal component of the velocity. Another shortcome was that the probe could not be inserted into the centre of the plasma jet due to dimensional restrictions and the entrance aperture was situated some 12 cm away from the centre and 5 cm above the substrate level. Due to these factors, the measurements performed should be regarded as an estimation of the argon ions' energy and are susceptible to large errors. More accurate values can be found elsewhere [3 (p. 33), 28].

The mass/energy analyser was optimised for this type of plasma by adjusting the various parameters available in the software that controls the ion extraction process until a maximum number of counts was achieved.

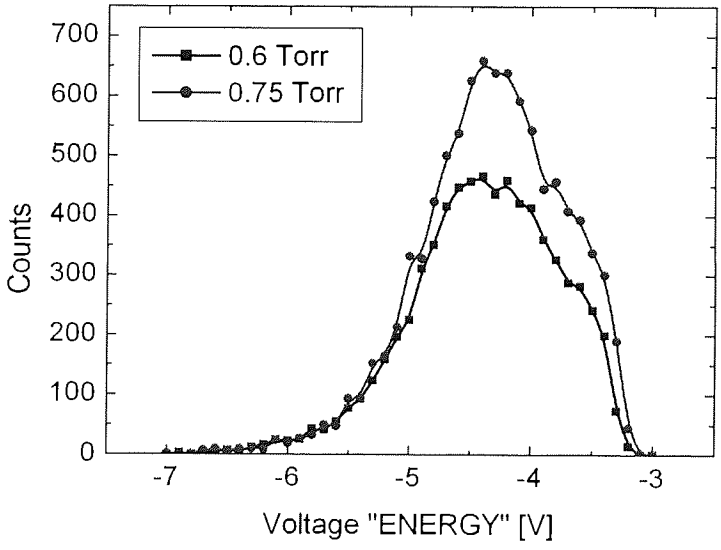

Figure 4.32 Ions Energy Distribution (IED) for a pure Argon expanding plasma at two different process pressures

The spectra recorded are presented in Figure 4.32. The maximum energy appears at a negative value of the parameter 'ENERGY'; this is because the EQP under estimates the value of the analysed ions and a correction should be applied to this energy, according to the following formula [113]:

$$E_i = \frac{R}{d} PLATES \cdot n\varepsilon - (ENERGY + AXIS) \cdot n\varepsilon \qquad \textbf{Eqn 4.1}$$

where R is the radius of the electrostatic sector, d is the distance between the plates in this sector, *PLATES* is the voltage between the plates, $n\varepsilon$ is the number of elementary charges of the ion, *ENERGY* is the voltage corresponding to the ions energy and *AXIS* is the braking potential before the ions enter the energy analyser.

Introducing the values set for the parameters *PLATES*=+7.4 *V* and *AXIS*=-36.0 *V* during the acquisition of the spectrum, taking into account that $\frac{R}{d} = 5.498$ for our EQP, and assuming a maximum value of the voltage *ENERGY* of -4.3 to -4.4 V (from Figure 4.32), the energy of the argon ions can now be calculated to be approximately $E_{i\parallel} = 0.3 - 0.4eV$ for the ions parallel to the MAE central axis.

Now, subtracting the MAE's length that is inserted in the vessel from the radius of the vessel, the distance from the central axis of the vessel to the MAE entrance aperture can be deterined. Measuing the distance from the top of the level where MAE is inserted, it can be calculated that the majority of ions are collected at a real angle of about 30° from the vertical axis of the chamber. Therefore, the real ion energy, perpendicular to the MAE central axis, will be $E_{i\perp} = 0.9 - 1.2eV$ close to the substrate level (65 cm downstream). The ionic radicals are expected to have slightly lower energy than the Ar ions, due to the additional collisions and reactions that take place in the plasma jet. This was confirmed by the slightly lower increase in the substrate temperature when the precursor gas was added when compared to the pure argon case.

4.2.1.2 Langmuir probe measurements

The Langmuir probe was used to measure the density of the ions close to the substrate level, for a pure Argon plasma jet at low processing pressures (~0.6 Torr) and normal operating plasma source conditions (40A current, 2.5 slm Ar flow). The density was deduced using the following formula [3 (p. 32)]:

$$n_{ion} = \frac{4I_{ion}}{S_{probe}} \frac{1}{e} \sqrt{\frac{\pi m_i}{8KT_i}} \qquad \textbf{Eqn 4.2}$$

where I_{ion} is the ionic saturation current, S_{probe} the area of the probe, e the electron charge, m_i the mass of the ions collected and kT_i the energy of the collected ions. Using the energy determined with the MAE the density of the argon ions can be calculated.

A typical Langmuir probe recorded I-V characteristic is presented in the following figure:

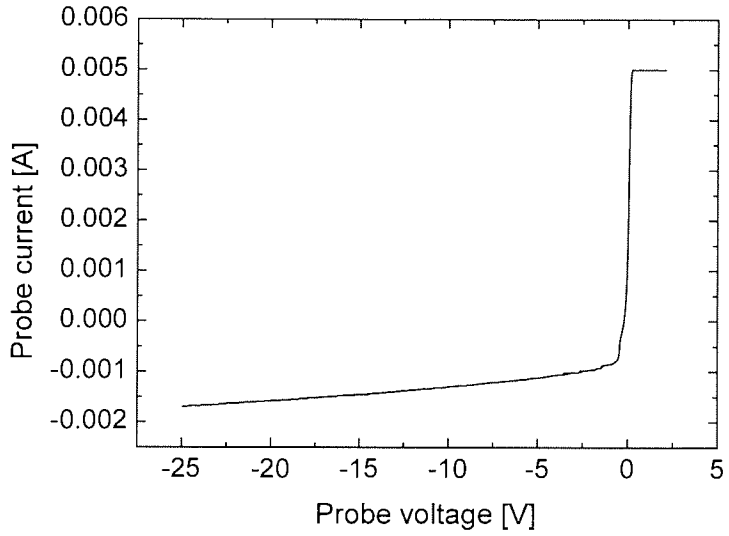

Figure 4.33 Typical Langmuir probe I-V characteristic for an expanding argon plasma at 0.6 Torr process pressure

The highest current gain possible with this type of Langmuir probe is 0.1A, not big enough for this type of plasma. For better sensitivity the maximum current was limited to 0.005 and the ionic part of the characteristic was analysed. The saturation ionic current will not be constant, due to the increase in size of the effective area of the probe as the voltage becomes more negative. Assuming the collecting area of the probe stays approximatively the same until the voltage reaches a negative value of 8 – 10V [3 (p. 33)], from Figure 4.33 that the saturation value for the ionic current can be estimated to be about 1 mA; the ion density can be now calculated: $n_i = 2.1 \cdot 10^{12}\ \mathrm{cm}^{-3}$ at 0.6 Torr chamber pressure and standard Ar flow (2.5 slm). This would correspond to a degree of ionisation in the flow of about 4%. The ion density would increase if the Ar flow, the process pressure or the source power is increased (in the range previously discussed), as was shown in the graphs dedicated to the Ar ion profiles in the section about the tests on the plasma sources.

Unfortunately, the plasma tip and ceramic connector next to tip were burned beyond recovery only after few experiments, not allowing the investigation of a larger matrix of plasma conditions.

4.2.1.3 Optical emission spectroscopy measurements

The optical spectroscope was used only for few experiments, to check the composition of the plasma. The optical fibre used to record the spectrum was placed in front of one of the windows of the deposition chamber in a special black adapter, to ensure that the entire signal received was coming from inside the plasma chamber. The other window of the chamber was blanked with a similar adapter. Since the signal received was an integrated signal, differences between different areas in the plasma could not be identified. The only information obtained from the spectrum was the species present in the plasma. The analysis of the recorded spectra proved to be quite complicated and not much information could be obtained from it, which led to emission spectroscopy to be abandoned after only a few trials.

An example of a large and narrow band spectra are shown in the following figures, for an argon – 3% hydrogen plasma mixture:

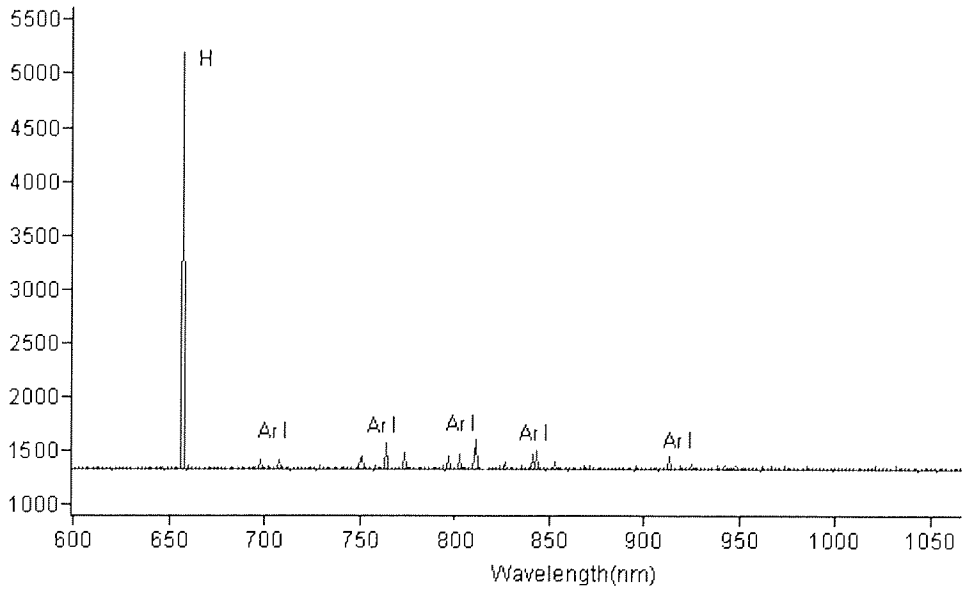

Figure 4.34 Large band visible-IR spectra for an argon – 3% hydrogen mixture plasma

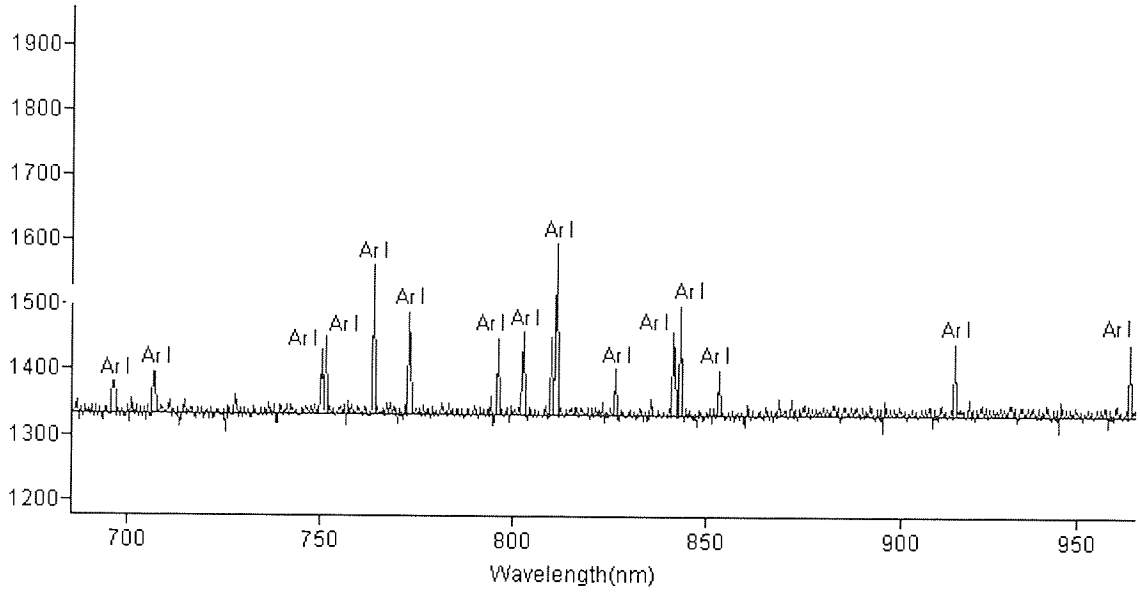

Figure 4.35 Narrow band IR spectra for an argon – 3% hydrogen mixture plasma

4.2.2 Deposition rates

One of the important parameters throughout all the experiments was the deposition rate. This parameter is particularly important for industrial applications, where automated machines are used for in-line production. The deposition rate was calculated by dividing the measured thickness of the film by the deposition time.

4.2.2.1 Deposition rate against relative flow

The results are presented separately for methane and acetylene and for different temperatures of the substrate during deposition and different pressure regimes.

At low pressures the maximum deposition rate was achieved at low relative methane to argon flows and low temperatures. This corresponds to the maximum number of atomic and molecular ions arriving at the surface, because the number of Ar ions produced is comparable with the number of methane molecules injected in the nozzle. The sticking coefficient of these radicals decreases with increasing temperature, decreasing the net deposition rate (see Figure 4.36).

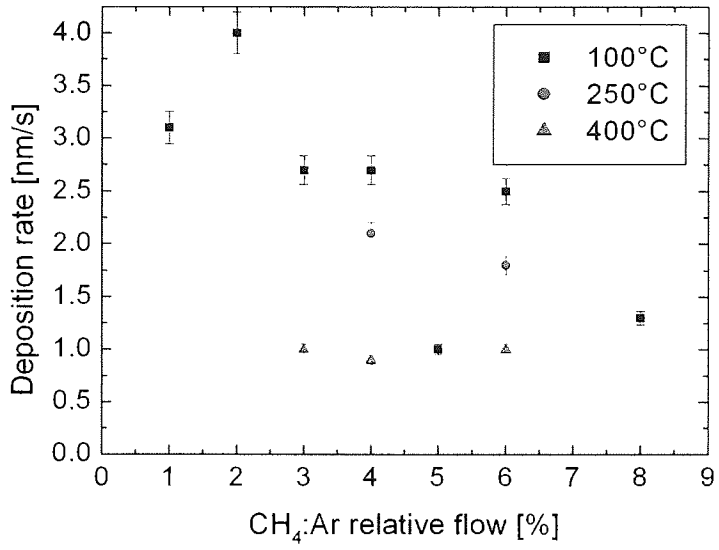

Figure 4.36 Deposition rate against methane relative flow for the low pressure regime (0.6 Torr) at three different temperatures with pure argon as a carrier gas

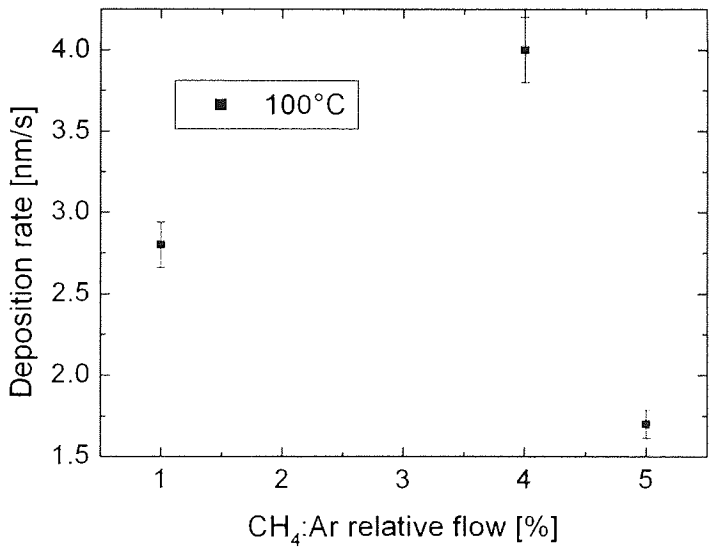

Figure 4.37 Deposition rate against methane relative flow for the medium pressure regime (1 Torr) at low temperatures with pure argon as a carrier gas

Only a few experiments were performed at intermediate pressures with pure argon as carrier gas and methane as precursor gas and only at low temperatures. The increase in pressure makes the plasma jet more confined and shifts the maximum deposition rates to slightly higher relative methane to argon flow values (Figure 4.37).

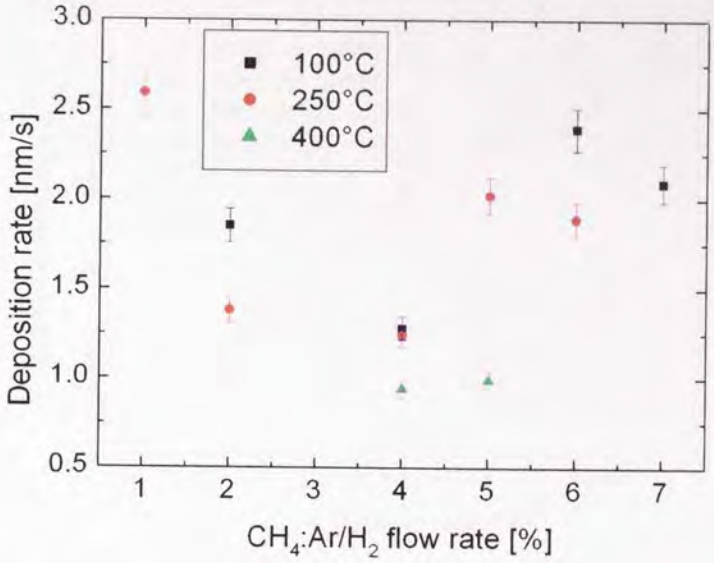

Figure 4.38 Deposition rate against methane relative flow for the high pressure regime (6-7 Torr) at three different temperatures with argon-3% hydrogen mixture as a carrier gas

When argon – 3% hydrogen mixture was used as a carrier gas the deposition rates were small. Increasing the pressures to higher values confines the plasma jet even more, making it rather unstable. Most of the experiments with methane and Ar/3% H_2 mixture were performed in this pressure regime, to enhance the deposition rate. In this case the trends for the deposition rate are rather ambiguous, the most plausible explanation being the instability of the plasma jet (see Figure 4.38). The reason for the lower deposition rates is the much lower degree of ionisation in the source in the case of argon/hydrogen mixture than for the pure argon case, the hydrogen molecules consuming a large part of the formed Ar ions, as will be discussed in Chapter 6.

When acetylene was introduced as a precursor gas the deposition rates increased significantly. Problems with injection in the nozzle which caused the incorporation of sooty particles in the film led to injection of acetylene via an injection ring, situated either close to the source exit, outside the plasma jet (Ring Up position, 9 cm from the nozzle), or about half way between the source exit and the substrate, inside the plasma jet (Ring Down position, 37 cm from the nozzle) (see Figure 4.39). The R_a roughness of these films decreased to acceptable values and the deposition rate increased constantly with the relative acetylene to argon flow.

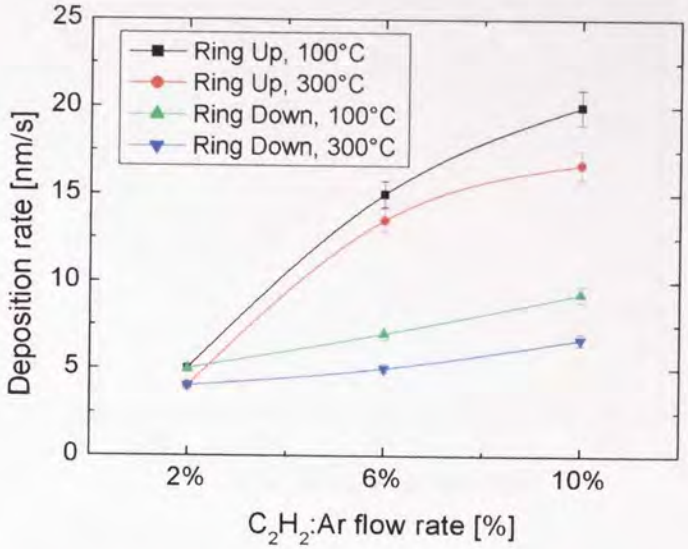

Figure 4.39 Deposition rate against acetylene relative flow for the low pressure regime (0.5 Torr) at two different substrate temperatures and two different injection positions with pure argon as a carrier gas

In the Ring Down position, because the quite narrow injection ring is situated close to a direct line between the source exit and substrate, it attenuates the plasma jet, influencing the geometry and the chemical composition of the plasma close to the substrate level. This decreases the deposition rate, but it still gives a good-enough value for industrial processing. The decrease of the deposition rate with substrate temperature is still present, but this effect is not as pronounced as in the methane case, due to the different chemical composition of the plasma at the substrate level. The growth of the film in this case takes place from different radicals, with different sticking coefficients that decrease with the increase of the substrate temperature.

In the case of the argon – 3% hydrogen mixture used as carrier gas a clear trend can be observed for all substrate temperatures. The deposition rate increases up to certain values of the relative acetylene to argon/hydrogen flow and then decreases abruptly. This is because in this case the presence of hydrogen is abundant and, beside the effects previously observed, a new effect becomes important: the etching of the film by atomic hydrogen.

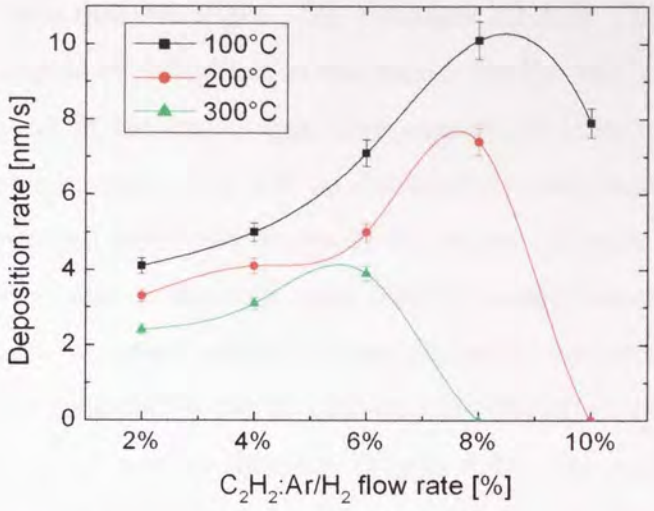

Figure 4.40 Deposition rate against acetylene relative flow for the low regime (0.6 Torr) at three different temperatures with argon-3% hydrogen mixture as a carrier gas

This effect can be clearly observed at high temperatures, when no films are formed at high relative flows. As the substrate temperature increases the etching rate increases, hence the lower relative flows needed at higher temperatures for no net deposition (see Figure 4.40).

4.2.2.2 Deposition rates against carrier gas

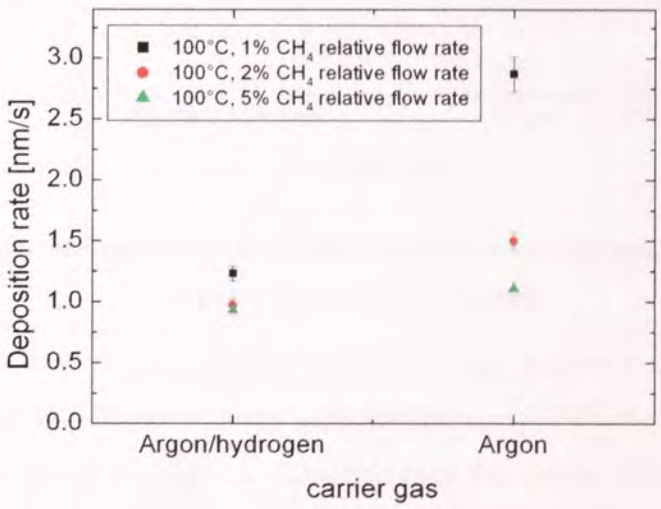

Figure 4.41 Deposition rate against the carrier gas for films grown from methane at low temperature, low pressures and at three relative flow rates

Deposition rate was influenced by the carrier gas, the pure argon gas always yielding higher deposition rates than the argon – 3% hydrogen mixture. This is mainly due to the difference in the degree of ionisation in the source for the two cases. When hydrogen molecules are present in the carrier gas, they consume a large part of the argon ions formed in the plasma channel. This will be discussed in more detail in Chapter 6. Thus, the presence of hydrogen molecules decreases the degree of ionisation by a factor of ~2 [28]. The degree of ionisation depends, apart from the composition of the carrier gas, on the power injected in the source and to a lower degree on the pressure in the deposition chamber. For the methane case it can be observed that the effect of carrier gas decreases with the increasing of the relative flow rate (Figure 4.41). This is because the degree of ionisation for both cases is quite low (0.5-1% for the Ar/H_2 mixture and 2-3% for pure Ar in the low power regime) at the lower cathode currents sustainable by the copper source.

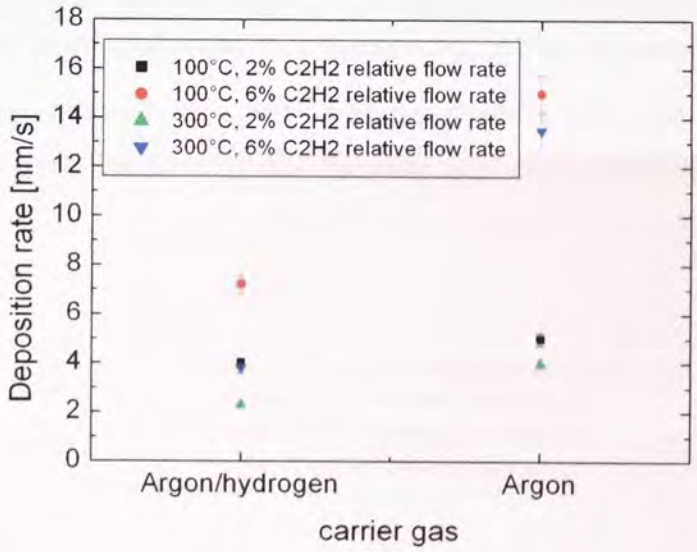

Figure 4.42 Deposition rate against the carrier gas for films grown from acetylene at low temperature and at three relative flow rates

In the case of acetylene injected via the injection ring, the power settings for the source were changed as well. The new source used for the acetylene set-up could sustain much higher powers injected in the plasma. This increased the degree of ionisation to about 6% in the case of pure argon and about 1-2% in the case of the argon -3% hydrogen mixtures. That is why the deposition rate was much higher in the case of 6% acetylene to argon relative flow (see Figure 4.42).

4.2.2.3 Deposition rate vs. substrate temperature

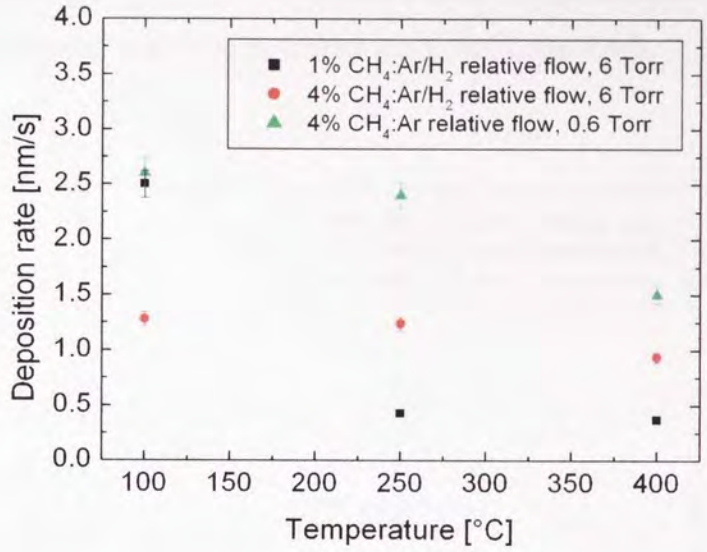

Figure 4.43 Deposition rate against temperature for films grown from methane at different methane relative flows and at different pressures, with argon-3% mixture, respectively Ar as carrier gas

The deposition rate generally decreased with the substrate temperature. When the source was close to the optimum loading this decrease was more pronounced, as can be seen from Figure 4.43.

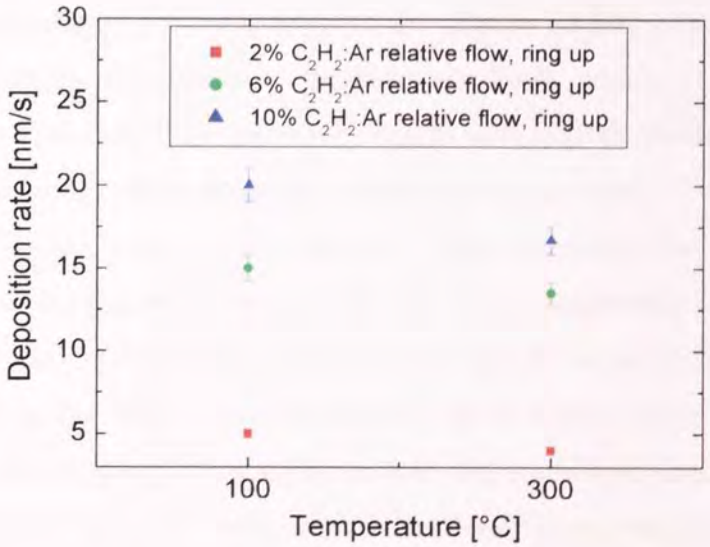

Figure 4.44 Deposition rate against substrate temperature for films grown from acetylene injected in the 'ring up' position for three different relative flows with argon as carrier gas

In the case of acetylene, the effect of substrate temperature on deposition rate was similar to the methane case, with a small decrease in deposition rate when pure argon was employed as carrier gas (see Figure 4.44) and a more abrupt decrease in the case of argon – 3% hydrogen mixture employed as carrier gas (see Figure 4.45).

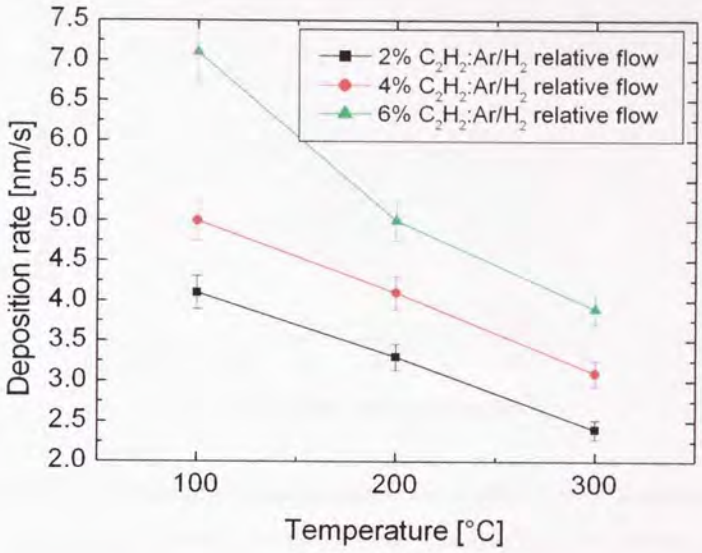

Figure 4.45 Deposition rate against substrate temperature for films grown from acetylene injected in the nozzle for three different relative flows and argon-3%hydrogen mixture as carrier gas

4.2.2.4 Deposition rate vs. pressure

The increases in process pressures leads to the plasma jet being more confined, which increases the density of particles at the substrate level, which, in turn, increases the deposition rates. However, there are two problems with high deposition pressures: firstly, the plasma jet becomes rather unstable at pressures higher than 5 Torr, which decreases the quality and homogeneity of the deposited films; secondly, the confinement of the plasma jet means that the maximum area that can be homogenously covered decreases (it is about 2 cm^2 for 6–7 Torr process pressure), which is not desirable for industrial applications, where the largest possible area should be covered in an homogeneous film. As can be seen from Figure 4.46 and Figure 4.47, the increase is almost linear in the case of pure argon carrier gas, for methane and acetylene: increasing the pressure about 10 times increases the deposition rate by a factor of 6 for methane; increasing the pressure by

25% increases the deposition rate by about 75% at similar powers injected in the plasma source.

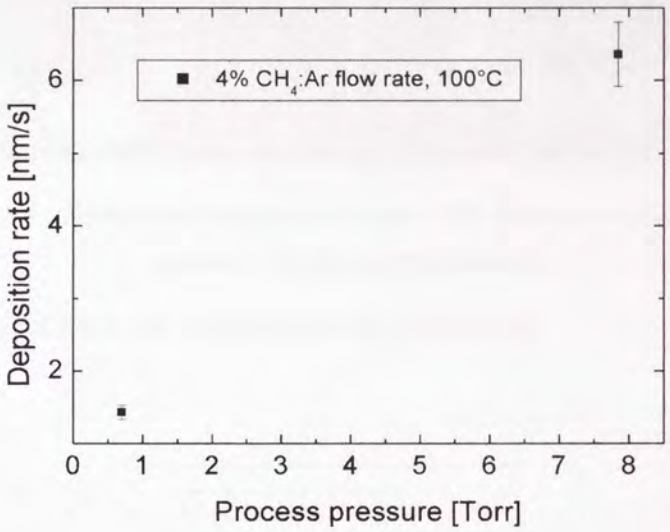

Figure 4.46 Deposition rate against process pressure for 2 films grown from methane at 4% relative flow and low substrate temperature, with argon as carrier gas

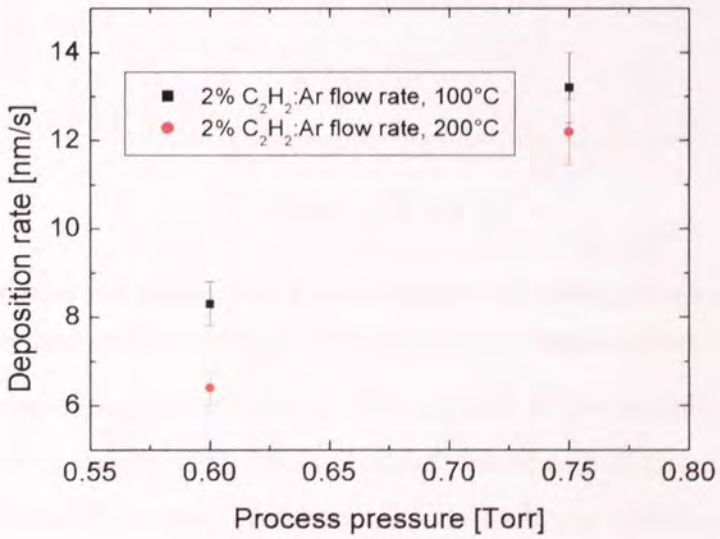

Figure 4.47 Deposition rate against process pressure for films grown from acetylene injected in the nozzle at 2% relative flow and two different temperatures, with pure argon as carrier gas

For comparison, pictures taken through a side window of the deposition chamber with the plasma jet (expanded and confined) are presented in Figure 4.48.

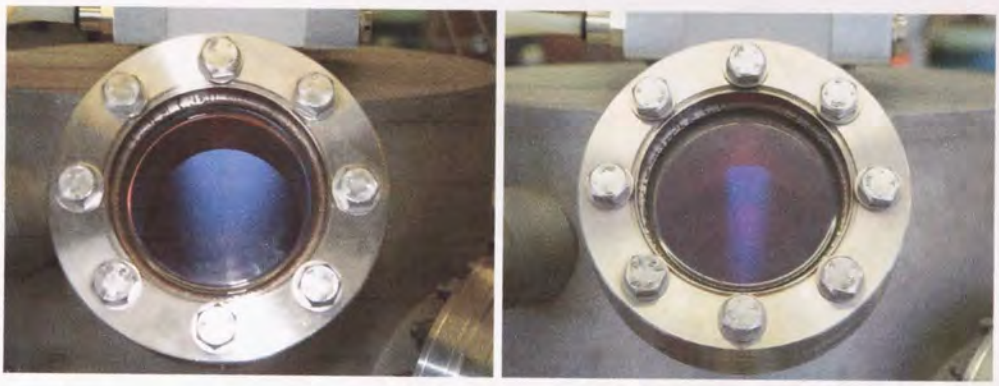

Figure 4.48 Picture of the plasma jet burning on argon – 3% hydrogen mixture: a) at low/medium pressures and b) at high pressures

4.2.2.5 Deposition rate vs. source power (current)

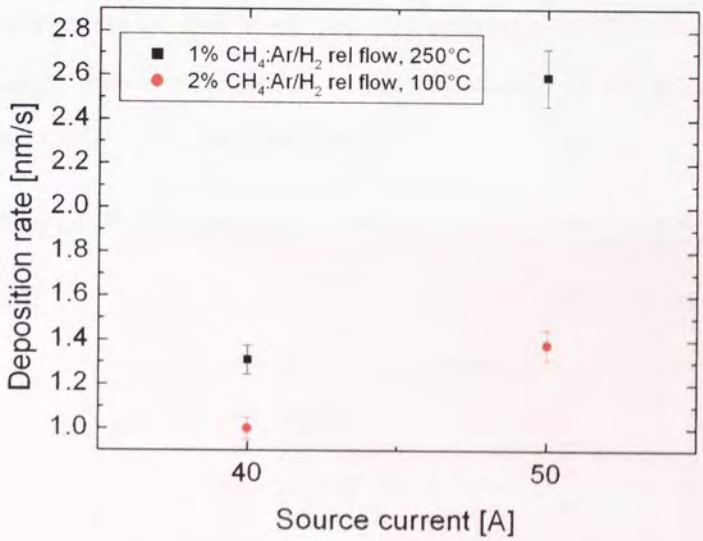

Figure 4.49 Deposition rate against source current (power) for films grown from methane at two relative flow rates and temperatures with argon-3% hydrogen mixture as carrier gas

The deposition rate increases with the power injected in the plasma, which is directly correlated with the source current. This is because the degree of ionisation in the plasma increases with the source current. If the source is close to the optimum loading, then the increase is more abrupt (see Figure 4.49).

4.2.3 Roughness

The R_a is a measure of the average roughness in the analysed area. It is given by the formula [114]:

$$R_a = \frac{1}{N}\sum_{i=1}^{N}|z_i - \bar{z}| \qquad \textbf{Eqn 4.3}$$

where $\bar{z}$ is the average height of all data points in the included area, N is the number of data points and z_i is the height of data point i.

For polished silicon, which was most commonly used as a substrate material, the R_a value was found to be about 2 nm. The R_a values for most films was calculated and compared. The roughness was calculated from an image with the size usually between 30×30 μm to 100×100 μm. If large peaks, that were not characteristic to the rest of the surface, were present in the image, they were ignored in the calculation of the average roughness. The results are detailed in the following sections.

4.2.3.1 Variation of R_a roughness with substrate temperature

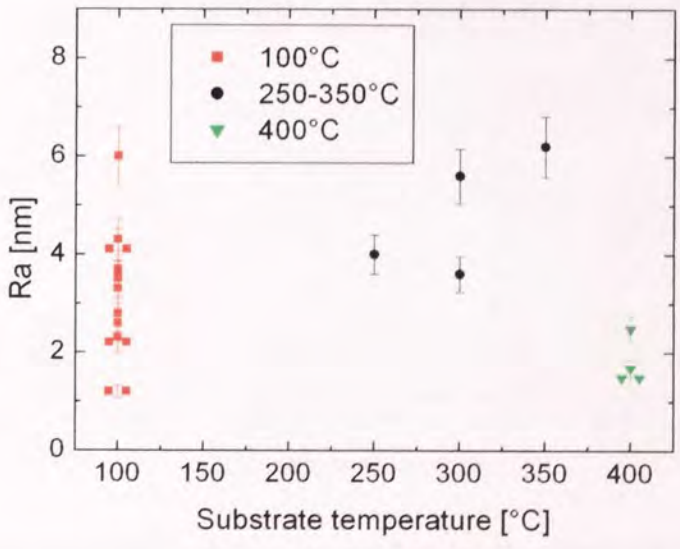

Figure 4.50 Roughness (R_a) against substrate temperature for films grown from methane with argon and argon-3% hydrogen mixture as carrier gas at different pressures

The R_a roughness did not show a clear variation with substrate temperature in the case of deposition from methane (Figure 4.50). The values were generally lower than 4-5 nm. Occasionally the values rose to 6-7 nm, and possible explanations for this would be incorporation in the film of sooty particles from the deposition chamber or, for the samples deposited in the high pressure regime, the instability of the plasma jet. The apparent large scatter in R_a for films grown at low temperature is due to the fact that pressure and precursor flow rate affect to some degree the chemistry in the plasma close to the substrate level, and this, in turn, affects the R_a roughness.

For the films grown from acetylene a general trend could be observed: films deposited at low substrate temperatures had R_a values lower than 2 nm, whereas for the film deposited at higher substrate temperatures, the R_a values increased up to 5 nm. This may be due to the different incorporation of hydrogen into the films at different temperatures: at low temperature more hydrogen is incorporated, making the surface smoother (see Figure 4.51). Annealing of the films was beyond the scope of this thesis, where films were intended for temperature sensitive substrates.

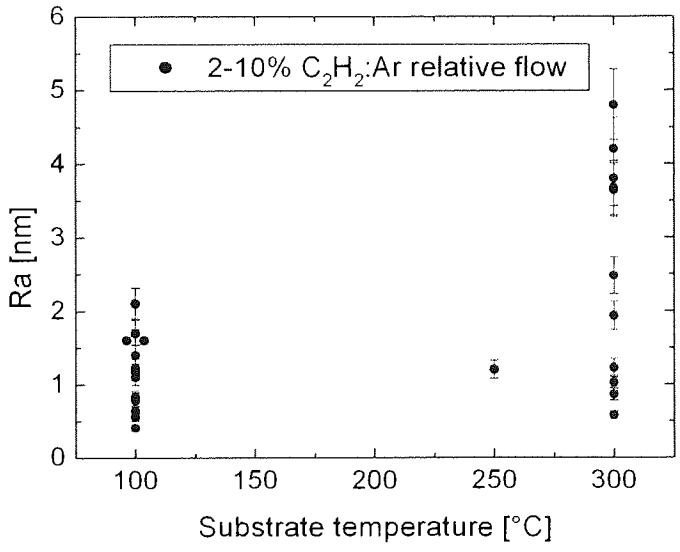

Figure 4.51 Roughness (R_a) against substrate temperature for films grown from acetylene with argon as carrier gas at different relative C_2H_2:Ar flows

Some films deposited from acetylene showed extremely high R_a values, due to the recirculation and introduction of sooty particles from the chamber in the plasma jet. This

problem was solved by introducing a special adapter which allowed the source to self-clean, as mentioned in Chapter 3. These films were omitted from the present study, because of their very poor quality and adhesion to the silicon substrates.

As an example, five AFM images for films grown from methane and acetylene are presented in the following images: two films from the methane series, deposited at low and high temperatures, two films from the acetylene series, deposited at low and high temperatures and one film where the incorporation of sooty particles was predominant.

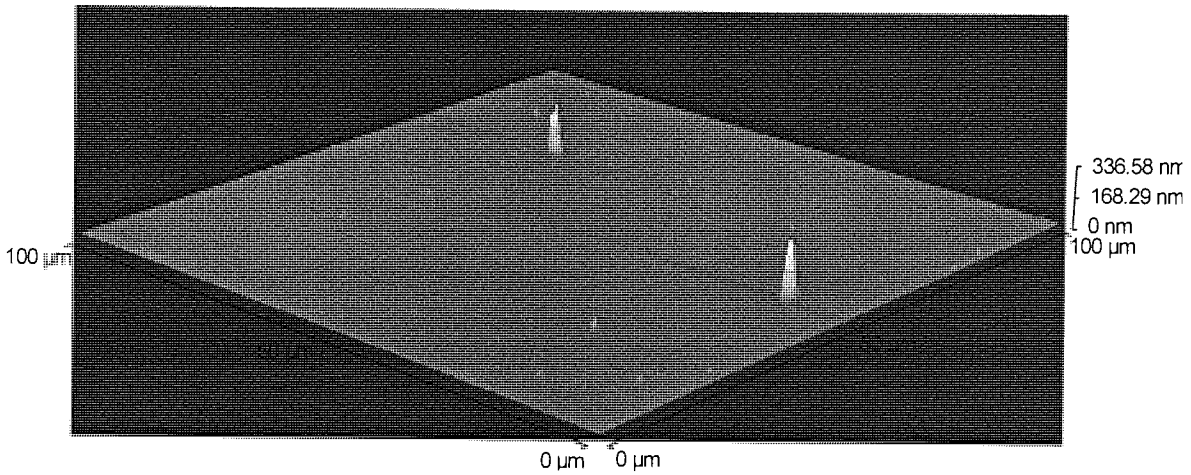

Figure 4.52 AFM image of a film deposited from methane at low temperature with argon – 3% hydrogen as carrier gas (A53)

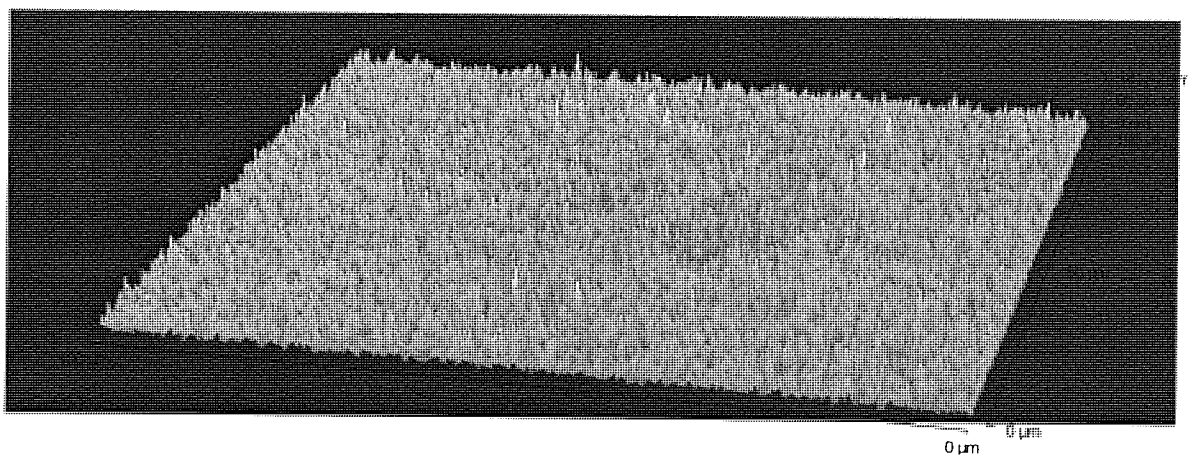

Figure 4.53 AFM image of a film deposited from methane at high temperature with argon – 3% hydrogen as carrier gas (A77)

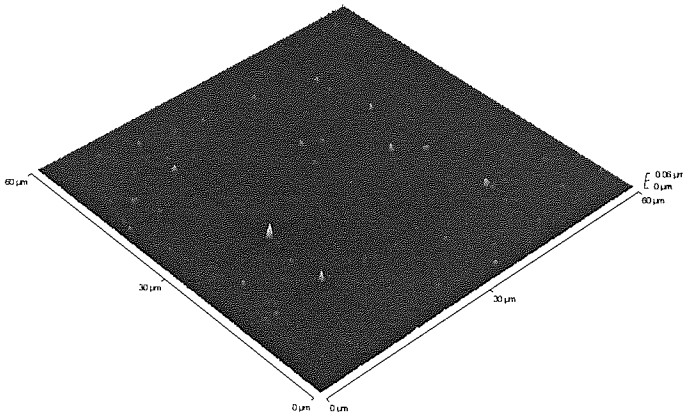

Figure 4.54 AFM image of a film deposited from acetylene at low temperature with argon – 3% hydrogen as carrier gas (E20)

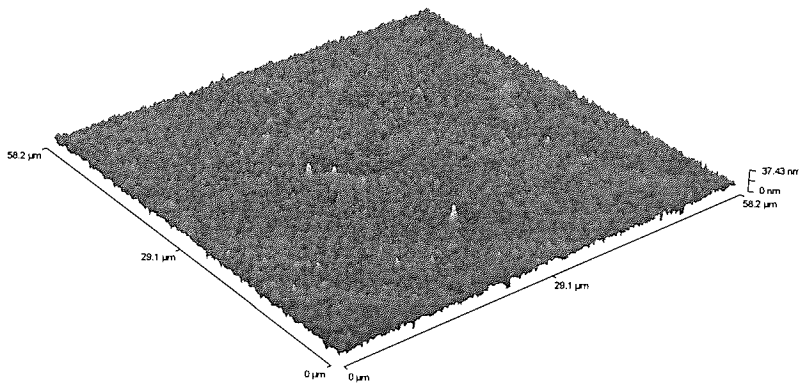

Figure 4.55 AFM image of a film deposited from acetylene at low temperature with argon – 3% hydrogen as carrier gas (E8)

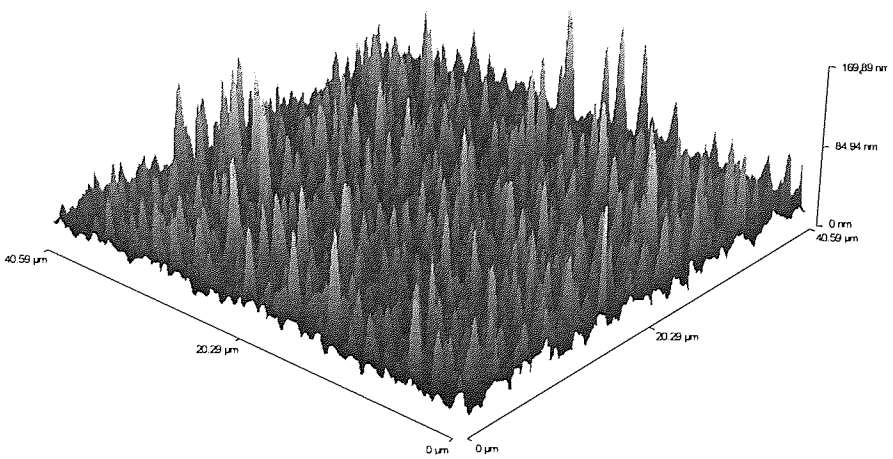

Figure 4.56 AFM image of a film deposited from acetylene at low temperature with argon as carrier gas before the special adapter was introduced (D33)

4.2.3.2 Variation of R_a values with acetylene flow

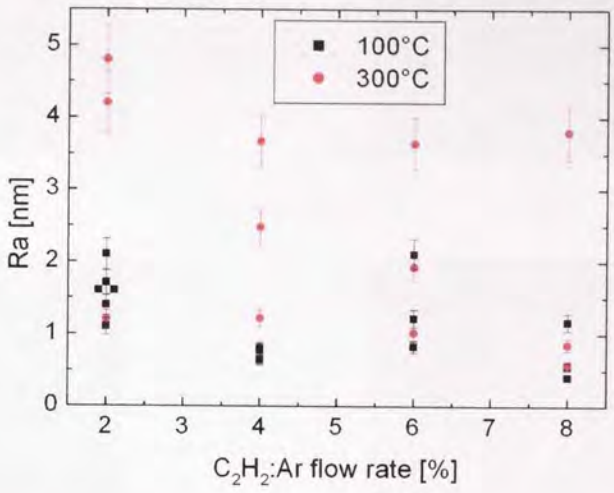

Figure 4.57 (R_a) against relative flow for films grown from acetylene with argon as carrier gas

The R_a values varied a little with the relative acetylene to argon flow, and no clear trend from low to high relative flows could be found. The small differences could be explained by the complex growth mechanism that will be discussed in Chapter 6. There are differences in the hydrogen content from low to high relative flows, but the main factor influencing the R_a values is still substrate temperature (see Figure 4.57).

4.2.3.3 R_a roughness values for deposition on different substrates

Amorphous carbon films were deposited on different substrates in low temperature conditions and medium relative acetylene to argon flow, for later implementation in different types of applications. The R_a values of the film surfaces generally followed the R_a values of the substrates. Since the exact area cannot be analysed prior to and after the deposition and the differences in R_a values for the substrates and the films are relatively small, the films are believed to be very smooth (<2 nm), irrespective of the substrate they are deposited on.

The AFM images of the virgin substrates surfaces, as well as the image of the films deposited on the different substrates are presented in Figure 4.58. The images are collected from areas between 10 × 10 μm and 100 × 100 μm, levelled with the AFM software and then left shading is applied.

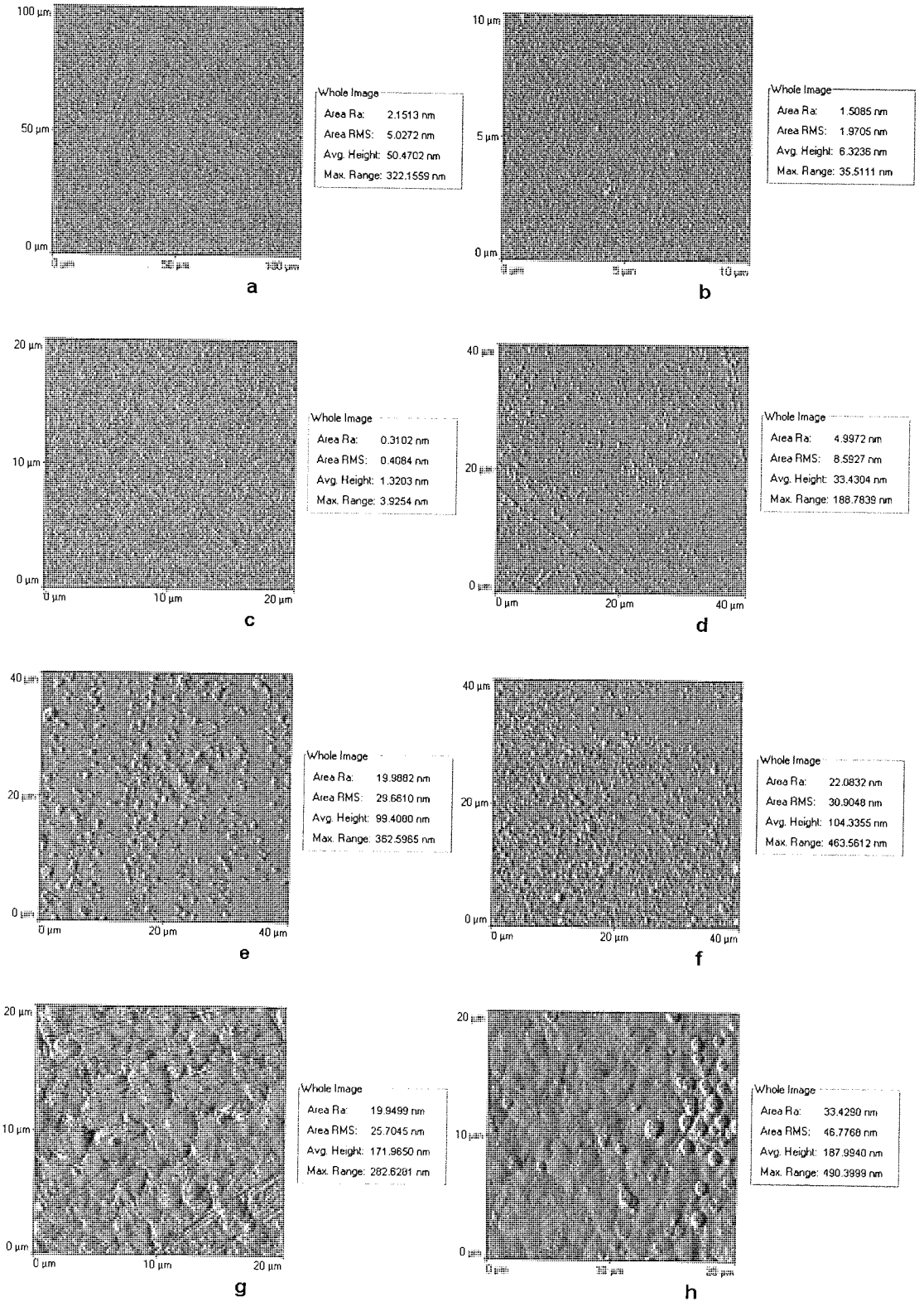

Figure 4.58 AFM images of a) virgin silicon substrate; b) a-C:H film on silicon; c) virgin glass substrate; d) a-C:H film on glass; e) virgin PET substrate; f) a-C:H film on PET; g) virgin PEEK substrate and h) a-C:H film on PEEK

4.2.4 Sp^3 fraction

4.2.4.1 Diamond and graphite

For the study of sp^3/sp^2 ratio in the carbon films, pure diamond and graphite films were analysed. The diamond sample was an industrially grown diamond film provided by Nixon Ltd. and the graphite sample was a pure graphitic disc provided by the Chemistry Department in Aston University. The XAES KLL spectra for these two samples, together with the spectrum of a typical carbon film sample are presented in Figure 4.59.

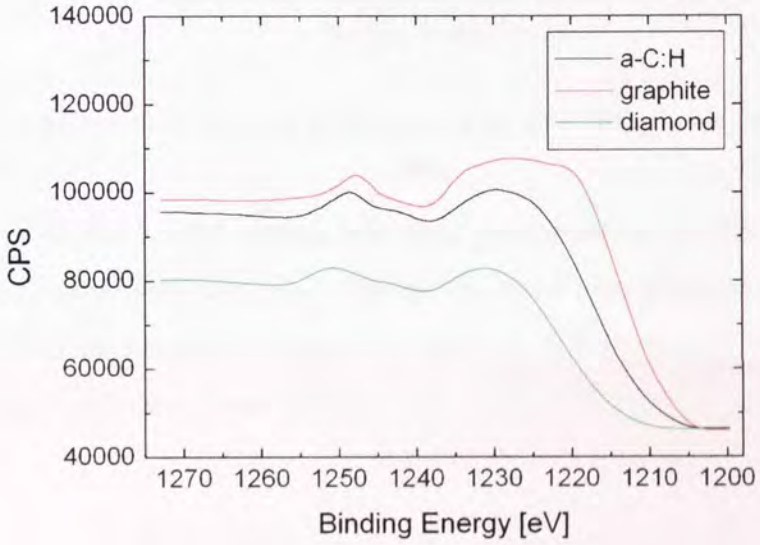

Figure 4.59 XAES KLL spectra for a diamond film, a graphite sample and an amorphous carbon hard film

These KLL spectra obtained from XAES were then differentiated by a Savinsky-Golay method, after a smoothing with 27 points, 2 passes was performed (Figure 4.60). The difference between the mean of the positive and negative peaks in the differentiated XAES spectra (D) was recorded and the values of *14.3 eV* – for the diamond film and *22.5 eV* – for the graphite disk were found respectively, identical to those reported by Lascovich [91, 92].

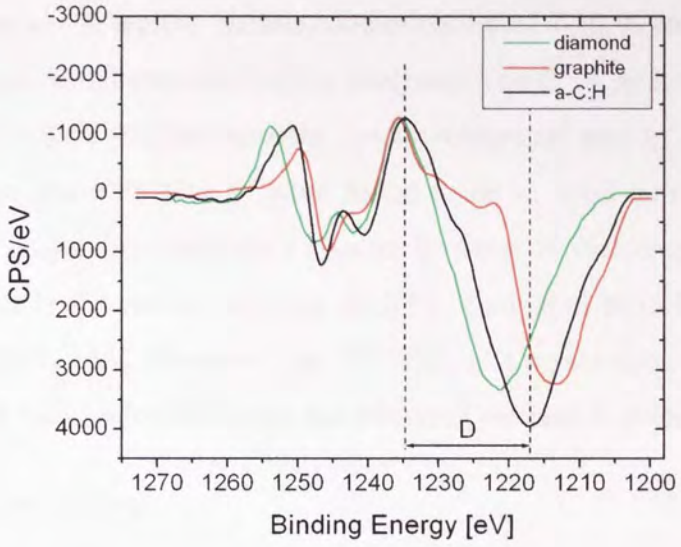

Figure 4.60 First derivative for the KLL XAES spectra for diamond, graphite and amorphous carbon film

The derivative of the XAES spectra was then performed on all the amorphous carbon films and the D value was calculated. The sp^3 fractions were deduced for the a-C:H films assuming a linear dependence between the diamond and graphite D values, as suggested by Lascovich [91, 92] (see Figure 4.61).

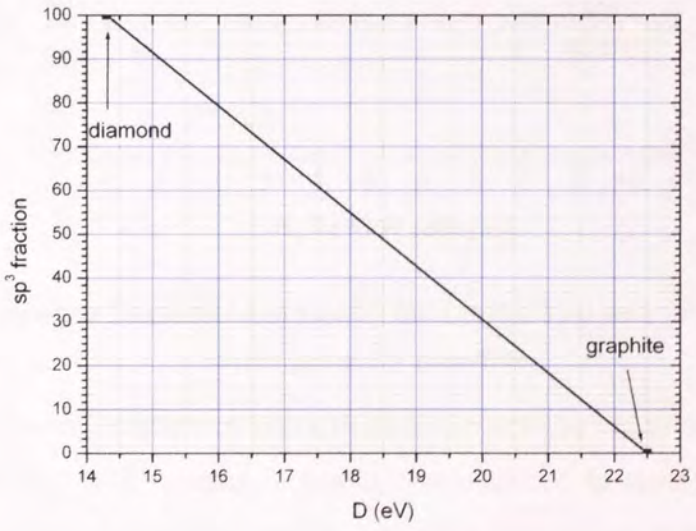

Figure 4.61 Linear dependence of sp^3 fraction with the D value

The C 1s and O 1s X-ray photoelectron spectra were also collected and smoothed with 9 points and 10 passes. A typical surface contamination of 7-10 % atomic concentration of oxygen was found for all the a-C:H films analysed. The C 1s peak was fitted assuming a difference of 0.7-0.8 eV [92] between the de-convoluted sp^2 and sp^3 peaks. The values for sp^3/sp^2 ratio from the XPS C1s fit were found to be in good correlation with the ones found from the Auger first derivative spectra in most of the samples, even though the penetration depth is 7.5 nm in the case of XPS, compared to only 2.0-2.5 nm for the XAES method [115, 116]. However, the XPS fitting is a very time consuming technique and the XAES D value calculation was the preferred method of determining sp^3/sp^2 ratios.

4.2.4.2 Methane series

4.2.4.2.1 Sp^3 fraction vs. relative flow

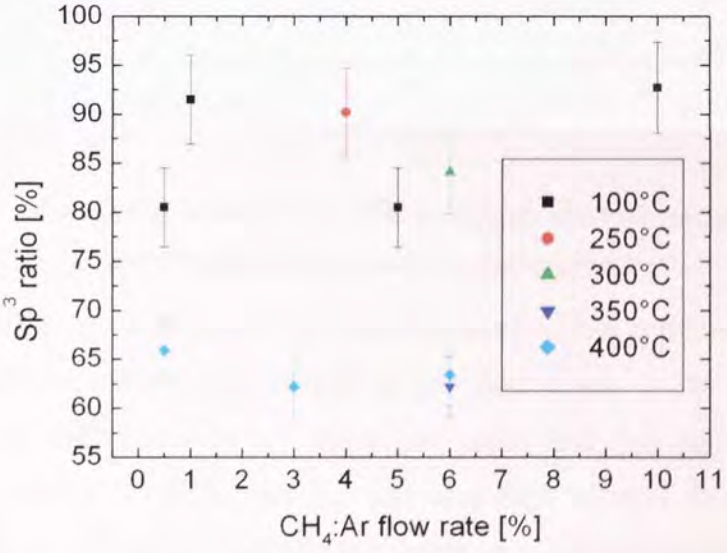

Figure 4.62 Sp^3 ratio as a function of flow rate for films grown from methane and pure argon as carrier gas at low pressures

The D value for the methane series was calculated over a limited number of scans (10 or 20) and a smoothing of 27 points, 2 passes was required to remove the noise in the recorded spectra. The sp^3 fractions appear to be very high (close to 95%) in some cases, and this is due to high incorporation of H in the films. The expected hydrogen content [at %] in the films is less then the C:H ratio in the precursor molecule, which is 1:4 in the

case of methane. In these cases, even though the majority of C atoms in the film are in the sp^3 hybridization, most of the bonds are saturated by H and this leads to polymer-like films. In certain deposition conditions the sp^3 fraction falls below 70%, but the hydrogen content decreases as well and these films are soft amorphous hydrogenated carbon films, with higher film density.

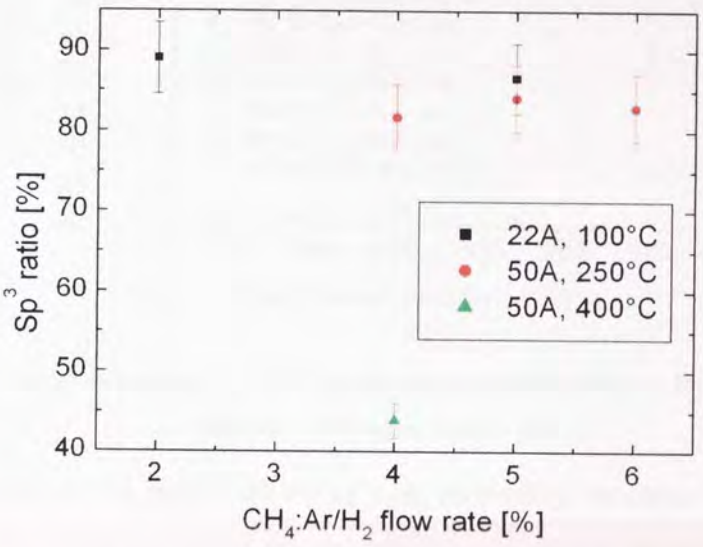

Figure 4.63 Sp^3 ratio as a function of relative flow for films grown from methane with Ar/H_2 3% mixture as carrier gas, at high process pressures

The variation of the sp^3 fraction with the methane relative flow is presented in Figure 4.62 and Figure 4.63 for pure argon as carrier gas and argon – 3% hydrogen mixture respectively. The differences in sp^3 ratios are small and this could be because the deposition mechanism is similar for the low and high relative flows in the case of methane. The small differences could be explained by a different hydrogen incorporation in the film, dictated by the slightly different plasma chemistry.

Since the D value is the difference between two energies and assuming an error of 0.2 eV in determining each of the values for the energy peaks the combined error in measuring the D values is $\pm 0.4eV$. This corresponds to a relative error of 5% in the sp^3 fraction.

4.2.4.2.2 Sp^3 fraction vs. temperature

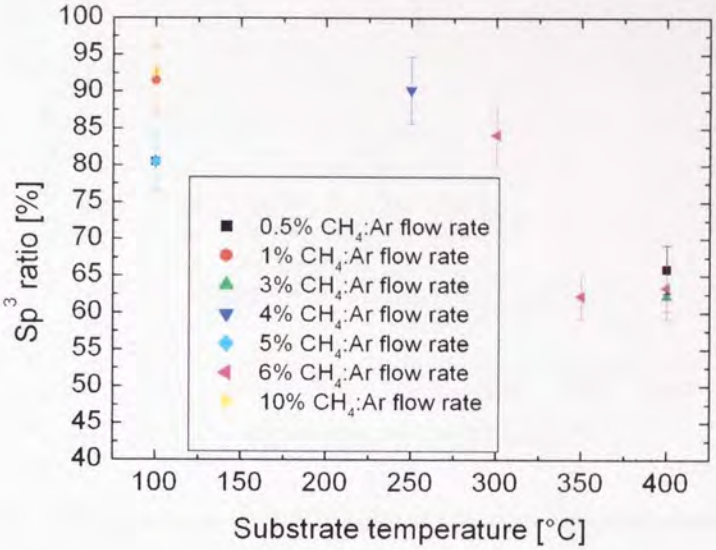

Figure 4.64 Sp^3 rates measured by XAES against substrate temperature for films grown from methane with Ar as carrier gas

The fraction of sp^3 carbon atoms decreases with increasing substrate temperature, due to the different sticking coefficient of the precursor molecules at the substrate level, which influences the growth mechanism. The differences in absolute values are rather small, but taking into account that incorporation of hydrogen is less at higher temperatures, these conditions give harder films (Figure 4.64). There is a threshold temperature of 350°C above which the films show an increased fraction of sp^2 hybridised carbon atoms, more evident in the Raman spectra analysis.

Similar trends are observed in the case of argon – 3% hydrogen mixture used as carrier gas, with a more abrupt decrease at higher temperatures; this is due to the enhanced etching rate of atomic hydrogen at higher temperatures (Figure 4.65). The sp^3 fractions are higher in the case of methane, due to incorporation of large fractions of H in the films, as will be seen in the RBS/ERDA results.

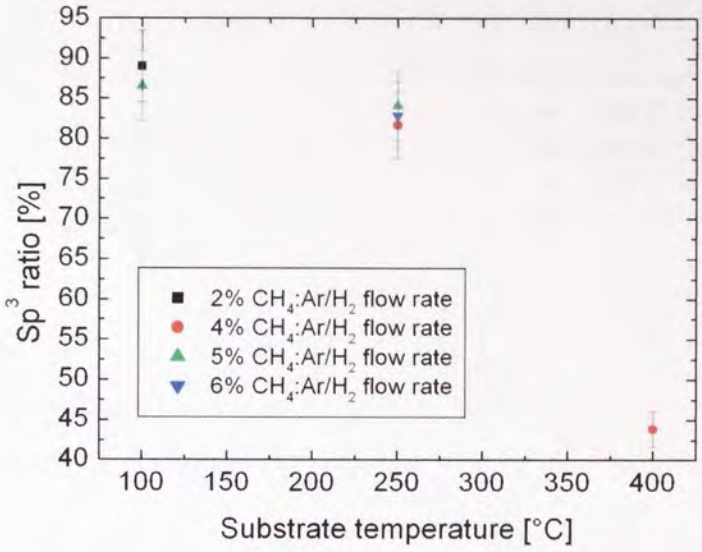

Figure 4.65 Sp^3 ratios measured by XAES against substrate temperature for films grown from methane with argon – 3% hydrogen mixture as carrier gas

4.2.4.3 Acetylene series

4.2.4.3.1 Sp^3 fraction vs. relative flow

In the case of amorphous carbon films grown from acetylene the sp^3 fraction decreased with the increasing relative acetylene to argon ratio from low relative flows to medium-high relative flows. This was due to the different deposition mechanism at low relative flows compared to the medium and high relative flows that will be discussed in more detail in Chapter 6.

Figures Figure 4.66 and Figure 4.67 present the variation of the sp^3 fraction in the films formed from acetylene injected in the source nozzle with the relative flow rate at low and medium pressures.

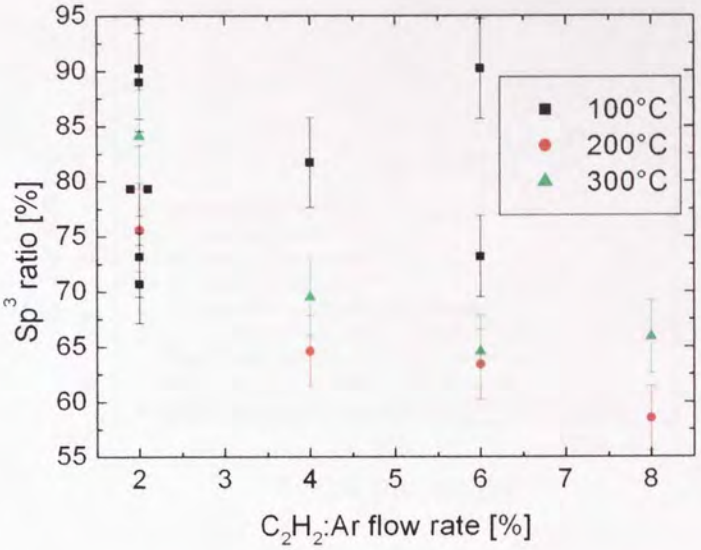

Figure 4.66 Sp^3 ratio measured by XAES against relative flow rates for films grown from acetylene injected in the nozzle with Ar as carrier gas

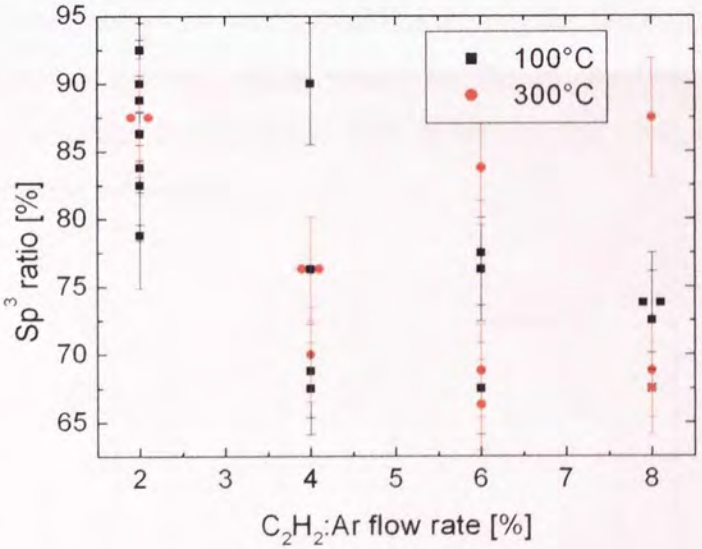

Figure 4.67 Sp^3 ratio measured by XAES against relative flow rates for films grown from acetylene injected in the nozzle with Ar as carrier gas at low pressures, under DC bias conditions

As can be seen from the above graphs the sp^3 fraction is still very high at low temperatures, due to higher incorporation of hydrogen bonded to carbon in the sp^3 hybridization under these conditions.

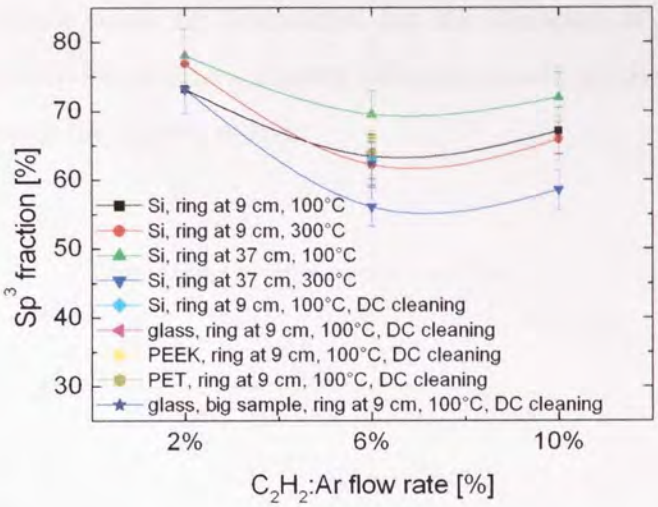

Figure 4.68 Sp^3 ratio measured by XAES against relative flow rates for films grown from acetylene on different substrates (included Silicon) injected via the ring with Ar as carrier gas

In the case of films grown from acetylene injected via the ring there is a small decrease in the sp^3 fraction absolute values, as can be observed from Figure 4.68. The trends are similar to those when acetylene was injected in the nozzle; the analysis of films formed on different substrates showed similar values for the sp^3 fraction, suggesting that the surface of the amorphous hydrogenated film is similar for films deposited in similar conditions on different substrates.

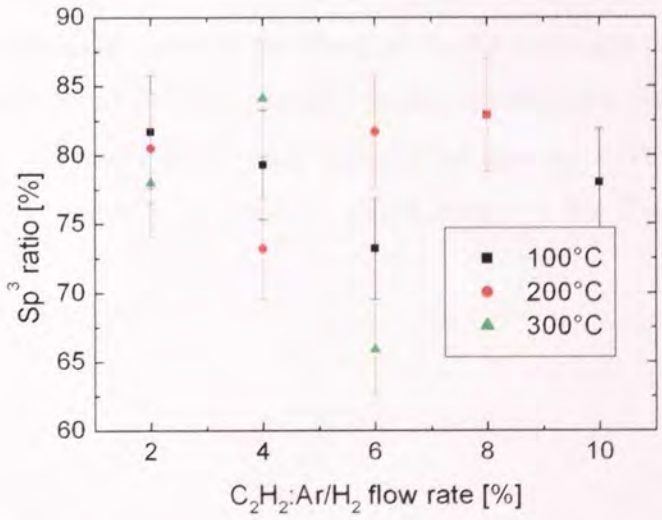

Figure 4.69 Sp^3 ratio measured by XAES against relative flow rate for films grown from acetylene injected in the nozzle with argon – 3% hydrogen mixture as carrier gas at low pressures

In the case of argon – 3% hydrogen mixture as carrier gas with acetylene injected in the nozzle no clear trends could be determined for the variation of sp^3 fraction with the relative flow. This could be due to a slightly different growth mechanism due to the small degree of ionisation in the plasma source.

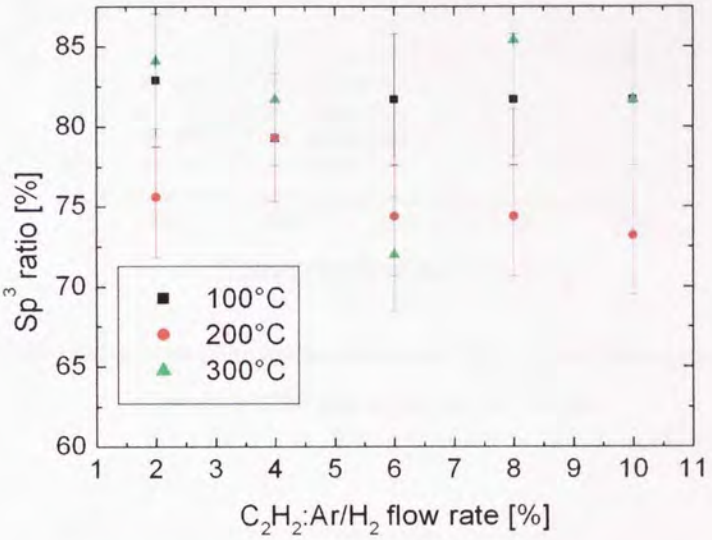

Figure 4.70 Sp^3 ratio measured by XAES against relative flow rate for films grown from acetylene injected in the nozzle with argon – 3% hydrogen mixture as carrier gas at medium pressures

4.2.4.3.2 Sp^3 fraction vs. temperature

For films grown with argon as a carrier gas the sp^3 fraction in the films was related to the amount of hydrogen incorporated in the films, so, as the hydrogen content decreases from low to medium-high relative flows, the sp^3 fraction decreased as well (see Figure 4.71). The decrease was not large in absolute values, but the sp^3 C-H polymeric bonds are replaced by sp^3 C-C diamond-like bonds, which confer to the films increased hardness and reduced modulus.

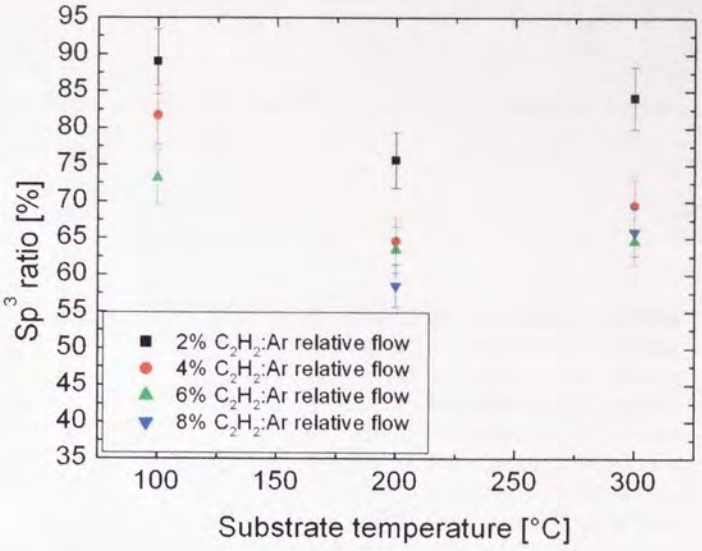

Figure 4.71 Sp^3 ratio against substrate temperature for films grown from acetylene injected in the source nozzle and argon as carrier gas

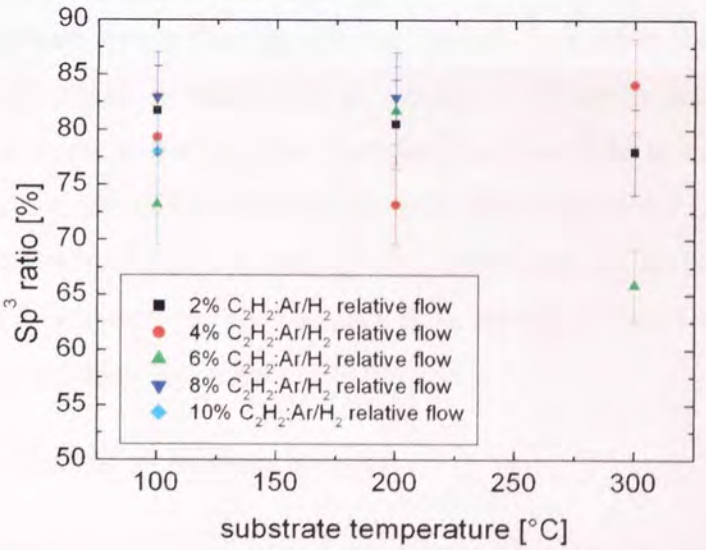

Figure 4.72 Sp^3 ratio against substrate temperature for films grown from acetylene injected in the nozzle and argon – 3% hydrogen mixture as carrier gas

For the case of argon – 3% hydrogen mixture (see Figure 4.72) the interpretation of the data is more ambiguous, due to the higher hydrogen content in the plasma and the different degree of ionization degree in the source, which makes the deposition model more complicated.

4.2.4.3.3 Sp^3 fraction vs. substrate bias

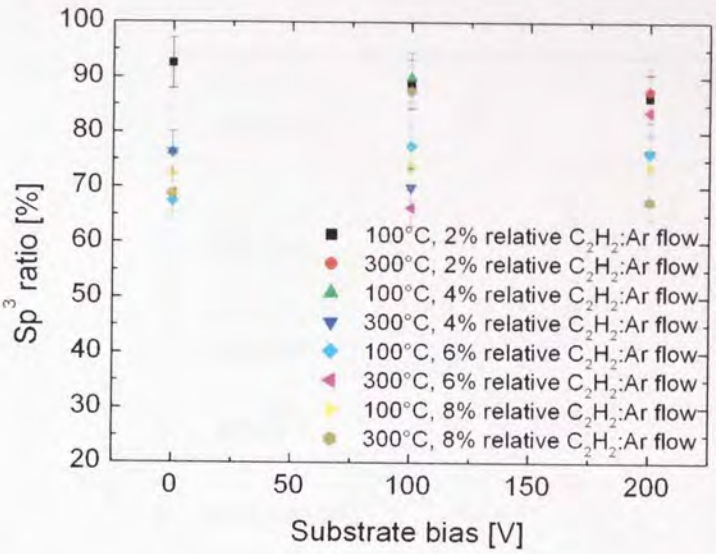

Figure 4.73 Sp^3 ratio against substrate bias for films grown from acetylene injected in the nozzle and argon as carrier gas

Normally the substrate was at floating potential (about -2V), while the Si samples were N doped with phosphorous, as mentioned in Chapter 3. When a negative DC bias was applied to the substrate to increase ion energies, this had little to no effect on the film properties, due to the insulating character of these films (Figure 4.73). After the first few layers were deposited the effect of biasing was diminished and no clear improvement in film quality could be observed. This became more obvious when hardness and reduced modulus were plotted against substrate bias voltage.

4.2.4.4 Interpretation of Raman spectra

Differences between the various types of amorphous films can be observed using Raman spectroscopy. Careful analysis of the spectra can determine the sp^3/sp^2 ratio in the films and the hydrogen content using a peak fitting procedure, but this was beyond the scope of this study. For an accurate analysis both UV and visible Raman are required [117]. The spectra are characterised by the presence of two peaks, D and G, which can change shape and position depending on the character and properties of the analysed material. The

differences between different types of deposited carbon materials are presented in Figure 4.74.

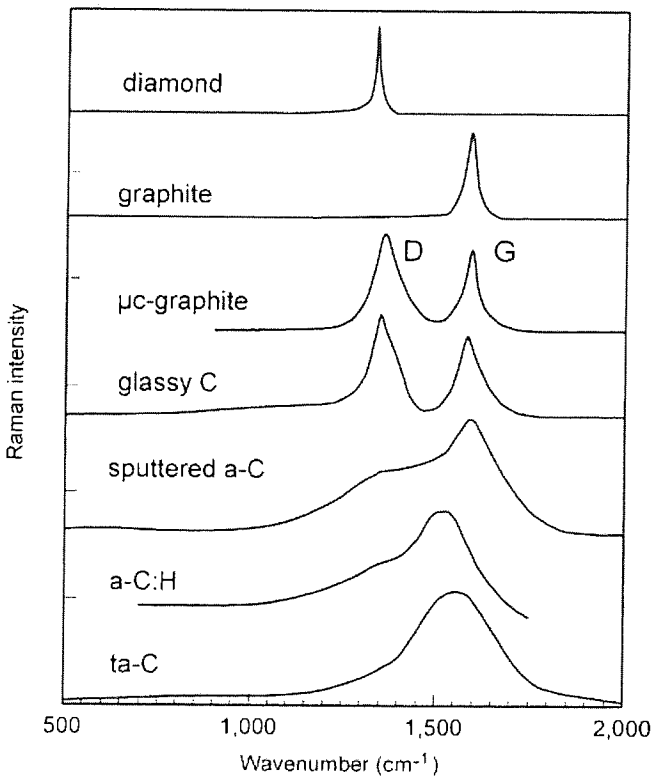

Figure 4.74 Raman spectra for different types of carbon coatings (from [2 (p. 165)])

A few selected samples from the methane series were analysed at Jobin-Yvon UK, Raman Division. Films with different characters could be observed. The results are presented in Figure 4.75 - Figure 4.79.

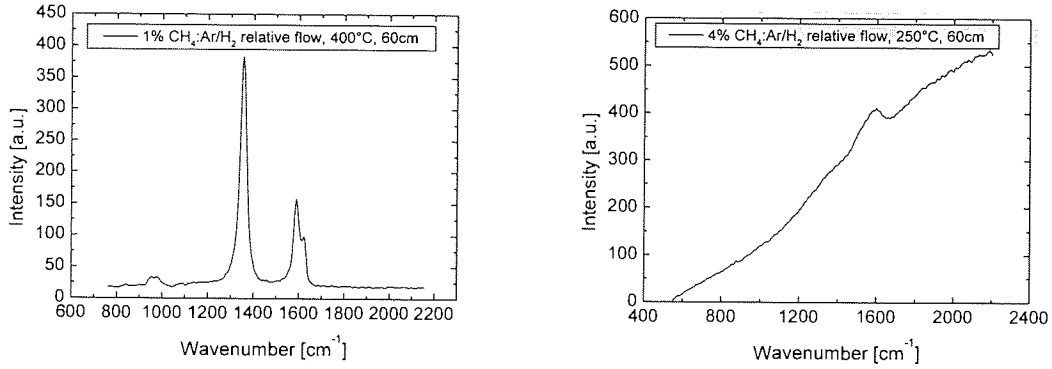

Figure 4.75 Raman spectra of two films grown from methane and argon – 3% hydrogen mixture as carrier gas at two different relative flows and two different substrate temperatures: low relative flow, high temperature (left); high relative flow, medium temperature (right)

As can be seen from Figure 4.75 films with different character can be formed using different set-up conditions. At high temperatures (above 350°C) the films formed showed a graphitic/glassy character, highlighted by the presence of the separated D and G peaks. At lower temperature the films showed amorphous hydrogenated carbon character, highlighted by the presence of a sloped background and the superimposing of the D and G peaks.

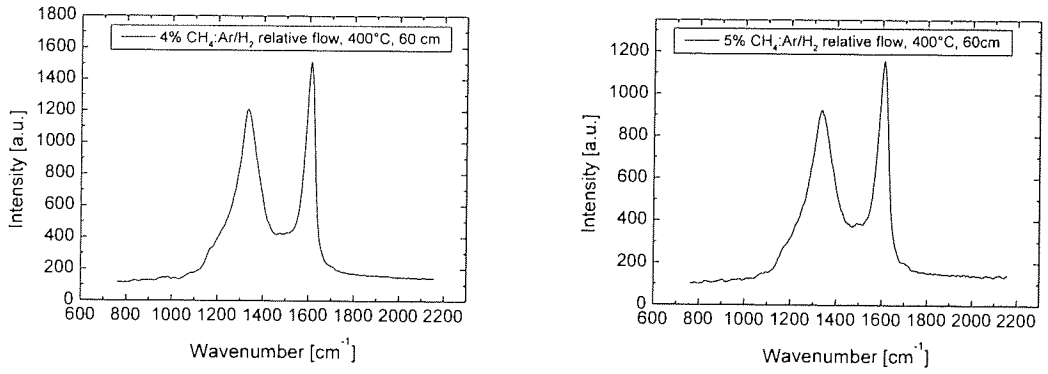

Figure 4.76 Raman spectra for two films grown from methane and argon – 3% hydrogen mixture in similar conditions – high relative flows, high temperatures

The films deposited at high temperatures showed a graphitic character with a clear separation of the D and G peaks. The character of the films at high relative flows was more towards graphitic carbon, whereas at lower relative flows resembled more the glassy carbon character (see Figure 4.76).

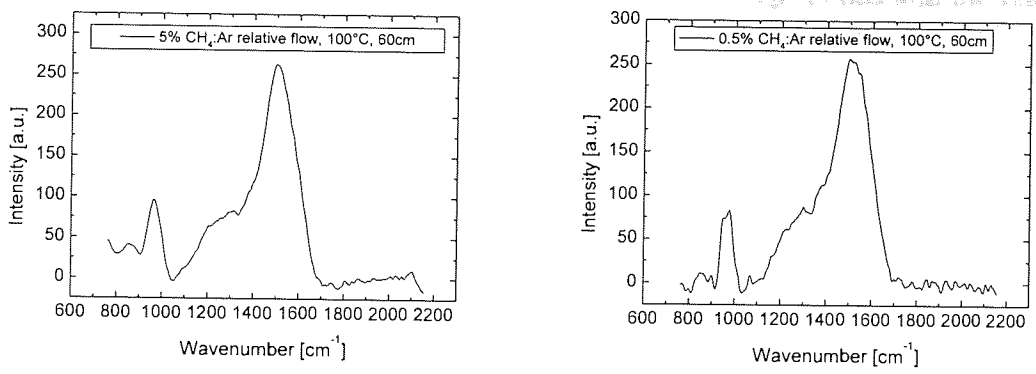

Figure 4.77 Raman spectra for two films grown from methane and argon as carrier gas at low temperatures and high relative flows (left) and low relative flows (right image)

As can be seen from Figure 4.77 films that have the amorphous hydrogenated carbon character can be obtained from methane and argon, at low and high relative flows and low temperatures. The relative flow does not have an important role in the case of methane, due to a slightly different deposition mechanism, which will be discussed in Chapter 6.

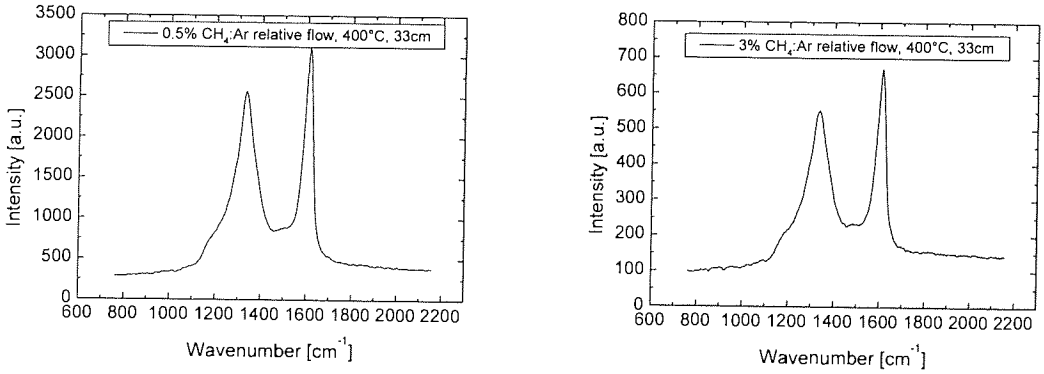

Figure 4.78 Raman spectra for two films grown from methane and argon as carrier gas at high temperatures, low relative flows (left image) and high relative flows (right image)

The same character was obtained for films grown with pure argon as carrier gas, with the two peaks, D and G, being separated at high deposition temperatures. The character of the film is the same from low to high relative flows (Figure 4.78).

The change in film character at higher temperatures is best illustrated in Figure 4.79. Films deposited under identical conditions dramatically change their character from a deposition temperature of 300°C to a deposition temperature of 350°C. This proves the existence of a threshold temperature of ~350°C which determines a process of so-called

graphitization in the films that favours the formation of C-C sp^2 bonds and the release of H from the film.

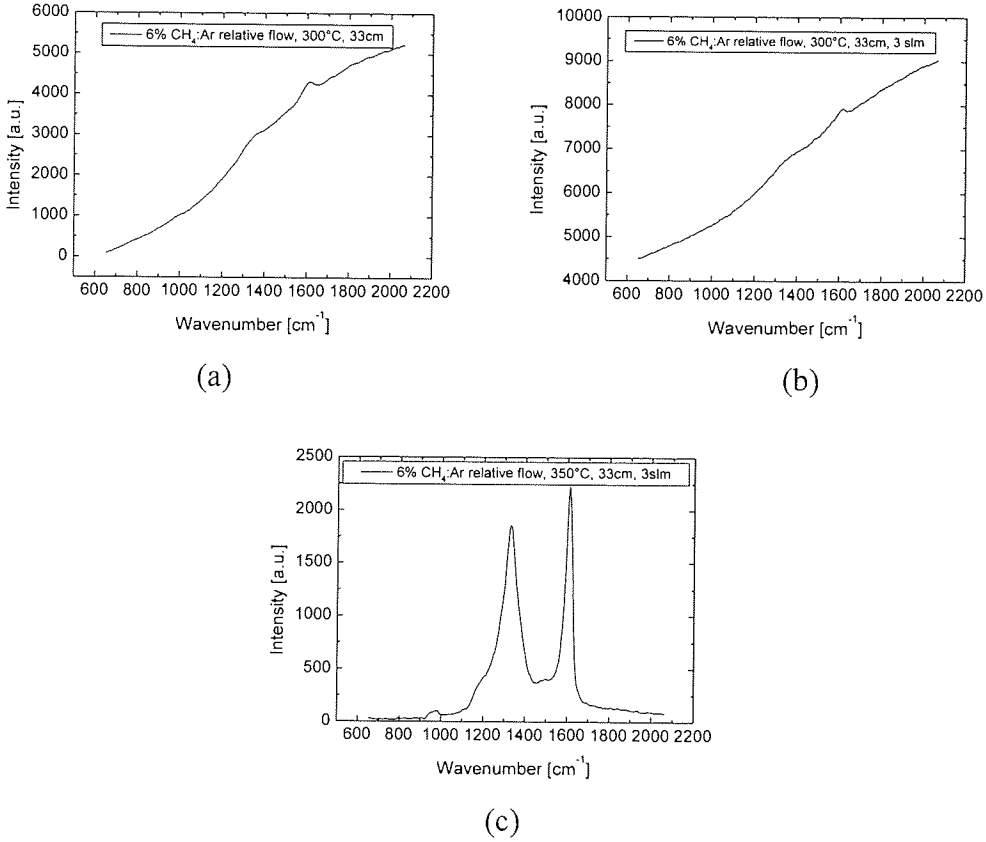

Figure 4.79 Raman spectra for films grown from methane and argon as carrier gas at high relative flows and slightly different substrate temperatures and carrier gas flows: 300°C, 2.5 slm Ar (a), 300°C, 3 slm Ar (b) and 350°C, 3 slm Ar (c)

General conclusions from the Raman study: for films deposited from methane a threshold temperature of ~350°C exists, above which the films show graphitic character. Deposition temperature should be limited to 300°C. The relative flows did not affect the character of the deposited films; the differences between high and low relative flows were minimal.

4.2.5 FTIR measuremts - relative and absolute hydrogen content

The relative hydrogen content in the films deposited from pure argon and acetylene (the high power series) were measured by FTIR at OTB Engineering by the author, assuming a direct dependence of the hydrogen content to the area of the FTIR peaks [2 (p. 181),

3 (p. 55)] and that most of the hydrogen present in the films is bonded to carbon [3 (p. 56)].

Some examples of the FTIR collected data is given in Figure 4.80, after the background silicon signal was subtracted.

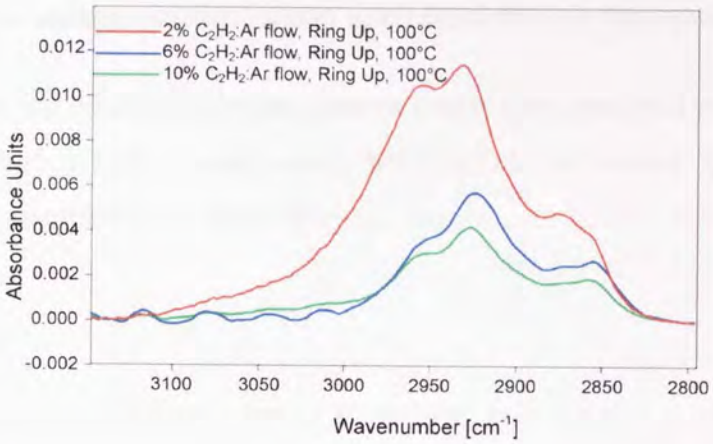

Figure 4.80 FTIR subtracted spectra for films grown from acetylene injected via the ring up position with pure argon as carrier gas, under high power conditions, at 100°C substrate temperatures

4.2.5.1 Relative content in acetylene high power series

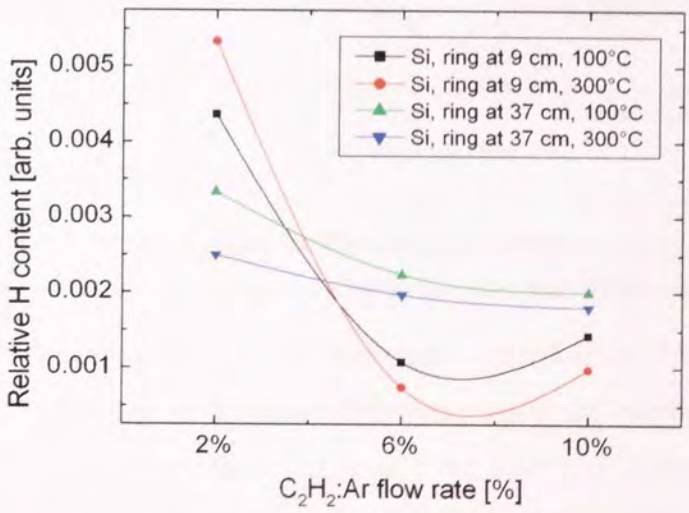

Figure 4.81 Relative hydrogen content for films deposited from acetylene injected via the injection ring with argon as carrier gas

The relative hydrogen content was calculated considering that the FTIR subtracted signal is proportional to the volume of the analysed carbon film. The spatial analysed area is the same for all films, but due to different film thicknesses, the volume is different.

Thus dividing the FTIR peak area by the film thickness will give a normalized value proportional to the hydrogen content in the films, as can be seen from Figure 4.81.

4.2.5.2 Absolute values (comparison with RBS/ERDA measurements)

Few samples from the relative hydrogen content graph were analysed externally by OTB Engineering (at Philips Laboratories) using RBS/ERDA techniques. With the absolute hydrogen content measured on these samples, the relative values were converted into absolute ones.

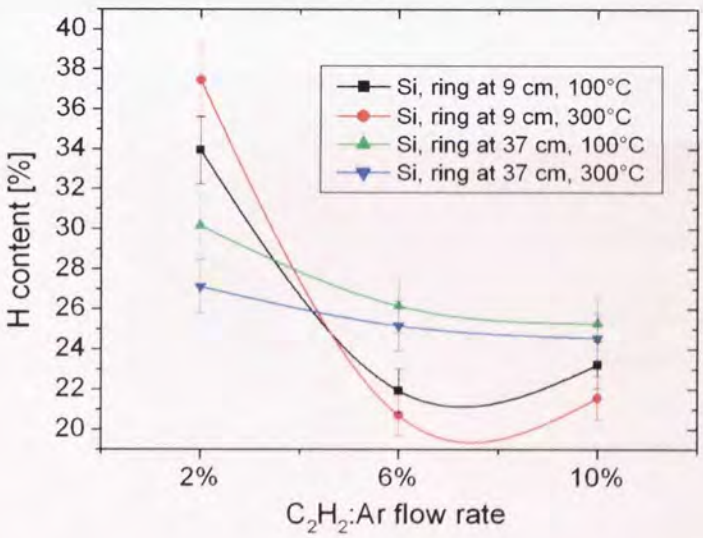

Figure 4.82 Absolute hydrogen content for films deposited from acetylene injected via the injection ring with argon as carrier gas after calibration with RBS measurements

There are sensible differences for the hydrogen content when the acetylene is injected close to the source exit or middle way between source and substrate holder. When the acetylene is injected at 9 cm from the nozzle the hydrogen content decreases abruptly from low relative flows to medium-high relative flows. In the case of acetylene injected at 37 cm from the nozzle a decrease can still be observed, but the differences in absolute values are not that large.

4.2.6 Hardness, Reduced Modulus and adhesion

The Nano Test Platform software automatically analyses the loading-unloading curves and calculates the hardness and reduced modulus of the films at the desired indentation depth.

Care must be taken when indenting these thin films [118], because influence from the substrate can affect the absolute values of the hardness and reduced modulus. The analysis was performed generally taking into consideration the 10% rule, and where this was not possible the maximum indentation depth was kept to 20% of the film thickness. Another factor that could influence the results is pile-up effects during the indentation, which was calculated to affect absolute values up to as much as 50% [104, 119]. Careful analysis of the loading unloading curves showed that our brittle amorphous films do not suffer from pile-up around the indenter. This was confirmed by calculating the ratio of the final depth to the maximum indentation depth, as proposed by Pharr [120].

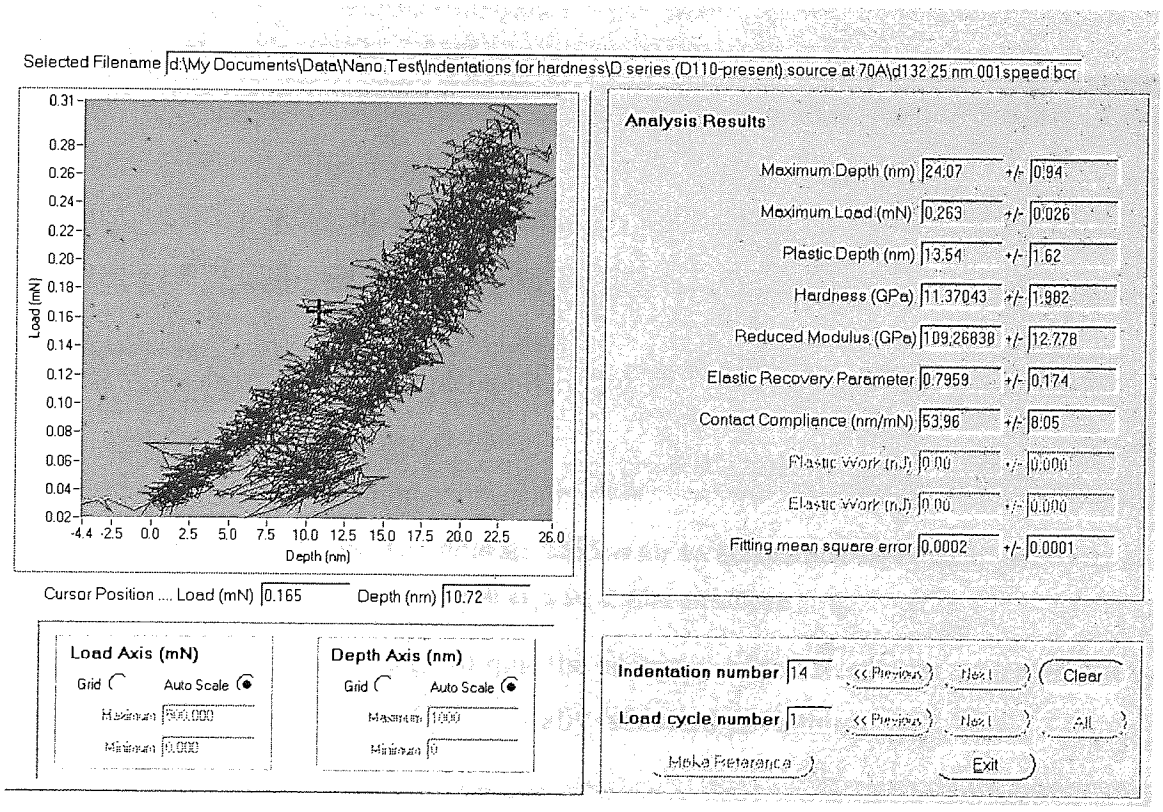

Figure 4.83 Load vs. depth NanoTest software window for an indentation experiment performed at 25 nm depth on a DLC film on silicon

Some images with typical loading-unloading curves and multiple scratch tests are presented in Figure 4.83 - Figure 4.86, together with the experimental conditions used during the indentation/scratch process:

For the analysis of thin films the indents were limited to an indentation depth of 25 nm. The collected signal was noisy, but was than smoothed and fitted by the NanoTest software. The results are presented as a mean of the distribution plus/minus the standard deviation which is usually between 20 to 30% of the mean value at these low indentation depths.

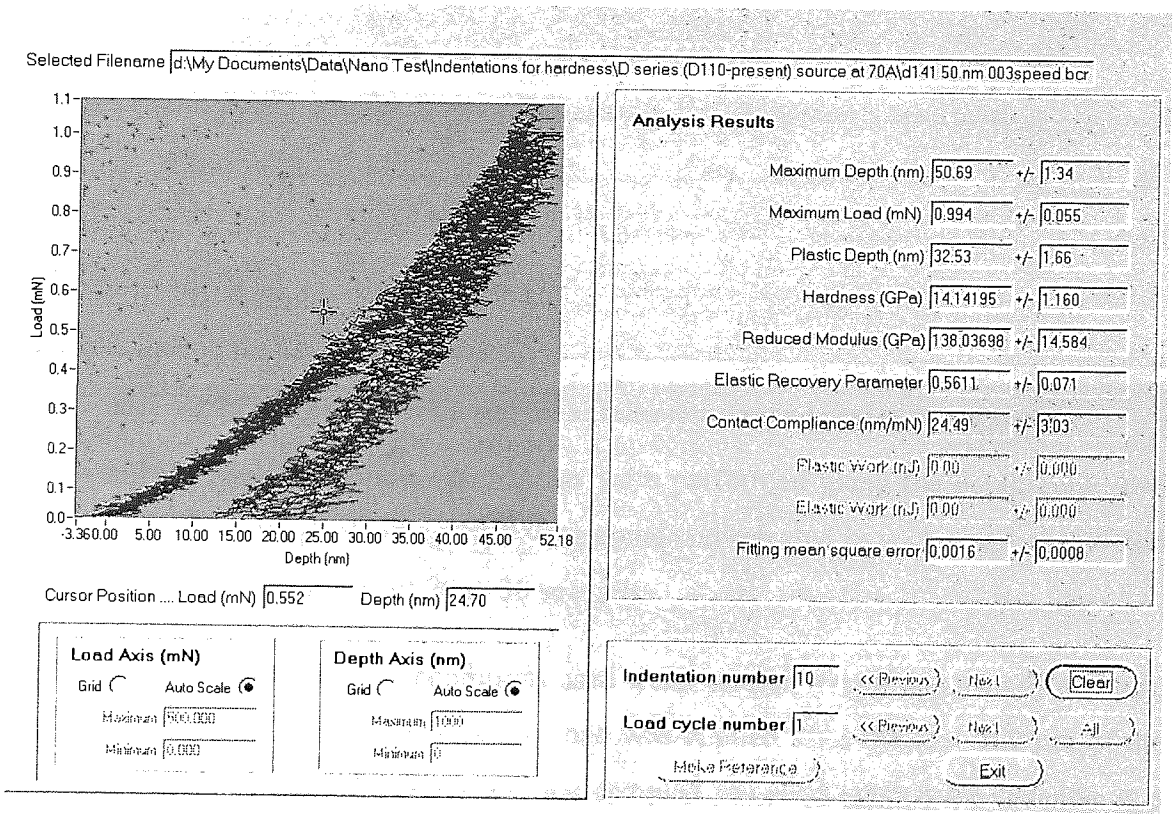

Figure 4.84 Load vs. depth NanoTest software window for an indentation experiment performed at 50 nm depth on a DLC film on silicon

At higher indentation depths (e.g. 50 nm) the accuracy of the results increases, and they are affected by an error of around 10% usually (standard deviation).

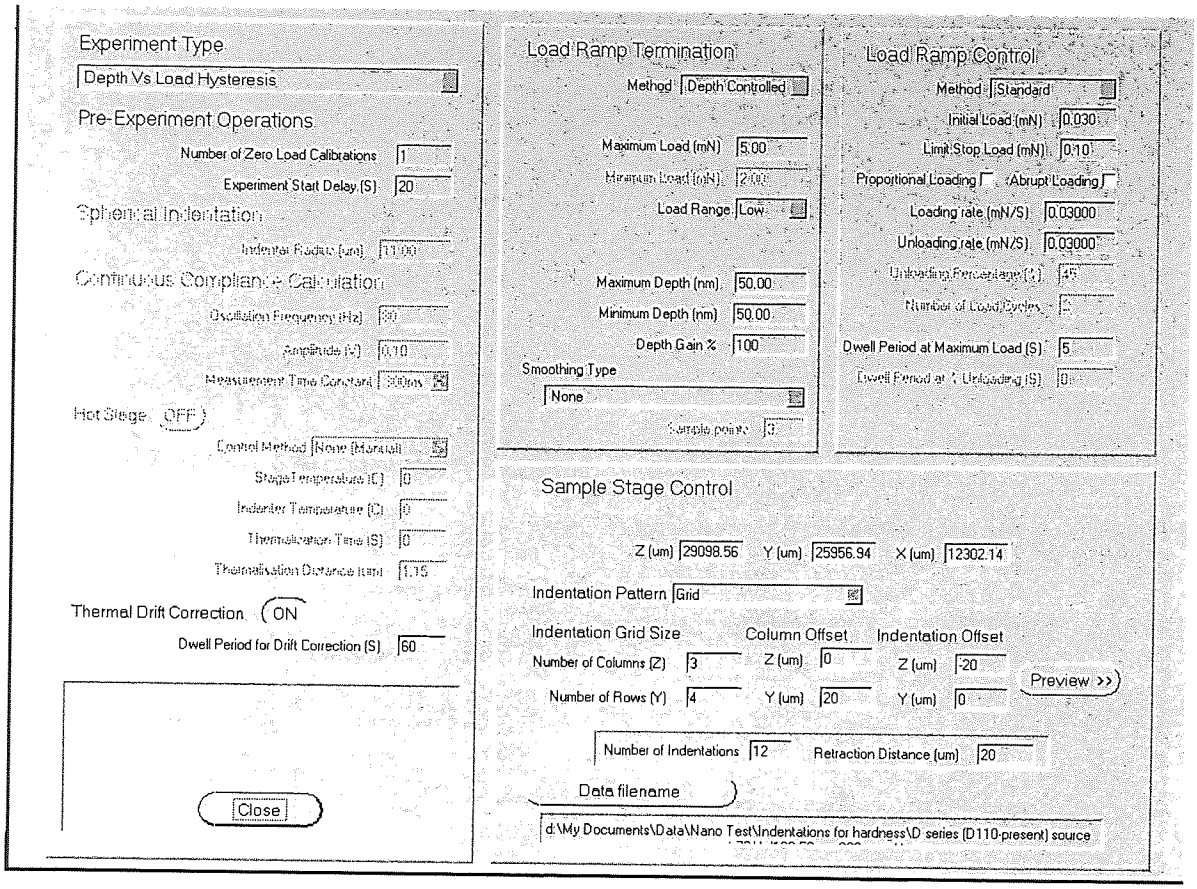

Figure 4.85 Test parameters details for an indentation experiment at 50 nm depth

The majority of the indentation experiments were performed using the depth controlled method, and the loading/unloading rates were equal and selected in such a way that would give a loading/unloading time of 20 to 30 seconds.

For the scratch tests, the typical conditions used were: scratch length was usually 600 μm, maximum force applied was 200 mN, the load was applied after the first 100 μm of the scratch, at a loading rate of 2 mN/s and the sampled travelled against the indenter at a speed of 5 μm/s in the z direction. The indenter used was NT Rockwell 25 μm radius.

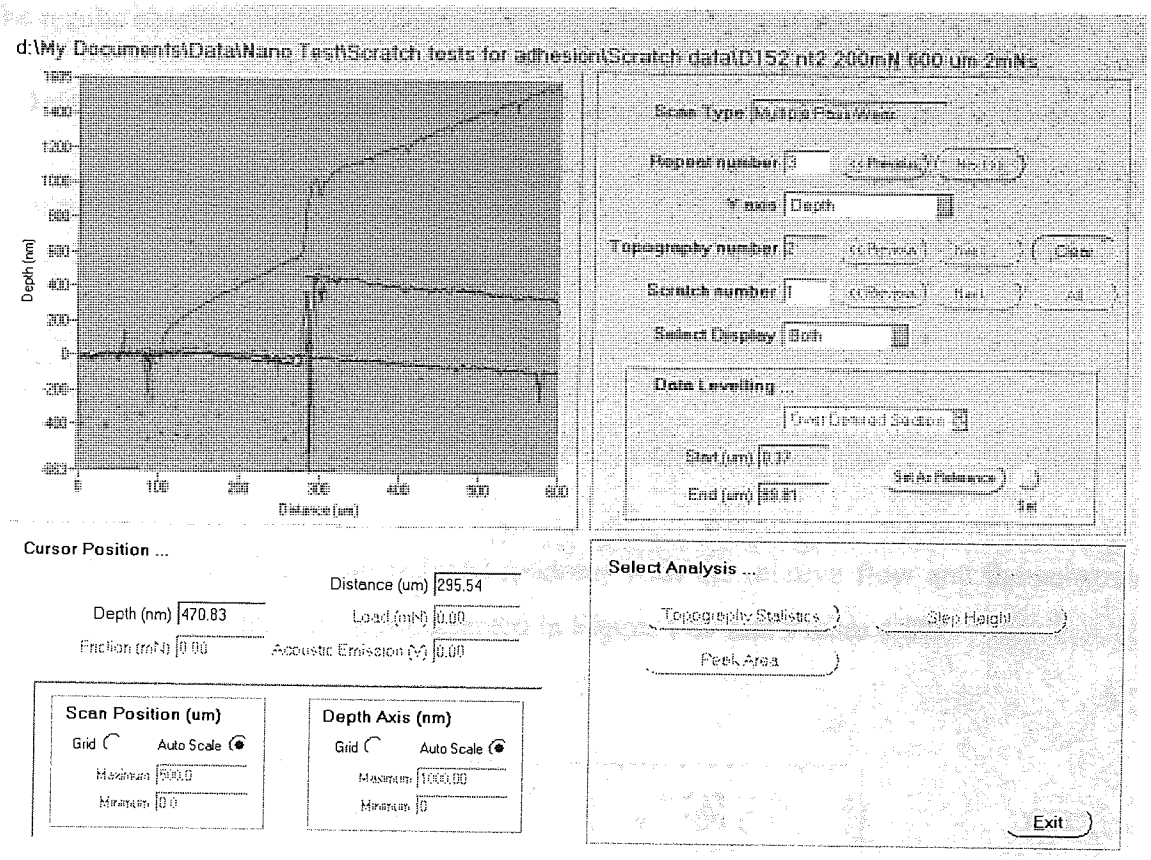

Figure 4.86 Topography before and after a 600 µm scratch on a DLC film on silicon made by a ramping 0 - 200 mN load

The topography of the surface was mapped before and after the scratch was made. The comparison between the two profiles gives information about the film thickness and where the penetration through the film occurs. The corresponding point on the load scale will give the critical load, which was then divided by the film thickness, in order to compare adhesion for films of different thicknesses.

4.2.6.1 Hardness for the methane series

Some of the samples from the methane - pure argon series were analysed retroactively by nanoindentation. Because of the long period elapsed between the deposition tine and the analysis time, these results should be regarded circumspectly. Other films from the methane series changed appearance with time, either delaminating from the substrates or absorbing water molecules on their surface and possible changing their mechanical properties.

The results obtained for the hardness and reduced modulus are presented in Table 4.1:

Table 4.1 Mechanical properties of few selected samples from the methane – pure argon series

Sample id	Source current [A]	Relative flow [%]	Substrate temperature [°C]	Refractive index	Hardness [GPa]	Reduced Modulus [GPa]
B9	30	1	100	1.6	3.4	-
B13	40	8	100	1.6	3.1	34.8
B18	50	6	400	2.2	2.1	60.4
B20	50	4	400	2.2	2.0	48.7
B23	25	0.5	100	1.5	3.9	33.5

The variation of hardness and reduced modulus with the relative flow and the substrate temperature during deposition is presented in Figure 4.87 and Figure 4.88:

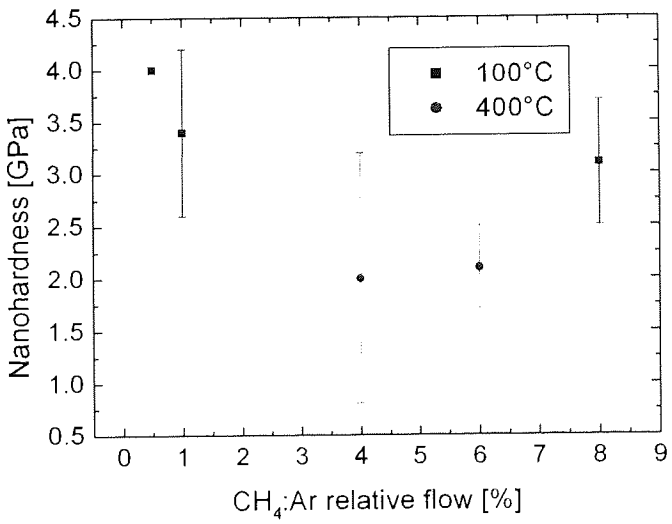

Figure 4.87 Nanohardness against relative flow for films grown from methane with pure argon as carrier gas at different source currents

As can be seen from Figure 4.87 and Table 4.1, the films deposited at higher temperatures have the lowest hardness (graphitic-like films), whereas film deposited at low and high relative flows at low temperatures have similar hardness, but still low in absolute values. The opposite trend was found for the reduced modulus (Figure 4.88), where the highest modulus is obtained at high deposition temperatures.

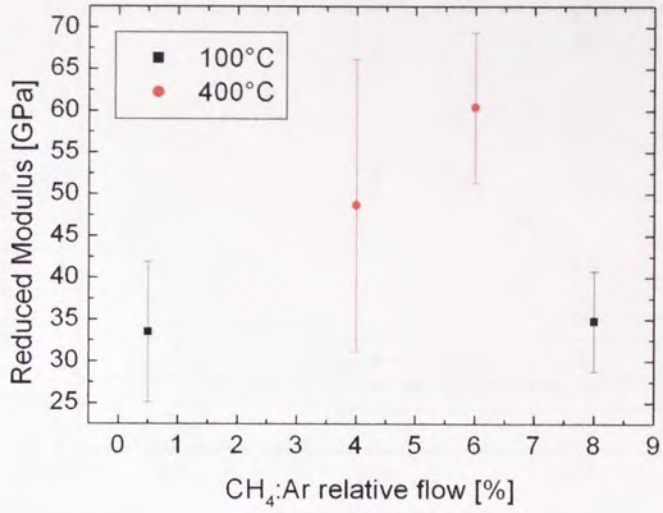

Figure 4.88 Reduced modulus against relative flow for films grown from methane with pure argon as carrier gas at different source currents

4.2.6.2 Hardness vs. acetylene relative flow

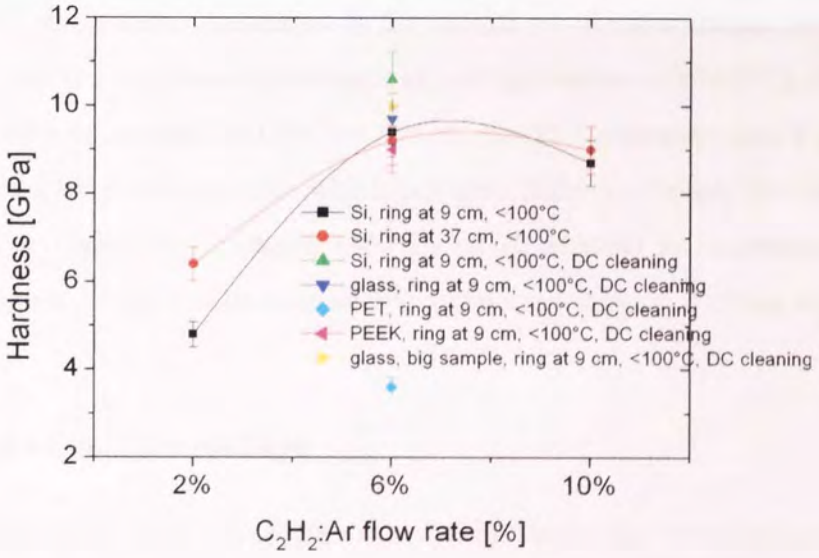

Figure 4.89 Nanohardness against relative flow for films grown on different substrates at low temperatures from acetylene injected via the ring with Ar as carrier gas (70A series)

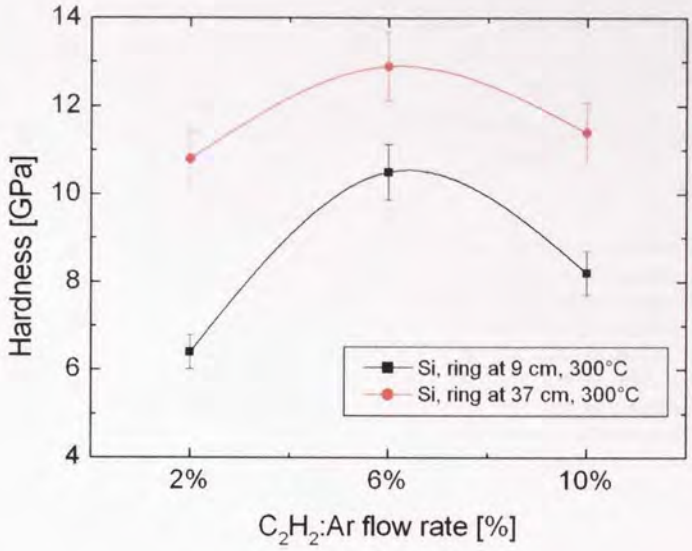

Figure 4.90 Nanohardness against relative flow for films grown on silicon at high temperatures from acetylene injected via the ring with Ar as carrier gas (70A series)

The analysis showed hardness and reduced modulus increased to a maximum at a C_2H_2 to Ar ratio of about 6% in the first set of experiments performed on silicon substrates, at 100°C and 300°C substrate temperatures. In the second set of experiments, when the best conditions were applied to different substrates at low temperatures (<100°C), the hardness remained at a value of around 10 GPa, except for the PET substrate (see Figure 4.89). This was due to the very soft substrate which probably deformed before the film did. The films deposited at higher temperatures (300°C) on Si showed an increased hardness, clearly observed in the experiments with acetylene injected through the ring situated at 37 cm (Figure 4.90).

4.2.6.3 Hardness vs. bias voltage

No clear trends could be observed in the case of films deposited when the substrate was biased. This is due to the insulating properties of the films, which results in the negative DC biasing having little effect on the energy of the depositing radical ions. Combined with the fact that the ion content is low in the flux of depositing particles the hardness showed similar trends to the case of no DC biasing being applied to the substrate; the hardness increases with the relative C_2H_2:Ar flow and with the substrate temperature.

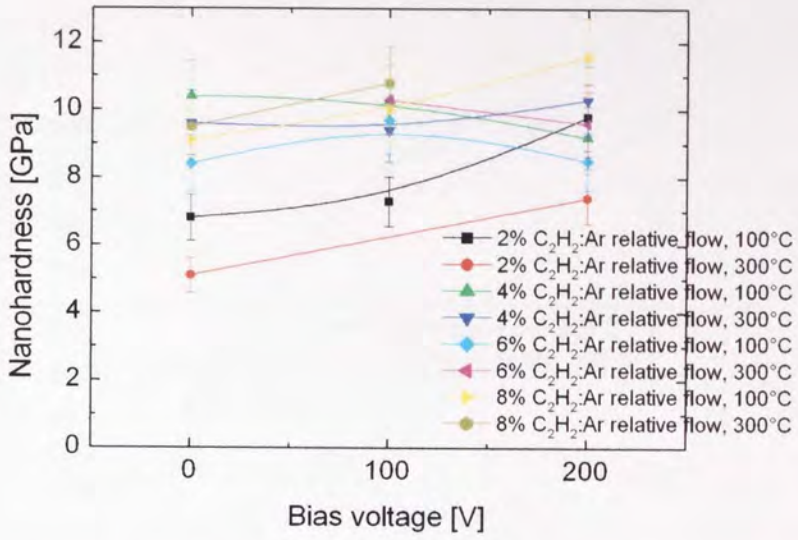

Figure 4.91 Nanohardness against bias voltage for films grown on silicon from acetylene injected via the nozzle with Ar as carrier gas (50A, bias voltage series)

4.2.6.4 Reduced modulus vs. flow

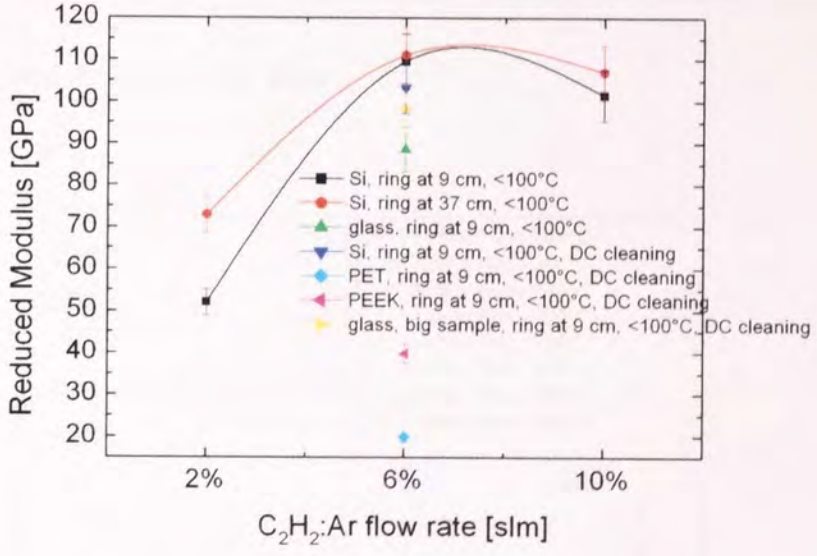

Figure 4.92 Reduced modulus against relative flow for films grown on different substrates at low temperatures from acetylene injected via the ring with Ar as carrier gas (70A series)

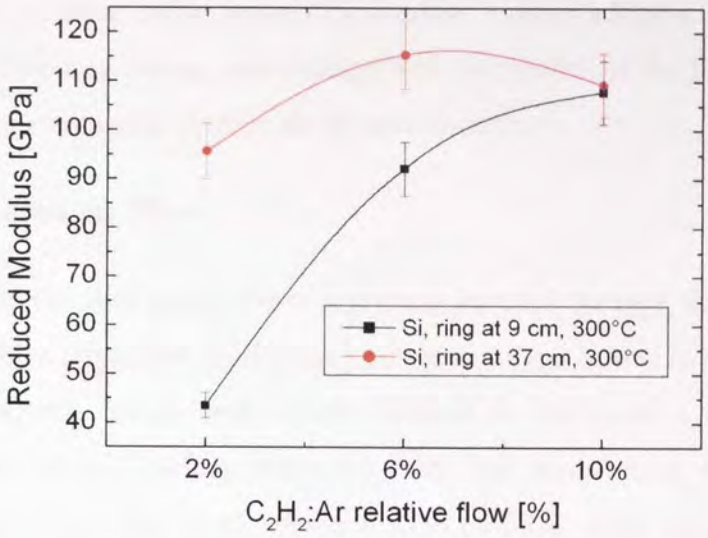

Figure 4.93 Reduced modulus against relative flow for films grown on silicon at high temperatures from acetylene injected via the ring, with Ar as carrier gas (70A series)

The same trends observed for nanohardness were observed for the reduced modulus, the only significant difference being that the elastic properties of both films deposition on plastic (PES, PEEK) were influenced by the softer substrate and yielded very low values.

4.2.6.5 Reduced modulus vs. bias

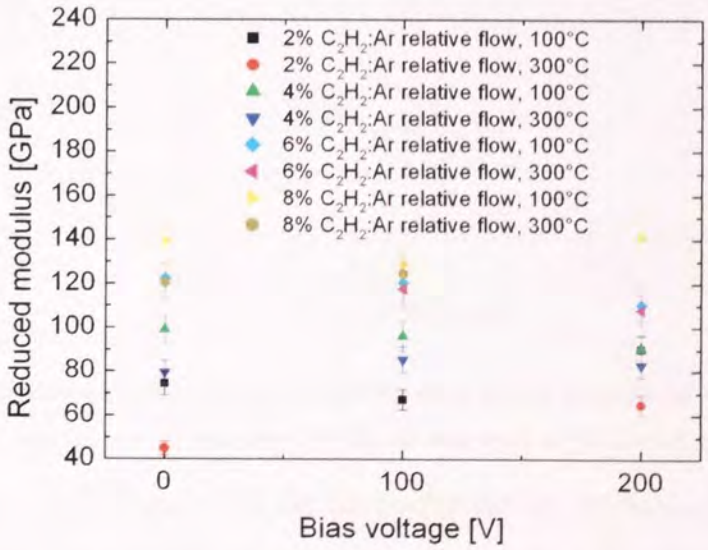

Figure 4.94 Reduced modulus against bias voltage for films grown on silicon from acetylene injected via the nozzle with Ar as carrier gas (50A, bias voltage series)

Similar to the nanohardness vs. voltage bias case, no clear trends could be distinguished for the reduced modulus values against bias, which confirmed the little influence that the DC bias had on the ions energy, and thus growth mechanism of the films. The differences are coming from errors associated with the measurements.

4.2.6.6 Adhesion vs. flow

The adhesion of the film grown from acetylene injected through the injection ring was measured for films deposited on different substrates. Due to the fact that the films have different thicknesses, which make them difficult to compare, a new parameter was introduced, the critical loading measured with the nanoscratch test divided by the thickness of the film. This is an approximative method, since the effects that happen during the scratch test can sometimes depart from linearity. Tests were performed on films deposited under the same conditions, but for different deposition times and thus with final different thickness. The ratio of critical loading/thickness was nearly the same.

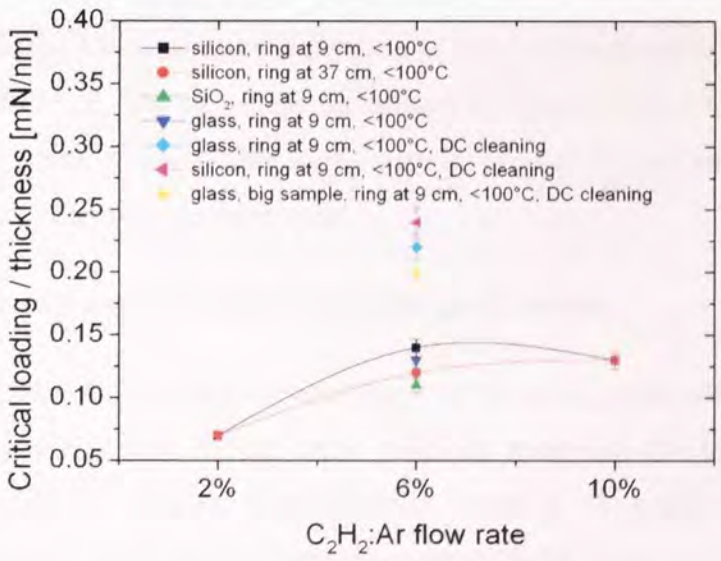

Figure 4.95 Adhesion against relative flow for films grown on different substrates at low temperatures from acetylene injected via the ring with Ar as carrier gas (70A series)

As can be seen from Figure 4.95 the best adhesion of the films to the substrate was measured for the films grown on substrates cleaned by a DC glow discharge prior to

deposition. This proved that removing any contaminants from the surface of the substrate is essential for good adhesion at low temperatures.

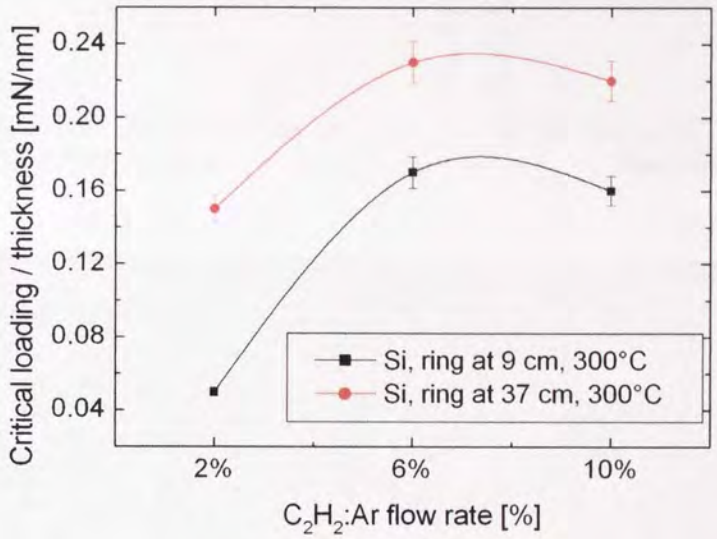

Figure 4.96 Adhesion against relative flow for films grown on silicon at high temperatures from acetylene injected via the ring, with Ar as carrier gas (70A series)

Due to the different mechanism of deposition at low and medium-high relative flows the adhesion was different. The values for the critical loading/thickness for the high substrate temperature experiments are similar to the ones calculated for low substrate temperature, when the DC pre-cleaning was employed.

4.2.6.7 Hardness and Reduced Modulus on E series

A few samples from the E series were analysed by the load-partial unload technique. This produces successive indents in the same position, removing the indenter to a certain predefined percentage of the previous maximum load. It is especially used for very thin films (i.e. < 100 nm), when single indentations are difficult to be made.

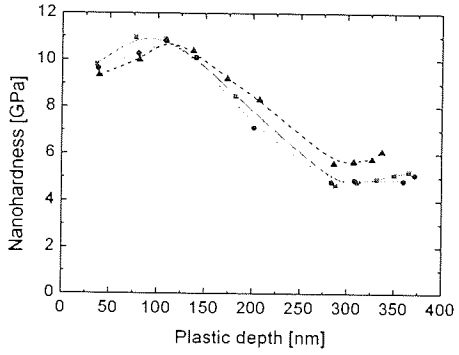

(a)

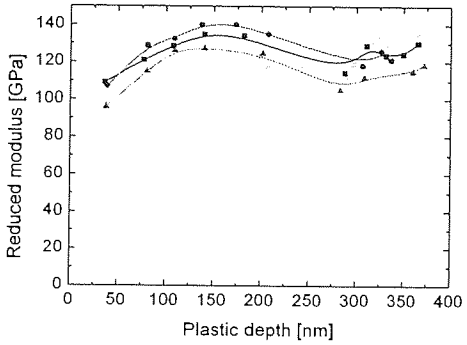

(b)

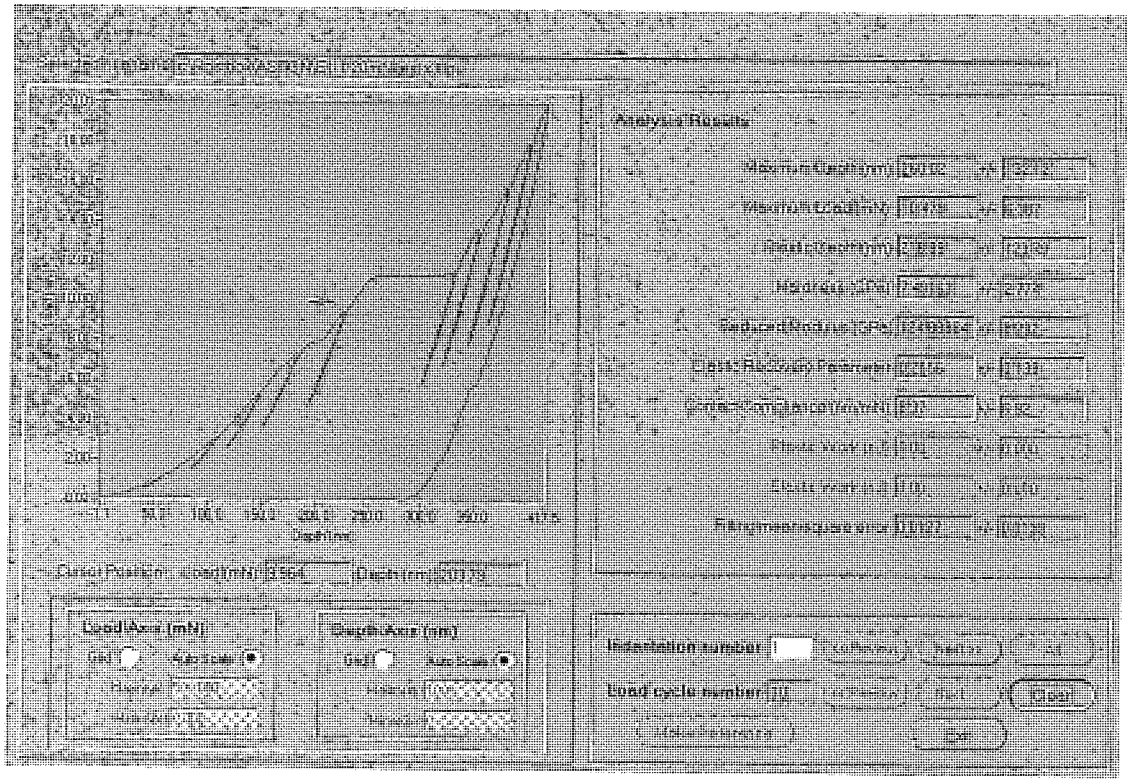

(c)

Figure 4.97 Nanohardness (a) and Reduced modulus (b) vs. plastic depth profile and events during load partial unload technique (c) for sample E1 (Ar - H_2 3% mixture as carrier gas, 2% C_2H_2:Ar relative flow, 40A source current, 100°C substrate temperature)

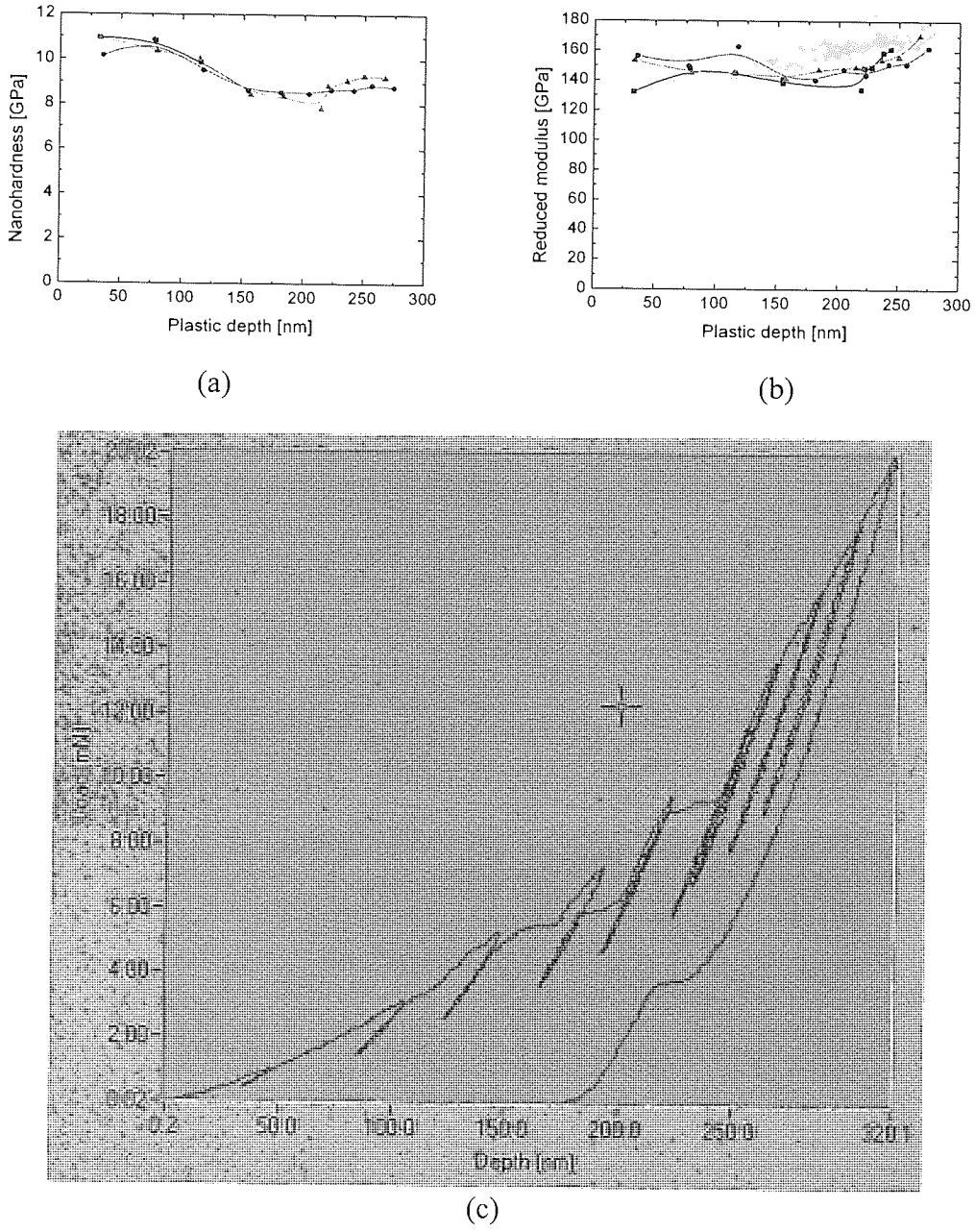

Figure 4.98 Nanohardness (a) and Reduced modulus (b) vs. plastic depth profile and events during load partial unload technique (c) for sample E8 (Ar - H_2 3% mixture as carrier gas, 6% C_2H_2:Ar relative flow, 40A source current, 300°C substrate temperature)

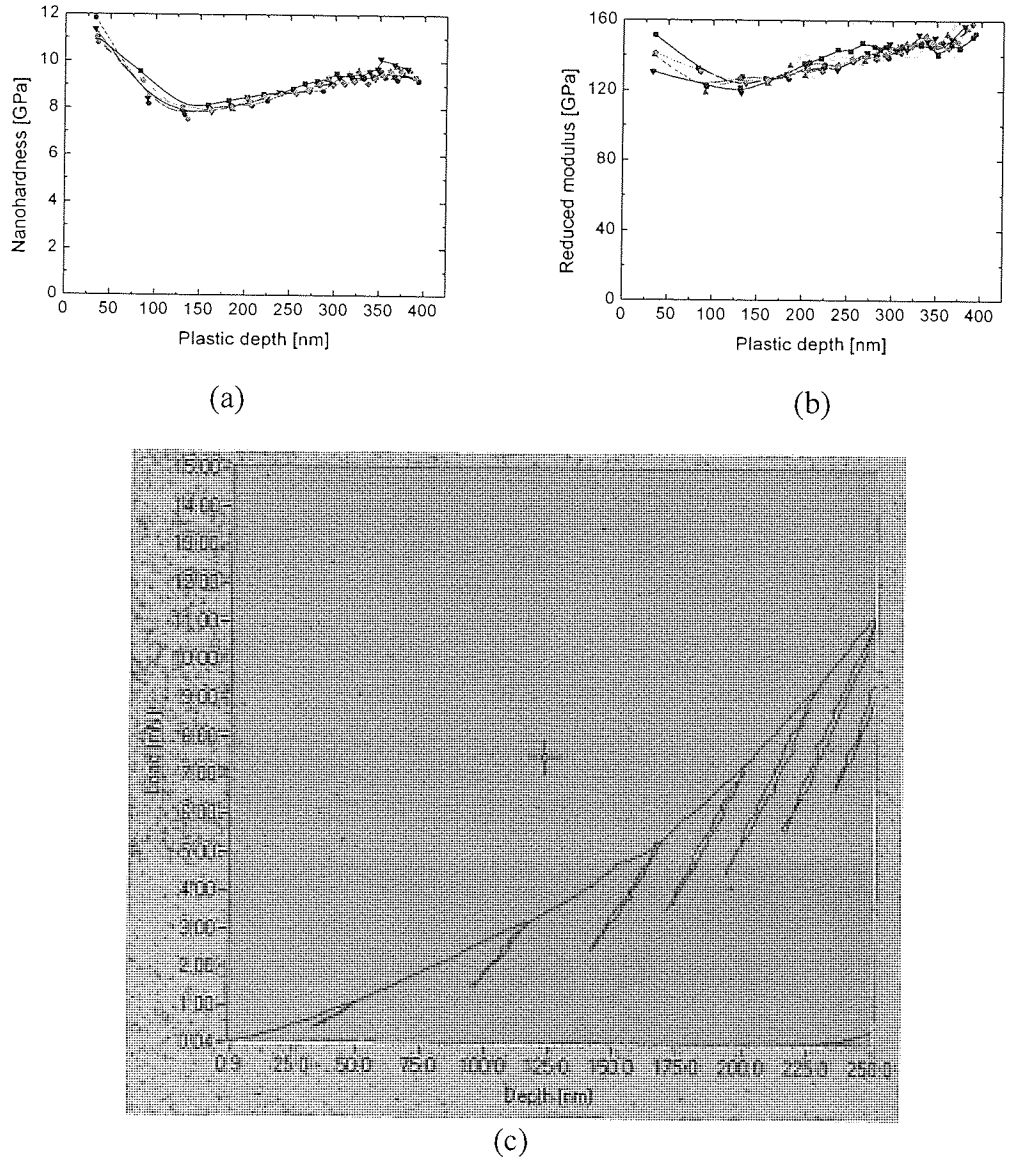

Figure 4.99 Nanohardness (a) and Reduced modulus (b) vs. plastic depth profile and events during load partial unload technique (c) for sample E14 (Ar - H_2 3% mixture as carrier gas, 8% C_2H_2:Ar relative flow, 40A source current, 200°C substrate temperature)

As can be observed from Figure 4.97 – Figure 4.99 the variation in nanohardness and reduced modulus are small with the different experimental conditions. The load partial-unload curves shows that several events happen during loading, such as yielding and cracking, blistering and delamination [121].

For comparison, the same technique is shown for a film from the D series (pure Ar as carrier gas) deposited under similar conditions.

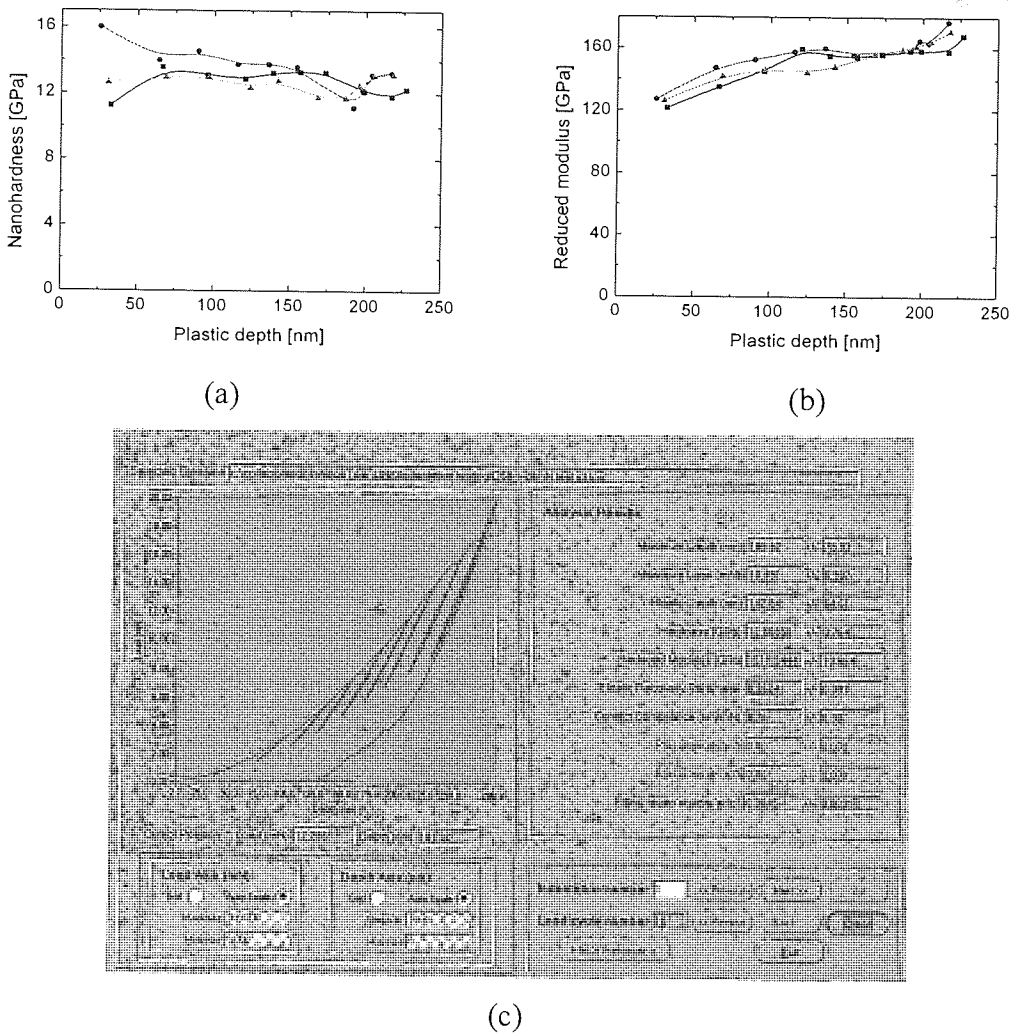

Figure 4.100 Nanohardness (a) and Reduced modulus (b) vs. plastic depth profile and events during load partial unload technique (c) for sample D58 (Ar as carrier gas, 8% C_2H_2:Ar relative flow, 40A source current, 300°C substrate temperature)

For this type of analysis test (load – partial unload) the absolute values are higher when compared to the results obtained via nanoindentation. This is because the loading-unloading curves are acquired at faster load rates in the initial stages of the load-partial unload cycles, which leads to an overestimation in hardness and reduced modulus.

The cracking-yielding events are not as frequent and of much smaller magnitude in the case of films grown from acetylene with pure argon as carrier gas. The presence of hydrogen is known to decrease the hardness of the films, but to improve the wear/friction properties [8]. These observations and the fact that deposition rates are lower when the

argon-3% hydrogen mixture is used as a carrier gas led to the decision of using only pure argon as carrier gas.

4.2.7 Density

As mentioned previously, few samples from the methane and acetylene series were analysed externally by OTB Engineering (at Philips Laboratories) with RBS/ERDA techniques, which enabled the calculation of film density, using the following formula:

$$RBS\ flux = density \cdot thickness \qquad \textbf{Eqn 4.4}$$

The results are presented in the following tables, separately for the methane and acetylene series.

Table 4.2 Film densities and other properties for selected samples from methane series

Sample	Rel. flow [%]	Temperature [°C]	n	Sp^3 [%]	H % [at %]	d [g/cm^3]
A47	1	250	1.61	80.5	32	1.09
B32	5	300	1.95	86.2	31	1.23
B33	5	350	2.10	62.2	31.5	1.32

Table 4.3 Film densities and other properties for selected samples from acetylene series

Sample	Rel. flow [%]	Temp [°C]	n	K360	Sp^3 [%]	Hardness [GPa]	H % [at %]	d [g/cm^3]
D111	2, RU	100	1.79	0.13	73.2	4.8	34	1.21
D113	6, RU	100	2.24	0.54	63.4	9.5	22	1.62
D133	10, RD	300	2.42	0.91	58.5	11.4	23	1.76

Where RU = Ring Up (at 9 cm from nozzle), RD = Ring Down (at 37 cm from nozzle) and K360 is the optical absorbance index at 360 nm that will be discussed in more detail in the next section.

As can be seen from Table 4.2 and Table 4.3 the density in the case of methane is low (~1.2-1.3 g/cm^3), whereas in the case of acetylene is between 1.2-1.8 g/cm^3. This correlates well with the hardness data, that showed all the films from the methane series to be soft (below 4 GPa).

The density and hardness values classify some of the films deposited from acetylene as hard amorphous carbon hydrogenated films, whereas the films deposited from methane could be categorised as polymer-like, soft hydrogenated amorphous or graphitic-like films. These results will be discussed in more detail in Chapter 6.

4.2.8 Optical properties

The refractive index and absorption coefficient were measured using two different ellipsometric set-ups. The refractive index for the methane series and the acetylene with argon – 3% hydrogen mixture as carrier gas was measured with a 632.8 nm laser ellipsometer at Aston University. The refractive index on acetylene with pure argon series could not be measured with this ellipsometer and selected samples from this series were measured at OTB Engineering with a spectroscopic ellipsometer with variable wavelength capable of accurately measuring thicker films.

4.2.8.1 Refractive index vs. substrate temperature

4.2.8.1.1 Methane series

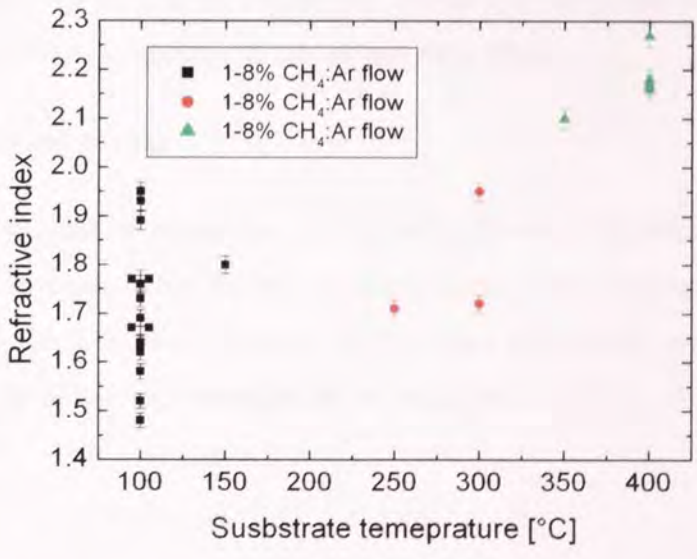

Figure 4.101 Refractive index against substrate temperature for films grown from methane and pure argon as carrier gas; films deposited at low, medium and high temperatures are grown at different relative CH_4:Ar flow rates and presented together

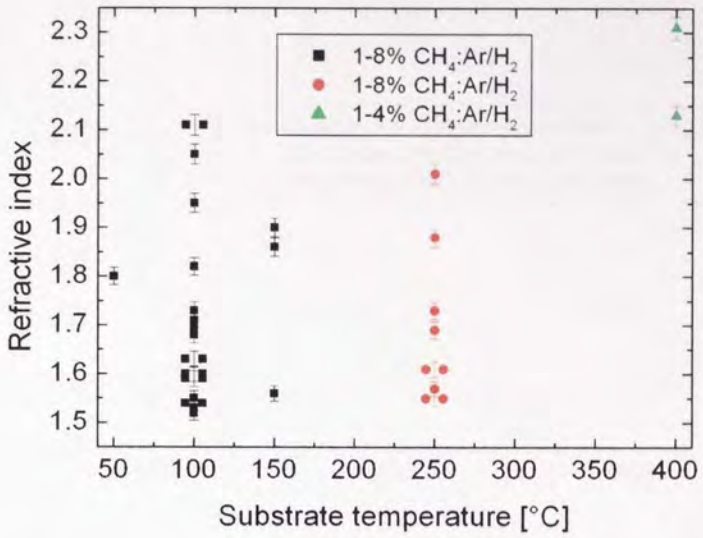

Figure 4.102 Refractive index against substrate temperature for films grown from methane and argon – 3% hydrogen mixture as carrier gas; films deposited at low, medium and high temperatures are grown at different relative CH_4:Ar/H_2 flow rates and presented together

As can be observed from Figure 4.101 and Figure 4.102 the refractive index is increasing with substrate temperature, which suggests that higher density films are formed at higher substrate temperatures. At the same time at the same substrate temperatures large differences in the refractive index are present, depending on the deposition conditions and especially on the relative methane to carrier gas flow rate.

4.2.8.1.2 Acetylene series

In the case of acetylene as precursor gas, for films grown in identical conditions a small increase in the absolute value of the refractive index was observed with the substrate temperature. As the substrate temperature increases the density of the deposited film increased, because of less incorporation of hydrogen into the film.

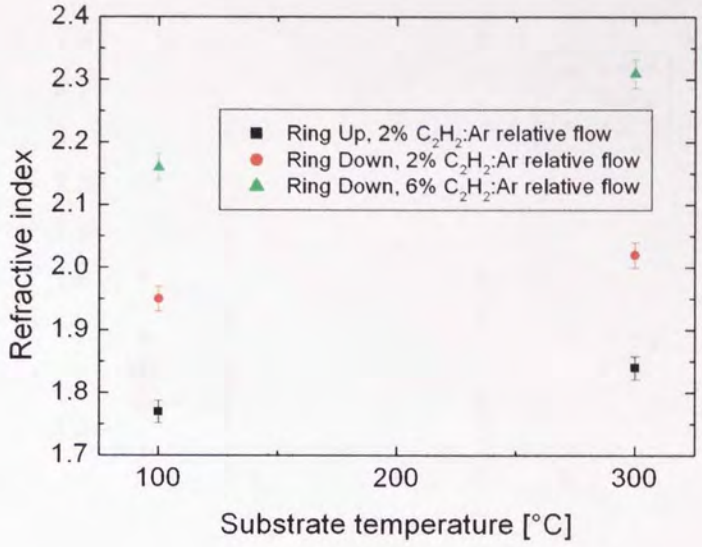

Figure 4.103 Refractive index against substrate temperature for films grown from acetylene and pure argon as carrier gas at different relative C_2H_2:Ar flow rates

4.2.8.2 Refractive index vs. relative precursor flow

4.2.8.2.1 Methane series

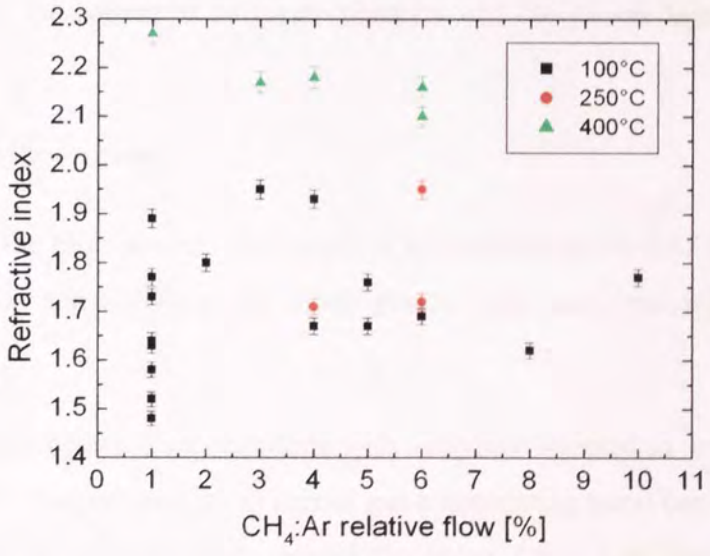

Figure 4.104 Refractive index against relative flow rate for films grown from methane and pure argon as carrier gas at different temperatures

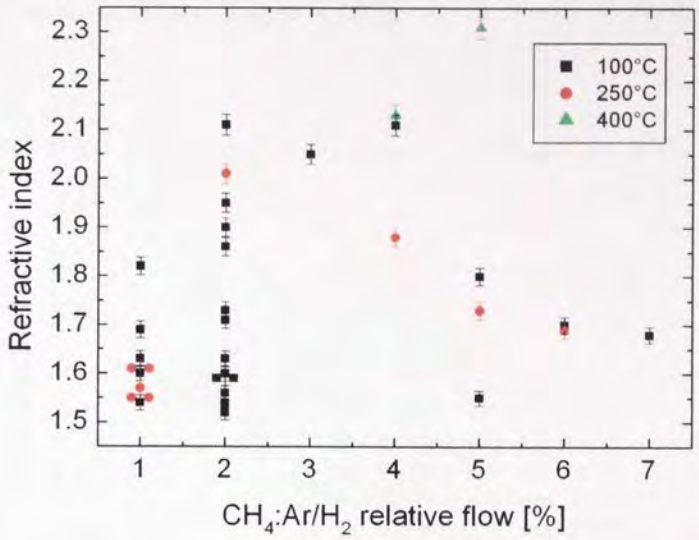

Figure 4.105 Refractive index against relative flow rate for films grown from methane and argon – 3% hydrogen mixture as carrier gas at different temperatures

As can be seen from Figure 4.104 and Figure 4.105 no real trends can be observed in the case of the films grown from methane with the CH_4:Ar and CH_4:Ar/H_2 relative flow. The large span of the results for the absolute value of the refractive index at the same relative flows can be explained by the variation of other plasma parameters during the deposition process, such as the source to substrate distance and the power injected in the plasma source.

4.2.8.2.2 Acetylene series

The films from the high power D series show an increasing trend of the refractive index with the C_2H_2:Ar relative flow, for films grown with acetylene injected via the ring (Figure 4.106)

In the case of films grown from acetylene with acetylene injected in the source nozzle and the argon – 3% hydrogen mixture as carrier gas a decreasing trend can be observed at low temperatures and a constant trend around the value 1.9 – 1.95 for medium and high temperatures. The decreasing trend is probably due to erroneous measurements performed with the ellipsometer. Some of these are likely to be close to the full cycle thickness or to

its maximum thickness limit, as would be suggested by the very high refractive index values measured on some films (Figure 4.107).

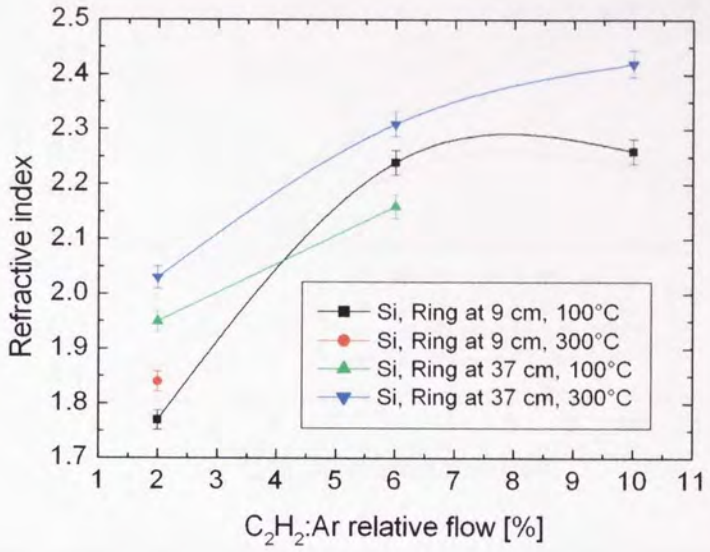

Figure 4.106 Refractive index against relative flow rate for films grown from acetylene and pure argon as carrier gas at different temperatures

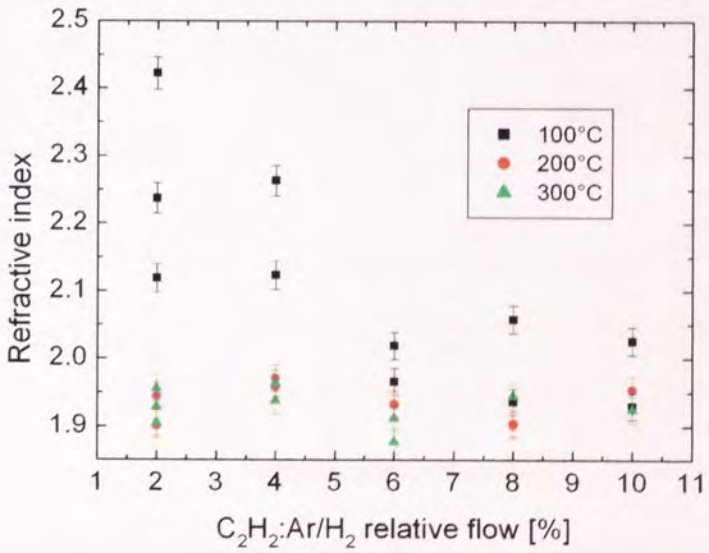

Figure 4.107 Refractive index against relative flow rate for films grown from acetylene and argon – 3% hydrogen mixture as carrier gas at different temperatures

4.2.8.3 Absorption vs. precursor flow

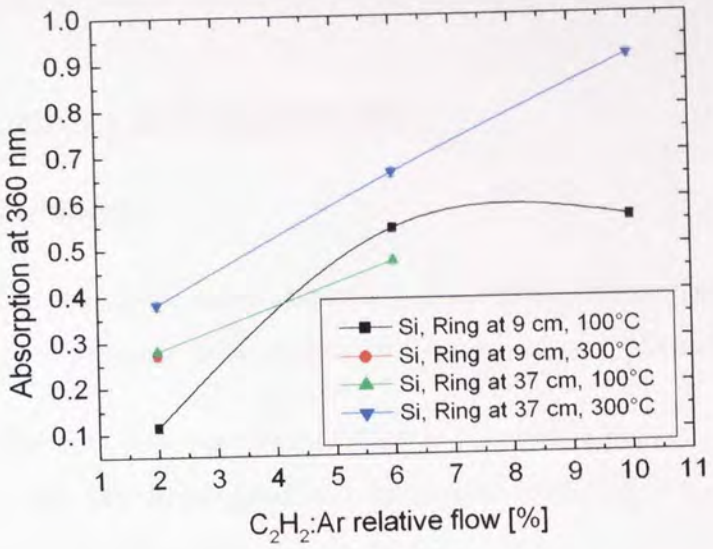

Figure 4.108 Absorption (K360) coefficient against C_2H_2:Ar flow for films grown from acetylene injected via the ring and pure argon as carrier gas at different substrate temperatures

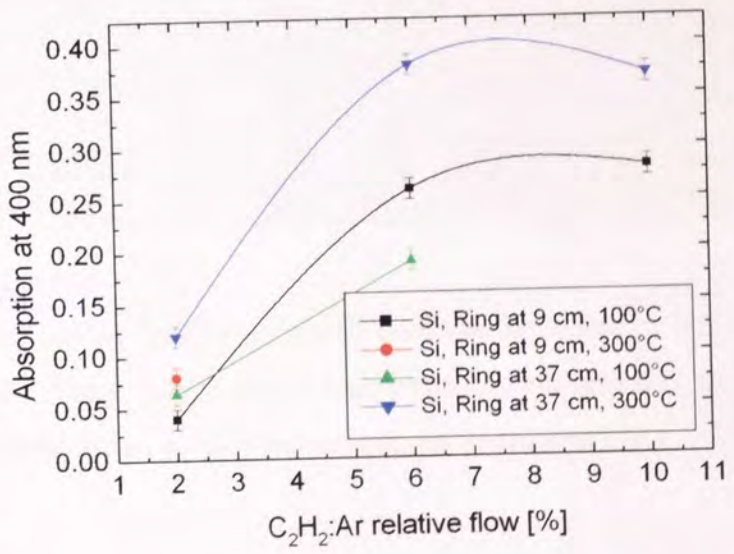

Figure 4.109 Absorption (K400) coefficient against C_2H_2:Ar flow for films grown from acetylene injected via the ring and pure argon as carrier gas at different substrate temperatures

The absorption was measured with the spectroscopic ellipsometer at OTB Engineering for selected samples from the high power D series (pure argon as carrier gas), on films grown from acetylene injected via the ring.

As can be seen from Figure 4.108 and Figure 4.109 the absorption is increasing with the relative C_2H_2:Ar flow. The absorption comes from the C-C bonds which are increasing with the relative flow, due to the increase in the density of the films.

4.3 Reproducibility and repeatability

4.3.1 Reproducibility

Reproducibility is one of the main principles of the scientific method, and refers to the ability of a test or experiment to be accurately reproduced, or replicated.

A series of experiments was reproduced, either in successive runs or in runs performed at different times. All the films produced in similar conditions revealed very similar properties, as shown in Table 4.4:

Table 4.4 Properties of deposited films in the same experimental conditions

Sample id	Rel flow [%]	Temperature [°C]	n	Sp^3 fraction [%]	Hardness [GPa]
D1	2%	100	1.89	70.7	4.5±0.8
D44	2%	100	1.91	73.2	4.8±0.9
D45	2%	100	1.90	70.7	4.6±0.8
D46	2%	100	1.86	70.7	4.2±0.9
D47	2%	100	1.90	74.4	4.7±1.0
D48	2%	100	1.90	74.4	4.9±0.8

The small differences in the film properties could be explained by either slight differences in the plasma chemistry, maybe due to a different contamination of the chamber walls, or by the experimental errors present in the analysis instruments (e.g. ~5% in the case of sp^3 fraction).

4.3.2 Repeatability

Repeatability is the variation in measurements taken by a single person or instrument on the same item and under the same conditions. A measurement may be said to be repeatable when this variation is smaller than some agreed limit.

The repeatability of the analysis instruments was tested many times, following the same analysis procedure and conditions when analysing different areas of the same sample. The results were always within the experimental errors. Some examples of these repeated analysis tests are presented in Table 4.5.

Table 4.5 Tests with various analysis techniques for repeatability check

Technique	Sample id	Experimental conditions	Results
Ellipsometry (refractive index n)	D77, area1	2% rel. flow, 100°C, nozzle injection	1.779
	D77, area2	2% rel. flow, 100°C, nozzle injection	1.780
XAES Sp^3 fraction [%]	D118, area1	6% rel. flow, 100°C, "ring up" injection	67.1±3.4
	D118, area2	6% rel. flow, 100°C, "ring up" injection	65.9±3.3
Nanoindentation Hardness [GPa]	D3, area1	6% rel. flow, 100°C, nozzle injection	8.7±1.5
	D3, area2	6% rel. flow, 100°C, nozzle injection	9.8±1.6

5 Modelling of plasma chemistry and film growth

This chapter presents an attempt to model the primary reaction in the ETP plasma and the growth mechanism of the amorphous hydrogenated carbon films on silicon. When the modelling was started it was already clear that acetylene was the better option for the precursor gas, and methane was ignored.

5.1 HyperChem® Release 5.1 Standard for Windows

HyperChem® [122 (p. 2)] is a molecular modelling and simulation program. The computational package offers many types of molecular and quantum mechanics calculations. The program runs under Windows and the user is able to build and display molecules, optimize the structure of molecules, generate and view orbitals, study the dynamic behaviour of molecules etc.

5.1.1 Structure of HyperChem

HyperChem consists of two basic components: a front end and a back end. The front end is what the user can see and what he interacts with. It provides a user interface to molecular modelling and provides the visualization of molecules and the results of computations. It is the molecular modelling component of HyperChem.

The back end is the component of HyperChem where molecular mechanical and quantum mechanical calculations are performed. It is the computational chemistry component of HyperChem.

Simply said the front end collects input from the user, initiates back end calculations, collects results from the back end, and then displays these results on screen or as log files.

The principal theory behind HyperChem is based on the concept of a potential energy surface which is a specification of the classical potential energy V (Figure 5.1). Energies and derivates of energy, such as forces on atoms, are necessary to build a potential energy surface. To find the stable structure means find the structure in which the forces on the

atoms are zero, i.e. calculate the local minimum of the potential energy surface [123 (p. 11)].

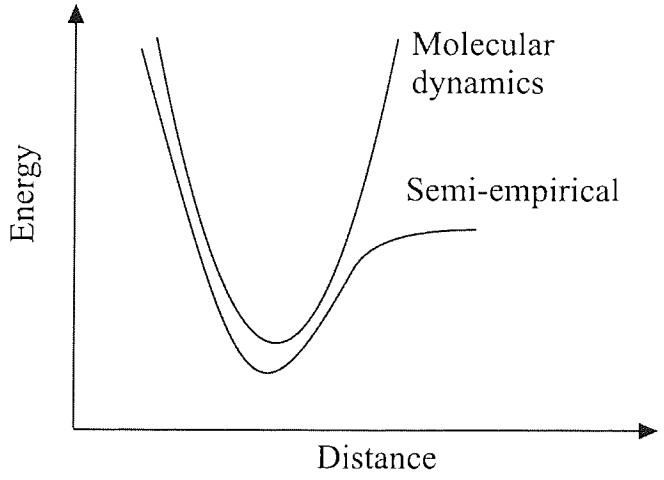

Figure 5.1 Potential energy V [after 123 (p. 132)]

5.1.2 Types of calculations

There are three types of calculations: single point, geometry optimization (minimization) and molecular dynamics [123 (p. 16, 132)].

5.1.2.1 Single point

A single point calculation performs a calculation at only a single point on the potential surface. The calculation provides the energy and the gradient of energy. Before single point calculation it is very useful to do a geometry optimization.

5.1.2.2 Geometry optimization

A geometry optimization samples single points on the potential energy surface and searches for local minimum. It is a starting point for molecular dynamics simulation.

5.1.2.3 Molecular dynamics

Molecular dynamics simulations calculate the future positions and velocities of atoms based on their current values. The motion of atoms follows Newton's laws. Molecular dynamics calculations provide information about thermodynamics and dynamic behaviour of molecules (kinetic energy, potential energy, total energy, temperature, time,

etc.). User's knowledge about experiment and molecular modelling are required for performing these simulations.

5.1.3 Calculation methods

HyperChem uses three types of methods in its calculations: molecular mechanics, semi-empirical quantum mechanics and ab initio methods. The first two methods belong to empirical methods [123 (p. 19)]. These can calculate values that are closer to experiment than ab initio methods. The accuracy of empirical method depends on the database used to parameterize the method (Figure 5.1)

5.1.3.1 Molecular mechanics

Molecular mechanics contain four force fields: MM+, AMBER, BIO+ and OPLS [123 (p. 83)]. Force fields use the equations of classical mechanics to describe the potential energy and physical properties of atoms that interact which each other by analytical functions (Figure 5.1).

5.1.3.2 Semi-empirical methods

Semi-empirical calculations combine quantum mechanical formulations with empirical parameters obtained from comparison with experiment (Figure 5.1). Semi-empirical methods are: Extented Hückel, CNDO, INDO, MINDO/3, MNDO, MDO/d, AM1, PM3, ZINDO/1 and ZINDO/S [123 (p. 92)].

5.1.3.3 Ab initio methods

Ab initio computations are based on quantum mechanics theory. Simulations are time consuming and require high computational power. HyperChem contains a database of basis sets (STO-3G, 3-21G, 6-21G, etc.) from which the user has to choose which one to use for calculations; then an optimization method must be chosen from the following: Polak-Ribiere, Stepest Descent, Fletcher-Reeves [122 (p. 211)]. Ab initio calculations can be used for limited numbers of atoms only.

After single point calculation in semi-empirical and ab initio mode, the user can compute and plot molecular properties such as electrostatic potential, spin and charge density.

5.2 Modelling of amorphous hydrogenated carbon growth

5.2.1 Short history on modelling DLC growth based on quantum mechanics

Molecular dynamic simulations have an important role to play in the determination of physical and electronic structure of DLC films [124, 125]. The most significant mechanism to identify is the deposition process. There are dual requirements of transferability and efficiency in modelling of the deposition process. In terms of transferability the preferred methods are those based upon density functional theory (DFT) where individual energetic ion arrive at a surface to build up a thin film in an atom-by-atom manner. These types of simulation require a considerable number of atoms ($\sim 10^3$) and long simulation times ($\sim 10^6$ steps) [126]. Most of the simulations refer to tetra amorphous carbon (ta-C), where no hydrogen is involved in the growth process.

The challenge in modelling DLC was, therefore, to find an interatomic potential capable of describing strained interactions, while remaining sufficiently efficient to allow the study of large systems and long time. Several transferable techniques in liquid-quench simulations have been applied. Local basis density functional (LBDF) and non-orthogonal tight-binding (NOTB) had success in describing the nature ta-C. Less accurate methods such as orthogonal tight-binding (OTB) and empirical potentials have provided a poor description of ta-C. Other important carbon simulation methods are the environment-dependent OTB approach and the tight-binding bond order (BOP), potential developed for hydrocarbons. However, the methods above neglect surface properties and formation mechanism; all attempts to model thin-film deposition have used one of these simpler techniques [126].

Environment-dependent interaction potential (EDIP) was created by Marks [126] and has satisfied both transferability and efficiency criteria for the first time. After that, first simulations of ta-C deposition have been made possible. EDIP has been derived by the inversion of ab initio cohesive energy curves of silicon [126]. Molecular simulations show that threshold energy below 10eV is required for the growth of ta-C films. These simulations are based on a model of surface insertion in which energetic burial leads to

the simultaneous processes of sp^3 promotion, densification, stress generation and surface growth [126].

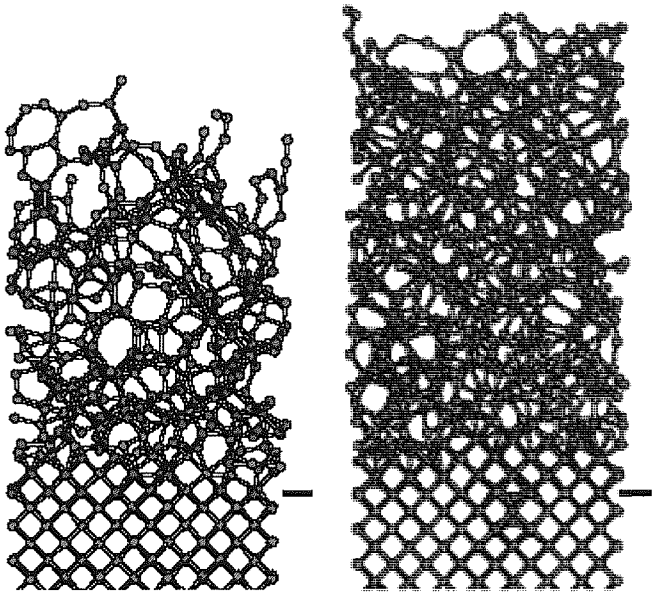

Figure 5.2 EDIP simulation of carbon thin film deposition with 1 eV atoms (left) and 70 eV (right) [126]

5.2.2 Modelling of diamond –like hydrogenated carbon films

The a-C:H film growth mechanism is much more difficult to model than the unhydrogenated case, but it is assumed that many similarities exist. At low impact energies it is probable that chemical processes may be the driving factor of the growth model, and this is why HyperChem program was used.

Recent studies have shown that the interaction between the Ar ions emerging from the plasma source and the acetylene molecules determines a complicated plasma chemistry leading to production specific radicals (C_3, C_3H, C_3H_2, etc.), important for the growth of good quality amorphous hydrogenated carbon films [48].

The modelling of a-C:H film growth on silicon substrates, presented in the following sections, is based on the plasma chemistry from these recent findings; it attempts to explain the formation of an sp^3 interconecting network between the incorporated carbon atoms.

5.2.2.1 Results and discussion

5.2.2.1.1 Computing the energy in PECVD chemical reactions

There are many possible reactions between argon ions and acetylene molecules (Figure 5.3). At low impact energy, which is the case for the cascaded arc plasma source, the most likely reaction is first a charge transfer reaction between the Ar ion and the acetylene molecule, followed immediately by a dissociative recombination.

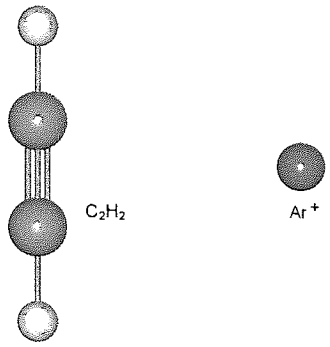

Figure 5.3 Acetylene molecule and argon ion [127]

The energies of formation have been calculated with HyperChem software. For calculations ab initio approach with basis set type of 3-21G was used. First, ionisation energy of argon ion was calculated, to compare it with the dissociation energy of acetylene.

$$Ar^+ + C_2H_2 \rightarrow Ar + C_2H_2^+ \qquad \textbf{Eqn 5.1}$$

$$Ar^+ + e^- \rightarrow Ar \qquad \textbf{Eqn 5.2}$$

The calculated energy was 14.8eV (341kca/mol). Gielen [3 (p. 66)] suggests that ionisation energy of argon is 15.75eV.

The dissociative recombination energy was calculated from the reaction:

$$C_2H_2^+ + e^- \rightarrow C_2H + H \qquad \textbf{Eqn 5.3}$$

It was found to be -5.1eV (-133.6 kcal/mol). For the same energy, measurements done by Gielen [3 (p. 67)] found a value of -5.3eV.

Negative or positive values of energy corresponds to exothermic reactions (heat is given out from the system) or endothermic reactions (heat is taken in by the system).

5.2.2.1.2 Simulations of interaction between radicals and simple C-Si surface

For simulations four typical species (C_2H, C_3, C_3H and C_3H_2) were used (Figure 5.4). According to the study done by Benedikt [48], C_3 radicals cause the fastest growth of a-C:H films. In the modelling of a-C:H films deposition, a carbon covered silicon surface was used to simulate interaction of radicals with a first layer of carbon atoms bonded to the silicon substrate during the deposition.

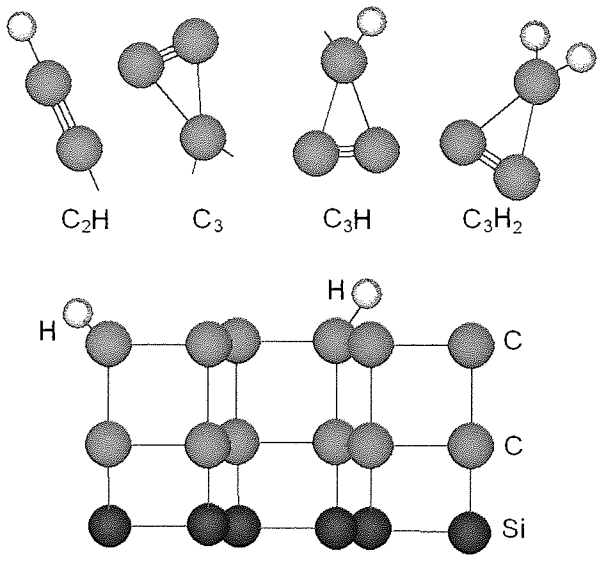

Figure 5.4 Four types of radicals used for simulation with a carbon covered silicon surface

In the first step a geometry optimization of each system was done and then molecular dynamics simulation (MD) with specific conditions was performed. For calculations semi-empirical method PM3 was employed. An example of a simulation is given in Figure 5.5. For each simulation a different velocity of the radical (5, 10, 50 and 100Å/ps) coming towards the surface was set up. Velocity of about 10Å/ps corresponds to the initial kinetic energy of radical E_{kin}=0.2eV, which was the energy measured by Langmuir probe close to the substrate region.

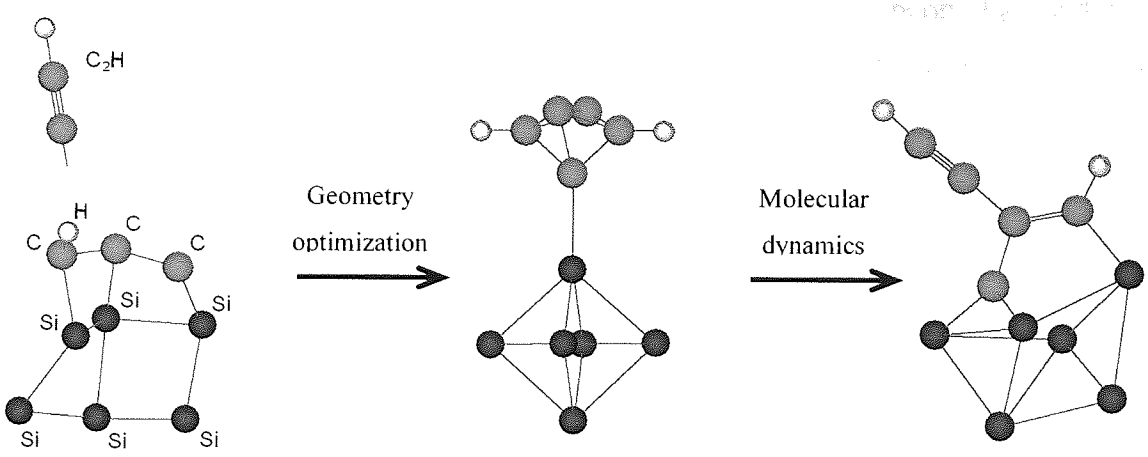

Figure 5.5 Simulation between C_2H radical and simple C-Si surface (MD: t=1ps, T=370K,v_{C2H}=10Å/ps)

After MD simulation the rearrangement of atoms was observed. The bond lengths in final configuration were: $C-C$ 1.45Å, $C=C$ 1.36Å, $C\equiv C$ 1.19Å, $C-Si$ 1.82Å, $Si-Si$ 2.65Å. These were compared with theoretical values ($C-C$ 1.43Å-graphite, 1.54Å-diamond, $C=C$ 1.34Å, $C\equiv C$ 1.20Å, $C-Si$ 1.70Å, $Si-Si$ 2.35Å) in an attempt to differentiate between the types of bonds created in the simulation.

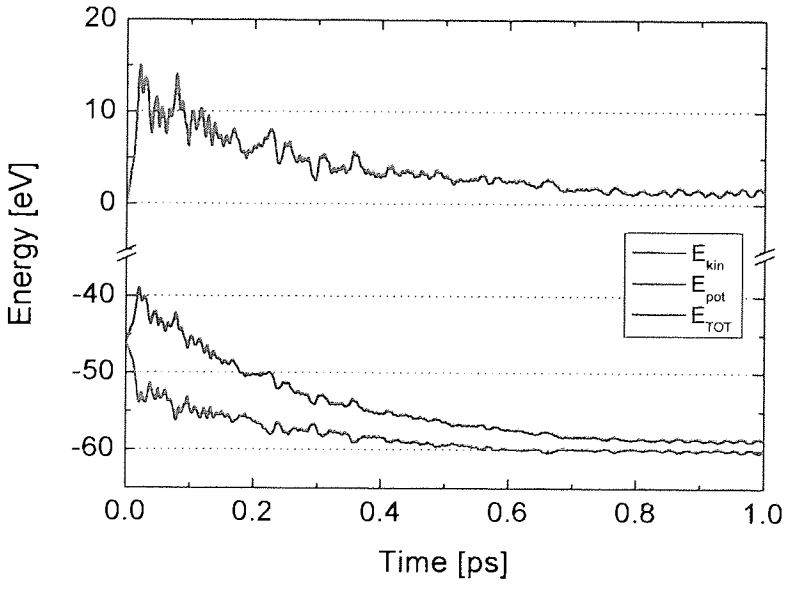

Figure 5.6 Time dependence of energy during MD simulation (v_{C2H}=10Å/ps, T=370K)

During the dynamics simulations kinetic energy E_{kin}, potential energy E_{pot} and total energy E_{TOT} of the whole system have been calculated. Time dependence of energy for the system with C_2H radical is shown in Figure 5.6.

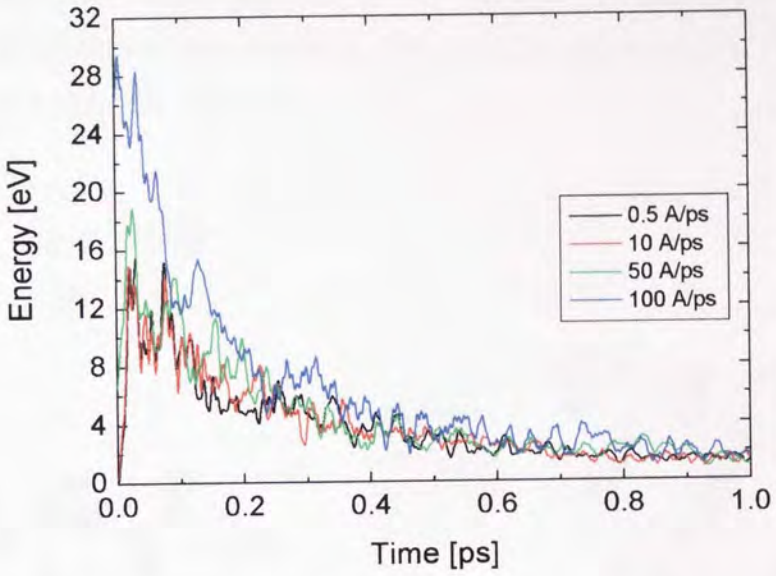

Figure 5.7 Time dependences of kinetic energy for system with C_2H radical (T=370K)

From the time dependences of kinetic energy (Figure 5.7) it can be seen that larger differences appeared in the beginning of simulations and from 0.8ps onward the kinetic energy of entire system saturated at 1 - 2eV.

Numbers of simulations for different radicals (C_2H, C_3 and C_3H) and simple surfaces have been performed for different conditions. Energy of entire system E_{TOT} is the sum of energies of each atom in the system:

$$E_{TOT} = \sum_{i=1}^{n} E_{ATOM_n} \qquad \textbf{Eqn 5.4}$$

From energies at the end of simulation and using Eqn 5.4 energies per atom have been calculated in each system. Energy per atom E_{ATOM} was in the range 4.2 - 4.8eV, in a relative good agreement with the energies computed by Marks (<10eV) [126]. After that, modelling of more complicated system was performed.

5.2.2.1.3 Modelling of radical deposition with large surface

First molecular dynamics simulation of a system where C_3 radicals coming towards the pure silicon surface was calculated (Figure 5.8). Conditions for MD simulation were t=1ps, T=363K and initial velocity of C_3 radicals 10Å/ps. After MD simulation rearrangement of atoms was observed. The bond lengths were $C-C$ 1.5Å, $C \equiv C$ 1.21Å, $C-Si$ 1.75Å, $Si-Si$ 2.65Å.

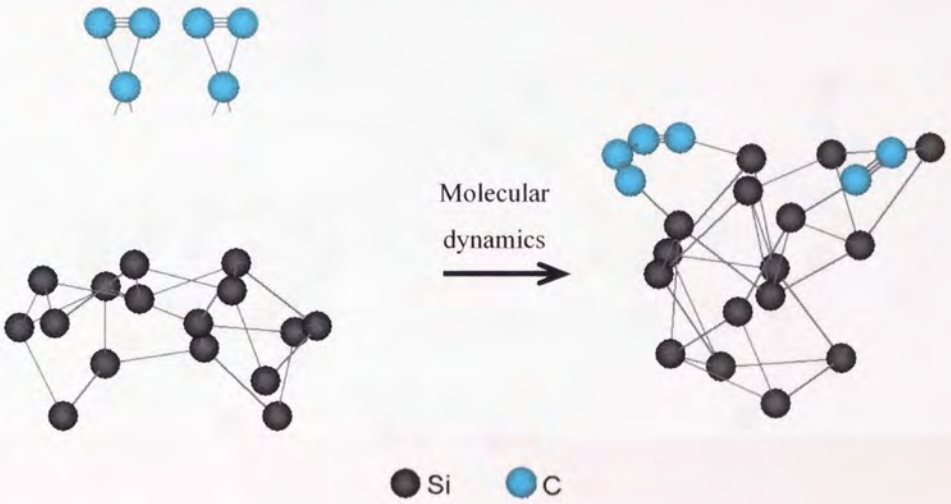

Figure 5.8 MD simulation of system with C_3 radicals and silicon surface (t=1ps, T=363K, v_{C3}=10Å/ps)

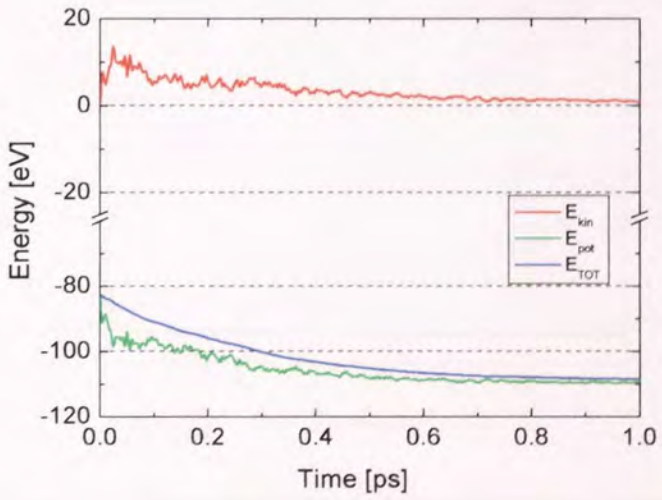

Figure 5.9 Time dependence of energy during MD simulation (v_{C3}=10Å/ps, T=363K)

Total energy E_{ATOM}=4.9eV at the end of simulation was calculated from time energy dependence in Figure 5.9 using Eqn 5.4.

Next simulation was done with the system composed of two C_3 radicals coming towards carbon-silicon surface (Figure 5.10). Conditions for MD simulation were t=15ps, T=363K, v_{C3}=10Å/ps. At the end of simulation the bond lengths in the final configuration of atoms were: $C-C$ 1.45Å, $C=C$ 1.32Å, $C-Si$ 1.73Å, $Si-Si$ 2.55Å.

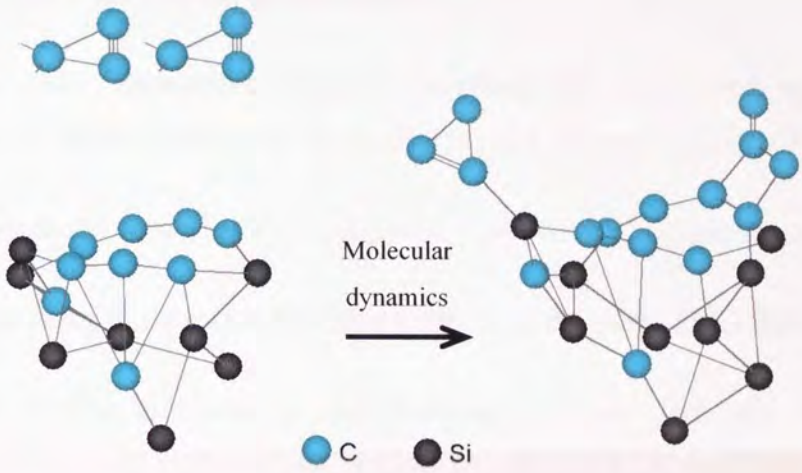

Figure 5.10 MD simulation of system with C_3 radicals and C-Si surface (t=1ps, T=363K, v_{C3}=10Å/ps)

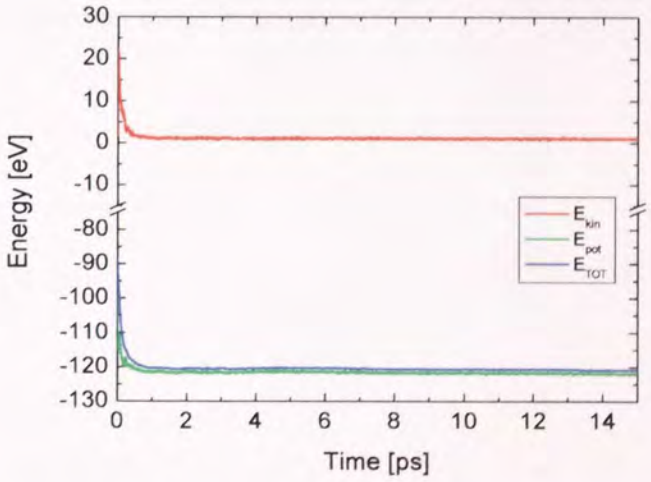

Figure 5.11 Time dependence of energy during MD simulation (v_{C3}=10Å/ps, T=363K, t=15ps)

Total energy of each atom E_{ATOM}=5.02eV and kinetic energy per atom $E_{ATOMkin}$=0.05eV at the end of simulation were calculated from time energy dependence in Figure 5.11 using Eqn 5.4. The energy saturates after 0.8 – 0.9ps from the start of MD simulation which suggests that an optimal time for the simulations is 1ps.

Modelling of more complicated systems, which should consider the formation of C-rings, as suggested by [128], was beyond the scope of this fundamental modelling study.

5.2.3 Summary of model predictions

- Ionization and dissociation energies computed are in a good agreement with experimental results provided by Benedikt [48] and Gielen [3 (p. 66, 67)];
- C-C sp^3 bonds are formed at low energies of about 4.2 - 5.2eV per atom;
- The energy of the system saturates after 0.8ps from the start of MD simulation;
- The bond lengths measured in carbon-silicon systems after MD simulation are: $C-C$ 1.47Å, $C=C$ 1.32Å, $C\equiv C$ 1.21Å, $C-Si$ 1.75Å, $Si-Si$ 2.60Å;
- One of the disadvantages of HyperChem modelling was that the simulations consumed a long time and required high computational power, so only systems with small number of atoms could be used.

6 Discussion

In the following chapter the results and the model of film formation is discussed. The chapter is divided into three different parts. In the first part the effect of the different parameters that were varied in the plasma deposition cell on the film properties is discussed. In the second part the mechanical, optical and chemical properties of the deposited films are compared. The section is divided into two different subsections, one for the films grown from methane and one for the films grown from acetylene, with the emphasis on the latter one. In the last part the model of film growth is considered.

6.1 Influence of plasma parameters on film properties

6.1.1 Energy of argon ions

Soft and hard amorphous hydrogenated carbon films were formed from methane and acetylene using a very low energy process. The cascaded arc plasma source produced argon ions with energies of 1 eV. At these energies, conventional electron impact ionisation could not take place. The only decomposition channel for the precursor gas could be via a charge exchange reaction between the argon ions and the precursor gas molecules, followed by a dissociative recombination with electrons, as seen in Chapter 2 (Eqn 2.5-2.8). The plasma chemistry was therefore controlled by the argon ions (ion induced chemistry), and not by the energetic electrons, which is the usual plasma chemistry for other deposition techniques (electron induced chemistry).

The radical production in the expanding plasma jet was a chemical process, dictated by the density of argon ions and electrons in relation with the density of precursor molecules. The energy of the formed radicals at the substrate level was too low (<0.5 eV) for any physical process, such as sputtering, subplantation, to be possible. The growth of the films took place from radicals, in the presence of a small fraction of radical ions, in a purely chemical process. It was thus a necessary condition to have very low argon ion energies in order to be able to grow the amorphous hydrogenated carbon using this process.

6.1.2 Effects of carrier gas and precursor gas

The carrier gas used in the plasma source had great influence mostly on the deposition rate. Films with similar properties were produced using both argon and argon – 3% hydrogen mixture. However, the films produced from argon – 3% hydrogen mixture were grown at much slower rates. This happened because the presence of hydrogen in the carrier gas drastically decreases the fraction of argon ions emerging from the plasma source as can be seen in the following reactions:

$$Ar^+ + H_2 \rightarrow ArH^+ + H$$
$$ArH^+ + e^- \rightarrow Ar + H^* \qquad \textbf{Eqn 6.1}$$

Thus there are fewer argon ions available for the dissociation of the precursor gas, and ultimately fewer active hydrocarbon radicals in the plasma jet. Additionally, the abundant presence of hydrogen in the plasma jet leads to etching of the film by atomic hydrogen, as seen in section 4.2.2.1.

In the later stages of the project the argon – hydrogen mixture was abandoned and all experiments were conducted with pure argon as carrier gas.

The precursor gas had great influence on the deposition rates and film properties. Films grown from acetylene were deposited at much higher growth rates compared to the films grown from methane under similar experimental conditions. There are two reasons for this. The first reason is that there are totally different chemistries in the plasma in the case of the two precursors. This is because the partial dissociation energy of methane and acetylene are different (4.30 eV [129] and 5.79 eV [130] respectively) and because the reactivity of the acetylene and methane with hydrocarbon radicals is different. This causes different growth mechanisms from the two precursors. Different reaction products are formed, with different sticking coefficients, from which the growth of the films takes place. The second reason is that, since methane has a C/H ratio of 1:4 (CH_4) compared to a C/H ratio of 1/1 present in acetylene (C_2H_2), more atomic hydrogen in released in the chamber in the case of methane; this recombines at the chamber walls to form hydrogen molecules [3 (p. 90)] that are reinserted in the plasma stream. They "consume" a

significant number of argon ions emerging from the plasma source and consequently lower the deposition rates, as seen from Eqn 6.1.

Half way through the project methane was abandoned as a precursor gas, because of the low deposition rates and the fact that the resulting films were too soft, with a hardness of 4 GPa, much less than a-C:H films produced from methane with other deposition techniques (sputtering, RF PECVD, etc), which are capable of producing films with hardness in the range 10-20 GPa.

6.1.3 Effect of precursor flow

In the next sections both growth models for films grown from methane and acetylene will be discussed. For simplicity the models will refer to only pure argon as a carrier gas. The argon – 3% hydrogen case results in similar processes in the plasma, but with a lower number of argon ions controlling the plasma chemistry.

6.1.3.1 Methane as precursor gas

In the case of methane as precursor gas this study revealed small differences between the film properties deposited at different methane to argon relative flows. This could be explained by the fact that the plasma chemistry is similar when the admixed CH_4 flow is increased.

It was assumed that in the charge transfer reaction between the argon ion and the methane molecule (Eqn. 2.7) all the energy of the argon ion was transferred to the methane ion. Thus the molecular ion CH_4^+ had an additional energy of 2.75 eV. This was the difference between the ionisation potential of Ar (15.75 eV [3 (p. 66)]) and the ionisation potential of methane (~13 eV [131]). This energy was realised when the dissociative recombination with an electron took place (Eqn. 2.9) or was further transferred to one of the dissociation products. A deposition model was proposed, based on the assumption that the first two channels are the most probable in Eqn 2.9.

A parameter F was defined, as in section 2.3.2, to be the flux of the precursor molecules divided by the flux of argon ions and electrons emerging from the plasma source:

$F = \frac{\Phi(CH_4)}{\Phi(Ar^+, e^-)}$. When the source was operating in underloading condition (F<1), the reaction products of Eqn 2.9 (CH_3, CH_2) were further dissociated by the surplus argon ions and electrons. This led to dissociation of methane into C and H atoms which deposit on the substrate with very low energies. The resulting films are polymer-like and of poor quality. When the source was operating in overloading conditions (F>1) two possibilities arose: either no further reactions took place between the excess methane molecules in the system and the dissociation products of Eqn 2.9 or, if further reactions happened, they led to products which do not deposit on the substrate. A rigorous study about the plasma chemistry from a cascaded arc source with methane as precursor gas had not been yet conducted, but the growth of the films probably takes place from CH_2 and CH_3 radicals in the presence of atomic hydrogen and possibly methane. This case led to soft amorphous hydrogenated films being formed, with little C-C sp^3 cross linking and with relatively high hydrogen incorporation.

6.1.3.2 Acetylene as precursor gas

Acetylene has an ionisation potential of 11.4 eV [48]. The additional energy transferred to the acetylene ion during the charge transfer reaction between the argon ion and acetylene molecule (Eqn. 2.5) is therefore 4.3 eV. This energy could be used to rearrange the geometrical structure of the $C_2H_2^+$ ion before the dissociative recombination reaction in such a way that it would favour the second dissociation channel from Eqn. 2.7, as suggested by [48]. In this way the production of CH radicals would exceed the production of C_2H in the dissociation of acetylene.

The relative flow of the acetylene to the argon flow was the parameter with the highest influence on film properties. This is because the chemistry of the plasma when acetylene is used as precursor gas is very different under different precursor load conditions, as seen in Chapter 2, section 2.3.2. At low relative flows there is no excess of C_2H_2 molecules present in the system and the reaction products from the dissociative recombination of acetylene ions are the ones that cause the film's growth: CH, C_2H, C_2, (see Eqn 2.7). They could be further dissociated by an excess of argon ions into C and H atoms. This case is similar to the growth from reaction products formed in case of low flow rates of methane;

hydrogen is abundant at the substrate level, due to the secondary dissociation of CH and C_2H. The sticking coefficients of the radicals formed are small, leading to low deposition rates and soft polymer-like films, similar to the ones obtained from methane.

When the relative flow is increased and the source is operated in overloading conditions (F>1) there is an excess of C_2H_2 molecules present. These molecules further react with the dissociation products of dissociative recombination reaction of acetylene (CH and C_2H), to form more radicals, such as C_3, C_3H, C_3H_2, C_4H_x, C_5H_x, C_6H_x in a complicated plasma chemistry, as discussed in Chapter 2 (Figure 2.45). From these species, it was found by [132] that C_3 and C_3H are the ones present in large densities at substrate level and contributed to the growth of hard, diamond-like amorphous hydrogenated carbon films.

These radicals incorporate into the growing film, in the presence of atomic hydrogen, to form a high cross linked C-C sp^3 network with low hydrogen content and low defect densities, due to the absence of energetic bombardment. The C_3 and C_3H radicals could exist in either linear or cyclic form [48], as can be seen from Figure 6.1. C_3 was found to have 5 times the density of C_3H at substrate level [48, 132], and was predicted to be the most important radical for growth. In addition, the two radicals can interchange in the following reaction:

$$C_3H + H \leftrightarrow C_3 + H_2 \qquad \textbf{Eqn 6.2}$$

Thus it is possible the relative density of these two radicals would change with the injection of acetylene in a different position, as it will be discussed later.

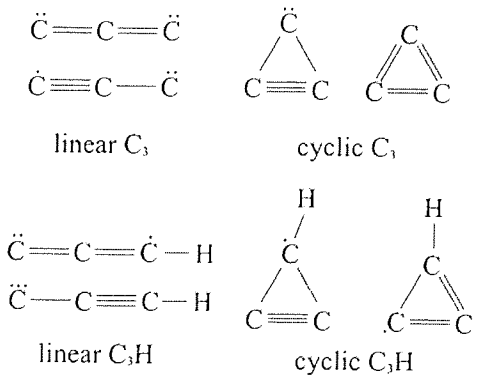

Figure 6.1 Linear and cyclic isomers of C_3 and C_3H radicals (after [46])

These radicals have very low energy when they incorporate in the growing film, as discussed previously. In addition, hydrogen has to be incorporated in the film, to maintain the film stoichiometry. Some C–C sp^3 bonds are already present in the cyclic isomers. They could incorporate directly in the growing film. The addition of hydrogen to other sp^2 C sites could supply enough energy to transform some of them into sp^3 sites. In this way a highly cross-linked network of sp^3 and sp^2 carbon and hydrogen atoms could be formed, which would confer a relative high hardness to these films. The growth rates and film quality are therefore dictated by the chemical processes at the substrate level.

6.1.4 Effect of substrate temperature

Substrate temperature during deposition affected the deposition rates as well as the film properties. Because the residence time of the neutrals at substrate level decreases with increasing substrate temperature [45], the sticking coefficient of the carbon species from which the growth takes place (CH_3 for methane; C_3 for acetylene, respectively) decreases also with increasing temperature [48]. This ultimately causes the deposition rate to decrease with increasing temperature. The decrease was more pronounced when methane was used as precursor gas. This can have two explanations. On one hand, the species responsible for growth in the case of methane and acetylene are different, so it is possible that the species formed from methane have lower sticking coefficients than the species formed from acetylene. On the other hand, there is more hydrogen present at the substrate level when methane is used. An increase in substrate temperature is known to enhance the etching rate of hydrogen, which can decrease the deposition rate [133].

In the case of films formed from acetylene the increase in substrate temperature affected somewhat the sticking coefficients of the species responsible for growth but also caused an increase in the release rate of hydrogen from the surface of the films, the resulting film being harder, with less hydrogen sp^3 bonded carbon but with higher average roughness as well.

Adhesion to the substrate was drastically influenced by the substrate temperature. Films deposited from acetylene showed the adhesion coefficient doubled when the deposition took place at high temperature (300°C), in comparison with a film deposited in similar

conditions, but at low temperatures (100°C). This was due to the fact that any remaining contaminants desorbed from the substrate surface with increasing substrate temperature, favouring a better cross-linking between film and substrate. Additionally, the extra thermal energy available at the substrate level was probably used for creating dangling bonds at the surface level, where radicals could add during the initial growth stage of the film.

6.1.5 Effect of process pressure

Process pressure had a moderate effect on deposition rate and an indirect effect on the film properties. With increasing process pressure the plasma jet became more confined. This is because more background carrier gas particles are present in the system at higher pressures, which increases the number of collisions at the source exit between the particles emerging from the source and the particles of the background carrier gas. Thus the area of the substrate that could be covered in the homogeneous film is reduced, which is not desired for industrial applications, where deposition on large area substrates is important. However, the net deposition rate increases with increasing process pressure, because of the increased density of the active radicals in the confined jet.

Most of the experiments with methane were performed at very high pressures (6 Torr), in an attempt to maximise the deposition rates. If the process pressure in the vacuum chamber exceeded a certain value (about 6 Torr) than the expanding jet changed shape from conical to cylindrical. The background gas could not be pumped at a constant rate and that caused the confined plasma jet to become unstable and wobble around the centre of the substrate. It is likely this was the reason for the ambiguous trends for these films and rather poor adhesion to substrate. Over time, the majority of these films either peeled off from the silicon substrates or absorbed water molecules from air. Exactly how this transformation took place is not fully understood, but it is believed that the polymer-like films formed from methane under high pressure conditions were not chemically passive and they reacted with water molecules or oxygen from the ambient air to form volatile products which then evaporated with time.

In the later stages of the project, when acetylene was used as a precursor gas, only the lowest possible pressures were used in an attempt to scale up the process for possible industrial applications.

6.1.6 Effect of source power

The power injected in the plasma jet was limited by the plasma source used. In the early stages of the project, when the initial copper version of the source was used, the maximum power injected in the plasma jet was limited by a maximum cathode current of only 50 amperes. In the later stages, after the copper plasma source was replaced with the improved molybdenum version, the maximum cathode current could be increased to 70 amperes.

The films properties were not greatly affected by power variations, the gain from the increased power being the higher deposition rates. At higher cathode arc currents more ions are produced in the plasma channel, which enhances the number of charge transfer and dissociative recombination reactions in the plasma. Thus more radicals important for growth (C_3) are available at the substrate level, which ultimately enhances the deposition rates.

The increase in cathode current did not affect ion and radical energies. However, in the later stages of the project the source was used only at maximum arc current (70A) and the resulting deposition rates were acceptable for industrial processing, even at substrate temperatures of 300°C.

6.1.7 Effect of precursor injection position

Different injection positions of the acetylene precursor gas were tried in the later stages of the project. Both deposition rates and film properties were affected by the injection position.

Initial injection in the nozzle of the source resulted in poor quality films, not adherent to substrates and with very high roughness due to a sooty material being deposited around the nozzle exit of the source. The abrupt increase in R_a roughness proved that these particles were transported by the plasma jet and incorporated into the depositing film.

Therefore, a special conical adapter was introduced between the source and vacuum chamber. This allowed the plasma back stream, formed next to the inner walls of the chamber, to reach and partially clean the source nozzle area. The quality of films improved, and big sooty particles did not incorporate in the films anymore. Still, the adhesion and hardness values were not satisfactory.

Insertion of acetylene through an injection ring brought an important improvement to film properties. When acetylene was injected with the ring situated at 9 cm away from the nozzle the deposition rates were similar to those obtained with injection in the nozzle. This was because the plasma chemistry remained very similar, acetylene being still injected outside the stream of the plasma jet and not very far from the nozzle injection point. However, this prevented completely the deposition of sooty particles around the nozzle area, which led to films with improved adhesion and lower surface roughness.

When acetylene was injected through the ring situated 37 cm away from the nozzle the deposition rates decreased. It was believed that this was due to the attenuation of the plasma jet by the injection ring. The reason was the small diameter of the ring, which caused it to be completely immersed in the plasma jet. This affected the geometry of the flowing plasma around the substrate level by reflecting a part of the active radicals towards the chamber walls. However, this lower injection position for acetylene showed an unexpected result. The films had higher hardness and elastic modulus than before. It was assumed that the plasma chemistry was affected by the change in acetylene injection position and the relative densities of the radicals at the substrate level changed consequently (C_3, C_3H, C_3H_2). This resulted in the deposition of harder material, at lower deposition rates. The films deposited at higher substrate temperatures and higher relative C_2H_2:Ar flows had now acceptable values for both adhesion and hardness (Figure 4.90).

6.1.8 Effect of in situ DC cleaning

One of the last improvements to be made to the set up was the employment of the DC air glow cleaning. The largest part of the experiments was performed without the in situ cleaning of the substrate. This was because in the early stages of the project the emphasis was more on producing films with good structural properties (high C-C sp^3 fraction, low

hydrogen content) at acceptable deposition rates (5 nm/s or more) and less on the mechanical properties.

In the later stages, when good quality films were produced from acetylene at high growth rates a clear difference was observed between adhesion of films produced at low substrate temperatures (<100°C) and adhesion of films deposited at higher substrate temperatures (300°C), i.e. the adhesion at high deposition temperatures was much better. Therefore, the in situ DC air glow discharge cleaning was introduced and it improved the adhesion of films deposited at low substrate temperatures to acceptable values (see Figure 4.95). The improvement was explained by a better cleanliness of substrates, which were now cleaned in situ and with high energy ions, without exposure to air between the cleaning and the deposition process.

One of the difficulties in comparing the adhesion of the films was the fact that they were of different thicknesses. A new factor for quantifying the adhesion was introduced, equal to the ratio of the critical loading to the film thickness. Films deposited in the same experimental conditions but of different thicknesses were compared. The results were consistent, but for future work the deposition time should be adjusted in such a way that all the films produced would have the same thickness. This would ease the set up of the hardness/scratch tests and the interpretation of results.

6.2 Correlations between film properties

6.2.1 Films grown with methane as precursor gas

Three films from the methane series were analysed by RBS/ERDA, as presented in Table 4.2. The densities, refractive index, hydrogen content and sp^3 of these films are compared in the next sections.

6.2.1.1 Film density and refractive index

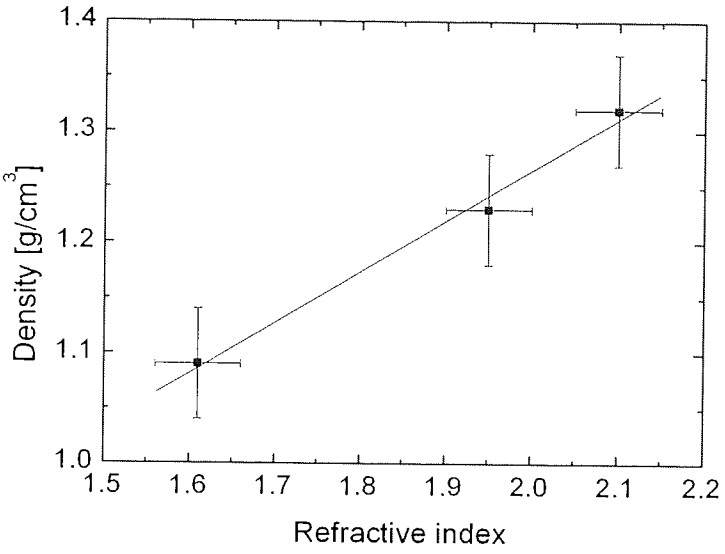

Figure 6.2 Film density against refractive index for methane series

The density of the three films from methane series was plotted against the refractive index, measured by the automatic ellipsometer. The results are presented in Figure 6.2. The carrier gas, relative flow and substrate temperature were different during deposition of these films. The substrate temperature can have an important role for the properties of these films, as was concluded from the Raman study. A small variation in the substrate temperature can cause the film to change their character, from soft amorphous to graphitic-like in this case.

Other differences, such as the different distance between the source nozzle and substrate (60 cm for first point, 33 for the second and third respectively) make a direct comparison between these films difficult.

However, some observations can be made. Firstly, there was a good correlation between the refractive index and density, as they almost fitted a straight line in the above graph. Secondly, the films deposited with pure argon as carrier gas were denser, even though the hydrogen incorporation was very similar for all three samples. This was a consequence of plasma chemistry combined with the substrate temperature effect. For example, in the case of the film grown with argon – 3% hydrogen it was likely that the growth take place

mainly from the CH_3 radical because the number of the argon ions emerging from the plasma was very low whereas in the case of the films grown with pure argon as carrier gas CH_2, CH, C, H and excess of CH_4 could also be present Moreover, the substrate temperature was increasing from the first to the third point in the above graph, which favoured the desorbtion of hydrogen. Even if the hydrogen content is similar in the three films, the radicals and their relative densities are likely to be different in the three cases. This would explain why density was different; thirdly, it should be noted that denser films do not necessarily mean harder films, since in the Raman study the third point showed an increase in its graphitic character compared to the second point. As was seen from the hardness analysis, all these films were soft (hardness < 4 GPa) and of low densities.

6.2.1.2 Film density and hydrogen content

It was expected that the measured densities will increase with decreasing hydrogen content. However, the RBS/ERDA analysis revealed the hydrogen content to be almost the same for the three different samples analysed, even though there were deposited under different experimental conditions. Thus, even though the film densities are slightly different, the differences can not be attributed to the hydrogen content (Figure 6.3), but more likely to a different growth mechanism for the three samples. The sample produced with argon – 3% hydrogen mixture had a lower film density, possibly due to the different densities of the radicals responsible for the films structure, as explained in the previous section. In this case the number of low energy argon ions available to decompose the methane molecules was low, because of their reactions with hydrogen, as discussed in section 6.1.2. This caused the radicals densities to decrease at the substrate level, and possibly changes in the relative densities of radicals, which resulted in lower deposition rates and films with lower densities.

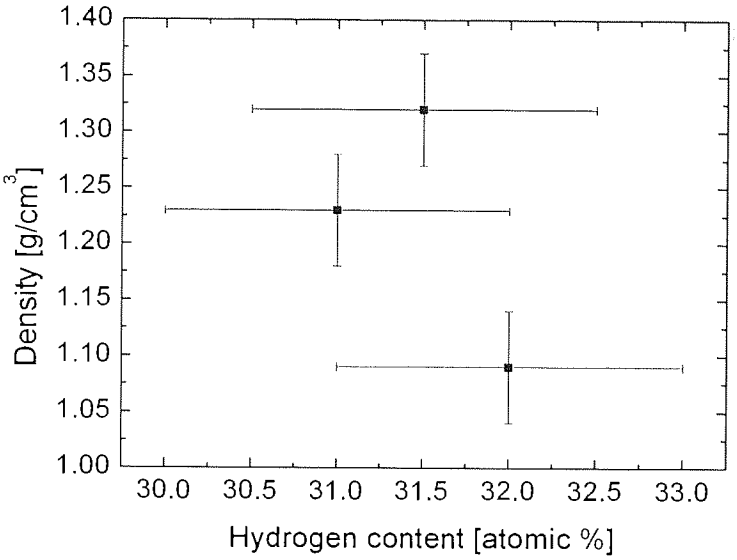

Figure 6.3 Film density against hydrogen content on films grown with methane as precursor gas and argon / argon – 3% hydrogen mixture as carrier gas

However, the differences in absolute values for film densities are small. This is because all the films formed from methane were either polymer-like, soft amorphous or graphitic-like films, with a maximum density of 1.35 g/cm^3, in good agreement with the sp^3 fraction and hardness measurements.

6.2.1.3 Film density and sp^3 fraction

No clear correlation could be found between the sp^3 fractions in the films and their measured densities. However, the decrease in sp^3 fraction from the far right to the far left points on the above graph at the same hydrogen incorporation and about the same density shows that discrete structural changes can happen in these soft amorphous carbon films, as revealed by the Raman study in Chapter 4, only by increasing the substrate temperature by 50°C. In this particular case a graphitisation of the films takes places, which can be observed by the decrease in sp^3 ratio, corresponding to an increase in sp^2 ratio. This can be explained by the following mechanism: the increase in temperature causes a decrease in the residence time of the neutral species present at the substrate level, modifying their relative densities; when the radicals chemically absorb into the growing film, the modified ratio between them does not favour the cross linking of C-C σ bonds, thus increasing the number of sp^2 bonds at the same hydrogen content.

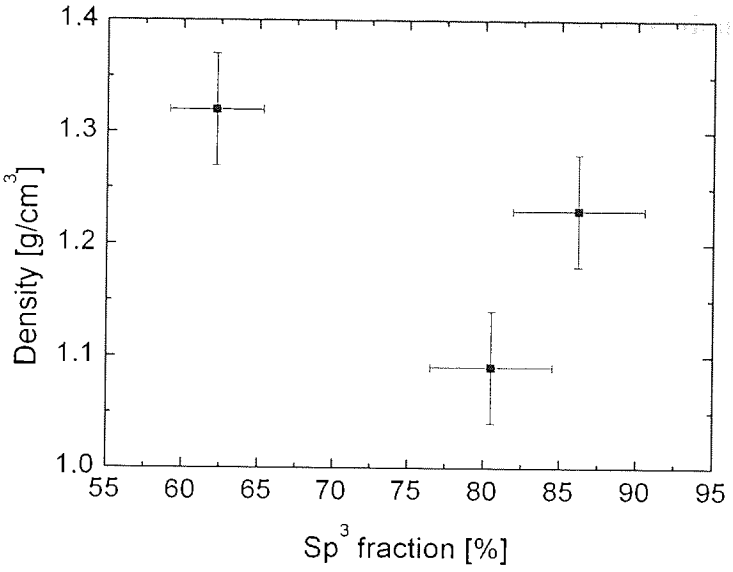

Figure 6.4 Film density against sp^3 fraction on films grown with methane as precursor gas and argon / argon – 3% hydrogen mixture as carrier gas

6.2.1.4 Hardness, sp^3 fraction and refractive index

Unfortunately, there was insufficient hardness data for the films grown with methane as precursor gas. Due to their deterioration with time the majority of films could not be analysed when the indentation/scratch tests became available, in the later stage of the project. However, indentation experiments were performed on five different samples deposited with pure argon as carrier gas (see Table 4.1), and the results are discussed below. The hardness for all these films was low. Taking into account the absolute errors for the hardness measurements there was little difference in the film properties for the films deposited from methane under different experimental conditions. A similar conclusion was reached from the Raman study also.

As was seen in the previous sections, there is a good correlation between the refractive index and film densities. However, no correlation could be found between the sp^3 ratio and density (refractive index). The mechanism of deposition is the one proposed in section 6.1.3.1.

All the films deposited from methane were considered either polymer-like, soft amorphous hydrogenated carbon or graphitic-like films. They all had low absolute values

for hardness and low film densities. The sp^3 ratios were rather high, which was expected for this type of films, with a high level of hydrogen incorporation. These films had similarities with the films deposited from acetylene in low relative flow conditions.

6.2.2 Films grown with acetylene as precursor gas

Three films from the acetylene series were analysed by RBS/ERDA, as presented in Table 4.3. The densities, refractive index, hydrogen content, sp^3 ratio and hardness of these films are compared in the next sections.

6.2.2.1 Film density and refractive index

The density of the three films from acetylene series was plotted against the refractive index, measured by the multiwave ellipsometer.

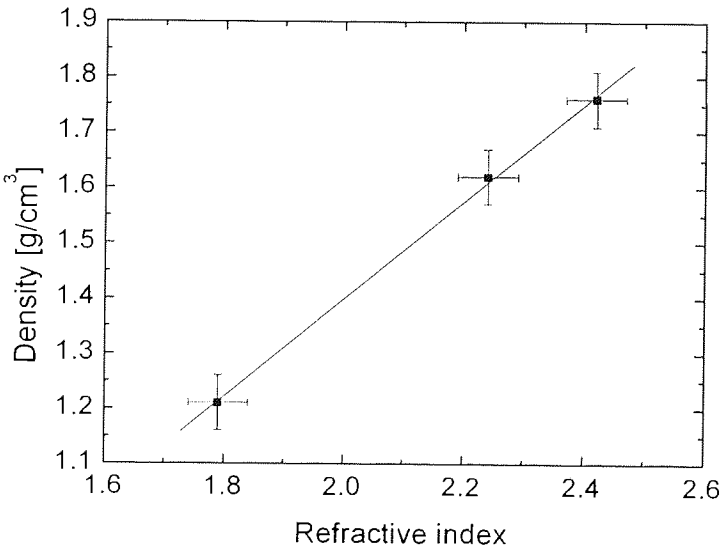

Figure 6.5 Density against refractive index on films grown with acetylene as precursor gas and argon as carrier gas

As can be seen from the Figure 6.5 there was an apparent linear correlation between the density of the films and refractive index, similar to the case of films grown from methane. A similar linear dependence was found by [134]. The relation is very useful because the density of the film can be estimated from the refractive index.

A linear relationship of the form $y = ax + b$ was deduced from the above graph, where $a = 0.92$ and $b = -0.46$. These coefficients were then applied to the data from the methane series. The calculated densities with the above formula were close to the experimental ones determined by RBS/ERDA. Therefore, from the limited number of RBS/ERDA experiment performed, it was concluded that measuring accurately the refractive index gives an indication about the density of the film, for either methane or acetylene. However, this relationship should be further investigated by determining film densities for other samples. Unfortunately, the access to the RBS/ERDA measurements was limited and only three samples from each series could be analysed.

Comparing the above relation with the results of [134] it was observed that the values only coincide at the lower refractive indexes (1.6-1.9), but differences were observed at the higher indexes. So the above relation is not universally valid.

6.2.2.2 Hardness and film density

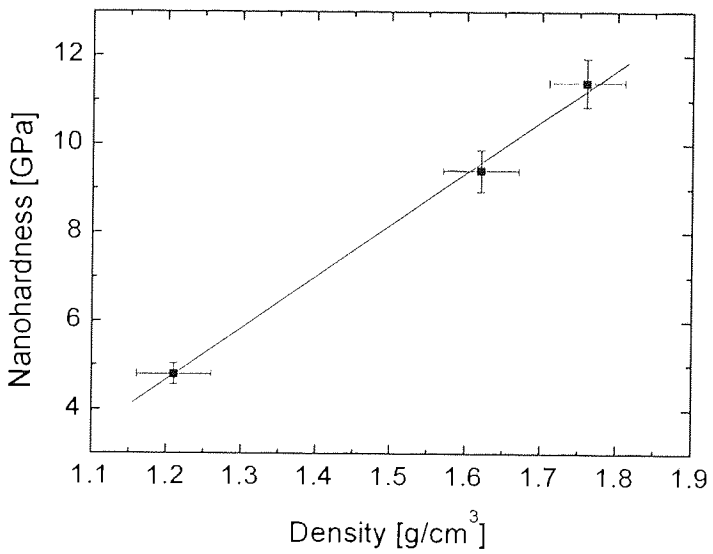

Figure 6.6 Nanohardness against density on films grown with acetylene as precursor gas and argon as carrier gas

Figure 6.6 shows a direct correlation between the measured nanohardness of the films and their measured densities. In the same way as in the previous paragraph a linear relation could be found between the two properties. In this way the density of the films can be

estimated from the above graph for a known hardness of the film. However, due to the limited number of samples analysed, this dependence should be further investigated. The mechanism behind this dependence would be: films with higher density had less hydrogen incorporated and an increased number of C-C sp^3 bonds, which caused the higher hardness.

The above dependence is not probable in the case of methane. Direct hardness measurements for the samples grown from methane for which the density was measured could not be performed, because the hardness test was not available at the time they were produced. However, the hardness tests performed retrospectively showed low hardness for the films grown from methane. It was then concluded, based on the limited data acquired, that the linear dependence of hardness with density is valid for the films grown from acetylene only.

6.2.2.3 Hardness and refractive index

From the previous two sections it was expected that a linear dependence would be found for hardness and refractive index, as shown in Figure 6.7.

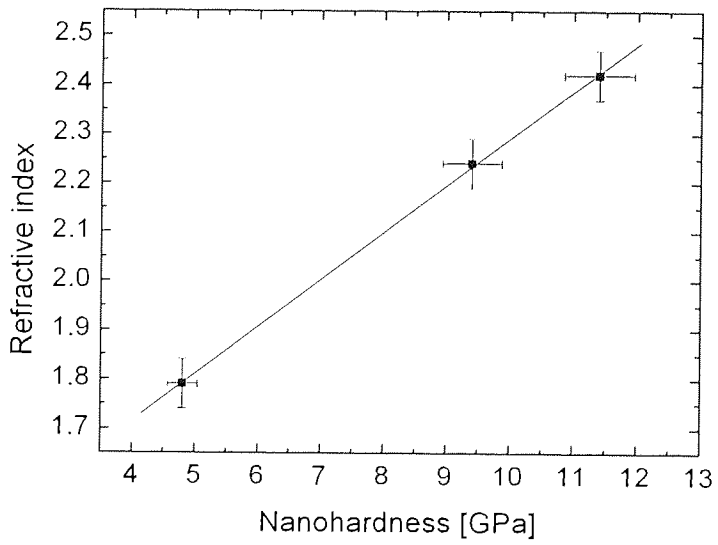

Figure 6.7 Refractive index against nanohardness on films grown with acetylene as precursor gas and argon as carrier gas

This relation is also specific to acetylene, and was not found in the case of films grown from methane. This apparent linear relation can be very useful also, because it would enable the estimation of the hardness of the film only from refractive index measurements, which can be produced quickly, compared to the long time required for a hardness measurement.

From the above discussion it may be possible to determine the density and refractive index, for a film grown from acetylene, from its nanohardness and vice versa. However, due to the limited access to RBS/ERDA equipment, the number of points analysed was not high enough to make a definite prediction on the above dependences and they should be further investigated. In the following sections, only the dependence of nanohardness with other film properties will be presented for the limited number of films analysed.

6.2.2.4 Hardness and hydrogen content

It was expected that harder films would form when less hydrogen is incorporated in the film. This is because the number of C-H sp^3 bonds should decrease with the decrease of hydrogen content. This general trend can be observed in the films grown with acetylene as precursor gas, as it is shown in Figure 6.8. However, the two points in the left hand side of the graph with very similar hydrogen content have different hardness. This is because of the different experimental condition used when producing the two films. But, even though the combination of the injection ring effect (different plasma chemistry) and the substrate temperature effect caused the hydrogen content to be similar, both these effects contribute to the higher hardness in the case of the film deposited with injection ring at 37 cm from the nozzle and at higher substrate temperature (sample D133 in Table 4.3).

As a general rule films with more hydrogen incorporated will be softer, but small differences are possible and the deposition parameters and mechanism has to be analysed with care in each case. A clear process dependant relation could not be established for these two parameters.

This apparent trend, showed in the above graph, was later confirmed by analysis of films produced after the end of this project, in the same deposition cell, but on larger area

substrates, where clear reduction of hydrogen content could be observed with the increase of nanohardness.

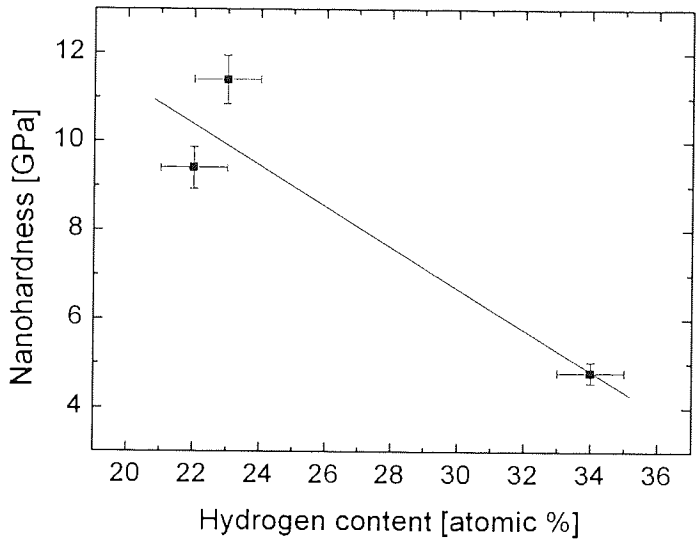

Figure 6.8 Nanohardness against hydrogen content on films grown with acetylene as precursor gas and argon as carrier gas

6.2.2.5 *Hardness and sp^3 fraction*

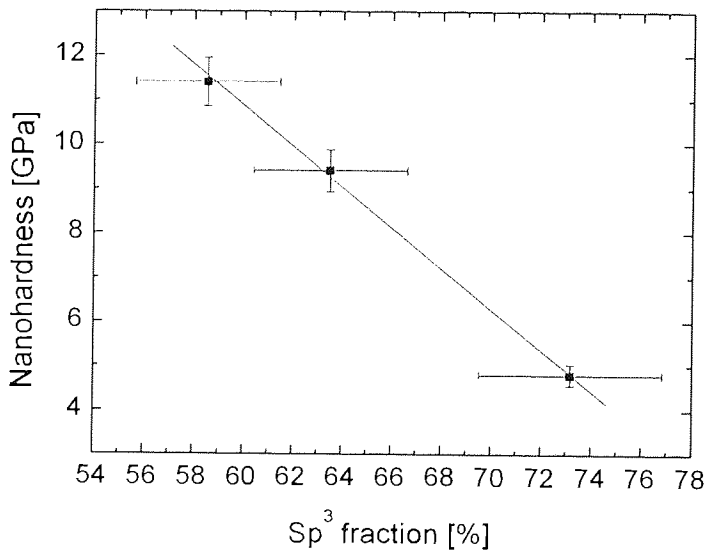

Figure 6.9 Nanohardness against sp^3 fraction on films grown with acetylene as precursor gas and argon as carrier gas

The sp^3 fractions shown in Figure 4.68 are higher than might be expected for this type of a-C:H film and this is due to the fact that XAES can not differentiate between C–C and C–H σ bonds. The sp^3 fraction varies inversely proportional with hardness, as it is shown in Figure 6.9. The dependence is apparently linear and can be explained as follows: at low C_2H_2:Ar flow ratio (2%) a large proportion of the sp^3 bonds come from polymeric C-H bonds, due to higher hydrogen incorporation in the film. These films are mainly polymer-like, with high sp^3 fractions but low hardness. As the C_2H_2:Ar ratio increases (6%), the total sp^3 fraction decreases due to a reduction of the amount of hydrogen in the film. This leads to a decrease in the number of polymeric C–H sp^3 bonds, whereas the increase in hardness suggests that the number of C–C sp^3 bonds has increased. Around this relative flow a saturation point is reached and at even higher C_2H_2:Ar flow ratio (10%) the variations in the sp^3 fraction and hardness are small. This result is in good agreement with the measurement performed by FTIR/RBS/ERDA, that showed an important decrease in the hydrogen content in the films from low C_2H_2:Ar flows (2%) to medium/high C_2H_2:Ar flows (6-10%) (see Figure 4.82).

It is known from literature that the process of plasma polymerisation results in polymers different in structure and composition from their classic analogues, grown from spin coating, spraying or evaporating processes [135] and that a complete fragmentation of the monomers is needed before the deposition process [136]. Yasuda [136] introduced a new parameter of wattage per molar mass and flow rate of monomer gas (W/MF). Low W/MF leads to partially undamaged monomer molecules and high W/MF to a nearly complete monomer fragmentation. When the growth of the polymer film takes place all fragments and atoms are arranged randomly by a statistical recombination process so that the structure of plasma polymers is quite different from real polymers. This explains why, in the case of the low flow regime, the films formed were polymer-like. The argon induced plasma chemistry led to partial or total decomposition of precursor gases into small fragments, which then incorporated into the growing films. In the medium and high flow regime, fragmentation of the precursor gas does not take place anymore and the films are softer or harder, depending on the precursor used.

The hardness and modulus measurements show that the best films are formed at C_2H_2:Ar relative flows higher than 6%. (Figure 4.89) There are small differences in the hardness of

the films deposited with acetylene injected at different positions (ring at 9 and 37 cm respectively), more clearly observed at high deposition temperatures (Figure 4.90). It was already discussed that the C_3 and C_3H radicals are the most important for the growth of hard amorphous hydrogenated films and it is known that their sticking coefficients decrease with increasing substrate temperature [48]. Also Eqn. 6.2 shows that these two radicals can easily interchange in the presence of atomic hydrogen. In this way the relative densities of these radicals can change with substrate temperature when they incorporate in the growing film. It was found that at a substrate temperature of 250°C the C_3 density is five time higher than C_3H. The dependence of their sticking coefficient is probably not linear. In this way, at low substrate temperatures, even though the densities could be higher in absolute values, their ratio may be different. Also, a little more hydrogen is incorporated in the films at lower temperatures, which would explain the small decrease in hardness.

Generally, the hardness is determined by the C–C sp^3 bonding and the amount of H in the films. However, a clear relation cannot be established between the three parameters in the case of hydrogenated amorphous films. For example, in films grown from acetylene, it is probable that under low relative flow conditions most of the hydrogen inserts into sp^3 C sites, as suggested by the deposition model. If is assumed that the number of C–H bonds is equal to the percentage of atomic hydrogen, it would be possible to subtract this ratio from the whole number of sp^3 bonds and deduce the number of C–C σ bonds. In the case of sample D111, for example, the sp^3 ratio was 75% (and thus sp^2 was 25%) and hydrogen content was 35% (atomic percentage). Subtracting the ratio of H bonded to sp^3 sites would leave a ratio of 49% for C-C σ bonds, almost double the sp^2 ratio. However, the indentation test shows hardness to be low (less than 4 GPa), so the film is polymer-like or soft hydrogenated amorphous carbon.

For the films with diamond-like character, deposited at medium and high relative flows, the hydrogen was probably inserted into sp^2 as well as sp^3 sites. A clear separation of the C–H and C–C sp^2 and sp^3 bonds was more difficult. However, the ratio between pure carbon σ bonds (sp^3) and π bonds (sp^2) was close to 1.5–1.7 in this case. Thus, even

6.2.2.7 *Differences for films deposited on plastics*

The plastic substrates (PET, PEEK) showed a different behaviour from the silicon and glass when they were analysed with the indenter/scratch test. The indentation curves did not have the same shape as before. The measured hardness and reduced modulus were significantly lower for the films deposited on plastic substrates, which suggests that the substrate contribution is still important for these hard films on soft substrates. It is likely that the substrate may plastically deform before the film does, which will affect the measurements performed [137]. One solution would be to further reduce the indentation depth to less than 10%, but this is difficult to do for thin films, where a practical lower limit of 10-15 nm for the indentation depth exists. Another possible solution would be to model the deformation process and try to extract the mechanical properties of the film, knowing the mechanical properties of the substrate.

The scratch tests for films deposited on plastics were completely different to the pattern observed on silicon or glass substrates. A critical loading value could not be determined, because the substrate was deforming before the critical loading was reached. A solution would be to use a different type of adhesion test for these softer substrates, such as a tape test.

6.3 Modelling of the film growth

As presented in Chapter 5, a growth model based on chemical interactions was developed for the first few layers of depositing hydrocarbon radicals. The model showed that C-Si bonds and sp^3 and sp^2 bonds can be formed at these low deposition energies, and was able to distinguish between the sp^1, sp^2 and sp^3 configurations of carbon by measuring the length of the formed bonds.

However, the model had several disadvantages. The number of molecules that could be used with HyperChem was limited by the long simulation times and the high computational power required. This causes differences between the experimental conditions and simulation. Moreover, after the simulation only few atomic layers were grown and the thickness of the simulated film is only few angstroms, whereas in

experiments it was hundreds of nanometres. Thus the properties of the two films cannot be directly compared. The model needs further development to try to include more radicals and to better reproduce the experimental conditions.

A solution would be to start from a ratio of 5:1 C_3 to C_3H radicals and send them simultaneously towards the geometrically optimised silicon surface. This step should be them repeated until the growing layer has a thickness of at least few nanometres. Then the same procedure could be repeated with a ratio of 10:2 and even 15:3 C_3 to C_3H radicals and the differences observed. However, this would require a much better processor–memory package, as well as an upgrade of the software version used, which allowed only a limited number of radicals to be used in the dynamic modelling.

The thesis gives an overall picture of the deposition mechanisms and film properties in the case of methane and acetylene. It confirms the main findings investigated by Gielen [3 (p. 16)], such as the improvement in films' quality with increasing acetylene relative flow from polymer-like to diamond like properties. However, the present study gives a much more detailed analysis of the films' properties with the different injection points of the precursor gas, the process pressure and substrate temperature, as well as with the relative precursor flow; it also investigates the properties of much thinner films compared to the ones used in Gielen's work, which could be used in various novel technical applications. Also, with the help of Benedikt's work [132], the growth mechanism is better understood in the case of acetylene and subsequently methane. The thesis also gives further insight into the reasons why films deposited from methane were of poor quality and suggests some ways forward to overcome the current problems, such as weak adhesion. Due to the reasons detailed above, it can be considered an advance over the previous work done in the field of low energy deposition of amorphous hydrogenated carbon films.

7 Conclusions and further work

This thesis is dedicated to the production and analysis of thin hydrogenated amorphous carbon films. A cascaded arc plasma source was used to produce a high density plasma of hydrocarbon radicals that deposited on a substrate at very low energies. The work was intended to create a better understanding of the mechanisms responsible for the film formation, by an extensive analysis of the properties of the films in correlation with the conditions used in the plasma cell.

Two different precursors were used, e.g. methane and acetylene and they revealed very different mechanisms of film formation and film properties. Methane was less successful, and the films formed did not differ very much in character and properties. Acetylene was a better option, and in this case the plasma parameters could be tailored to change the character of films, from polymer-like to diamond-like carbon.

7.1 Testing sources

Multiple tests were performed on the cascaded arc plasma source, in order to asses the best parameters and configuration that would allow the source to operate more efficiently and to become more reliable. Several conclusions were reached from these tests:

i. The 4 mm channel plasma source was easier to operate and overall better than the 3-mm channel source

ii. The best distribution of the ion density profile, desired for homogeneous deposition of large area substrates, was obtained in the low flow regime, at 2.5 slm Ar flow

iii. The improvements in the materials from which the source was made and in the cooling water system made the source more reliable and able to sustain higher powers, which increased the degree of ionisation in the plasma

iv. The improvements in the design of different parts of the source made it more reliable to be used frequently, with a high number of ignitions during a short time or to be operated at maximum power over longer periods of time.

7.2 Deposition from methane

Films deposited from methane as precursor gas were soft, with poor adhesion to the substrate and decomposed with time. Several conclusions have been reached regarding the properties of these films in correlation with the cell parameters. A deposition model was proposed.

i. Deposition rates were low in absolute values and decreased with the increase in hydrogen content in the carrier gas and with the increase in substrate temperature; they increased with the increase of process pressure and source power.

ii. Deposition at very high process pressures resulted in high deposition rates, but the films formed had poor quality and ambiguous trends.

iii. The average roughness (R_a) did not show clear trends with variation of substrate temperature, precursor flow, process pressure or carrier gas used; the absolute values were generally lower than 4-5 nm.

iv. The sp^3 fraction did not show clear trends with variation of precursor flow, process pressure, carrier gas used or substrate temperature up to 350°C; the absolute values were between 75 – 90% and decreased to 50-60% in the case of films deposited at substrate temperatures of 350°C or more.

v. Hydrogen content was similar for the selected samples analysed and was assumed to be relatively high in all deposited films (more than 30%)

vi. The hardness and elastic modulus of the few selected samples analysed was low, which suggests that these films are either polymeric-like or graphitized.

vii. Refractive index correlated well with film density, based on the limited data acquired by RBS/ERDA; Refractive index values were low for films deposited at

low substrate temperatures and low flows and increased with the increase of substrate temperature and precursor flow.

A deposition mechanism was proposed, based upon the reaction product of the dissociative recombination of CH_4^+. There were small differences between the chemistries in the plasma at low and high precursor flow rates and substrate temperatures, all leading to formation of polymer-like films.

7.3 Deposition from acetylene

Films deposited from acetylene as precursor gas were harder, with better adhesion to the substrate and stable with time. Different substrates were tried, such as silicon, glass and plastics. The deposition process was scaled up to large area substrates. A deposition model was adopted and discussed.

i. Deposition rates were an order of magnitude higher in absolute values compared with deposition rates measured for films grown from methane; the deposition rates decreased with the increase in hydrogen content in the carrier gas, with the increase in substrate temperature and with lowering the injection position for acetylene; they increased with the increase of precursor flow rate, process pressure and source power. At high precursor flow rate and substrate temperature, with argon/hydrogen mixture as a carrier gas no films were deposited.

ii. Similar film properties were measured in the case of films produced under DC bias conditions, probably due to the insulating properties of these films and the small fraction of ions present at substrate level

iii. The average roughness (R_a) increased with the increase of the precursor flow rate and with the increase of substrate temperature, but did not depend of the precursor gas used. The absolute R_a values were generally lower than 1-2 nm for low temperature deposition.

iv. The sp^3 fraction decreased from low to medium/high precursor flow and with increasing substrate temperature, due to a decrease in the hydrogen incorporation.

v. The hydrogen content decreased with the increase of precursor flow rate and substrate temperature. This decrease was more pronounced for films deposited with injection ring situated at 9 cm from the nozzle

vi. The hardness and elastic modulus of the films were inverse proportional to the sp^3 ratios; they increased from low to medium/high precursor flows. Films deposited at low precursor flows were polymeric (soft hydrogenated amorphous carbon), whereas films deposited at medium/high flows were diamond-like (hard hydrogenated amorphous carbon).

vii. Based on the limited RBS data the refractive index and film density correlated linearly with hardness; they increased with the increase in precursor gas flow rate and with the increase in substrate temperature.

viii. Absorption coefficient correlated well with the refractive index and showed relative high values for the hard hydrogenated amorphous films.

ix. Injection position of the precursor gas showed differences in the properties of the deposited films; the best films were grown with the ring situated at 37 cm from the source nozzle, at higher substrate temperatures (300°C).

x. DC air glow cleaning improved adhesion of films deposited at low temperatures to acceptable values, similar to the ones recorded at high temperatures.

A deposition mechanism was proposed, based upon the reaction product of the dissociative recombination of $C_2H_2^+$. There were large differences between the chemistry in the plasma at low and medium/high precursor flow rates. This corresponded to large differences in film properties from low to medium flow rates, when films change their character form polymer-like to diamond like, whereas the differences between films deposited at medium and high precursor flow rates were small.

Modelling of the film growth on silicon substrates was initiated and explained the formation of sp^2 and sp^3 bonds at these low energies. However, further improvements to the model are needed.

7.4 Further work

Further work should concentrate on improving the deposition cell and analytical tools/tests. For the industrial implementation of these films, large area substrates will have to be coated.

A new version of the substrate holder – shutter assembly should be built to be able to accommodate homogeneous deposition of larger substrates. A higher pumping speed system will be needed, to lower the process pressure. Films should be deposited from acetylene using similar conditions as in the above study and increasing further the precursor flow rate.

Another improvement to the deposition cell could be the RF biasing of the substrate holder. This is expected to increase energies of depositing radicals and further improve the adhesion and possibly the hardness of films. The RF bias will be applied after acetylene is dissociated and the plasma chemistry is stabilised. However, it is possible that the biasing will have little effect or even damage the films and it may have to be used only in the early stages of deposition, to increase the ions energy (and hence adhesion) and then switched off, to preserve the low energy processes occurring in the plasma.

A doped layer could be grown on the top of the hard films to improve the friction and wear properties of the films. An ideal candidate for doping would be fluorine, easy to be inserted in the system from CF_4 precursor [3 (p. 124)].

The analytical tests could be improved by modifying the Hiden Langmuir probe/Mass Energy Analyser to be able to take measurements in the deposition environment. This would give further insight to species, relative densities and energies in the plasma during growth.

Another improvement could be a tape type adhesion test, which could compare adhesion between the films deposited on different substrates (including plastics).

Furthermore, a nanotribometer would be useful to perform quick friction/wear tests on the film surface and reproduce accurately the conditions from the environment the films are to be used in.

References

[1] S.R.P. Silva, *Properties of amorphous carbon*, Institution of Engineering and Technology, 2002, p. 3.

[2] J. Robertson, *Diamond-like amorphous carbon*, Materials Science and Engineering, R 37 (2002) 129–281.

[3] J.W.A.M. Gielen, *Plasma beam deposition of amorphous hydrogenated carbon*, PhD Thesis, Technical University of Eindhoven, 1996.

[4] H.O. Pierson, *Handbook of Carbon: Graphite, Diamond and Fullerenes: Properties, Processing and Applications*, Wiliam Andrew Publishing, 1994.

[5] http://www.azom.com/details.asp?ArticleID=1630#_Key_Properties

[6] A.J.M. Buuron, *Plasma deposition of carbon materials*, PhD Thesis, Technical University of Eindhoven, 1993.

[7] http://www.anatechltd.com/Diamond_Coating/default.html

[8] A. Erdemir, *The role of hydrogen in tribological properties of diamond-like carbon films*, Surf. Coat. Technol. 146-147 (2001) 292–297.

[9] W. Jacob and W. Moller, *On the structure of thin hydrocarbon films*, Appl. Phys. Lett. 63 (1993) 1771–1773.

[10] E. Nasser, *Fundamentals of Gaseous Ionisation & Plasma Electronics*, Wiley, 1971.

[11] http://www.allaboutspace.com/subjects/astronomy/glossary/indexp.shtml

[12] R.L. Layberry, *Computer simulation of Radio-Frequency methane/hydrogen plasmas and their interaction with GaAs surfaces*, PhD Thesis, Aston University, 1999.

[13] Y. Xiang et al., *Investigation on preparation and properties of thick DLC film in medium-frequency dual-magnetron sputtering*, Vacuum 80 (2005) 324–331.

[14] K. Bewilogua et al., *DLC based coatings prepared by reactive d.c. magnetron sputtering*, Thin Solid Films 447 –448 (2004) 142–147.

[15] N. Savvides and B. Window, *Unbalanced magnetron ion-assisted deposition and property modification of thin films*, J. Vac. Sci. Technol. A 4 (1986) 504-508.

[16] K.E. Cooke et al., *The industrial application of pulsed DC bias power supplies in closed field unbalanced magnetron sputter ion plating*, Surf. Coat. Technol. 177–178 (2004) 789–794.

[17] X. Ding et al., *Ion beam assisted deposition of diamond-like nanocomposite films in an acetylene atmosphere*, Thin Solid Films 345 (1999) 82–85.

[18] J.J. Cuomo et al, *Sputter deposition of dense diamond-like carbon films at low temperature*, Appl. Phys. Lett. 58 (1991) 466–468.

[19] J. Hao et al., *Effect of deposition pressure on microstructure and properties of hydrogenated carbon nitride films prepared by DC-RF-PECVD*, Journal of Non-Crystalline Solids 351 (2005) 3671–3676.

[20] M. Weiler et al., *Preparation and properties of highly tetrahedral hydrogenated amorphous carbon*, Phys. Rev. B 53 (1996) 1594-1608.

[21] M. Weiler et al., *Deposition of tetrahedral hydrogenated amorphous carbon using a novel electron cyclotron wave resonance reactor*, Appl. Phys. Lett. 72 (1998) 1314–1316.

[22] A.A. Voevodin et al., *Comparative study of wear-resistant DLC and fullerene-like CNx coatings produced by pulsed laser and filtered cathodic arc depositions*, Surf. Coatings Tech. 197 (2005) 116–125.

[23] D.-J. Jan et al., *Deposition of nitrogen-containing diamond-like carbon films on acrylic substrates by an ion beam process*, Vacuum 74 (2004) 531–538.

[24] J. Franks, *Properties and applications of saddle-field ion sources*, J. Vac. Sci. Technol. 16 (1979) 181-183.

[25] Gh. Popa, *Plasma Physics*, "Al. I. Cuza" University Publishing House, Iasi, 2000 (In Romanian).

[26] Jonathan B. Wills et al., *Number density and temperature of acetylene in hot-filament and arc-jet activated CH_4/H_2 gas mixtures measured using diode laser cavity ring-down absorption spectroscopy,* Diamond Relat. Mater. 12 (2003) 1346–1356.

[27] N.P. Rao et al., *Hypersonic plasma particle deposition of nanostructured silicon and silicon carbide*, J. Aerosol. Sci. 29 (1998) 707–720.

[28] Stephane Mazouffre, *Transport Phenomena in Plasma Expansions Containing Hydrogen,* PhD Thesis, Technical University of Eindhoven, 2001.

[29] S.E. Selezneva et al., *Stationary supersonic plasma expansion: continuum fluid mechanics versus direct simulation Monte Carlo method*, J. Phys. D: Appl. Phys. 35 (2002) 1362–1372.

[30] M.C.M. van de Sanden, J.M. de Regt and D.C. Schram, *The behaviour of heavy particles in the expanding plasma jet in Argon,* Plasma Sources Sci. Technol., 3 (1994) 501–510.

[31] R.F.G. Meulenbroeks et al., *The argon-hydrogen expanding plasma: model and experiments,* Plasma Sources Sci. Technol., 5 (1995) 74–85.

[32] J.J. Beulens, M.J. de Graaf and D.C. Scham, *Axial temperatures and electron densities in a flowing cascaded arc: model versus experiment,* Plasma Sources Sci. Technol., 2 (1993) 180–189.

[33] K.T.A.M. Burm, W.J. Goedheer and D.C. Schram, *Simulations of geometrically pinched argon plasmas using an extended one-dimensional model*, J. Phys. D: Appl. Phys. 34 (2001) 2000–2015

[34] M.C.M. van de Sanden, J.A. Tobin, *The expanding thermal arc plasma: the low-flow regime*, Plasma Sources Sci. Technol. 7 (1998) 28–35.

[35] K. Yamamoto et al., *The sp^3 bond fraction in carbon films prepared by mass-separated ion beam deposition*, Diamond Relat. Mater. 10 (2001) 895–899.

[36] Y. Lifshitz, S.R. Kasi, J.W. Rabalais, W. Eckstein, *Subplantation model for film growth from hyperthermal species*, Phys. Rev. B41 (1990) 10468-10480.

[37] H. Hofsass, H. Feldermann, R. Merk, M. Sebastian, and C. Ronning, *Modeling of the ion-beam growth of covalently-bonded diamond-like materials*, Appl. Phys. A 66 (1998) 153–156.

[38] D.R. McKenzie, D. Muller, B.A. Pailthorpe, *Compressive-stress-induced formation of thin-film tetrahedral amorphous carbon*, Phys. Rev. Lett. 67 (1991) 773–776.

[39] I. Koponen, M. Hakovirta, R. Lappalainen, *Modeling the ion energy dependence of the sp^3/sp^2 bonding ratio in amorphous diamondlike films produced with a mass-separated ion beam*, J. Appl. Phys. 78 (1995) 5837–5839.

[40] N.A. Marks, *Thin film deposition of tetrahedral amorphous carbon: a molecular dynamics study*, Diamond Relat. Mater., 14 (2005) 1223–1231.

[41] Titanah et al., *The effect of hydrogen on the electronic and bonding properties of amorphous carbon*, J. Phys. Condens. Matter. 18 (2006) 10803-10816

[42] W. Jacob, *Surface reactions during growth and erosion of hydrocarbon films,* Thin Solid Films, 326 (1998), 1–42.

[43] C. Hopf, A. von Keudell, W. Jacob, *The influence of hydrogen ion bombardment on plasma-assisted hydrocarbon film growth,* Diamond Relat. Mater., 12 (2003) 85–89.

[44] A. von Keudell, T. Schwarz-Sellinger, W. Jacob, *Simultaneous interaction of methyl radicals and atomic hydrogen with amorphous hydrogenated carbon films*, J. Appl. Phys. 89 (2001) 2979–2986.

[45] A. von Keudell et al., *Deposition of dense hydrocarbon films from a nonbiased microwave plasma*, Appl. Phys. Lett. 62 (1993) 937–939.

[46] M.C.M. van de Sanden, *Radical and ion formation in an expanding thermal plasma used for thin film deposition*, Power Point Presentation, private communication, 2005

[47] A.M. Derkatch et al., *Branching ratios in dissociative recombination of the $C_2H_2^+$ molecular ion*, J. Phys. B 32 (1999) 3391–3398.

[48] J. Benedikt, *Acetylene Chemistry in Remote Plasmas: Implications for the a-C:H Growth Mechanism*, PhD Thesis, Technical University of Eindhoven, 2004.

[49] A.M. Mebel, R.I. Kaiser, *An ab initio study on the formation of interstellar tricarbon isomers l-$C_3(X^1\Sigma_g^+)$ and c-$C_3(X^3A_2')$*, Chem. Phys. Lett. 360 (2002) 139–143.

[50] Paolo Tosi et al., *Charge transfer of krypton ions with methane molecules from thermal energy to 10 eV*, Chemical Physics 209 (1996) 227–233.

[51] V.G. Anicich et al., *A SIFT ion molecule study of some reaction in titan's atmosphere. Reactions of N^+, N_2^+ and HCN^+ with CH_4, C_2H_2 and C_2H_4*, J. Am. Soc. Mass. Spectrom. 15 (2004) 1148–1155

[52] E.-C. Yang et al., *The theoretical study of reaction paths and transition station on coupling reaction of methane through plasma*, J. Molecular Structure (Theochem) 626 (2003) 121–126.

[53] K.K. Hirakuri et al., *Application of DLC films as masks for integrated circuit fabrication*, Diamond Relat. Mater. 12 (2003) 1013–1017.

[54] Yasushi Komatsu et al., *Application of the diamond-like carbon films in the integrated circuit fabrication process,* Diamond Relat. Mater. 8 (1999) 2018–2021.

[55] J. Seth et al., *Lithographic application of diamond-like carbon films*, Thin Solid Films. 34 (1995) 92–95.

[56] A. Grill, *From tribological coatings to low-k dielectrics for ULSI interconnects*, Thin Solid Films 398 –399 (2001) 527–532.

[57] P.R. Schwoebel, I. Brodie, *Surface-science aspects of vacuum microelectronics*, J. Vac. Sci. Technol. B 13 (1995) 1391.

[58] W. Choi et al., *Spatial variation of field emission current on nitrogen-doped diamond-like carbon surfaces by scanning probe method*, Diamond Relat. Mater. 10 (2001) 863–867.

[59] Y. Umehara et al., *Effects of sp^2/sp^3 bonding ratios on field emission properties of diamond-like carbon films grown by microwave plasma chemical vapour deposition*, Diamond Relat. Mater. 11 (2002) 1429–1435.

[60] S.R.P. Silva et al., *Electron field emission from carbon-based materials*, Thin Solid Films 482 (2005) 79–85.

[61] J. Robertson, *Requirements of ultrathin carbon coatings for magnetic storage technology*, Tribol. Int. 36 (2003) 405–415.

[62] P. Beer et al., *Antiabrasive coatings in a new application – wood rotary peeling process,* Vacuum 53 (1999) 363–366.

[63] M.A. Djouadi et al., *Antiabrasive coatings: application for wood processing*, Surf. Coat. Technol 116–119 (1999) 508–516.

[64] H. Fukui et al., *Cutting performance of DLC coated tools in dry machining aluminum alloys*, Surf. Coat. Technol. 187 (2004) 70–76.

[65] H. Hanyu et al., *The improvement of cutting performance in semi-dry condition by the combination of DLC coating and CVD smooth surface diamond coating*, Surf. Coat. Technol. 200 (2005) 1137–1141.

[66] M. Alton-Alaluf et al., *The influence of diamond-like carbon films on the properties of silicon solar cells*, Thin Solid Films 303 (1997) 273–276

[67] M. Alone-Alaluf et al., *Properties of GaAs solar cells coated with diamond-like carbon films* , Thin Solid Films 320 (1998) 159–162.

[68] V.G. Litovchenko, N.I. Klyui, *Solar cells based of DLC films – Si structures for space application,* Solar Energy Materials & Solar Cells 68 (2001) 55–70.

[69] V.S. Veerasamy et al., *Diamond-like amorphous carbon coatings for large areas of glass*, Thin Solid Films 442 (2003) 1–10.

[70] L. Hang et al., *Optimisation of diamond-like carbon films by unbalanced magnetron sputtering for infrared transmission enhancement*, Thin Solid Films 515 (2006) 357–361.

[71] P.E. Kondrasov et al., *Use of diamond-like carbon films in X-ray optics,* Diamond Relat. Mater. 6 (1997) 902–905.

[72] D.P. Drowling et al., *Application of diamond-like carbon films as hermetical coatings on optical fibres,* Diamond Relat. Mater. 5 (1996) 492–495.

[73] M. Smietana et al., *Optical properties of diamond-like cladding for optical fibres*, Diamond Relat. Mater 13 (2004) 954–957.

[74] G. Dearnaley, J. H. Arps, *Biomedical applications of diamond-like carbon (DLC) coatings: A review*, Surf. Coat. Technol. 200 (2005) 2518–2524.

[75] R. Hauert, *A review of modified DLC coatings for biomedical applications*, Diamond Relat. Mater. 12 (2003) 583–589.

[76] P.D. Maguire et al., *Mechanical stability, corrosion performance and bioresponse of amorphous diamond-like carbon for medical stents and guidewires*, Diamond Relat. Mater. 14 (2005) 1277–1288.

[77] V-M Tiainen, *Amorphous carbon as a bio-mechanical coating – mechanical properties and biological applications*, Diamond Relat. Mater. 10 (2001) 153–160.

[78] R. J. Narayan, *Nanostructure diamondlike carbon thin films for medical applications*, Mater. Sci. Eng. C 25 (2005) 405–416.

[79] R. Hauert, *An overview of the tribological behaviour of diamond like carbon in technical and medical applications*, Tribol. Int. 37 (2004) 991–1003.

[80] R. Pennings, *Mounting and leak-testing a plasma cascaded arc source*, internal OTB Engineering report.

[81] D.M. Hoffman and J.H. Thomas, *Confined oxygen glow discharge cleaning of silicon*, J. Vac. Sci. Technol. A4(3) (1996) 536–538.

[82] M. Li and H.F. Dylla, *Reducing of outgassing rate by glow discharge cleaning*, J. Vac. Sci. Technol. A 13(3) (1995) 571–575.

[83] M.C.M van de Sanden, private communication, 2005.

[84] J D Swift, M R J Shwar, *Electrical Probe for Plasma Diagnostics*, London: ILIFFE, 1970.

[85] Hiden Analytical, EQP/EQS operating manual, 1994.

[86] SPEX, 270M Rapid Scanning Imaging Spectrograph/Monocromator User Manual, 1992.

[87] http://www.mikropack.de/e/tfm/elli/theory.html

[88] Rudolph Research, AutoEL® III Automatic Ellipsometer Instruction Manual, 1982.

[89] TopoMetrix User's Manual, Version 3.05, 85-10086, Rev. C, 1996.

[90] E. Sourty, *The tribology of linear tape recording systems*, PhD Thesis, Aston University, 2002.

[91] J.C. Lascovich, R. Giorgi, S. Scaglione, *Evaluation of sp^2/sp^3 ratio in amorphous carbon structure by XPS and XAES*, Appl. Surf. Sci. 47 (1991) 17–21.

[92] J.C. Lascovich, S. Scaglione, *Comparison among XAES, PELS and XPS techniques for evaluation of Sp^2 percentage in a-C:H,* Appl. Surf. Sci. 78 (1994) 17–23.

[93] P. Merel, M. Tabal, M. Chaker, S. Moisa, J. Margot, *Direct evaluation of sp^3 content in diamond-like carbon films by XPS*, Appl. Surf. Sci. 136 (1998) 105–110.

[94] P. Patsalas, M. Handrea, S. Logothetidis, M. Gioti, S. Kennou, W. Kautek, *A complementary study of bonding and electronic structure of amorphous carbon films by electron spectroscopy and optical techniques*, Diamond Relat. Mater. 10 (2001) 960–964.

[95] J. Filik, P.W. May, S.R.J. Pearce, R.K. Wild, K.R. Hallam, *XPS and laser Raman analysis of hydrogenated amorphous carbon films*, Diamond Relat. Mater. 12 (2003) 974–978.

[96] E.C. Samano et al., *DLC thin films characterized by AES, XPS and EELS*, Appl. Surf. Sci. 202 (2002) 1–7.

[97] Horiba Group, *Derivation of physical parameters from Raman spectra of hard carbon films*, Raman Spectroscopy Application Note, A.N. no. 07, February 2000.

[98] F. Adar et al., *FT-IR and Raman microscopy on a united platform*, Spectroscopy 18:2 (2003) 34–40.

[99] A.C. Ferrari et al., *Resonant Raman spectra of amorphous carbon nitrides: the G peak dispersion*, Diamond Relat. Mater. 12 (2001) 905–910.

[100] A.A. Ogwu et al., *The effect of the substrate bias on the Raman spectra and thermal stability of diamond-like carbon (DLC) and silicon-modified DLC films prepared by plasma-enhanced chemical vapour deposition (PECVD)*, J. Phys. D: Appl. Phys. 32 (1999) 981–987.

[101] J.R. Shi et al., *Ultraviolet and visible Raman studies of nitrogenated tetrahedral amorphous carbon films*, Thin Solid Films 366 (2000), 169–174.

[102] D.J. Gardiner, P.R. Graves (editor), *Practical Raman Spectroscopy*, Springer Verlag - Berlin, 1989.

[103] Micro Materials Nano Test User's Manual, version 2.0, 2003.

[104] W.C. Oliver and G.M. Pharr, *An improved technique for determining hardness and elastic modulus using load and displacement sensing indentation experiments*, J. Mater. Res. 7 (1992) 1564–1583.

[105] http://www.micromaterials.co.uk/NanoTestIndentationAnalysis.htm

[106] J.F. Lin, P.J. Wei, J.C. Pan, C-F Ai, *Effect of nitrogen content at coating film and film thickness on nanohardness and Young's modulus of hydrogenated carbon films*, Diamond Relat. Mater. 13 (2004), 42–53.

[107] H. Kim, D.H. Jung, B. Park, K.C. Yoo, J.J. Lee, J.H. Joo, *The effect of substrate bias voltage and the deposition pressure on the properties of diamond-like carbon produced by inductively coupled plasma assisted chemical vapour deposition*, Surf. Coat. Technol. 193 (2005), 255–258.

[108] P. Bruno, G. Cicala, A.M. Losacco, P. Decuzzi, *Mechanical properties of PECVD hydrogenated amorphous carbon coatings via nanoindentation and nanoscratching techniques*, Surf. Coat. Technol. 180-181 (2004), 259–264.

[109] J.P. Quinn, P. Lemoine, P. Maguire, J.A. McLaughlin, *Ultra-thin tetrahedral amorphous carbon films with strong adhesion, as measured by nanoscratch testing*, Diamond Relat. Mater. 3 (2004), 1385–1390.

[110] S.J. Bull, *Nanoindentation of coatings*, J. Phys. D: Appl. Phys. 38 (2005), R393–R413.

[111] http://www.jascofrance.fr/pdf/ftir.pdf

[112] http://sis.bris.ac.uk/~sd9319/spec/IR.htm

[113] I.A. Rusu, *Contributions to the study of micro and macroscopic phenomena in the unhomogenous regions of low temperature plasma*, PhD Thesis, Iasi, 2001 (In Romanian).

[114] ThermoMircoscopes user's guide to AutoProbe CP and M5, Part III: Software Reference, 48-101-1101, Rev. B, May 2000.

[115] D. Briggs and M.P. Seah (editors), *Practical Surface Analysis*, 2nd edition, vol. 1 (1990) Chapter 5, p 270.

[116] J.F. Watts and J. Wolstenholme, *An Introduction to Surface Analysis by XPS and AES*, (2003), p 92.

[117] C. Casiraghi et al, *Bonding in hydrogenated diamond-like carbon by Raman spectroscopy*, Diamond Relat. Mater. 14 (2005) 1098-1102.

[118] M.J. Bamber, K.E. Cooke, A.B. Mann, B. Derby, *Accurate determination of Young's modulus and Poisson's ratio of thin films by a combination of acoustic microscopy and nanoindentation*, Thin Solid Films 398-399 (2001) 299–305.

[119] A.C. Fischer-Cripps, *Critical review of analysis and interpretation of nanoindentation test data*, Surf. Coat. Technol. 200 (2006) 4153–4165.

[120] G.M. Pharr, *Measurement of mechanical properties by ultra-low load indentation*, Mater. Sci. Eng. A253 (1998) 151–159.

[121] B.D. Beake, *Mechanical properties of DLC films on Silicon probed by nanoindentation*, private communication, May 2004.

[122] *HyperChem® Release 5 for Windows®. Getting Started.* Hypercube, Inc. Canada, 1998.

[123] *HyperChem® Computational Chemistry*. Hypercube, Inc. Canada, 1994.

[124] Z.J. Li et al., *Investigation of ion-beam-assisted deposition DLC films by molecular dynamics simulation*, Surf. Coat. Techol. 192 (2005) 64–69.

[125] V. Kolobov, R. Arslanbekov, *Deterministic Boltzmann solver for electron kinetics in plasma reactors for microelectronics applications*, Microelectronic Eng. 69 (2003) 606–615.

[126] N. Marks, *Modelling diamond-like carbon with the environment-dependent interaction potential*, Journal of Physics: Condens. Matter 14 (2002) 2901-2927.

[127] B. Zlamal, *Modelling of diamond-like hydrogenated carbon films using HyperChem*, internal presentation of Surface Science Research Group, Aston University, 2005.

[128] S. Stoykov et al., *Plasma chemistry and growth of nanosized particles in a C_2H_2 RF discharge*, J. Phys. D: Appl. Phys. 34 (2001) 2160–2173.

[129] http://wine1.sb.fsu.edu/chm1045/Bonding/Strength/Bond09.htm

[130] L.A. Curtiss, J.A. Pole, *Theoretical study of the C-H bond dissociation energy of acetylene*, J. Chem. Phys. 91(4) (1989) 2420–2432.

[131] http://www.hnu.com/secure/technology/photoionization.html

[132] J. Benedikt et al., *Threshold ionization mass spectrometry study of hydrogenated amorphous carbon films growth precursors*, Chem. Phys. Lett. 402 (2005) 37-42.

[133] W.M.M. Kessels et al., *A model for the deposition of a-C:H using an expanding thermal arc*, Surf. Coat. Technol. 98 (1998) 1584 – 1589.

[134] T. Schwartz-Sellinger, A von Keudell, W. Jacob, *Plasma chemical vapor deposition of hydrocarbon films: The influence of hydrocarbon source gas on the film properties*, J. Appl. Phys. 86 (1999) 3988–3996.

[135] S. Kruger et al., *Characterisation of plasma polymers by thermoluminescence*, Surf. Coat. Technol. 201 (2006) 543–552.

[136] H.K. Yasuda, *Glow discharge polymerization*, J. Polym Sci.: Macromol. Rev. 16 (1981) 199–293.

[137] B.D. Beake, G.J. Leggett, *Nanoindentation and nanoscratching testing of uniaxially and biaxially drown poly(ethylene terephthalate) film*, Polymer 43 (2002) 319–327.

Appendix – Publications

1. Cascaded arc deposited diamond like hydrogenated carbon films

T. Zaharia, B. Zlamal, J.L. Sullivan, S.O.Saied, R.C.M. Bosch, M.D. Bijker, *Juniormat '05 Conference Proceedings*, Brno, Czech Republic, September 20-21, 2005.

2. Fast deposition of diamond-like hydrogenated carbon films

T. Zaharia, J.L. Sullivan, S.O.Saied, R.C.M. Bosch, M.D. Bijker, *Diamond Relat. Mater.* 16 (2007) 623-629.

3. Physical properties of ultra fast deposited micro and nano thickness amorphous hydrogenated carbon films for medical devices and prostheses

T. Zaharia, J.L. Sullivan, S.O. Saied, R.C.M. Bosch, M.D. Bijker, *Proceeding of the Institution of Mechanical Engineers, Part H, Journal of Engineering in Medicine*, 2006, article in press

CASCADED ARC DEPOSITED DIAMOND LIKE HYDROGENATED CARBON FILMS

T. ZAHARIA[1], B. ZLAMAL[2], J.L. SULLIVAN[1], S.O.SAIED[1], R.C.M. BOSCH[3], M.D. BIJKER[3]

[1] *Surface Science Group, SEAS, Aston University, Aston Triangle, B4 7ET, United Kingdom*
[2] *Institute of Materials Science and Engineering, FME, Brno University of Technology, 616 69, CZ*
[3] *OTB Group, Luchthavenweg 10, 5657 EB, Eindhoven, The Netherlands*

ABSTRACT

Diamond like hydrogenated carbon films have been formed on different substrates at very low energies and temperatures by PECVD process employing acetylene as the precursor gas. The plasma source was of a cascaded arc type with Ar as carrier gas. The films grown at ultra fast rates were found a practical thickness limit of ~1 μm above which delamination from the substrate occurred.

Deposition on Si (100), glass and plastic substrates has been studied and the films characterized in terms of sp^3 content, roughness, hardness and adhesion.

Deposition rates up to 20 nm/sec have been achieved at substrate temperatures below 100°C. The typical sp^3 content of 60-75% in the films was determined by a combination of XPS and XAES techniques.

The hardness and adhesion of the films was measured using a MicroMaterials Nano Test Indenter/Scratch tester. Hardness was found to vary from 5 to 11 GPa depending on the admixed acetylene flow. Adhesion was found to increase drastically when in situ cleaning of the substrate was employed.

Modelling of the film growth on Si substrate and of dissociation patterns in the plasma was attempted using HyperChem® software.

1. INTRODUCTION

The interest in diamond like carbon films has been growing over the last two decades due to their unique properties such as high hardness, chemical inertness, high band gap and biocompatibility [1].

In this work DLC hydrogenated films have been formed at very low ion energies (less than 1eV) and low substrate temperatures (less than 100°C) using acetylene as a precursor gas, on different substrates (silicon, glass, PET, PEEK). The films were analysed as a function of the plasma parameters in terms of sp^3 fraction, hardness and adhesion.

The existing deposition models [1-6] consider the physical interactions, where in fact chemical processes may be the driving factor at low impact energies [7].

2. EXPERIMENTAL SET-UP

The deposition set-up is shown in Figure 1. The plasma source is a cascaded arc using Ar as carrier gas. This creates an Expanding Thermal Plasma (ETP) in the vacuum chamber [8]. When the precursor gas is injected in the nozzle or via an injection ring the gas molecules are dissociated and ionised and this gives rise to a high flux of particles (neutrals and ions) directed

towards the substrate. Typical ionisation in the plasma jet is between 2 to 10% of the total carrier gas volume [9].

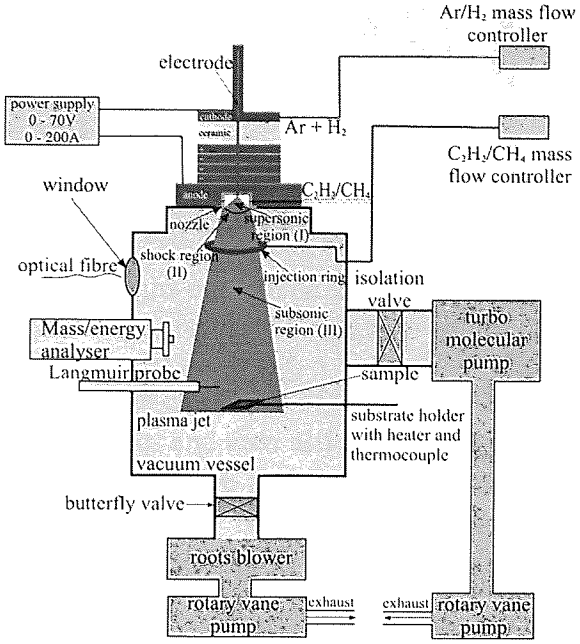

Figure 1. The schematics of the experimental set-up

Pressures and flow rates during each experimental run were maintained in the vacuum chamber by a roots blower pump. Prior to each experiment, the vacuum chamber was pumped down to a base pressure of less than 5×10^{-6} Torr using a turbomolecular pump. Two different positions for the injection of the precursor gas were used, i.e. "ring up" and "ring down" position.

The plasma Ar jet was analysed using a Hiden Mass/Energy analyser and a Hiden Langmuir electrical probe to monitor the species, concentrations and energy of the ions.

The topography and surface roughness of the films was mapped with a Thermo Microscopes M5 atomic force microscope, used in contact mode.

Sp^3 fractions were determined by a combination of XAES and XPS techniques [10] in a VG Escalab 200D spectrometer. The X ray source used was Al Kα (1486.6 eV).

Hardness was measured with a Micro Materials NanoTest 500 instrument using a Berkovich indenter. The indentation depth was kept to 10% of the film thickness to minimise the influence from the substrate [11]. Scratch tests were performed on each sample with a Rockwell indenter. The scratch length was 600 μm and the maximum force applied during the tests was typically 200 mN. To quantify the adhesion of the film to the substrate the critical loading divided by the film thickness was calculated and compared for each sample.

3. RESULTS

The energy analyser indicated that the energy of the Ar ions in the region close to the sample holder was around 0.3 eV. Langmuir probe current-voltage characteristic showed that the Ar ions density in the downstream region was 3.5×10^{18} m^{-3}. The deposition rates increased with the increase in relative C_2H_2:Ar flow and reached values of 20nm/s for 10% C_2H_2 relative flows. The relative hydrogen atomic concentration was found to decrease with the increase in relative C_2H_2:Ar flow to typical values of 22-23% for 6-10% C_2H_2 relative flows.

AFM mapping of the film's surfaces revealed that the deposited films were smooth, with roughness values (Ra) similar to the virgin substrates (Figure 2).

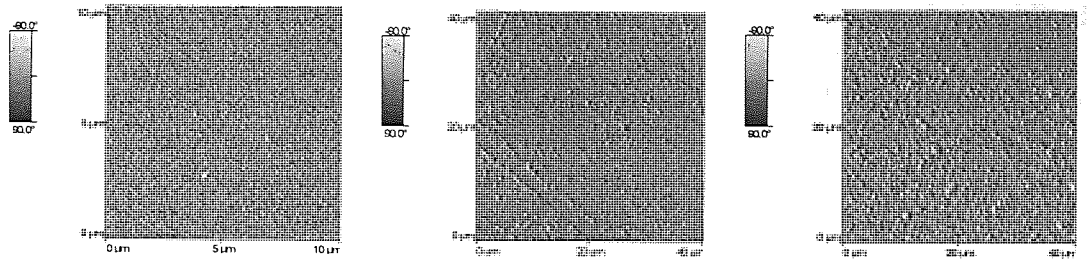

Figure 2. AFM images of a-C:H films on: silicon substrate (left) (Ra=1.5nm); glass substrate (middle) (Ra = 4.5nm) and PET substrate (right) (Ra = 22nm)

Sp^3 fractions were calculated from the derivative of the C KLL XAES spectra. The raw spectrum was smoothed with 27 points, 2 passes and then differentiated by a Savinsky-Golay method. The difference between the mean of the positive and negative peaks (D) [10] was monitored for all films. Typical sp^3 fractions found were 60-75%, higher than expected for this type of films, due to the presence of polymeric sp^3 C-H bonds at the same binding energy as C-C sp^3 bonds.

The software provided with the Nano Tester automatically calculates the hardness of the films at the desired indentation depth. Comparing the topography of the surface before and after each scratch allowed the identification of the critical loading. This value was then divided by the thickness of each film. The results are presented in Figure 3.

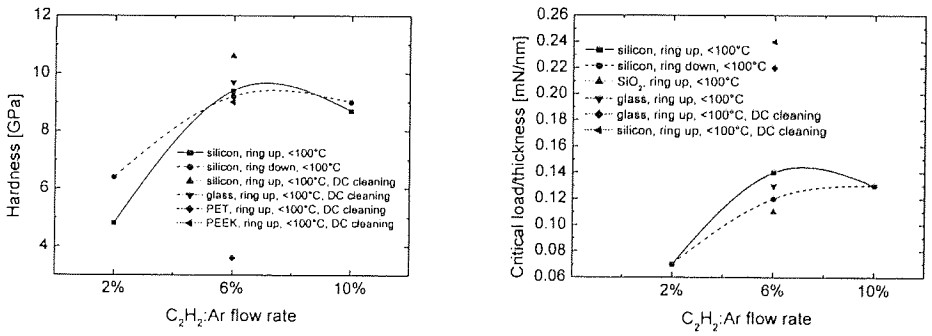

Figure 3. Hardness (left image) and adhesion (right image) against C_2H_2 relative flow for a-C:H films grown from acetylene on different substrates and under different conditions

The hardness measurements show that harder films are formed at 6% C_2H_2:Ar flow ratio. The indentations on films deposited on softer substrates (PET, PEEK) were difficult to analyse. The adhesion tests show a similar trend to hardness, and adhesion was found to improve drastically when an extra step of in situ DC plasma cleaning was employed.

4. MODELLING

Simulations of systems with C_2H, C_3, C_3H and C_3H_2 radicals coming towards the silicon surface were performed using Hyperchem software package. The silicon surface was built and geometrically optimized to find its minimum energy. The molecular dynamics (MD) simulations of each system with specific conditions were performed. For calculations, the semi-empirical method PM3 was used [12] and typical conditions were: velocity of radical v=10Å/ps, simulation time t=1ps, temperature T=363K. After the MD simulations the rearrangement of

atoms was observed (see Figure 4). The bond lengths $C-C$ (1.50Å), $C=C$ (1.32Å), $C\equiv C$ (1.21Å), $C-Si$ (1.75Å), $Si-Si$ (2.60Å) were measured and compared with theoretical values in an attempt to differentiate between the types of bonds created in the simulations. During the MD calculations kinetic energy E_{kin}, potential energy E_{pot} and total energy E_{TOT} of the whole system were computed. From the saturated values at the end of the MD simulations, energy per atom E_{ATOM} (4.2 ÷ 5.2eV) and kinetic energy per atom $E_{ATOMkin}$ (0.05 ÷ 0.15eV) were derived.

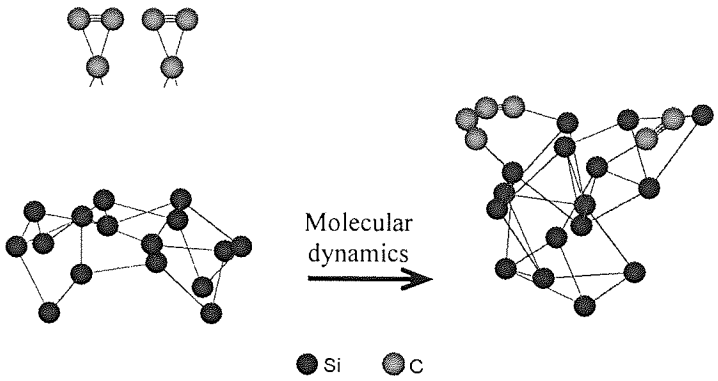

Figure 4. MD simulation for C_3 radicals and Si surface (t=1ps, T=363K, v_{C3}=10Å/ps)

5. CONCLUSION

DLC hydrogenated films have been obtained using acetylene as precursor gas at very low energies and low deposition temperatures. The growth rates for these films were very high (~20 nm/sec), the surface of the films was smooth and followed the roughness of the virgin substrate (Ra < 3nm for Si substrates), the sp^3 fraction was 60%-70% and the hardness was around 11 GPa. The adhesion to substrate was improved drastically by in situ substrate cleaning.

The mechanism of deposition is not yet well understood, but the film properties are comparable to hydrogenated DLC films produced by other methods. The main advantage is the very fast growth rates and the simplicity of the equipment involved.

REFERENCES

[1] J. Robertson, Mater. Sci. Eng., R 37 (2002) 129.
[2] Y. Lifshitz, S.R. Kasi, J.W. Rabalais, W. Eckstein, Phys. Rev., B41 (1990) 10468.
[3] H. Hofsass, H. Feldermann, R. Merk, M. Sebastian, C. Ronning, Appl. Phys., A 66 (1998) 153.
[4] D.R. McKenzie, D. Muller, B.A. Pailthorpe, Phys. Rev. Lett. 67 (1991) 773.
[5] I. Koponen, M. Hakovirta, R. Lappalainen, J. Appl. Phys. 78 (1995) 5837.
[6] N.A. Marks, Diam. Rel. Materials, *Thin film deposition of tetrahedral amorphous carbon: a molecular dynamics study*, Article in Press.
[7] J. Benedikt, *Acetylene Chemistry in Remote Plasmas: Implications for the a-C:H Growth Mechanism*, PhD Thesis, Technical University of Eindhoven, 2004
[8] M.C.M. van de Sanden, J.M. de Regt and D.C. Schram, Plasma Sources Sci. Technol., 3 (1994) 501.
[9] J.W.A.M. Gielen, *Plasma beam deposition of amorphous hydrogenated carbon*, PhD Thesis, Technical University of Eindhoven, 1996.
[10] J.C. Lascovich, S. Scaglione, Appl. Surf. Sci. 78 (1994) 17.
[11] J.F. Lin, P.J. Wei, J.C. Pan, C-F Ai, Diamond Relat. Mater. 13 (2004) 42.
[12] HyperChem® Computational Chemistry Manual, Hypercube Inc., Canada, 1994, p. 122.